Fabrication and characterization of nanotextures for light management in photovoltaic and optoelectronic devices

vorgelegt von

univ. dipl. inž. el.
Marko Jošt
geb. in Celje, Slowenien

von der Fakultät IV – Elektrotechnik und Informatik
der Technischen Universität Berlin
zur Erlangung des akademischen Grades

Dr. der Ingenieurwissenschaften

-Dr. Ing. -

genehmigte Dissertation

Promotionsausschuss:

Vorsitzender:	Prof. Dr. Janez Krč, University of Ljubljana
Gutachter:	Prof. Dr. Bernd Rech, Technische Universität Berlin
	Prof. Dr. Bernd Szyszka, Technische Universität Berlin
	Prof. Dr. Marko Topič, University of Ljubljana
	Prof. Dr. Janez Trontelj, University of Ljubljana

Tag der wissenschaftlichen Aussprache: 21. Juni 2017

Berlin, 2017

Zahvala/Acknowledgement

Iskreno se zahvaljujem svojemu mentorju ***prof. dr. Marku Topiču*** za sprejem v LPVO in mentorstvo med doktorskim izobraževanjem. Brez njegovih izkušenj, vodstva in pregleda nad področjem bi raziskovalni rezultati in doktorska naloga ne bili v takšni obliki kot so. Poleg številnih nasvetov in obilice pomoči sem še posebej hvaležen za možnost raziskovanja v Berlinu in omogočen doktorat na Tehnični univerzi v Berlinu.

Zahvalil bi se tudi ***prof. dr. Janezu Krču*** za uvod v področje upravljanja s svetlobo ter nasvete, ideje in pomoč pri sistemih za merjenje sipane svetlobe.

Sodelavcem LPVO se zahvaljujem za prijetno delovno okolje, pomoč pri raziskovanju in številne zanimive debate ob jutranji kavi. Vsak nasvet in ideja sta prišla še kako prav pri raziskovanju.

I gratefully acknowledge ***Prof. Dr. Bernd Rech*** for accepting me at Institute for Silicon Photovoltaics, Helmholtz-Zentrum Berlin, Germany and supervision at Technical University Berlin. I thank ***Dr. Steve Albrecht*** for his mentorship and introduction into the world of perovskites during my stay in Berlin. I also thank ***members*** at Institute for Silicon Photovoltaics, Helmholtz-Zentrum Berlin for warm hospitality and help with my research, especially ***Lukas, Moritz, Paul, Steffen*** and ***Oleksandra*** for a friendly and relaxed working environment.

I acknowledge ***Dr. Ivan Gordon*** and ***Christos Trompoukis*** for providing the silicon master with inverted pyramids and ***Prof. Dr. Christophe Ballif*** and ***Etienne Moulin*** for providing the TCO samples. I thank ***Dr. Hana Uršič Nemevšek*** and ***Prof. Dr. Barbara Malič*** from K5 department at Institute Jozef Stefan for using their AFM.

Posebna zahvala gre tudi mojim staršem in bratu, ki so mi v vseh letih izobraževanja nudili podporo, vzpodbudo in številne nasvete.

Za finančno podporo se zahvaljujem ***Javni agenciji za raziskovalno dejavnost Republike Slovenije ter Javnemu skladu Republike Slovenije za razvoj kadrov in štipendije.***

Abstract

Light management is an important aspect of photovoltaics to assure efficient exploitation of solar energy and improve the efficiency of solar cells. Efficient light management is based on anti-reflection and light scattering. The former results in increased light in-coupling, and the latter prolongs the optical path in the active layer of a solar cell; consequently, the conversion efficiency increases. Both effects are usually induced by textured surfaces, either within the device structure or on top of the device. In the doctoral dissertation, we focus on fabrication and characterization of textured light management layers. The created light management (LM) foil is then applied on top of perovskite solar cells to enhance the perofromance and analyze the improvements in the fabricated devices.

The Ultra-Violet Nanoimprint Lithography (UV NIL) is used to create the textured LM foils. It is a novel approach for replicating textured surfaces. The process is cost-effective, simple and faster compared to other texturization techniques. In the replication process, the texture surface from the master is transferred to the replica with the help of the intermediate stamp and the UV sensitive lacquers coated on the substrates. We present the replication process and thoroughly characterize the created replicas using surface morphology and transmittance measurements. Good transfer fidelity and moderate thermal stability up to 200 °C were obtained. During the thermal stability test the samples that were exposed to high temperature (200 °C) for a longer time (>30 min) turned slightly yellow. The yellowing effect resulted in diminished total and diffuse transmittance of light for the wavelengths below 500 nm. Similar effect is also observed during the outdoor testing where different configurations were tested, some samples were placed on a white and some on a black surface. After three-month exposure to outdoor environmental conditions the samples turned yellow. Samples on black surface heated more and the yellowing effect was severer than for the samples on white surface. Additionally, the lacquer slightly melted which is confirmed by lower σ_{RMS} values. This shows that replication lacquers with more stable chemical composition are needed for use in real outdoor applications. If the LM foil is used inside the device, an additional

conductive layer of transparent conductive oxide (TCO) has to be deposited on top of the LM foil to form electrical contact as the UV NIL lacquers are non-conductive. In our case, a gallium doped ITO (GITO) is used as a TCO. The successfulness of the deposition is confirmed by sheet resistance, optical (transmission) and surface morphology measurements.

To fulfill their role, the created replicas should preserve the light scattering properties of the master. For the light scattering characterization, a novel camera-based system is developed. It enables measurements of the spatial angular distribution function (3D ADF) of scattered or emitted light using a digital camera. 3D ADF is determined from the digital image captured from a flat screen. We present two solutions. The first uses a reflective screen and a lens to broaden the angular range. The second uses a transmissive screen positioned at 45°, enabling measurements of all the polar angles. With the developed camera-based systems we can quantify transmitted or reflected light scattered by textured samples or emitted light from light sources in a few seconds. In the dissertation, both setups are described, and main transformations of the acquired digital image to obtain the 3D ADF are explained. The systems are validated on randomly nanotextured transparent samples and a periodically textured non-transparent sample. Good matching is obtained with rigorous simulations, and measurement results carried out with the conventional goniometric angular resolved scattering system. The system with the transmissive screen is used to characterize the created replicas.

To test the functionality of the created LM foils in a real application, inorganic-organic perovskites that have proven to be an effective class of materials for fabricating efficient solar cells are used. We apply an LM foil created by UV NIL on the glass side of an inverted (p-i-n) perovskite solar cell with 16.3% efficiency. The obtained 1 mA cm^{-2} increase in the short-circuit current density translates to a relative improvement of 5% in cell performance, which results in a power conversion efficiency of 17.1%. To support the experimental findings, optical 3D simulations based on experimentally obtained parameters are used. A good match between the simulated and experimental data is obtained, validating the model. Optical simulations reveal that the main improvement in device performance is due to a reduction in total reflection and that relative improvement in the short-circuit current of up to 10% is possible for large-area devices. The optical model is also used to analyze the potential of monolithic perovskite/silicon-heterojunction tandem devices that can theoretically overcome the efficiencies of the single junction solar cells. We consider four different device designs in the optical

simulations: the planar device, the device built on back- and both-side textured Si wafer, and the device with the textured LM foil. For each of these four designs, the current matching point is simulated to evaluate device efficiencies. The results reveal that the device built on a both-side textured silicon wafer, which is the best performing configuration, can reach 15% relative higher efficiency than planar device. The obtained results show the potential of LM foils for improving the device performance of perovskite solar cells and pave the way for further use of optical simulations in perovskite single junction or tandem solar cells.

Razširjeni povzetek

Uvod

Za zmanjševanje onesnaževanja okolja in omejitev globalnega segrevanja postajajo obnovljivi viri energije vedno pomembnejši. Še posebej svetlo prihodnost ima fotovoltaika, saj je sonce neusahljiv in brezplačen vir energije, ki je dostopen na celotni zemeljski obli. V primerjavi z ostalimi viri energije pridobivanje elektrike iz sončne energije ne povzroča nastajanja izpušnih plinov, ogljični odtis pa je tudi z vključeno proizvodnjo sončnih fotonapetostnih modulov vsaj dvajsetkrat manjši v primerjavi s fosilnimi gorivi. Optimizacija proizvodnih procesov je tudi znižala energijsko vračilno dobo sončnih elektrarn (PV sistemov), ki je za osrednjo Evropo padla na dve leti za polikristalne silicijeve module in tudi pod dve leti za tankoplastne sončne celice. Celo Kitajska, eden izmed največjih onesnaževalcev na svetu, je prepoznala potrebo po čistejšem okolju. Tako je poleg vodilne vloge v proizvodnji sončnih fotonapetostnih modulov, prevzela tudi vlogo največjega proizvajalca elektrike iz sončne energije. Njen pospešen vstop na fotovoltaični trg je povzročil drastičen padec cen in eksponentno rast kumulativne nameščene moči po svetu. V zadnjem letu smo v svetovnem merilu namestili za 70 GW sončnih elektrarn, skupna nameščena moč pa je presegla 300 GW. Potencial in prednosti uvrščajo fotovoltaiko med najpomembnejše trajnostne energetske tehnologije na področju obnovljivih virov in tudi v energetiki nasploh.

Osnovni fotonapetostni gradnik je polprevodniška sončna celica. Lastnosti polprevodniškega materiala, predvsem energijska reža, so tiste, ki najbolj vplivajo na učinkovitost pretvorbe sončne celice. Za enospojne sončne celice je teoretična limita (Shockley-Queisser limita) pri standardnih testnih pogojih 33,7 % za energijsko režo 1,34 eV. Na podlagi polprevodnika ločimo več tipov sončnih celic. Najpogostejše so kristalne silicijeve sončne celice (prva generacija), ki dosegajo visoko učinkovitost pretvorbe (do 26,3 %) in največji tržni delež ($>$ 86 %) na svetovnem trgu. Druga generacija so tankoplastne sončne celice, kjer je aktivna plast debela le par mikrometrov, v primerjavi s 150 ali več μm pri kristalnih silicijevih sončnih celicah. Popularnost tankoplastnih sončnih celic temelji na pričakovanih nižjih stroških izdelave. Zaradi

tanjših plasti potrebujemo manj materiala, proizvodni stroški pa so zaradi nizkotemperaturnih procesov nižji in energetsko učinkovitejši. Tipična predstavnika sta CIGS in CdTe, ki sta dosegla tudi masovno industrijsko proizvodnjo. Sončne celice tretje generacije (organske, elektrokemijske, perovskitne) obetajo še nižje proizvodne stroške, a industrijske proizvodnje še niso dosegle. So pa v zadnjem času v znanstveni sferi veliko pozornosti pritegnile perovskitne sončne celice, saj so v le nekaj letih raziskovanja dosegle učinkovitost pretvorbe do 22,1 %, kar je najhitrejši porast do sedaj. Kljub nizkim stroškom proizvodnje in visokim učinkovitostim pretvorbe, pa perovskitne sončne celice vseeno čaka še dolga pot. Predvsem stabilnost in majhna površina do sedaj izdelanih celic predstavljata glavni oviri do množične proizvodnje, a hiter razvoj in obsežne raziskave dajejo upanje na industrijsko proizvodnjo vsaj za nišne aplikacije.

Upravljanje s svetlobo v tankoplastnih sončnih celicah

Tankoplastne sončne celice predstavljajo nizkocenovno alternativo običajnim kristalnim silicijevim sončnim celicam, saj so za njihovo izdelavo potrebne nižje temperature, porabi se manj materiala, izdelamo pa lahko celo upogljive celice. V primerjavi s kristalnimi silicijevimi sončnimi celicami so tankoplastne tanjše, kar se v splošnem lahko odrazi v manjši absorpciji svetlobe. Ker je učinkovitost pretvorbe sončnih celic v veliki meri odvisna od absorpcije v aktivni plasti, je za povečanje absorpcije v tanjših absorpcijskih plasteh potrebno skrbno upravljanje svetlobe. Ena izmed najuspešnejših tehnik povečanja absorpcije svetlobe v tankoplastnih sončnih celicah je teksturiranje površine, bodisi na zgornji ali spodnji plasti celice. Teksturirane površine z nanometrsko ali mikrometrsko hrapavastjo povzročajo protiodbojni efekt ali sipanje svetlobe (velikost posameznih struktur enaka ali večja valovni dolžini), kar podaljša optično pot v aktivni plasti. S tem povečamo svetlobno generirani tok celice, in če se ne spremenijo električne lastnosti (napetost odprtih sponk V_{OC} in polnilni faktor FF), tudi učinkovitost pretvorbe.

Teksturirane plasti lahko vpeljemo na ali pa v strukturo sončne celice. Lahko na sprednjo stran stekla v superstrat konfiguraciji pritrdimo teksturirano folijo za upravljanje s svetlobo (LM folija) ter s tem zmanjšamo odbojnost in povzročimo sipanje svetlobe. Lahko pa teksture vpeljemo znotraj strukture. V tem primeru so teksturirane površine prozorni prevodni oksidi (TCO, nanešen na steklo v superstrat konfiguraciji) ali teksturirani substrati (teksturirani zadnji odbojnik na plastični ali kovinski foliji), lahko pa v strukturo vključimo tudi dodatne plasti. Za obetaven način vpeljave želenih tekstur

v sončne celice se je v zadnjih letih izkazala tehnologija vtisa vnaprej pripravljenih nanostruktur v prozorne in na temperaturo odporne lake.

Ena izmed takih replikacijskih tehnik je UV nanovtisna litografija (UV NIL). Vzorci (teksture) so narejeni z mehansko deformacijo viskoznih polimerov (lakov), v katere vtisnemo teksturirani kalup, čemur sledi strjevanje laka z UV svetlobo (UV NIL). V kombinaciji z nanosom TCO na vtisnjeno plast se lahko izognemo dragi izdelavi TCO z naravno ali z dodatno obdelavo dobljeno teksturo. S procesom UV NIL prenesemo hrapavost površine s kalupa na repliko, pri čemer se ohrani morfologija kalupa in posledično sipanje svetlobe. Sipano svetlobo lahko nato karakteriziramo s kotno odvisno spektroskopijo (ARS), ki nam omogoča določiti funkcijo kotne porazdelitve (ADF) prepuščene in odbite sipane svetlobe (kako je svetloba sipana pod različnimi koti). Tipično določimo ADF z goniometričnimi sistemi, ki pa so počasni in merijo odziv le v eni ravnini (1D). Primernejši so sistemi s kamero, kjer sipano svetlobo projiciramo na zaslon in jo nato zajamemo s kamero. To nam omogoča hitrejšo in popolnejšo analizo sipane svetlobe v 3D prostoru.

V doktorski disertaciji smo se posvetili izdelavi in karakterizaciji plasti za upravljanje s svetlobo. Plasti smo izdelali s procesom UV NIL za replikacijo teksturiranih površin. Izdelane replike smo testirali in karakterizirali, med drugim tudi s sistemom za merjenje sipane svetlobe. V ta namen smo razvili dva sistema, enega z refleksijskim in enega s transmisijskim zaslonom. Delovanje in potencialne izboljšave z uporabo LM folije smo preverili na primeru perovskitnih sončnih celic. Delovanje brez in z LM folijo smo analizirali tako eksperimentalno kot tudi teoretično z optičnimi simulacijami.

UV nanovtisna litografija

UV NIL je nizkocenovna in visoko ločljivostna tehnika repliciranja tekstur. Njena glavna uporaba je pri vključevanju dodatnih (teksturiranih) plasti v strukturo sončnih celic za povečanje sipanja svetlobe in njenega ujetja ali za povečanje proti-odbojnega efekta. Poleg boljšega izkoriščanja vpadne svetlobe v sončnih celicah se UV NIL uporablja tudi za vpeljavo lastnosti nanotekstur rastlinskega in živalskega sveta, kot je hidrofobnost.

V strukturi sončne celice so teksturirane površine ponavadi TCO-ji, narejeni iz SnO, ZnO ali podobnih materialov. Naravna rast teh polikristalnih materialov običajno kaže naključno porazdelitev teksturiranosti, npr. piramidaste strukture pri LPCVD postopku ali kraterske oblike, ki jih dobimo pri jedkanju z magnetronom nanešenih plasti.

Vendar pa so simulacije pokazale, da so v nekaterih primerih za ujetje svetlobe primernejše periodične strukture (sinusne, piramide, invertirane piramide, nanostolpci). Za izdelavo takšnih struktur so potrebni zapleteni in/ali dragi postopki (fotolitografija z jedkanjem, litografija z ionskim snopom (FIB), litografija z elektronskim snopom (EBL), reaktivno jedkanje z ioni (RIE)) in kar je še pomembneje, pri večini teh postopkov je substrat silicij, ki ni prozoren. UV NIL nam omogoča replikacijo poljubnih tekstur s prozornimi laki, ki jih lahko nato vključimo v strukturo sončnih celic. Še več, izdelamo lahko tudi plasti z dvojno teksturizacijo, npr. periodične piramide (lak) + piramidaste naključne strukture z LPCVD nanosom ZnO na lak. S procesom NIL lahko izdelamo strukture velikosti nekaj deset nanometrov. Postopek je hiter, poceni in uporaben tudi v kolutni (roll-to-roll) proizvodnji.

Replicirane teksture so narejene z mehansko deformacijo viskoznih polimerov (lakov) pri vtisu teksturiranih kalupov. Replika je narejena preko vmesnega koraka, kjer izdelamo negativno repliko oz. štampiljko. Strjevanje lakov tako pri štampiljki kot pri repliki poteka pod vplivom UV svetlobe, po čemer je proces tudi dobil svoje ime. Vsaka štampiljka se lahko večkrat uporabi pri izdelavi replik, zaradi česar je ponovljivost ena izmed ključnih lastnosti procesa.

Uspešen prenos teksture s kalupa na repliko je najpomembnejši dejavnik za ohranitev lastnosti teksture (sipanje svetlobe, hidrofobnost itd.). Vernost prenosa določamo z morfološkimi meritvami z mikroskopom na atomsko silo (AFM) in optičnimi meritvami, merjenjem transmisije in kotne porazdelitve svetlobe. Za lažjo primerjavo morfologij lahko s podrobno kvantitativno post-analizo določimo različne parametre, kot so σ_{RMS} hrapavost, povprečni kot Θ_{avg}, korelacijska dolžina l_{c} in Fourierjeva analiza. Takšna analiza tudi z uporabo prosto dostopnih orodij za analizo (npr. Gwyddion) zahteva veliko časa, zato smo posebej za naš primer v okolju MATLAB® razvili orodje za analizo AFM meritev AFM Analyzer, ki omogoča hiter in enostaven izračun parametrov hrapavosti. Grafični vmesnik AFM Analyzer-ja omogoča enostavno izbiranje meritev, avtomatizirano določanje parametrov hrapavosti in grafični prikaz analize. Z enim klikom lahko analiziramo vse AFM meritve v direktoriju, omogoča pa nam tudi vrstični pregled meritve, in sicer po dve vrstici v x in y smeri. Vse izračunane podatke lahko enostavno shranimo.

V sklopu doktorske disertacije smo predstavili vse korake v procesu replikacije tekstur s postopkom UV NIL. Za izdelavo replik smo za kalup uporabili napršen ZnO:Al, jedkan v HCl, kar povzroči naključno teksturiranost kraterske oblike. Izdelane replike

smo temeljito karakterizirali z optičnimi in morfološkimi meritvami. Optične meritve so pokazale, da laki, iz katerih so replike izdelane, prepuščajo svetlobo brez izgub v vidnem in dolgovalovnem spektru, v UV delu pa je absorpcija večja. To je tudi pričakovano, saj prav ta absorpcija povzroči njihovo strditev. Meritev kotne porazdelitve sipane svetlobe je pokazala razlike med sipanjem svetlobe na kalupu in repliki, kar je posledica različnih lomnih količnikov kalupa in lakov za izdelavo replike. AFM meritve so razkrile zelo visoko vernost prenosa, parametri hrapavosti kalupa in replike so zelo podobni. Tudi v primeru, da isto štampiljko uporabimo dvanajstkrat, ostanejo tako morfološki kot tudi optični parametri primerljivi, kar nakazuje na visoko ponovljivost procesa. Analizirali smo tudi termično stabilnost lakov. Analiza je pokazala, da laki preživijo do 200 °C in pri segrevanju ne izpuščajo plinov. Vseeno je daljša izpostavljenost visokim temperaturam povzročila rumenenje, kar se odrazi v zmanjšani transmisiji v valovnem območju pod 500 nm ter s tem negativno vpliva na delovanje naprav, kjer je LM folija uporabljena. Pri 633 nm, kjer smo merili 3D ADF, večjih sprememb nismo opazili, čeprav deluje 3D ADF na prvi pogled ožji za segrevane replike, a se tega v 1D grafih ne vidi. Termogravimetrijska analiza je poleg minimalnega uhajanja pokazala tudi, da na replike negativno deluje tudi ponavljajoče spreminjanje temperature. Medtem ko smo merili težo vzorcev, smo jih odstranili z grelne plošče in so se začasno ohladili. Rezultat so bile bolj staljene oz. zaobljene strukture kot pri vzorcih, ki so bili samo na eni temperaturi.

Vtisnjene plasti oz. replike se v sončnih celicah uporabljajo zunaj ali pa znotraj sončne celice. V primeru, da jo uporabljamo kot teksturirano LM folijo na vrhu celice, mora replika vzdržati zunanje pogoje brez degradacije. Zato smo izvedli trimesečno testiranje pri zunanjih pogojih na strehi Fakultete za elektrotehniko, Univerze v Ljubljani. Izdelali smo replike z ravno in teksturirano površino ter jih testirali v različnih konfiguracijah, in sicer steklo spodaj in lak zgoraj ter lak spodaj in steklo zgoraj. Prva ponazarja konfiguracijo, kjer je replika zunaj celice, druga pa ponazarja primer, kjer je replika znotraj celice. Prav tako smo preverili razliko med repliko na črni in beli površini. V času testiranja smo redno merili transmisijo, na koncu pa izvedli še AFM meritve in meritev s termično kamero. Rezultati merjenja transmisije so razkrili postopno rumenenje, ki je bilo na koncu preizkusnega obdobja vidno tudi s prostim očesom. Poleg zmanjšanja totalne in difuzne transmisije pod 500 nm smo opazili tudi zmanjšanje difuzne transmisije v celotnem valovnem območju. Razlog za znižanje transmisije so razkrile AFM meritve, kjer smo izmerili manjšo σ_{RMS} kljub večjemu številu prašnih delcev, ki so se nabrali na površini. Vzrok za nižje vrednosti parametrov hrapavosti je verjetno v

dolgotrajni izpostavljenosti povišanim temperaturam (test je bil namreč izveden poleti) in ponavljajočim se temperaturnim spremembam, ki so rahlo spremenile teksturo. Najslabše so se namreč odrezale replike, postavljene na črno površino. Meritve s termično kamero, izvedene septembra, so pokazale, da se lahko replike segrejejo tudi nad 40 °C, ta vrednost pa je bila julija zagotovo še višja. To je verjetno tudi razlog za rumenenje.

Teksturirane replike lahko vpeljemo tudi v strukturo sončne celice, ponavadi na steklo v superstrat konfiguraciji. V tem primeru prevzame tekstura replike vlogo teksture TCO-ja, a ker replike niso prevodne, je nanos TCO-ja vseeno potreben. Da ohranimo izbrano teksturo, mora biti nanos TCO tanek. V ta namen smo izdelali replike z ravno in teksturirano površino ter nanje napršili GITO, z galijem dopirani ITO. Za kalup pri izdelavi replik smo uporabili na steklo napršen ZnO:Al, jedkan v HCl. Naprševanje GITO-ja je bilo uspešno, GITO se je dobro prijel na repliko in se ni odlepil niti po daljšem času. Z GITO-m napršene replike so imele zmerno prevodnost, ki se je izboljšala po temperaturni obdelavi pri 200 °C. AFM meritve so pokazale, da se je tekstura odlično ohranila, iz česar sklepamo na konformno rast GITO-ja. Tudi temperaturna obdelava pri 200 °C ni poškodovala teksture, plast GITO-ja je verjetno delovala kot zaščita. Dosegli smo visoko transmisijo (> 80 %) v širokem valovnem območju. Prevodnost in transmisijo bi lahko še izboljšali, a postopek ni bil optimiziran za nanos na replike, ampak na steklo.

Rezultati so pokazali, da je UV NIL primeren postopek za replikacijo tekstur. Eno štampiljko lahko uporabimo večkrat z visoko vernostjo prenosa, pri čemer se ohranijo tudi lastnosti sipanja svetlobe. Prav tako je uspešen nanos TCO-ja na repliko. Vseeno je testiranje pri zunanjih pogojih razkrilo rumenenje in rahlo zmanjšanje hrapavosti replik. To pomeni, da so za uporabo v aplikacijah nujni laki z večjo stabilnostjo in obstojnostjo.

Organsko-anorganske perovskitne sončne celice

Organsko-anorganske perovskitne (v nadaljevanju perovskit) sončne celice so nov razred sončnih celic, ki je postal popularen v zadnjih letih predvsem zaradi visoke učinkovitosti pretvorbe in poceni izdelave. Prvo delujočo celico so izdelali leta 2009 z izkoristkom 3,8 %. Pravi razcvet pa se je začel leta 2012, ko so zamenjali tekoč elektrolit s trdim materialom za transport vrzeli (HTM – hole transport material) ter izboljšali stabilnost in učinkovitost pretvorbe na 9,7 %. Leta 2016 je učinkovitost pretvorbe že dosegla 22,1 %, kar velja za najhitrejši porast v učinkovitosti pretvorbe v zgodovini.

Perovskit ima kristalno zgradbo ABX_3, kjer je A velik kation, metilamonij ($CH_3NH_3^+$), etilamonij ($CH_3CH_2NH_3^+$), formamidinij ($NH_2CHNH_2^+$) ali celo cezij (Cs^+).

Kation B je ponavadi svinec (Pb^{2+}), lahko pa uporabimo tudi kositer (Sn^{2+}). X je halidni ion, običajno jodid (I^-), bromid (Br^-) ali klorid (Cl^-) ali njihova kombinacija (npr. $I_{3-x}Br_x$). Možne so različne A, B in X kombinacije, ki se odrazijo v različnih optoelektronskih lastnostih. Le-te so pri perovskitih odlične. Perovskiti so odlični absorberji vidne svetlobe, energijsko režo, ki je 1,55 eV za $CH_3NH_3PbI_3$, pa lahko spreminjamo z vključitvijo bromidnih ali kloridnih ionov. Zaradi visokega absorpcijskega koeficienta je tipična debelina perovskitnih sončnih celic le okoli 300 nm. Prav tako ima perovskit visoko mobilnost elektronov in vrzeli ter dolge rekombinacijske čase in difuzijske dolžine.

Perovskitne sončne celice so se razvile iz elektrokemijskih sončnih celic. Prve celice so ohranile mezoporozno strukturo in takšne celice še vedno sodijo med najučinkovitejše perovskitne sončne celice. Možne so tudi planarne konfiguracije, kjer so vse plasti gladke, saj ima perovskit visoke mobilnosti in dolge difuzijske čase. Zaradi ločitve nosilcev naboja je perovskitni absorber ukleščen med materiala za transport elektronov (ETM) in vrzeli (HTM). Naloga ETM in HTM je, da selektivno prepustita en tip nosilcev, drugemu pa prehod preprečita. Glede na to, na kateri strani perovskita se nahajata, ločimo med navadno (n-i-p) in invertirano (p-i-n) konfiguracijo. Pri konfiguraciji n-i-p je ETM med sprednjim kontaktom in perovskitom, HTM pa med perovskitom in zadnjim kontaktom. Pri p-i-n je situacija ravno obratna.

Ponavadi so celice izdelane na steklenih substratih, kjer je že nanešen TCO. Naslednje plasti so tipično nanešene z vrtenjem, tako ETM in HTM kot tudi perovskitne plasti, nekatere materiale pa lahko tudi naparimo. Pri nanašanju z vrtenjem so materiali raztopljeni v topilu, zato mu sledi tudi segrevanje, da topilo odstranimo. Zadnji kontakt je običajno naparjen. Izdelava perovskitne plasti je rahlo zahtevnejša. Formacija perovskitne kristalne strukture je običajno izvedena iz dveh prekurzorjev, npr PbI_2 in CH_3NH_3I. Nanos je nato izveden z različnimi postopki, kot so naparevanje, nanašanje s potapljanjem (dip-coating) ter enokoračno (one-step) ali dvokoračno (two-step) nanašanje z vrtenjem (spin-coating). Nato je potrebno izvesti še temperaturno obdelavo pri povišani temperaturi (80–120 °C), pri kateri prekurzorja reagirata in tvorita kristalno strukturo.

Nanašanje z vrtenjem je trenutno najbolj razširjena in najučinkovitejša metoda izdelovanja perovskitnih sončnih celic. Posledično je izdelava hitra in enostavna. Vseeno nas kljub doseženim visokim izkoristkom od masovne proizvodnje loči še veliko. Površina celic je namreč majhna, okoli 1 cm^2, celice pa so dokaj nestabilne. Napredek je sicer v zadnjem času očiten; raziskovalci so izdelali celice, ki s primerno enkapsulacijo preživijo

tudi 6 mesecev. Perovskitne sončne celice verjetno ne bodo nadomestile konvencionalnih sončnih celic, lahko pa imajo vlogo v tandemu z njimi, saj lahko tako znatno izboljšamo delovanje silicijevih sončnih celic.

S primerno izbiro in razmerjem halidnih ionov lahko s perovskiti dosežemo idealno razmerje energijskih rež za tandem s silicijevimi celicami (1,73 eV : 1,12 eV). Prvi poskusi so že pokazali obetavne rezultate tako 4-sponČnih kot tudi monolitnih 2-sponČnih tandemskih celic (4- and 2-terminal). Pri tandemskih celicah sta zaradi kompleksnosti izdelave, večjega števila plasti in ujemanja tokov obeh celic načrtovanje in izbira materialov in njihovih debelin še večjega pomena. V tem primeru je uporaba optičnih simulacij ključnega pomena, saj nam simulacije pomagajo predvideti delovanje ter s tem prihranijo čas in zmanjšajo število neuspešnih oz. neoptimalnih eksperimentalnih poskusov.

Tudi pri tandemskih sončnih celicah sta refleksija in podaljšanje optične poti pomembna dejavnika delovanja celice. Trenutne monolitne eksperimentalne celice niso izdelane na siliciju s teksturiranima obema stranema, saj nam tehnologija izdelave perovskitnih celice tega še ne omogoča. Lahko pa delovanje izboljšamo z uporabo LM folije in to preverimo z optičnimi simulacijami. V doktorski disertaciji se osredotočimo na monolitne 2-sponČne tandemske perovskit/silicijeve heterospojne sončne celice, kjer z optičnimi simulacijami predvidimo delovanje različnih konfiguracij brez in s teksturiranimi posameznimi plastmi.

V sklopu doktorske disertacije smo izdelali enospojne perovskitne sončne celice s p-i-n invertirano strukturo, kjer smo za HTM uporabili polimer PTAA. Konfiguracija izdelane sončne celice je bila steklo/ITO/PTAA/perovskit/PCBM/BCP/Ag. Perovskitno plast smo izdelali z enokoračnim nanašanjem z vrtenjem in postopek izdelave podrobno opisali. Končna velikost posamezne celice je bila 4 x 4 mm^2, na vsakem substratu pa je bilo 6 celic. Celice so dosegle visoko učinkovitost pretvorbe 16,1 %. Z dodatkom hipofosforne kisline (HPA) v raztopino perovskitnih prekurzorjev smo poskusili delovanje še izboljšati. HPA naj bi zmanjšala površinsko napetost med HTM in perovskitno plastjo. Tako bi bilo perovskitnih kristalov manj, a bi bili večji. Meritve so pokazale, da HPA izboljša morfologijo perovskita, na električno delovanje pa, razen manjšega izboljšanja FF, HPA ni imela vpliva. Te celice smo nato uporabili za testiranje delovanja LM folije. LM folijo smo izdelali s postopkom UV NIL, za kalup pa smo uporabili naključno teksturirano silicijevo rezino s piramidami velikosti do 8 μm. Pri *J-V* meritvah se je pokazalo 5-% relativno izboljšanje, dosegli smo učinkovitost pretvorbe

17,1 %. Izboljšanje je bilo predvsem na račun zmanjšanja refleksije, ki se je skoraj prepolovila, ter s tem povečanja kratkostične tokovne gostote J_{SC}. V_{OC} in FF sta ostala nespremenjena. Podobne izboljšave, čeprav z nižjim izkoristkom sončnih celic, smo dobili tudi, če smo namesto PTAA za HTM uporabili PEDOT:PSS. Vendar pa so EQE meritve pokazale manjše izboljšanje kot *J-V* meritve. Vzrok za nižji J_{SC} pri meritvah EQE v primerjavi z *J-V* meritvami smo pripisali uhajanju svetlobe iz celice, ki je posledica loma svetlobe na teksturi in majhne površine celice. Le-ta je tako majhna (4 x 4 mm^2) in steklo v primerjavi z njo tako debelo (1,1 mm), da velik del svetlobe zapusti območje aktivne plasti, še preden jo doseže. To ugotovitev smo preverili z optičnimi simulacijami. Zanje smo uporabili optični simulator CROWM, ki omogoča simulacije tankoplastnih struktur, kot so plasti perovskitnih sončnih celic, z debelimi plastmi v strukturi, kot so steklo, LM folija ali silicijeva rezina. CROWM obravnava tanke plasti koherentno, po principu prenosnih matrik, debele plasti pa nekohernetno, na osnovi sledenja žarkov. Vhodne parametre smo pridobili eksperimentalno. Debeline posameznih plasti smo določili iz presečne SEM meritve, *n* in *k* parametre pa s pomočjo *R&T* meritev ali literature za perovskit. Dobili smo zelo dobro ujemanje za EQE in refleksijo, tako za celico brez LM folije kot za celico z LM folijo, kjer smo omejili aktivno površino. Tako smo potrdili domneve o uhajanju svetlobe iz celice. Z dobrim ujemanjem za celici s PTAA in PEDOT:PSS kot HTM smo validirali optični model. V nadaljnjih simulacijah smo se osredotočili na celice s PTAA kot HTM. Simulacija z neomejeno aktivno površino je pokazala, da lahko za velike celice, kakršne so potrebne za sončni modul, pričakujemo okoli 10-% relativno izboljšanje. Validirani optični model smo nato uporabili, da raziščemo izgube v simulirani sončni celici. Ugotovili smo, da največ izgub predstavlja prav odboj od sprednje plasti (stekla), ki ga učinkovito zmanjšamo z LM folijo. Preostale izgube so skoraj zanemarljive, razen v primeru, ko imamo realno, omejeno celico s teksturo, kjer je velik del izgubljen zaradi uhajanja svetlobe. LM folija je učinkovita tudi v primeru, da imamo debelejšo plast perovskita, kjer podaljšanje optične plasti ni več relevantno. Tudi v primeru, da je perovskitna plast debela 1 μm, lahko pričakujemo do 8 % višji J_{SC}, saj zaradi zmanjšanja refleksije pride v celico večja količina svetlobe. Pokazali smo tudi, da z LM folijo izboljšamo V_{OC}. V tem primeru uporabimo tanjšo perovskitno plast, a je zaradi izboljšanja z LM folijo tok enak, koncentracija nosilcev pa večja, kar se odrazi v 36 mV večji V_{OC}. Za konec smo predvideli še izboljšanja z različnimi teksturami LM folije. Primerjali smo naključne piramide, ki smo jih tudi eksperimentalno testirali, periodične piramide, "cornercube" teksturo ter konkavno parabolično U in

konvkesno parabolično O teksturo. Vse teksture so izboljšale delovanje, za najboljšo se je izkazala tekstura "cornercube" s 15-% izboljšavo ob pravokotnem upadu svetlobe.

Optični model smo preverili tudi na monolitni tandemski perovskit/SHJ sončni celici, povzeti iz literature. Za perovskit smo povzeli podatke iz literature z energijsko režo 1,55 eV. Ponovno smo dobili dobro ujemanje med meritvijo EQE in optičnimi simulacijami, kar pomeni, da lahko optični model uporabimo tudi za simulacije tandemskih sončnih celic. Testirali smo monolitne perovskit/SHJ sončne celice v štirih različnih konfiguracijah. Merilo za izboljšanje je J_{SC} v točki tokovnega ujemanja (pri dvosponočni izvedbi sta celici vezani zaporedno in tokova obeh celic morata biti enaka za optimalno delovanje), za dosego le-te pa smo spreminjali le debelino perovskitne plasti, debeline ostalih plasti so bile konstantne. Začeli smo s planarno konfiguracijo, kjer so vse plasti gladke. Nato smo testirali celico, kjer je zadnja stran silicijeve rezine teksturirana, ter celico, kjer sta obe strani teskturirani. Druga opcija se je izkazala za izredno učinkovito, J_{SC}/učinkovitost pretvorbe smo izboljšali za 15 %. Žal ta možnost v praksi še ni izvedljiva, saj nanašanje z vrtenjem ni primerno za teksture mikrometrskih dimenzij. Izboljšanje je bilo spet predvsem na račun zmanjšanja refleksije ter tudi podaljšanja optične poti za dolgovalovno svetlobo v siliciju. Povečanje J_{SC} v siliciju je takšno, da moramo to kompenzirati z debelejšo perovskitno plastjo. Na koncu smo preverili še delovanje z LM folijo, ki smo jo postavili na vrh planarne tandemske celice. Testirali smo različne teksture LM folije, enako kot pri enospojnih perovskitnih sončnih celicah. Ponovno se je z LM folijo delovanje izboljšalo in spet je najboljša tekstura "cornercube". Nadaljnje izboljšave se skrivajo predvsem v izbiri ustreznejše energijske reže (1,73 eV namesto 1,54 eV), za kar bi potrebovali ustrezne n in k spektre, in pa optimizaciji debelin preostalih plasti. Smiselna bi bila tudi zamenjava HTM spiro-OMeTAD-a, saj ta poleg refleksije predstavlja na račun absorpcije glavni vir optičnih izgub.

Rezultati so potrdili, da lahko z LM folijami izboljšamo delovanje tako enospojnih kot tudi tandemskih perovskitnih celic. Za napovedovanje izboljšanja lahko uporabimo validirani optični model ter tako privarčujemo na času in denarju.

Sistemi za določanje sipane svetlobe s kamero

Kotna porazdelitev (ADF) sipane svetlobe na nanoteksturiranih površinah je pri tankoplastnih sončnih celicah močno povezana z učinkovitostjo pretvorbe. Ponavadi jo določamo s tehniko kotne odvisne spektroskopije (ARS), ki nam da pomemben podatek o učinkovitosti teksture za povečanje absorpcije v strukturi in s tem tudi višje

učinkovitosti pretvorbe naprave. Tipični ARS sistemi so goniometrični sistemi, ki merijo ADF sipane prepuščene in odbite svetlobe pri vsakem kotu sipanja posebej, ampak le v eni ravnini in pri izbrani valovni dolžini. Če predpostavimo rotacijsko simetrijo sipane svetlobe (pri naključni teksturizaciji), nam takšna meritev zagotovi dovolj informacij za določitev prostorskega (3D) ADF, vendar ga ne ovrednoti v celoti. Goniometrični ARS sistemi so zanesljivi in natančni, pri čemer je meritev dolgotrajna, še posebej pri visoki ločljivosti. Prav ti dve pomanjkljivosti goniometričnih ARS sistemov, meritev v le eni ravnini in počasnost, odpravijo sistemi ARS s kamero.

Sistemi ARS s kamero temeljijo na zaslonu, na katerega ujamemo/projiciramo sipano svetlobo, in kameri, s katero to svetlobo nato zajamemo. Glede na vrsto zaslona ločimo med sistemoma z refleksijskim in transmisijskim zaslonom. V sklopu doktorskega izobraževanja smo postavili oba sistema. Pomembno je, da zaslon odbito ali prepuščeno svetlobo tudi razprši, saj jo le tako lahko zajamemo s kamero. Sliko s kamere je potrebno še obdelati, da iz vrednosti posameznih pikslov določimo vrednosti ADF pri posameznih kotih v prostoru. Sistemi na osnovi CCD kamere so kompaktni, poceni in omogočajo določitev sipanja svetlobe v širokem območju kotov z enim zajemom slike (nekaj sekund) pri posamezni valovni dolžini.

V sistemu z refleksijskim zaslonom zajamemo s kamero svetlobo, ki se odbije od zaslona. Tako se izognemo izgubam v zaslonu zaradi absorpcije in lomljenju ter sipanju svetlobe v zaslonu. Kot zaslon smo uporabili bel papir, ki ima visoko odbojnost ter skoraj lambertianovo porazdelitev sipane svetlobe. Za zožitev funkcije sipane svetlobe smo uporabili polkrožno lečo in s tem dobili kompaktnejši sistem. Motnjam in nasičenju kamere zaradi spekularnega žarka smo se izognili tako, da smo slednjega spustili skozi izdelano luknjico v zaslonu.

V sistemu s transmisijskim zaslonom ujamemo svetlobo, ki jo zaslon prepusti skozi, v tem sistemu je torej kamera postavljena za zaslon. Kot transmisijski zaslon smo uporabili prosojno in razpršujoče pleksi steklo in polprosojno steklo z belim sipalnim premazom. Prednost transmisijskih zaslonov v primerjavi z refleksijskimi je zajem večjih kotov, saj ima postavitev elementov manjši vpliv na vidni kot kamere (vzorec lahko zastre pogled kameri). Nadgradnja sistema z refleksijskega na transmisijski zaslon omogoča meritve tako prepuščene kot tudi odbite svetlobe. V sistemu smo ohranili luknjico za prepustitev spekularnega ali laserskega žarka, lečo pa smo izpustili. Za dosego čim večjega območja kotov smo postavili zaslon pod kotom 45°. Tako lahko pomerimo vse polarne kote od 0°do 90°. Pri tem izgubimo del informacije pri azimutnih kotih. To

smo nadoknadili tako, da smo vzorec zasukali za 180° in pomerili ADF še enkrat. Na ta način lahko pomerimo ADF v skoraj celotni (pol)sferi.

V doktorski disertaciji smo opisali postavitev obeh sistemov in obdelavo slik za izračun ADF iz vrednosti pikslov na sliki. Podrobno smo karakterizirali vse uporabljene zaslone, saj se sipana svetloba z vzorca še enkrat sipa na zaslonu. Tako je pri obdelavi podatkov potrebno vedeti, pod kakšnim kotom pade posamezen žarek sipane svetlobe na zaslon ter pod kakšnim kotom ta žarek na zaslonu nato vidi kamera. Utežitveno funkcijo, s katero utežimo vrednosti pikslov za določeni prostorski kot, odčitamo iz ADF zaslona na podlagi vpadnega in izhodnega kota. Pri meritvah smo uporabili rdeč laser pri valovni dolžini $\lambda = 633$ nm. Oba sistema smo validirali z goniometričnim ARS sistemom na primeru teksturiranih TCO vzorcev z različnimi morfologijami, referenčnega svetila ter periodičnih uklonskih mrežic. Dobili smo dobro ujemanje, ki je potrdilo primernost sistemov za merjenje sipane svetlobe. Pravilnost meritev so potrdile tudi simulacije, ki so pokazale dobro ujemanje na primeru heksagonalno razporejenih lukenj na silicijevem substratu. Izvedli smo tudi podrobno analizo pogreškov zaradi vključitve leče, ki se jim lahko izognemo z natančno postavitvijo elementov, ter prikazali, kako lahko s sistemom s kamero izračunamo delež difuzne svetlobe (haze).

Razviti sistemi za merjenje sipane svetlobe s kamero so močno orodje za natančno karakterizacijo ADF in porazdelitev jakosti sevanja (LID) in se lahko uporabljajo kot nadzorno orodje v industrijski proizvodnji. Naključno, periodično in kvazi-periodično teksturirani vzorci in viri svetlobe, npr. LED, so natančno karakterizirani v zelo kratkem času (nekaj sekund).

Zaključek

Disertacijo smo sklenili z zaključnim poglavjem, kjer smo predstavili glavne ugotovitve. Navedeli smo tudi objave, kjer smo predstavili rezultate disertacije, in izvirne prispevke k znanosti.

Objave

Rezultati doktorske disertacije so bili predstavljeni v naslednjih izvirnih znanstvenih člankih, objavljenih v mednarodnih revijah s faktorjem vpliva:

- JOŠT, Marko, KRČ, Janez, TOPIČ, Marko. “Camera-based angular resolved spectroscopy system for spatial measurements of scattered light,” *Applied Optics*, vol. 53, no. 21, p. 4795, Jul. 2014

- JOŠT, Marko, KRČ, Janez, TOPIČ, Marko. "Camera-based ARS system for complete light scattering determination/characterization," *Measurement Science and Technology*, vol. 27, no. 3, p. 035202, Mar. 2016
- JOŠT, Marko, ALBRECHT, Steve, KEGELMANN, Lukas, WOLFF, Christian M., LANG, Felix, LIPOVŠEK, Benjamin, KRČ, Janez, KORTE, Lars, NEHER, Dieter, RECH, Bernd, TOPIČ, Marko "Efficient Light Management by Textured Nanoimprinted Layers for Perovskite Solar Cells", poslano v ACS Photonics

Trije prispevki so bili po recenzijskem postopku objavljeni v revijah brez faktorja vpliva ali konferenčnih zbornikih:

- TOPIČ, Marko, JOŠT, Marko, SEVER, Martin, FILIPIČ, Miha, LOKAR, Žiga, LIPOVŠEK, Benjamin, ČAMPA, Andrej, KRČ, Janez. "Design challenges for light harvesting in photovoltaic devices," in *Proc. SPIE*, 2016, vol. 9898, p. 98980D–98980D–7
- JOŠT, Marko, TOPIČ, Marko. "Efficiency limits in photovoltaics: Case of single junction solar cells," *Facta universitatis - series: Electronics and Energetics*, vol. 27, no. 4, pp. 631–638, 2014
- JOŠT, Marko, ALBRECHT, Steve, LIPOVŠEK, Benjamin, KRČ, Janez, KORTE, Lars, RECH, Bernd, TOPIČ, Marko "Back- and Front-side Texturing for Light-management in Perovskite / Silicon-heterojunction Tandem Solar Cells," Energy Procedia, vol. 102, pp. 43–48, Dec. 2016

Rezultati so bili predstavljeni tudi na naslednjih mednarodnih konferencah:

- European Photovoltaic Solar Energy Conference
  - 2015: 3D camera-based system for measurements of scattered or emitted light
- European Materials Research Society Meeting
  - 2016: Back- and front-side texturing for light-management in perovskite / silicon-heterojunction tandem solar cells
- International Conference on Microelectronics, Devices and Materials
  - 2013: Camera-based measurement of light scattering intensity distribution

- 2014: UV nanoimprint lithography for replication of textured surfaces in thin-film photovoltaics
- 2015: Nanoimprinted textures on glass as a substrate for GITO deposition
- 2016: Hypophosphorous acid as an additive for inverted perovskite solar cells

Izvirni prispevki k znanosti:

Ocenjujemo, da pričujoča doktorska disertacija vsebuje naslednje izvirne prispevke k znanosti:

- AFM analyzer s ključnimi parametri hrapavosti mikro- in nano-tekstur
- Izboljšanje upravljanja s svetlobo v perovskitnih sončnih celicah, ki temelji na validiranem optičnem modelu in simulacijah
- Sistem s kamero, lečo in refleksijskim zaslonom za merjenje prepuščene sipane svetlobe s kamero vključno s transformacijskim modelom in kalibracijskim postopkom za zajem sipane svetlobe pod velikimi koti
- Sistem s kamero za merjenje tako prepuščene kot odbite sipane svetlobe sipane svetlobe s transmisijskim zaslonom vključno s transformacijskim modelom in kalibracijskim postopkom za zajem sipane svetlobe v celotni sferi

Zusammenfassung

Lichtmanagement ist ein wichtiger Aspekt der Photovoltaik, um eine effiziente Nutzung der Solarenergie zu gewährleisten und die Effizienz von Solarzellen zu verbessern. Ein effizientes Lichtmanagement basiert auf Antireflexion und Lichtstreuung. Erstere verringert Verluste durch Reflexion des einfallenden Lichtes. Letztere verlängert den optischen Weg in der aktiven Schicht einer Solarzelle und erhöht damit die Absoprtion des einfallenden Sonnenlichtes. Dadurch wird der Wirkungsgrad erhöht. Beide Effekte werden üblicherweise durch strukturierte Oberflächen entweder innerhalb des Schichtstapels oder auf der Oberseite des Bauteils eingebracht. Diese Dissertation konzentriert sich auf die Herstellung und Charakterisierung von texturierten Schichten zur Verbesserung des Lichtmanagements. Dazu wird eine texturierte Lichtmanagementfolie (LM-Folie) mit passendem Brechungsindex auf Perovskit-Solarzellen aufgetragen, um eine Verbesserungen in den gefertigten Solarzellen zu ermöglichen und diese anschließend im Detail zu analysieren.

Zur Herstellung der texturierten LM-Folien wird Ultraviolett-Nanoimprint-Lithographie (UV NIL) verwendet. Es ist ein neuartiger Ansatz für die Replikation von texturierten Oberflächen. Der Prozess ist kostengünstig, einfach und schneller als andere Texturierungstechniken. Hierbei wird die Texturoberfläche von einem Master auf ein Duplikat mit Hilfe eines Zwischenstempels übertragen und UV-empfindliche Lacke auf die Substrate aufgetragen. Wir stellen den Replikationsprozess vor und charakterisieren die erzeugten Duplikate mit Oberflächenmorphologie und Transmissionsmessungen. Dabei konnte eine hohe Reproduzierbarkeit der zu transferierenden Oberfläche und eine moderate thermische Stabilität bis zu 200 °C realisiert werden. Während des thermischen Stabilitätstests verfärbten sich die Proben, die für eine längere Zeit ($>$ 30 min) einer hohen Temperatur (200 °C) ausgesetzt waren, gelblich. Der Vergilbungeffekt führte zu einer verminderten Gesamt- und diffusen Durchlässigkeit für Licht mit Wellenlängen unter 500 nm. Ein ähnlicher Effekt wird auch während der Outdoor-Tests beobachtet. Hierbei wurden verschiedene Konfigurationen getestet. Einige Proben wurden auf einer weißen und einige auf einer schwarzen Oberfläche platziert. Nach dreimonatiger

Exposition gegenüber den Umgebungsbedingungen verfärbten sich die Proben gelb. Proben auf schwarzer Oberfläche erhitzten sich stärker und die Vergilbung war stärker als jene der Proben auf weißer Oberfläche. Zusätzlich kam es zu einem leichten Schmelzen des Lacks, was durch niedrigere σ_{RMS}-Werte bestätigt werden konnte. Dies zeigt, dass Replikationslacke mit einer stabileren chemischen Zusammensetzung für den Einsatz in realen Anwendungen benötigt werden. Wenn die LM-Folie innerhalb des Gerätes verwendet wird, muss eine zusätzliche leitfähige Schicht aus einem transparenten leitfähigen Oxid (TCO) auf der Oberseite der LM-Folie abgeschieden werden, um einen elektrischen Kontakt zu bilden, da die UV-NIL-Lacke nicht leitend sind. In unserem Fall wird ein Gallium dotiertes ITO (GITO) als TCO verwendet. Der Erfolg der Ablagerung wird durch Messungen des Flächenwiderstands, der Oberflächenmorphologie und durch optische Messungen (Transmission) bestätigt.

Eine für die Anwendung wichtige Grundvoraussetzung ist, dass die erzeugten Repliken die genaue Oberflächentextur und damit die Lichtstreuungseigenschaften des Masters bewahren. Für die Messungen der Lichtstreuung wird ein neuartiges kamerabasiertes System entwickelt. Es ermöglicht die Bestimmung der räumlichen Winkelverteilungsfunktion (3D ADF) von gestreutem oder emittiertem Licht mit einer Digitalkamera. Die 3D ADF wird aus dem digitalen Bild ermittelt das auf einem Schirm aufgenommen wurde. Wir stellen zwei Lösungen vor: Die erste verwendet einen reflektierenden Bildschirm und eine Linse, um den Winkelbereich zu erweitern. Die zweite verwendet einen lichtdurchlässigen Schirm, der bei 45 ° positioniert ist und die Messungen aller Polarwinkel ermöglicht. Mit diesem System können wir sowohl transmittiertes oder reflektiertes Licht, gestreut von strukturierten Proben, als auch direktes Licht von Lichtquellen in wenigen Sekunden quantifizieren. In dieser Dissertation werden beide Setups beschrieben. Die Transformationen des erfassten digitalen Bildes zur Bestimmung des 3D ADF werden erläutert. Die Systeme werden mithilfe einer zufällig nanotexturierten transparenten Probe und einer periodisch strukturierten, nicht transparenten Probe validiert. Eine gute Übereinstimmung wird mit rigorosen Simulationen und Messergebnissen erzielt, die mit einem herkömmlichen goniometrischen, winkelabhängig aufgelösten Streusystem durchgeführt werden. Das System mit dem lichtdurchlässigen Bildschirm wird verwendet, um die erstellten Duplikate zu charakterisieren.

Um die Funktionalität der erzeugten LM-Folien in einer realen Anwendung zu testen, werden anorganisch-organische Perovskite verwendet, die sich als wirksame

Materialklasse für die Herstellung effizienter Solarzellen erwiesen haben. Wir prozessieren eine mit UV NIL hergestellte LM-Folie auf der Glasseite einer invertierten (p-i-n) Perovskit-Solarzelle mit 16,3% Wirkungsgrad. Durch die LM-Folie erhöht sich der Kurzschlussstroms um 1mA/cm² was zu einer beachtlichen relativen Verbesserung des Wirkungsgrades von 5% auf einen Gesamtwirkungsgsrad von 17,1% führt. Zur Unterstützung der experimentellen Ergebnisse werden optische 3D-Simulationen, die auf experimentell gewonnenen Parametern basieren, verwendet. Es wird eine gute Übereinstimmung zwischen den simulierten und experimentellen Daten erhalten, die das Modell validiert. Die optischen Simulationen zeigen, dass die wesentliche Verbesserung der Bauteileffizienz auf eine Verringerung der Totalreflexion zurückzuführen ist. Für großflächige Solarzellen ist eine relative Verbesserung des Kurzschlussstroms von bis zu 10% möglich. Das optische Modell wird auch verwendet, um das Potential von monolithischen Perovskit/Silizium-Heterojunction-Tandemgeräten zu analysieren, welche theoretisch die Effizienz der Einzelsolarzellee überwinden kann. Wir betrachten vier verschiedene Bauweisen in den optischen Simulationen: planar Solarzellen, Zellen auf rück- oder beidseitig texturierten Si Wafer, und planare Zellen mit einer texturierten LM-Folie auf der Frontseite. Für jede dieser vier Designs wird das Stromgleichgewicht zwischen den beiden Subzellen simuliert, um deren Effizienz zu bewerten. Dabei erzielt die Zelle auf dem beidseitig strukturierten Silizium-Wafer die bestmöglichen Ergebnisse. Eine relative Steigerung der Effizienz um 15% im Vergleich zur planaren Solarzelle kann erreicht werden. Des Weiteren wird das Potenzial von LM-Folien zur Verbesserung der Bauteileffizienz von Perovskit-Solarzellen gezeigt und der Weg für den weiteren Einsatz optischer Simulationen in Perovskit-Einzel- oder Tandem-Solarzellen geebnet.

Table of contents

List of symbols and constants

Symbol	*Unit*	*Description*
α	°	Screen angle
A		Absorptance
ADF	a.u.	Angular distribution Function
ADF_{screen}	a.u.	ADF of the screen
β	°	Light incident angle on the screen
d	nm	Thickness, distance
δ	rad	Angular step
Eg	eV	Energy band-gap
φ	°	Azimuthal angle
FF	%	Fill factor
γ	°	Angle between the camera and the scattered beam position on the screen
H		Haze
h_{pp}	nm	Peak-to-peak value
J_{SC}	mA cm^{-2}	Short-circuit current density
J_{SC_JV}	mA cm^{-2}	Short-circuit current density from J-V measurement
J_{SC_EQE}	mA cm^{-2}	Short-circuit current density from EQE measurement
J_{SC_SIM}	mA cm^{-2}	Simulated short-circuit current density
k	$1.38*10^{-23}$ m^2 kg s^{-2} K^{-1}	Boltzmann constant
k		Extinction coefficient
λ	nm	Wavelength
l_c	nm	Correlation length
n		Real part of the complex refractive index
n	cm^{-3}	Electron concentration
Ω	srad	Solid angle
p	nm	Period
p	cm^{-3}	Hole concentration
P	W	Power
PCE	%	Power conversion efficiency

Symbol	*Unit*	*Description*
PCE_{JV}	%	Power conversion efficiency from *J-V* measurement
PCE_{MPP}	%	Power conversion efficiency from MPP tracking
PCE_{EQE}	%	Power conversion efficiency from EQE measurement
R		Reflectance
R_{dif}		Diffuse reflectance
R_{EQ}	mA cm^{-2}	Equivalent reflection current density loss
R_{sh}	Ω sq^{-1}	Sheet resistance
R_{SIM}	mA cm^{-2}	Simulated equivalent reflection current density loss
R_{tot}		Total reflectance
SBV		Specular beam value
σ_{RMS}	nm	Root-mean-square roughness
t	s	Time
T		Transmittance
T	°C	Temperature
T_{dif}		Diffuse transmittance
T_{spec}		Specular transmittance
T_{tot}		Total transmittance
Θ	°	Scattering angle, polar angle
Θ_{avg}	°	Average angle
τ_n	ns	Electron lifetime
τ_p	ns	Hole lifetime
V_{OC}	V	Open-circuit voltage

List of abbreviations

Abbreviation	*Description*
AFM	Atomic force microscopy
a-Si:H (i)	Hydrogenated amorphous silicon, intrinsic
a-Si:H (n)	Hydrogenated amorphous silicon, n-type doped
a-Si:H (p)	Hydrogenated amorphous silicon, p-type doped
Ag	Silver
AM 1.5G	Air mass 1.5 global solar spectrum
AR	Anti-reflection
ARC	Anti-reflection coating
ARS	Angular resolved spectroscopy
ASTM	American Society for Testing Materials Standards Organization
Au	Gold
BC	Back contact
BCP	Bathocuproine
Br	Bromine
C60	Buckminsterfullerene
c-Si	Crystalline silicon
$CaTiO_3$	Calcium titanate
CCD	Charge-coupled device
$CH_3NH_3PbI_3$	Methylammonium lead iodide
$CH_3NH_3^+$	Methylammonium
CH_3NH_3I	Methylammonium iodide
$CH_3CH_2NH_3^+$	Ethylammonium
CIGS	Copper indium gallium (di)selenide
Cl	Clorine
CROWM	Combined ray optics / wave optics numerical model
Cs	Caesium
CuI	Copper(I) iodide
CuSCN	Copper(I) thiocyanate
DMF	*N*,*N*-dimethylformamide
DMSO	Dimethyl sulfoxide

Abbreviation	*Description*
DSSC	Dye-sensitized solar cells
EBL	Electron beam lithography
EQE	External quantum efficiency
ETM	Electron transport material
FC	Front contact
FFT	Fast Fourier Transfrom
FIB	Focused Ion Beam
FTO	Flourine doped tin oxide
GBL	γ-butyrolactone
GITO	Gallium doped ITO
GUI	Graphical user interface
HCl	Hydrogen chloride
HeNe	Helium-neon
HI	Hydrogen iodide
HPA	Hypophosphorous acid, H_3PO_2
HTM	Hole transport material
I	Iodine
ICBA	1′,1″,4′,4″-Tetrahydro-di[1,4]methanonaphthaleno [1,2:2′,3′,56,60:2″,3″][5,6]fullerene-C60
ISO	International Organization for Standardization
ITO	Indium tin oxide
KOH	Potassium hydroxide
LED	Light emitting diode
LiF	Lithium fluoride
LM	Light management
LPCVD	Low-pressure chemical vapor deposition
MoO_3	Molybdenum trioxide
MPP	Maximum power point
$NH_2CHNH_2^+$	Formamidinium
NIL	Nanoimprint lithography
NIR	Near-infrared
NiO_x	Nickel oxide
NPD	N,N′-Di(1-naphthyl)-N,N′-diphenyl-(1,1′-biphenyl)-4,4′-diamine
Pb	Lead
$PbAc_2$	Lead acetate
PbI_2	Lead iodide
PCBM	[6,6]-phenyl-C61-butyric acid methyl ester
PDMS	Polydimethylsiloxane

Abbreviation	*Description*
PEDOT:PSS	Poly polystyrene sulfonate
PET	Polyethylene terephthalate
polyTPD	Poly[N,N'-bis(4-butylphenyl)-N,N'-bisphenylbenzidine]
PTAA	Poly [bis (4-phenyl) (2,5,6-trimentlyphenyl) amine]
RF	Radio frequency
RIE	Reactive ion etching
SEM	Scanning electron microscope
SHJ	Silicon-heterojunction
Si	Silicon
Sn	Tin
SnO_2	Tin oxide
spiro-OMeTAD	N2,N2,N2′,N2′,N7,N7,N7′,N7′-octakis(4-methoxyphenyl)-9,9′-spirobi[9H-fluorene]-2,2′,7,7′-tetramine
STC	Standard test conditions
TCO	Transparent conductive oxide
TiO_2	Titanium dioxide
TIS	Total integrating scattering
TGA	Thermogravimetric analysis
UV	Ultraviolet
UV NIL	UV Nanoimprint Lithography
VIS	Visible light
ZnO	Zinc oxide
ZnO:Al	Zinc oxide, doped with aluminum
ZnO:B	Zinc oxide, doped with boron

1 Introduction

1.1 General introduction to the field

In pursuit of a cleaner environment and limiting global warming, the renewable energy sources are becoming more and more important. Especially photovoltaics (PV) has a bright future due to inexhaustible and free solar energy. The Sun is by far the most abundant energy source, providing more energy in one hour than it is consumed by the mankind in a whole year. Compared to other energy sources, it is also the most evenly spread over the globe. This gives every nation a chance of a fuel-, cost- and pollution-free energy generation; however, countries closer to equator naturally benefit more, e.g. Sicily receives solar irradiation of 1900 kWh m^{-2}, Slovenia 1200 kWh m^{-2} and Germany 1000 kWh m^{-2} [1].

The electricity from solar energy generation itself is emission free, and even with the inclusion of solar panel production, the carbon footprint is 20 times lower than from burning fossil fuels [2]. Optimization of the production processes has also decreased the energy payback time of the PV systems, reaching around 2 years in middle Europe for the conventional multi-crystalline silicon technology and even less for thin-film technologies. Accelerated entry of China on the PV market has caused a massive increase in solar module production, which has resulted in a drastic drop in prices and growth in cumulative installation of PV systems. In the last 10 years the installation growth has been exponential with over 70 GW installed last year, exceeding 300 GW overall. Even China, one of the most notorious polluters in the world, has recognized the need for a clean environment and is now a leader in PV production and deployment [3]. The potential and benefits of the PV make it one of the most prominent players in the renewable energy field and also in the energy sector in general.

The basic unit for photovoltaic solar energy conversion is a solar cell based on a semiconductor material, where conversion of solar energy into electric energy is caused by a photovoltaic effect. Semiconductor material properties, mainly the energy bandgap, are the most important factors to determine the efficiency of conversion. For a single

junction device, the (Shockley-Queisser) limit is 33.7% at bandgap of 1.34 eV under standard test conditions (STC) [4], [5]. Using a variety of semiconductor materials, different types of solar cells with different conversion efficiencies exist. The conventional, first generation solar cells are mono- and multi-crystalline silicon solar cells, which reach the highest conversion efficiencies (26.3%, [6]) and have the highest, dominant share ($> 86\%$) in the global market [3]. The second generation of solar cells are the so-called thin-film solar cells. Compared to a 150 μm thick silicon absorber in a conventional Si solar cell, the absorber is only a few microns thick. The main representatives of this class are CIGS, CdTe and amorphous silicon solar cells. The popularity of thin-film devices is based on anticipated lower costs due to small material consumption and low energy production processes, while still reaching high efficiencies (above 20% for a solar cell). Lately, solar cells with an even lower cost potential are being researched (third generation). Organic and dye-sensitized solar cells (DSSC) had both shown promise; however, recent discovery of perovskite solar cells has shaken the research community. In only a few years, the perovskite solar cell conversion efficiency rocketed to 22.1% [6]. Despite cheap manufacturing and high efficiencies, the perovskite solar cells still have a long way to go. The main deficiencies are a small area of the device, stability issues and lead toxicity. Nevertheless, the research on perovskite solar cells has only yet begun and its extensiveness gives hope for successfully overcoming the challenges for either an industrial production or becoming an affordable and suitable solution for niche applications.

1.2 Topic of the thesis

The recent drop in solar module prices, the progress in energy storage systems and the entry of new players, such as Tesla Solar [7], on the market has increased the popularity and interest in the PV. Still, further cost reductions in solar cell production are needed for PV to successfully rival conventional energy sources or become attractive for everyday powering applications. Thin-film solar cells [8] present such a low-cost alternative to conventional crystalline solar cells, since low temperature processes are used for fabrication, less semiconductor material is consumed and even flexible photovoltaic modules can be produced. However, in comparison to crystalline solar cells, thin-film solar cells are much thinner, which generally results in a lower absorption of light. As the conversion efficiency of a solar cell is strongly related to the level of light

absorption in the active layers, light management techniques need to be implemented to enhance absorption in thinner absorber layers [9].

One of the most successful techniques to increase the absorption of light in thin-film solar cells is surface texturing in nanometer feature size, either at the top or at the bottom of the device [10]. Nanotextured surfaces in the solar cell device result in anti-reflection (AR) and a light scattering effect (features size equal or greater than wavelength [11]), which increases light in-coupling and prolongs the optical light path in the active layer, respectively. This increases the photocurrent of the device; as long as electrical properties (open-circuit voltage and fill factor) remain unchanged, the increase in photocurrent is directly transferred to an increase of conversion efficiency [12].

The AR coatings are usually flat and reduce the reflection (usually at the air/glass interface) by adjusting the refractive index changes at the interfaces and the of the layers. Depending on the number of the layers, they are optimized for a narrow (less layers) or broader region of wavelengths (multiple layer stack). Some of the technologies, such as crystalline silicon, also take anti-reflection properties of the native surface texture [13]. Alternatively, one can apply a textured light management (LM) foil on the front glass side in a superstrate cell configuration. As a result, in both cases the light in-coupling is increased, thereby increasing the absorption and photocurrent of the device.

Inside the device, textured surfaces are introduced by transparent textured superstrates (glass carrier covered with surface textured transparent conductive oxide (TCO)) [10], [14], textured substrates (steel or plastics, covered with textured back reflector), or by additional layers integrated into the structure. In the last years, the technology of embossing a pre-fabricated nanotexture on a master in a transparent heat resistant lacquer layer has been shown as a promising way to introduce the desired texture in the solar cell structure [15]–[21].

A novel, low-cost and effective approach of embossing textures, either on a small- or large-area scale, is nanoimprint lithography (NIL) [15]. Patterns (textures) are created by mechanical deformation of polymers (lacquers) in a soft phase by imprinting the master texture into an imprint lacquer, followed by curing. Curing can be done either by heat (thermoplastic NIL) or by UV light (UV NIL). Combined with TCO deposition on top of the imprinted layer, this combination can replace an expensive TCO with a native or with post-processing obtained texture.

It has been proven that NIL process replicates the surface roughness and maintains scattering abilities of their masters [16], [17]. To characterize light scattering properties of surface-textured superstrates or substrates, different measurement techniques are used. One of the most common is angular resolved spectroscopy (ARS), which enables to determine angular distribution function (ADF) of scattered light – how the light is scattered in different angles [22], both in transmission and reflection. ADF is typically measured by goniometric systems, which are slow and only measure ADF in one plane. This is where camera-based systems offer an effective solution. In camera-based systems, the scattered light is projected on a screen and captured with a camera. This enables a fast and more complete analysis which is also suitable for industry.

In the doctoral dissertation, we focus on the fabrication and characterization of light management layers and the analysis of their functioning in perovskite solar cells. UV NIL is used to create the textured surfaces. The created replicas are also characterized with a camera-based light scattering measurement system. Two systems, one with a reflective and one with a transmissive screen, based on a digital CCD camera to determine 3D ADF of the transmitted and the reflected light were developed for this purpose. To test the replicas' performance in a real application, the created LM foils are applied on the top side of the perovskite solar cells. The performance of the devices without and with the LM foil is analyzed experimentally and theoretically by using optical simulations.

1.3 Outline of the thesis

The doctoral dissertation is structured as follows:

Chapter 1 provides a general introduction to the thesis.

Chapter 2 focuses on the UV Nanoimprint Lithography process that is used for the replication of the textures. First the replication process is described. The created replicas are thoroughly characterized by AFM and transmittance measurements. Transfer fidelity and optical parameters are determined. Suitability of the replicas for further use is checked. Thermal stability of the lacquers is investigated. The replicas are subjected to outdoor testing under environmental conditions. Finally, the replicas are used as substrates for the deposition of the transparent conductive oxide.

Chapter 3 is devoted to perovskite solar cells. First, perovskite material characteristics, single junction and tandem devices based on perovskite absorber are presented. Then, the fabrication and characterization of the perovskite solar cells is explained. The textured light management foil is used to further improve the performance of the devices. In the final part of the chapter, optical simulations are used to support the experimental findings and provide further insight into the potential of the light management foils for the perovskite solar cells. The optical model is validated and applied to simulate textured light management foils in both single junction and tandem perovskite devices.

Chapter 4 is dedicated to camera-based light scattering measurement systems. Two different systems are presented, one with a reflective and one with a transmissive screen. The mathematics behind the image processing from raw camera image to a 3D Angular Distribution Function of scattered light is explained and properties of the screens are analyzed. Both systems are validated on a set of textured transparent conductive oxides.

Chapter 5 reviews the most important results of the research, presents conclusions, provides an outlook for further research, lists the publications and summarizes original scientific contributions of this dissertation.

Several parts of this thesis have been peer-reviewed and published or are about to be published in scientific journals. The author of this thesis is the first author of all the publications.

The contents of sections 3.2., 3.3 and 3.4 on the experimental analysis and optical modelling of perovskite single junction solar cells with LM foil have been submitted under the title "Efficient Light Management by Textured Nanoimprinted Layers for Perovskite Solar Cells" to the journal *ACS Photonics*.

The contents of section 3.4.4 on optical modelling of tandem perovskite/silicon heterojunction solar cells was published in 2016 under the title "Back- and Front-side Texturing for Light-management in Perovskite / Silicon-heterojunction Tandem Solar Cells" in the journal *Energy Procedia* and is listed with the DOI number: 10.1016/j.egypro.2016.11.316.

The contents of section 4.2 on the camera-based light scattering measurement system with a reflective screen was published in 2014 under the title "Camera-based

angular resolved spectroscopy system for spatial measurements of scattered light" in the journal *Applied Optics* and is listed with the DOI number: 10.1364/AO.53.004795.

The contents of section 4.3 on the camera-based light scattering measurement system with a transmissive screen was published in 2016 under the title "Camera-based ARS system for complete light scattering determination/characterization" in the journal *Measurement Science and Technology* and is listed with the DOI number: 10.1088/0957-0233/27/3/035202.

2 UV Nanoimprint Lithography

This chapter is devoted to fabrication of textured surfaces. For this purpose, we utilize UV Nanoimprint Lithography, a replication process where a texture is transferred from a master to a replica. There are multiple advantages of UV Nanoimprint Lithography. One textured master, created by complex and expensive processes, can be replicated multiple times, making texturization time- and cost- effective. The replicas are transparent, which enables us to introduce textures that can otherwise only be made on non-transparent substrates. The created replica can be used as a light management layer, either on top of the device or inside it. When put on top of the device, the replica should endure outdoor environmental conditions for longer periods of time without deterioration in performance. When the replica is used inside the device, the deposition of other layers on top of it will follow. This requires the texture to be preserved during the deposition process and the next layer to successfully adhere on the replica. In this chapter, all these topics are covered. We inspect transfer fidelity and optical parameters of the replicas. Outdoor testing, thermal stability testing and deposition of transparent conductive oxide are carried out to determine suitability of replicas for use in solar cell structures.

2.1 Introduction

Higher conversion efficiencies of solar cells can be achieved by material and process optimization and also by increasing light in-coupling using light management techniques. Under light management, we consider anti-reflection (AR) and light trapping (LT) effects, which can be achieved by planar AR coatings (ARC) and/or textured interfaces between different layers of solar cell stacks [12]. The planar ARCs are usually flat and reduce the reflection by optimal thickness and refractive index grading of the layers at the interfaces (usually air/glass interface). The textured interfaces can either be integrated inside a cell structure by texturing the front electrode, typically the transparent conductive oxide (TCO) [23], [24], or by applying light management (LM) foils on the front glass side in a superstrate cell configuration [25], [26]. Textured foils

have an advantage over the ARCs, especially in planar devices with flat interfaces, as they can both reduce the reflection as well as scatter (for nano-sized texture features) or refract (for micro-sized features) light, which prolongs the optical path and induces light trapping [27]. As a result, the photocurrent density is enhanced [12].

Textured surfaces in thin-film photovoltaics are commonly random. They are either formed by natural growth (e.g. by the growth of poly-crystalline layers such as LPCVD ZnO:B [28] resulting in pyramid-like features) or fabricated by etching the existing layers (such as magnetron sputtered ZnO:Al etched in HCl [29], resulting in crater-like features or a silicon wafer with <100> orientation etched in KOH, resulting in randomly distributed pyramids [30]–[32]). The simulations, however, showed that sometimes periodical 1D or 2D features (sinusoids, pyramids, inverted pyramids, nanorods) trap light more efficiently [33]. To create such textures, complex and/or expensive processes are needed, e.g. photolithography with etching, Focused Ion Beam (FIB), Electron Beam Lithography (EBL), Reactive Ion Etching (RIE) [34]. The typical substrates for textures are silicon and nickel, which are not transparent. The usage of such textures is consequently limited, especially as an ARC on top of the cell. Therefore, in the last years the technology of embossing a pre-fabricated nanotexture on a master in a transparent lacquer layer has become a promising way to introduce a desired texture in the solar cell structure [15]. This way we can integrate such a texture in the solar cell that is (can only be) made on nontransparent substrates.

An effective novel approach of embossing textures, either on a small or a large scale, is the nanoimprint lithography (NIL) process [35]. It is a low-cost and high-resolution technique of replicating textures. The replicated textures are created by mechanical deformation of polymers (lacquers) in a soft phase by imprinting a master texture into an imprint lacquer. The replica of the master is made with the help of an intermediate step, where a negative replica/stamp is made first. Each stamp can be used several times to create replicas, making reproducibility one of the key factors in the process. Two main techniques to create a stamp are thermoplastic NIL (imprint is carried out under heat) and UV NIL (imprint under ultra-violet (UV) light), while the creation of (positive) replicas is usually carried out under the UV light. The thermoplastic NIL uses PDMS, a silicon-based organic polymer [36], as a stamp, while the UV NIL uses UV sensitive lacquers for both stamp and replica [17], [37]. In the dissertation, the focus is on UV NIL, where the curing of both stamp and replica lacquers is done using a UV light

[16]–[19]. UV NIL is accurate in nanometer scale, fast, cheap and also applicable for roll-to-roll manufacturing.

UV NIL has found many uses in different research fields. The most common is the fabrication of nanostructures for light scattering and trapping [16], [18], [19], back reflectors [37] or anti-reflective coatings [20], [21] in thin-film solar cells. Furthermore, with UV NIL, double structured textures can be introduced, e.g. periodical pyramids (lacquer) + pyramid-like random nanotexturing from LPCVD of ZnO:B on top of the lacquer [38]. However, when integrated inside the device structure, the textured replicas can replace the TCO's texture, but not its conductivity. The lacquers are made from non-conductive polymers, therefore the deposition of a TCO material is still needed. Besides light harvesting improvements for solar cell application, the advantages of UV NIL technology are also used in some other fields, such as biology when replicating textures from animals [39] or plants [40], [41] to implement nanotextured characteristics, such as hydrophobicity.

In this chapter, the UV NIL replication process is presented with all the steps explained. The obtained replicas are thoroughly characterized. Atomic Force Microscopy (AFM) measurements are carried out to investigate the fidelity of the texture transfer by comparing root-mean-square roughness, σ_{RMS}, correlation length, l_c, and average angle of the features, Θ_{avg}. AFM analyzer software has been developed for an easier and fast analysis of the obtained AFM scans; the software is shortly described. Reflection, transmission and light scattering measurements determine the suitability of the replicas for further use in photovoltaics as light management layers, either outside or inside the device. Optical parameters of the UV NIL lacquers, needed for optical simulations, have been extracted. Thermal stability of the replica lacquer has been examined. Outdoor testing has been performed to test the durability performance of the replicas as a light management foil in outdoor conditions, based on their transmission and preservation of the scattering abilities. A TCO was sputtered on the replicas to investigate the possibility of the replica's integration inside the device. TCO coated replicas are then characterized electrically by sheet resistance and optically by total and diffuse transmission.

2.2 Experimental

2.2.1 Sample fabrication

The UV NIL replication process is carried out in air in the following steps (as schematically shown in Figure 2.1):

i. A textured sample is used as a master for the replication.
ii. A stamp lacquer, deposited on a substrate (lacquer 1/substrate 1), is imprinted on the textured master.
iii. Viscous lacquer adjusts to the structure of the master and is cured under UV illumination. Lacquer 1/substrate 1 become a stamp.
iv. After the separation of the stamp (negative replica) from the master, the stamp can be used as a (quasi)master and is imprinted in the lacquer 2 deposited on a substrate 2.
v. UV illumination cures the second lacquer.
vi. Once separated from the stamp, the acquired (positive) replica is ready for use in photovoltaic devices.

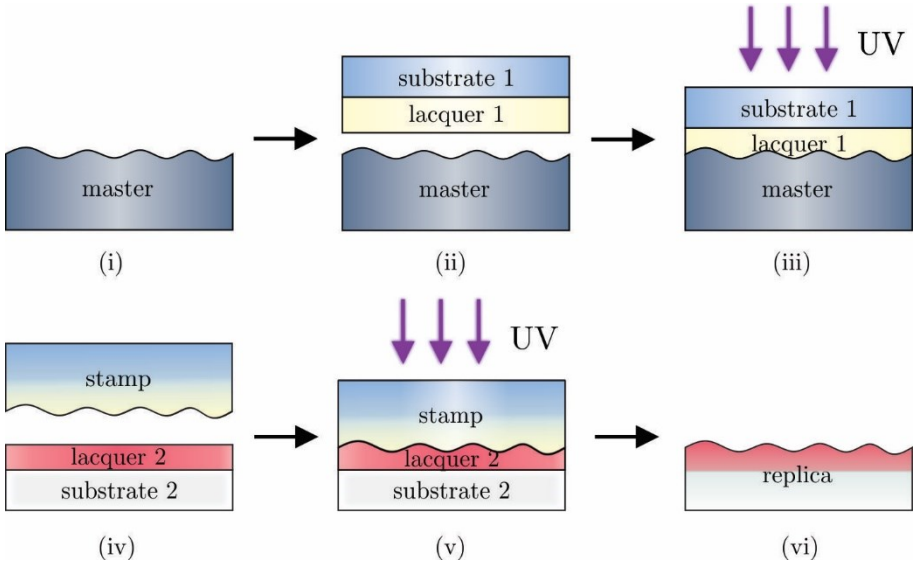

Figure 2.1: UV NIL replication process with depicted steps. Viscous lacquer is imprinted (ii) in a textured master (i) and cured with UV light (iii). After the separation a stamp is obtained. To create a replica (vi), the procedure is repeated (iv, v) with the stamp taking the place of a master.

Hostaphan PET film and glass slide (Corning Eagle glass, 1 mm thick) were used as substrates for the stamp and the replica, respectively. Commercially available lacquers

(provided by CCoatings) are used. Lacquer S-12 is used for the creation of a stamp and is designed to adhere to the PET film, used as a stamp substrate. Lacquer MO-18 is used for a replica and is designed to adhere to a glass substrate, however, primer P-8 is used to improve the adhesion. MO-18 is also heat resistant up to 200 °C and can endure some further deposition processes. Additionally, the two lacquers are designed so that they do not stick to each other during the replication process and their separation is possible. Both can either be deposited on the substrates using the doctor blade technique - the thickness of the layer before the imprint is 50 µm – or by dripping a small amount of lacquer on the master or replica substrate and then placing stamp substrate or stamp onto it. UV LEDs with a peak wavelength at $\lambda = 368$ nm were used to cure the lacquers. $t = 5$ min was more than enough to provide 1.5 J cm^{-2} needed to cure the lacquers. 5 min ultrasonic is recommended after the replica fabrication. Otherwise, sometimes replicas get covered by a thin greasy layer for which no explanation has been found.

2.2.2 Sample characterization

After the fabrication, the replicas were analyzed to determine the transfer fidelity and establish suitability for further use. AFM was used to determine the surface morphology of the samples and transfer fidelity. Measurements were carried out using Asylum research MFP-3D™ AFM. Non-contact tapping mode was used and multiple randomly chosen spots on each sample were measured. The resolution was 256 x 256 points for 10 x 10 μm^2 and 5 x 5 μm^2 areas, and 512 x 512 for 20 x 20 μm^2 areas. The results were analyzed using AFM analyzer, a software tool developed for this purpose. The reflectance and transmittance were measured using Lambda 950 Perkin Elmer spectrophotometer. The scanning was done in a broad wavelength range, from 300 nm to 1200 nm with a step of 5 nm. 3D ADF measurements were performed using camera-based light scattering measurement system, described in section 4.3. Laser with $\lambda = 633$ nm was used as an illumination source.

2.2.3 AFM analyzer software

AFM analyzer is a software for automatized analysis of the AFM measurements. It is a standalone software with a GUI. However, since it was developed in MATLAB® it needs a MATLAB Compiler Runtime (MCR) release 2013a (8.1) 64-bit to run. It was written as an alternative to a free SPM (scanning probe microscopy) analyzer

(a)

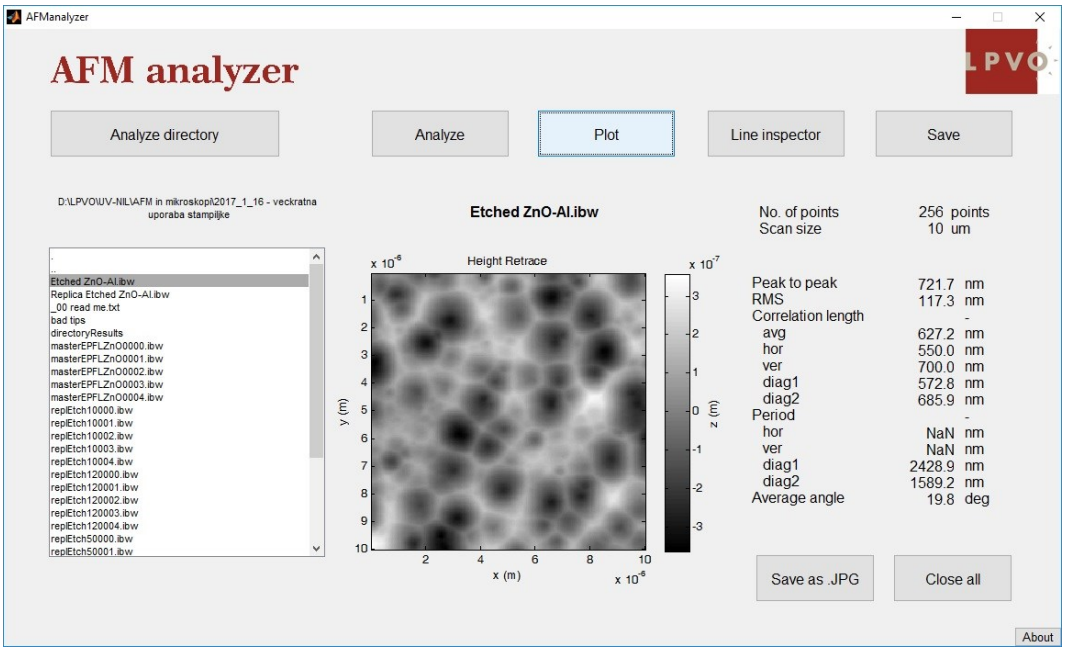

(b)

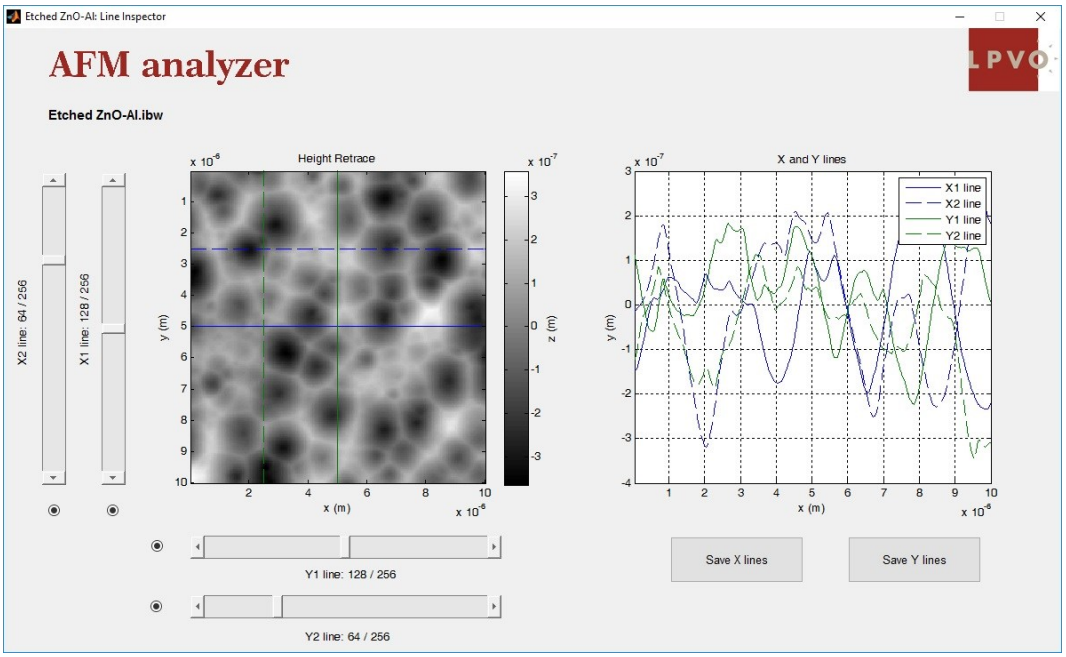

Figure 2.2: (a) AFM analyzer GUI and (b) Line inspector panels showing the analysis of a replica of an etched ZnO:Al master.

Gwyddion to simplify and speed up the basic AFM analysis with predefined built-in analysis functions. The AFM analyzer enables simple selection of measurements, automatized calculation of roughness parameters and graphical presentation of the analysis.

The AFM analyzer's user interface makes it easy to switch between measurements and to select functions. The selected measurement can be analyzed only, or also graphically presented with only one click. Line inspector enables scanning overview of the measurements, comparing two lines each in x and y directions. All calculated data can be easily saved. In addition, the AFM analyzer enables automated analysis of the whole directory of measurements. This is especially useful when many similar AFM measurements were performed. The analyzer currently supports the following file formats:

- .ibw (Asylum Research),
- .tiff (Park Systems),
- .000 (only for a specific AFM),
- .txt files generated from Gwyddion.

Figure 2.2 (a) shows the AFM analyzer GUI, presented on a case of a replica of an etched ZnO:Al master. The main panel in the GUI consists of a list box on the left side where a file is selected, plot in the middle where a raw AFM scan is shown, and calculated roughness parameters on the right side. The desired command is selected by clicking on the appropriate button. By choosing "Analyze", the parameters are calculated, by choosing "Plot" the parameters are calculated and plotted. The Line inspector (Figure 2.2 (b)) shows a raw AFM scan on the left side and plotted line scans on the right side. The desired line is selected with a slider and the line points can be saved. Sliders can be turned on and off to show only one line in x or y direction.

2.2.3.1 Calculated parameters

The AFM analyzer calculates the most important roughness parameters:

- Peak to peak value, h_{pp}
- Root mean square roughness, σ_{RMS}
- Correlation lengths, l_c:
  - Average
  - Horizontal, vertical and both diagonal lines
- Period: this is useful when analyzing periodic samples, p
  - Horizontal, vertical and both diagonal lines
- Average angle, Θ_{avg}

To obtain correlation lengths, first 2D autocorrelation (see Figure 2.3 (a), top right corner) is calculated using in-built Matlab functions. Next horizontal, vertical and two

diagonal lines through the center (0,0) are extracted. The correlation length of each line is considered as a distance between the maximum m and m*e^{-1}. When all four are obtained, they are averaged to get the average correlation length. Similarly, the period is the distance from the m to the first peak.

To calculate average angle, first gradients in x and y direction are calculated using: v=(dx/dz, dy/dz). The angle in a point (x,y) is φ=atan(|$v(x,y)$|). If all φ are averaged, we get the average angle.

(a)

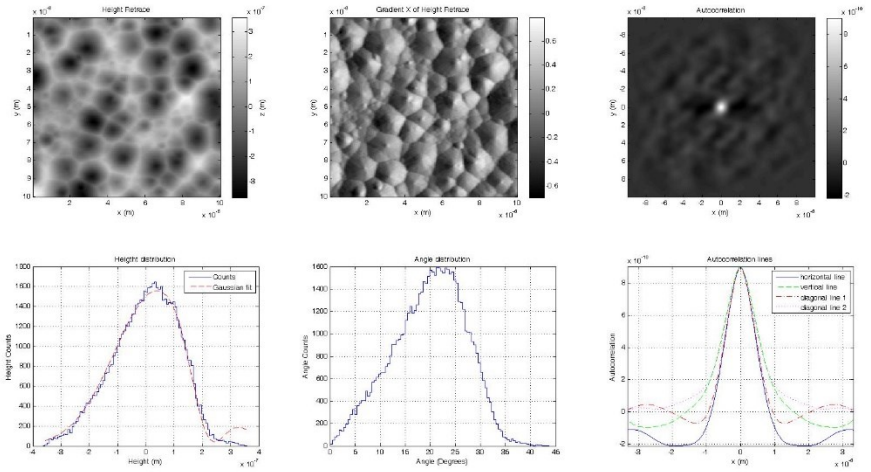

(b)

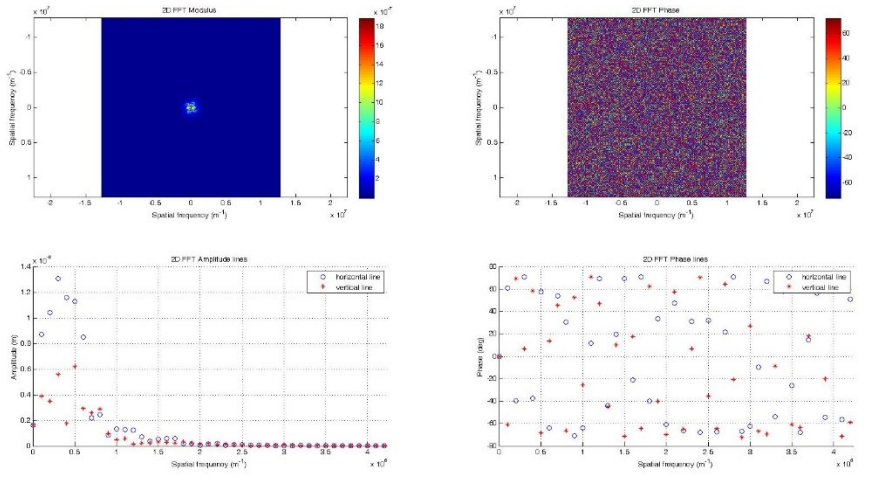

Figure 2.3: AFM analyzer analysis of an etched ZnO:Al master: (a) Window 1 showing raw AFM scan, height distribution (left column), gradient in x direction, angle distribution (middle column), autocorrelation, correlation lines – horizontal, vertical and both diagonals (right column). (b) Window 2 showing 2D FFT modulus, horizontal and vertical FFT amplitude lines (left column), 2D FFT phase, horizontal and vertical FFT phase lines (right column).

The analysis can also be graphically presented. Two pop-up windows with different plots are created and are shown in Figure 2.3. In the first one, the plots from which the roughness parameters are calculated are shown, and in the second the FFT analysis is presented.

Window 1: spatial analysis

- Raw AFM scan
- Height distribution
- Gradient in x direction
- Angle distribution
- Autocorrelation
- 1D correlation lines
  - horizontal, vertical and both diagonals

Window 2: FFT analysis

- 2D FFT modulus
- Horizontal and vertical FFT amplitude lines
- 2D FFT phase
- Horizontal and vertical FFT phase lines

2.2.3.2 Saving

All the obtained data from the AFM analyzer can be saved. By clicking button "Save" a folder with the name of the sample in the current directory is created. The following .txt files are created inside the folder:

- AFMdata – contains AFM scan and its axis
- Angle distribution
- 1D Correlation – horizontal, vertical and diagonal
- FFT modulus data
- FFT phase data
- Height distribution
- Statistics
  - Sample name
  - Scan size
  - Sample points
  - σ_{RMS}
  - Average correlation length
  - Average angle
- x and y lines in Line inspector

Additionally, a .jpg file of a top view of a raw AFM scan is created by clicking on the "Save as .JPG" button.

2.3 Optical parameters of the UV NIL lacquer

Optical parameters, such as transmittance T, reflectance R and refractive index n and k spectra, have to be known when integrating a replica into a device structure. The optical losses caused by the replica should be minimal. When used as a front textured layer, as is in our cases, it should transmit as much light as possible and reflect as little. Figure 2.4 (a) shows typical R and T spectra for a replica (lacquer MO-18) with flat surface. More than 91% of light is transmitted and less than 9% reflected, meaning there is no absorption for the wavelengths above 400 nm. Below 400 nm, however, there is strong absorption of UV light. This is expected since UV light is needed to cure the lacquers and must therefore be absorbed. Using measured R and T, n and k spectra, needed to conduct optical simulations, can be calculated using R&T method [42]. The thickness of the UV NIL lacquer was in the range of 85 - 95 μm. Obtained n and k spectra are shown in Figure 2.4 (b). n and k spectra of the ZnO:Al, found in the literature [43], are also shown in the figure. n of the cured replica (lacquer 2) is 1.55 which is close to the n of the glass. The imaginary part $k = 0$ above 400 nm, confirming there is no parasitic absorption in the UV NIL lacquer for wavelengths $\lambda > 400$ nm. Note that due to the measurement system artefact at 860 nm, there is a slight error in the measurements. To eliminate this error when calculating the n and k spectra the data around 860 nm was interpolated.

(a) (b)

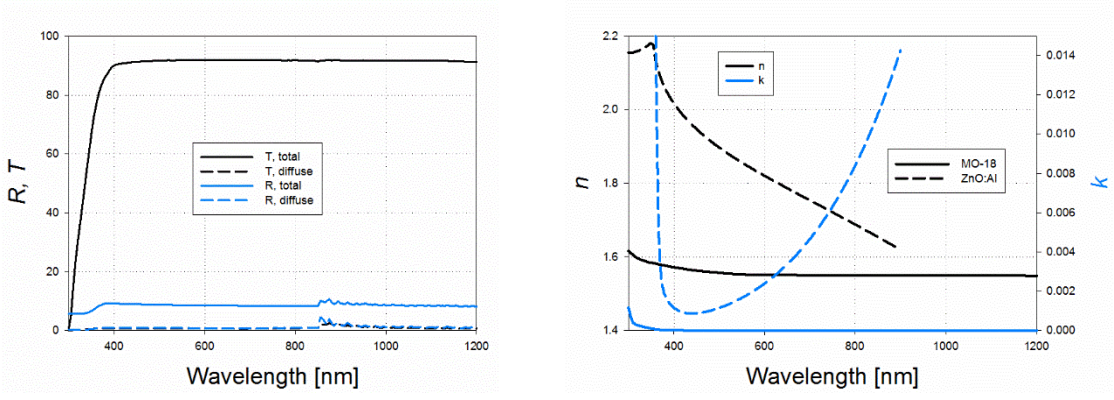

Figure 2.4: (a) typical total and diffuse R and T spectra for a replica with a flat surface. (b) n and k spectra extracted from R and T spectra for the lacquer MO-18 (solid lines). n and k spectra of the ZnO:Al are also shown (dashed lines).

2.4 Master vs replica

First, we compare a textured master and its replica. A sputtered and then etched in HCl ZnO:Al sample was chosen as a master. Since the successfulness of the replication process is mostly determined by the fidelity of the texture transfer, we show Figure 2.5 (a) and (b) AFM scans of the master and replica, respectively. Crater-like features, typical for etched ZnO:Al are observed. Visually, the features on the scan of the master and replica look very similar, both in lateral size and height. This is confirmed by roughness parameters extracted from the AFM scans. Similar values for σ_{RMS}, l_{c} and Θ_{avg} confirm a high fidelity of the texture transfer.

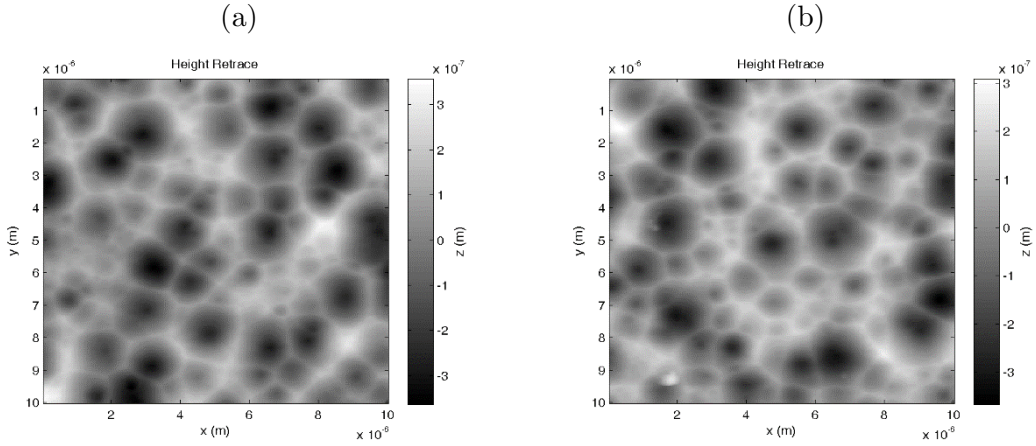

σ_{RMS} = 117.3 nm
l_{c} = 627.2 nm
Θ_{avg} = 19.8°

σ_{RMS} =112.1 nm
l_{c} = 643.2 nm
Θ_{avg} = 19.1°

Figure 2.5: AFM scan of an etched ZnO:Al (a) master and (b) its replica with roughness parameters, extracted from AFM measurements, for both scans.

While the surface morphologies are almost identical, the optical parameters are very different due to master and replica being different materials. This results in different transmittance spectra that is shown in Figure 2.6 (a). The master has a total transmittance of 80%, with a strong absorption below 400 nm, while the replica has a high 90% transmittance with the UV absorption not as strong as in the master. The diffuse part, however, is much more pronounced in the master. This is also expected since the n of the ZnO:Al is higher than the n of the lacquer (Figure 2.4 (b)). This means that when the scattered beams leave the material and propagate in air, they are scattered into wider angles in the ZnO:Al case. Higher the difference in n, higher the difference in diffuse spectra. This is also observed in the ADF. Figure 2.6 (b) shows line scans, while Figure

2.6 (c) and (d) show 3D ADF. The signal ADF is approximately 1.6 times higher for the ZnO:Al sample which is also the ratio in diffuse part (50:30) between the two samples at the illumination wavelength of 633 nm. Here must be mentioned, that in an application the replica will be coated with a TCO, which will bring replica's optical properties closer to the ones of the master.

(a) (b)

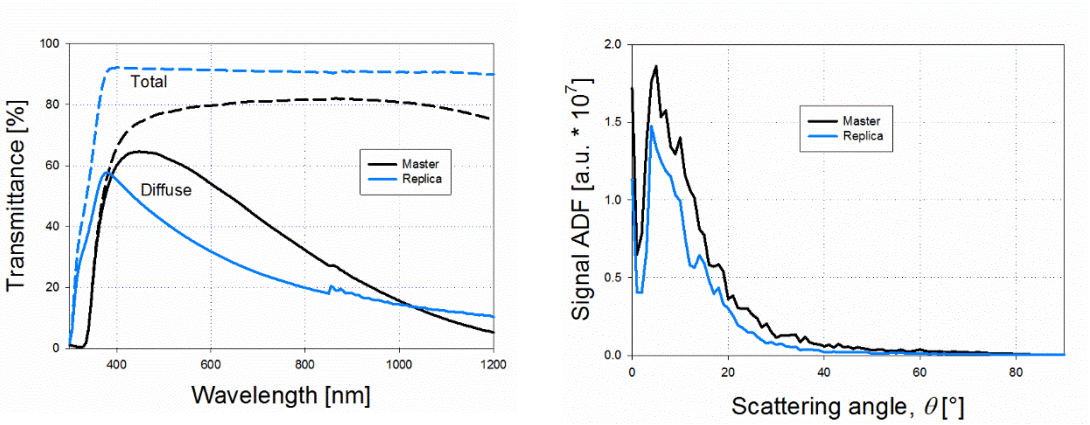

(c) (d)

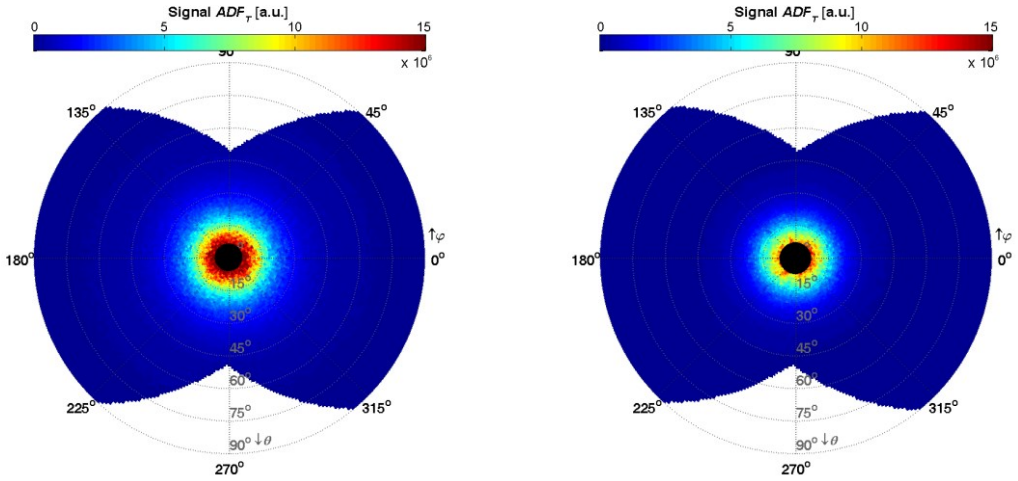

Figure 2.6: (a) Transmittance, (b) ADF line scans and (c) and (d) 3D ADF results of the master and replica. Etched ZnO:Al (a) was used as a master. Laser with $\lambda = 633$ nm was used as an illumination source for the 3D ADF measurements.

2.5 Process reproducibility

One of the biggest advantages of the UV NIL process is the possibility of reusing the stamp. From one master, we can create several stamps and we can use each stamp several times to create a large amount of replicas. This way, not only can we introduce complex textures into the device structure, but make introducing textures into device structure time- and cost-effective. However, this makes repeatability one of the key factors of the replication process.

To test the transfer fidelity after multiple replication processes, we created a stamp from an etched ZnO:Al master and used it to create 12 replicas. Transfer fidelity was then determined by measuring surface morphology with AFM, total and diffuse transmittance and ADF of the replicas. The AFM results are presented in Table 2.1. Overall, the roughness parameters of the master are the highest, with all the replicas faring slightly worse, especially replica 12. However, all 25 measurements (5 per sample) were performed using the same tip, the order of the measurements of the samples is stated in the table. This might cause some of the values being lower than in reality due to the tip being worn out, especially for the samples at the end. For example, ninth replica that was measured first, has higher σ_{RMS} than both first and fifth replica. Nevertheless, roughness parameters of the last replica (replica 12) are slightly lower.

Table 2.1: Roughness parameters, extracted from AFM measurements, for an etched ZnO:Al master and replicas after multiple replication processes (1, 5, 9 and 12). Samples were measured one by one, 5 measurements per sample were done. The order of the AFM measurement is also stated.

Sample name	Measurement order	σ_{RMS} [nm]	l_c [nm]	Θ_{avg} [°]
Master	3	115.0 ± 7.2	611.0 ± 47.5	19.6 ± 0.4
Replica 1	2	103.3 ± 7.3	636.8 ± 29.8	17.6 ± 0.4
Replica 5	5	101.3 ± 8.5	627.2 ± 26.2	17.5 ± 0.9
Replica 9	1	110.3 ± 6.5	632.2 ± 24.7	18.9 ± 0.5
Replica 12	4	97.6 ± 4.3	592.4 ± 29.7	17.4 ± 0.2

Light scattering measurements are shown in Figure 2.7. Both transmittance and ADF measurements show no real difference between any of the replicas, fabricated with the same stamp. Despite the roughness parameters having lower values, all the graphs show that scattering properties remain very similar even if the stamp was used several

times beforehand. This proves that a stamp can be used several times without any deterioration in performance.

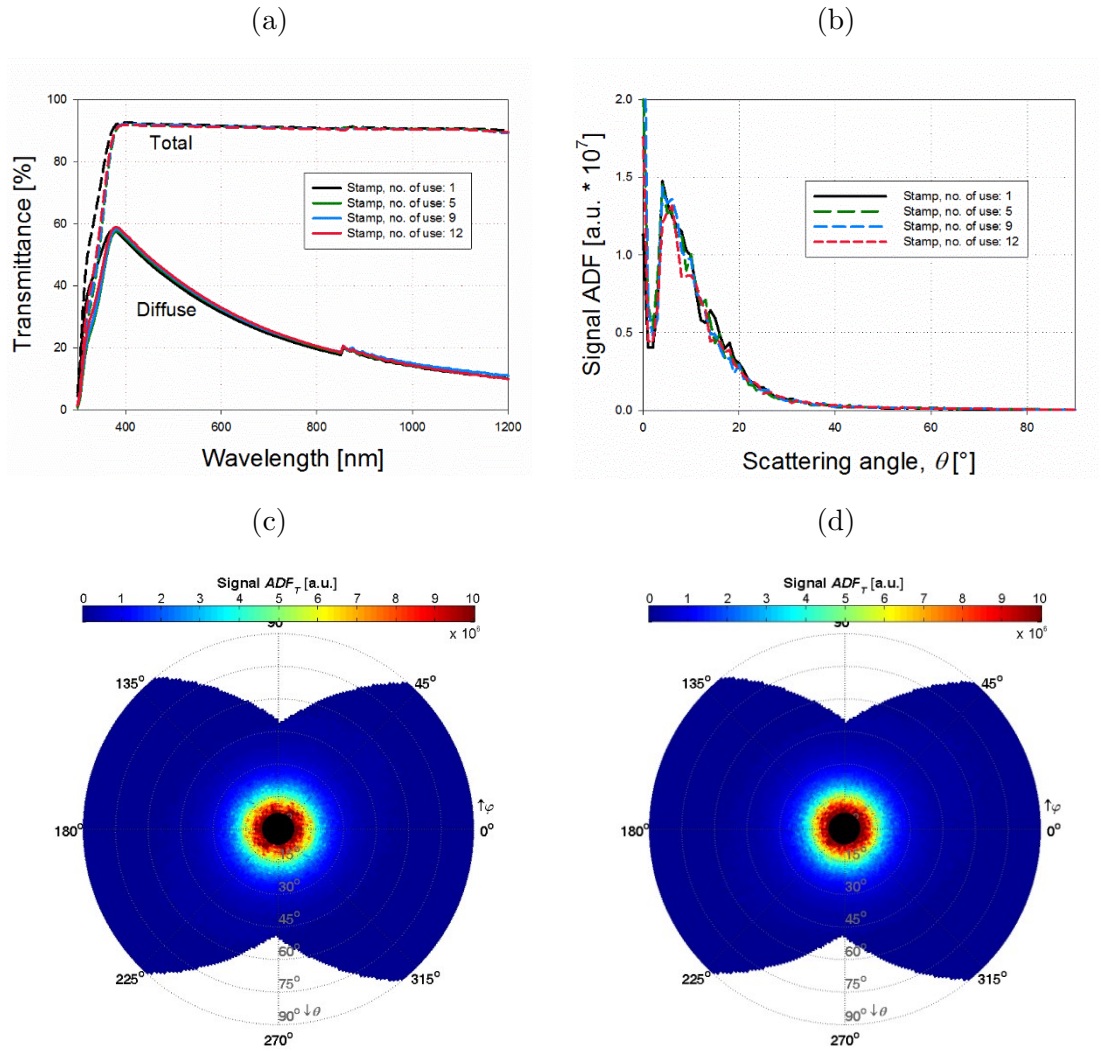

Figure 2.7: (a) Transmittance, (b) ADF line scans results of different replicas (1, 5, 9 and 12) created with the same stamp, (c) and (d) 3D ADF of the first and ninth replica. Laser with λ = 633 nm was used as an illumination source for the 3D ADF measurements.

2.6 Thermal stability of the UV NIL lacquer

The UV NIL lacquers are polymers which means they are likely to be sensitive to high temperatures. According to specifications, the lacquers should be thermally stable up to 200 °C, making them suitable for some of the low temperature (deposition) processes. Nevertheless, we still carried out some tests. 9 replicas from the previous section were heated on a hot plate at different temperatures (100, 150 and 200 °C) for different times (15 min, 30 min and 60 min) as stated in Table 2.2, 3 replicas were not

heated (1, 5 and 9). Since the samples survived without any visible changes (replicas 3 and 4, heated at 200 °C, turned slightly yellow), replicas 1 and 5 were heated at 200 °C for 120 and 180 min, respectively. The replica 9 was heated at 250 °C. It survived the heating, however, on the removal from the hot plate, the lacquer cracked, presumably due to fast cooling of the sample. Lacquers, heated at 300 °C, crack during the heating.

Table 2.2: Thermal stability testing conditions for different samples. Temperature and time of the testing for each replica are stated. Replicas 1,5 and 9 were first used as reference samples ($t = 0$ min) and later used at 200 °C (replicas 1 and 5) and 300 °C (replica 9).

	100 °C	150 °C	200 °C
0 min	Replica 9	Replica 5	Replica 1
15 min	Replica 10	Replica 6	Replica 2
30 min	Replica 11	Replica 7	Replica 3
60 min	Replica 12	Replica 8	Replica 4
120 min			Replica 1
180 min			Replica 5

2.6.1 Results and discussion

After the testing, the replicas were characterized by transmittance, ADF and AFM measurements. For the temperatures T = 100 and 150 °C there is almost no change in total and diffuse transmittance due to heating. However, the samples that were heated at 200 °C experience drop in total transmittance below 500 nm, which is then also transferred to a drop in diffuse transmittance in the same wavelength range. Naturally, longer the heating, higher the drop. This can also be seen visually as the samples turned yellower, the longer they were heated. At 633 nm, where the 3D ADF was measured, a small change can be observed. The 3D ADF is a bit narrower, however, the extracted line scans are still very similar. The heated samples have slightly lower values but no real trend can be observed. The results indicate that heating causes chemical change (yellowing) in the lacquer.

Since the transmittance measurements only showed changes for the samples heated at T = 200 °C, we performed AFM measurements for those samples only. The results are shown in Table 2.3. The drop in values of the roughness parameters increases with the duration of heating. However, this drop is surprisingly small, especially compared to some previous result, obtained during thermogravimetric analysis (TGA).

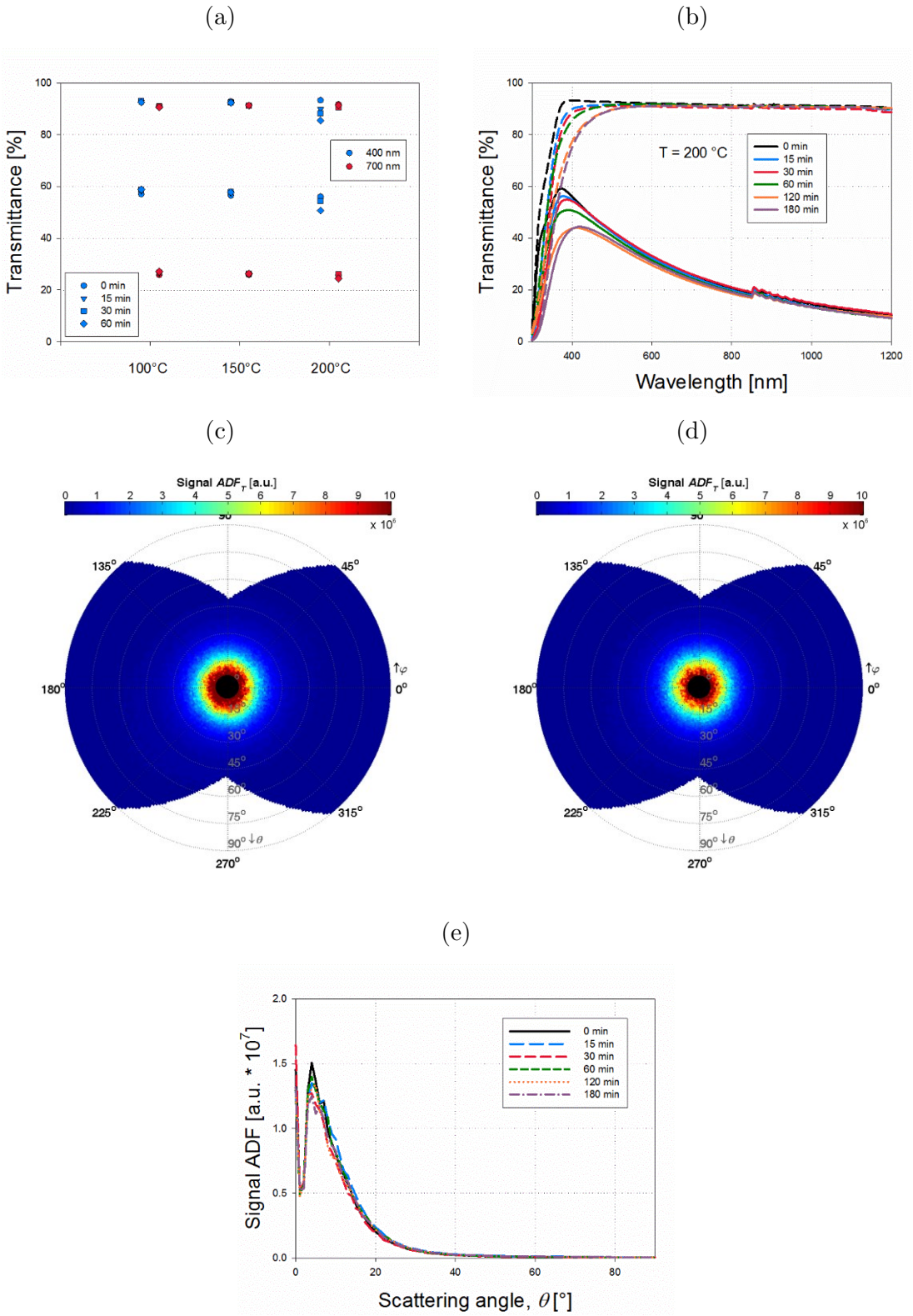

Figure 2.8: Total and diffuse transmittance (a) at λ = 400 and 700 nm for samples heated at different temperatures and (b) for samples heated at 200 °C. 3D ADF of the replicas heated for (c) 15 min and (d) 120 min. (e) ADF line scans for all the samples heated at 200 °C. Laser with λ = 633 nm was used as an illumination source for the 3D ADF measurements.

Table 2.3: Roughness parameters, extracted from AFM measurements, for the replicas that were heated at 200 °C for different periods of time.

Sample name	Time @ 200 °C	σ_{RMS} [nm]	l_c [nm]	Θ_{avg} [°]
Replica 2	15	105.5 ± 6.8	660.9 ± 51.5	17.5 ± 0.6
Replica 3	30	103.7 ± 2.6	610.7 ± 16.0	18.5 ± 0.3
Replica 4	60	99.5 ± 6.3	642.8 ± 53.3	16.9 ± 0.4
Replica 1	120	97.5 ± 5.6	631.5 ± 45.6	17.0 ± 0.6
Replica 5	180	98.1 ± 7.4	670.5 ± 86.2	16.6 ± 0.3

2.6.1.1 Thermogravimetric analysis

Thermogravimetric analysis (TGA) was performed to determine the outgassing of the lacquers during heating. This time a different master was used, LPCVD ZnO:B. The replica was heated at a constant temperature T = 170 °C and weight was measured every 15 minutes. Since the hot plate used does not enable simultaneous weighing, the samples were briefly taken off the plate during the heating before being put on again, and did therefore cool down a bit. The results of the TGA are shown in Figure 2.9 (a). Only 3% of the weight was lost, confirming low degassing. This means that replicas can be used in different processes without contaminating the machines.

Afterwards, morphology of the master, replica and heated replica were measured using AFM. The AFM scans are shown in Figure 2.9 and extracted roughness parameters in Table 2.4. The comparison between master and replica reveals excellent transfer fidelity. However, compared to the samples discussed above, the change after heating is drastic. Even visually the replica looks melted, which is then confirmed by almost 25% drop in σ_{RMS} and almost 50% drop in Θ. It is surprising that the samples reacted differently to heating, especially as this samples were heated at 30 °C lower temperature. An unlikely explanation is that the two textures are different and it is easier to melt pyramid-like features which have peaks (maxima) than crater-like features which have valleys (minima). It is also possible that there is an effect of the temperature change that occurred during the weighing. Each time the sample was weighted, it cooled down and was then heated again. The lacquer at T = 250 °C also cracked only after they were removed from the hot plate. This would also explain some of the results in the next section where samples were tested outdoor and exposed to multiple changes in temperature.

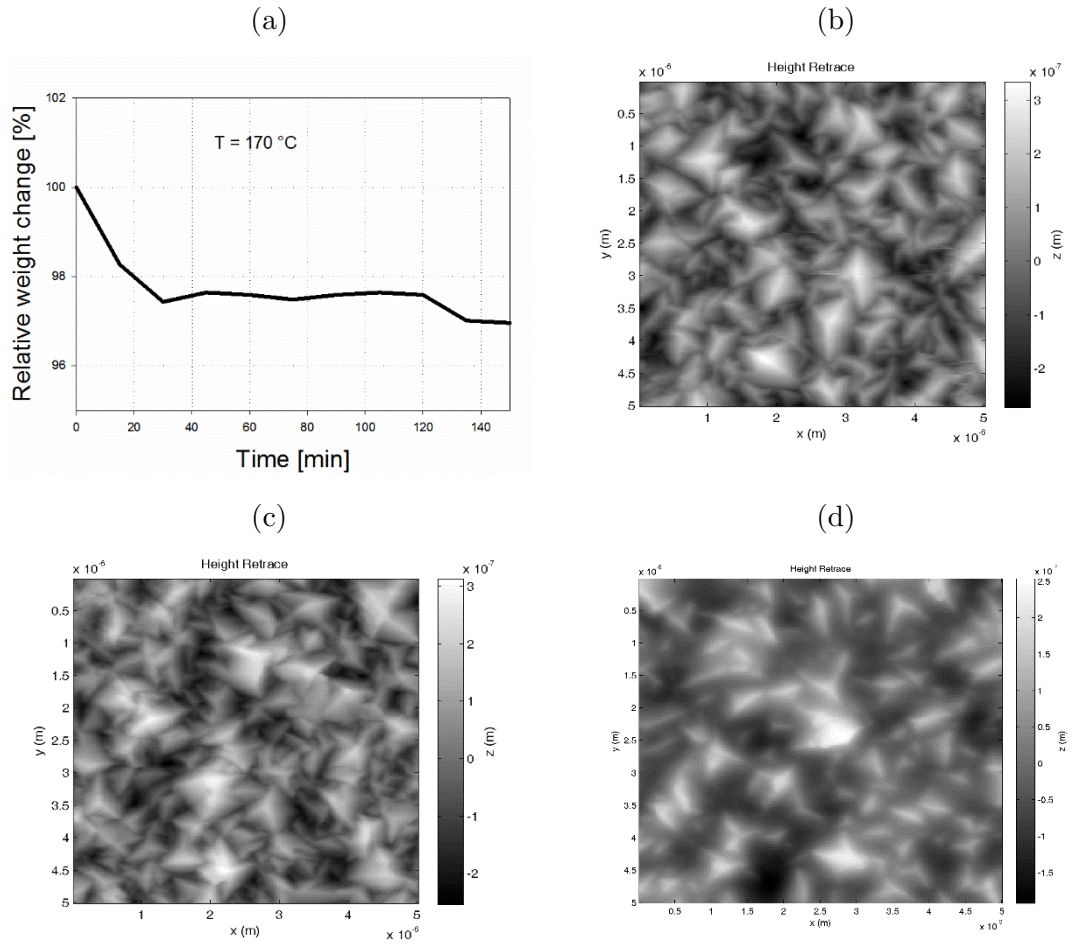

Figure 2.9: (a) TGA graph of the replica heated at T = 170 °C for 150 min. AFM scans of LPCVD ZnO:B (b) master, (c) replica and (d) replica after TGA test.

Table 2.4: Roughness parameters, extracted from AFM measurements, for an LPCVD ZnO:B (b) master, (c) replica and (d) replica after 150 min of TGA at 170 °C.

Sample name	σ_{RMS} [nm]	l_c [nm]	Θ_{avg} [°]
Master	96.3 ± 1.2	222.0 ± 11.9	41.2 ± 1.8
Replica	93.0 ± 3.9	244.5 ± 23.4	37.3 ± 2.5
Replica after heating	72.0 ± 2.9	317.5 ± 18.3	22.4 ± 0.6

2.7 *Outdoor testing of the UV NIL replicas*

One of the possible uses of created UV NIL replicas is as a light management foil on top of the device. In this configuration, the foil is the top layer and as such exposed to different environmental conditions that might chemically alter the layer or damage its surface. To test the endurance and durability of UV NIL replicas, a set of samples was

placed on the roof of the Faculty of Electrical Engineering, University of Ljubljana, next to solar PV modules as shown in Figure 2.10 (a). The following samples were fabricated (see Figure 2.10 (c) for more details):

- Replicas with flat surface (glass as a master)
  - 1 sample with sun/lacquer/glass configuration
    - 1 part on a white surface (slightly in air) – (1)
    - 1 part on a dark (black) surface – (1 d)
  - 1 sample with sun/glass/lacquer configuration – (2)
  - 1 reference sample, kept in a cupboard – (3)
- Replicas with textured surface (etched ZnO:Al as a master)
  - 1 sample with sun/lacquer/glass configuration
    - 1 part on a white surface (slightly in air) – (4)
    - 1 part on a dark (black) surface – (4 d)
  - 1 sample with the sun/glass/lacquer configuration – (5)
  - 1 reference sample, kept in a cupboard – (6)

2.7.1 Results and discussion

The outdoor testing lasted three months, it began on June 11, 2015 and finished on September 22, 2015. During that time, the samples endured different conditions from sunny and hot weather (>35 °C) to heavy rain (Table 2.5). Their transmission was tested regularly while AFM measurements were performed after 2 months. The images with a Flir E series thermal camera (Figure 2.10 (b)) were done on the last day of the testing, which was a sunny day. They show that the samples can heat up well above the air temperature. There is also a significant difference between the samples on a black surface and samples that are slightly in air. As observed from the thermal image, the T reached 40 °C on a black surface and around 25 °C on a white one. During the hottest days, those temperatures could have been even twice as high with the high temperature lasting for several hours. Additionally, the samples with lacquer facing down (2 and 5) appear to be cooler than those with lacquer facing up (1 and 4). The reason for that could be due to different emissivity of the lacquer and glass, therefore the camera detects them differently. Also, the reflectance of sample in glass/lacquer configuration is less than 2% higher than in the lacquer/glass configuration and this should not result in such high

temperature difference. Long exposure to UV light or temperature also made samples yellower compared to the ones in cupboard (Figure 2.10 (d)).

(a)

(b)

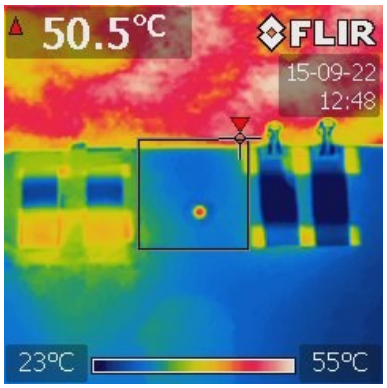

(c)

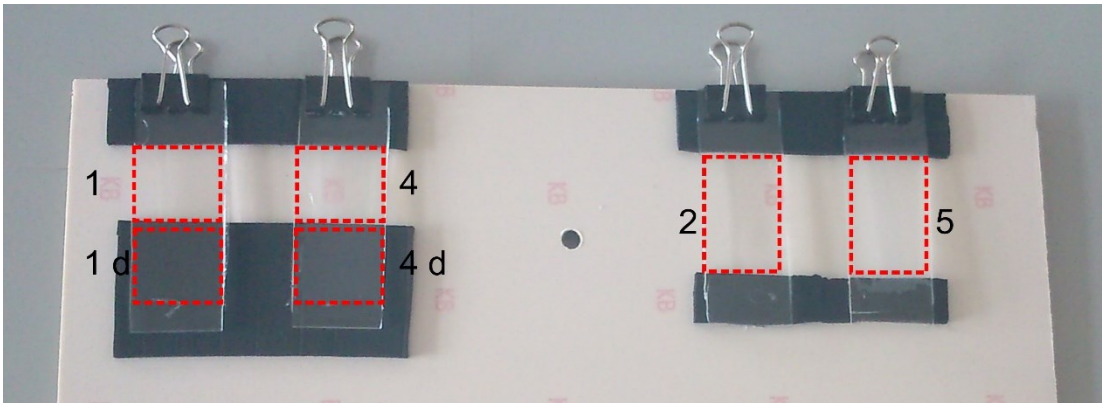

(d)

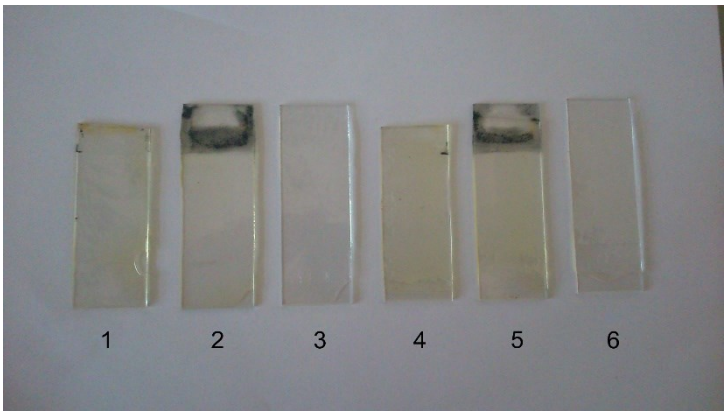

Figure 2.10: Photos of the outdoor investigated samples (a) in a testing environment at an outdoor PV module monitoring site, (b) with a thermal camera on a sunny day, (c) on a plate with different testing positions denoted just before the test and (d) samples after 42 days of outdoor testing.

Table 2.5: Testing days with dates when the samples from the 3-month outdoor testing were measured, measurements performed on that day and weather conditions since the last test.

Testing day	Date	Measurement	Weather conditions since the last test
Day 0	11.6.2015	*T*	-
Day 1	12.6.2015	*T*	Sunny and warm, up to 30°
Day 4	15.6.2015	*T*	Hot, a little rain on Sunday
Day 7	18.6.2015	*T*	Warm, cloudy and rain
Day 11	22.6.2015	*T*	Occasional rain
Day 19	30.6.2015	*T*	Often heavy rain
Day 26	7.7.2015	*T*	Hot and sunny, up to 35°
Day 33	14.7.2015	*T*	Hot and sunny, up to 35°
Day 42	23.7.2015	*T*	Hot and sunny, up to 35°
Day 50	31.7.2015	*T*	Cloudy and rainy, T below 25°
Day 63	13.8.2015	*T,* AFM	Sunny and warm, over 30°
Day 75	25.8.2015	*T*	Cloudy, rainy
Day 91	10.9.2015	*T*	Mixed weather
Day 102	21.9.2015	*T*, thermal camera	Mixed weather

2.7.1.1 Optical measurements

Transmission measurements were performed on days listed in Table 2.5. The selected results for two different wavelengths (400 and 700 nm) for days 0, 1 19, 50 and 91 are shown in Figure 2.11 (a) and (b) and results for each sample on those days are shown in Figure 2.11 (c) and (d). Figure 2.11 (e) and (f) show measurements from day 50 and measurements for sample 5, respectively. Graphs for other samples can be found in the appendix. Both total and diffuse transmission were measured. A few conclusions can be drawn. The samples remain highly transparent in a broad wavelength range and textured replicas preserve their scattering properties. However, already on the first day their transmittance below 500 nm (blue dots) decreased significantly. This is attributed to the yellowing effect due to exposure to sun UV light and high T which is even more pronounced after longer time (Figure 2.10 (b) shows samples after 42 days). After three months, on day 91, the transmittance of the samples outdoor dropped even further in the UV-blue spectrum, especially for the samples on the dark surface. Reduced total transmission under 500 nm also causes drop in the diffuse transmission peak for textured

replicas. Additionally, the diffuse spectra are lower compared to the reference samples in the whole wavelength range.

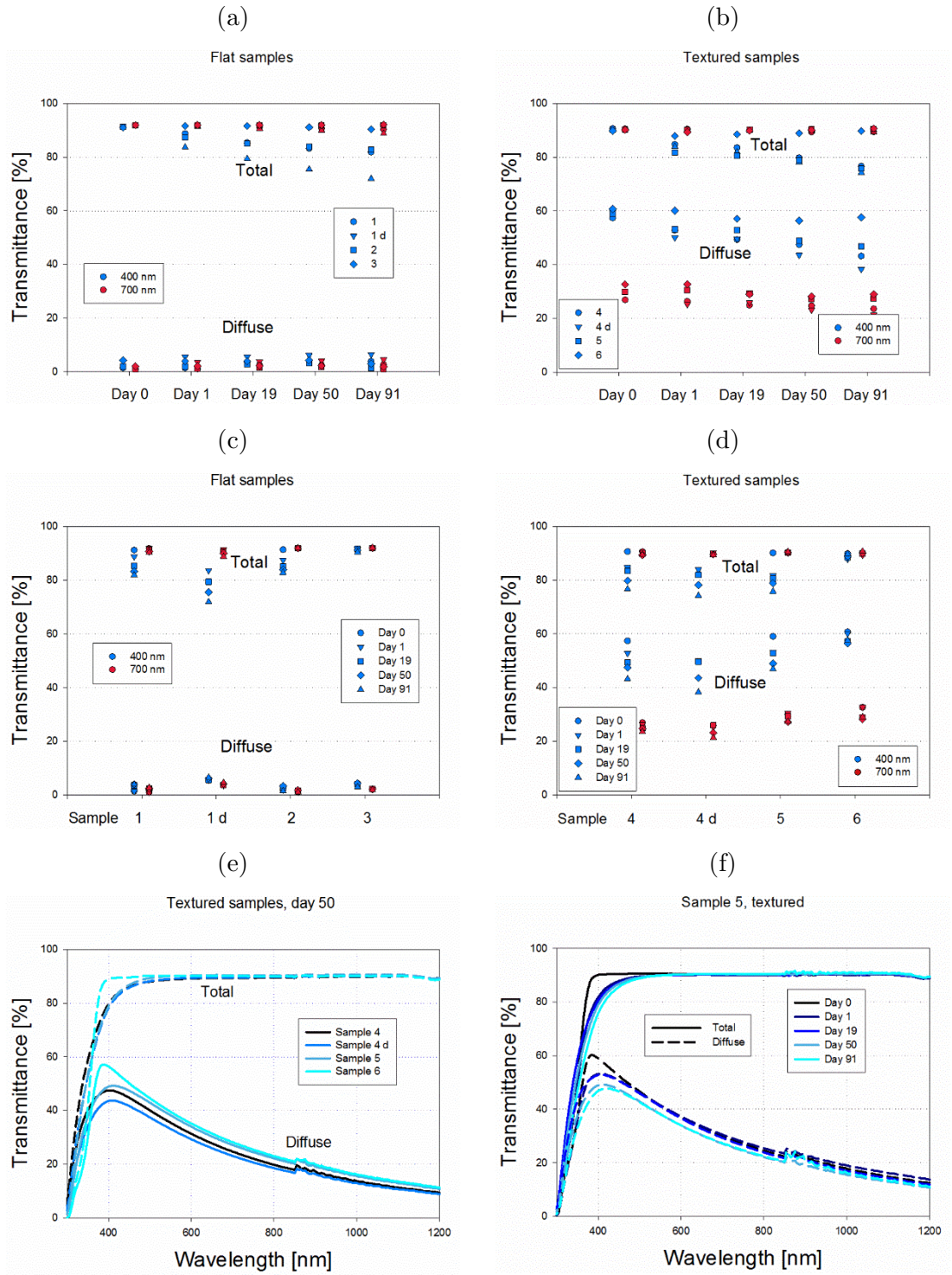

Figure 2.11: (a) and (b) Transmittance on different days (0, 1, 19, 50 and 91) and (c) and (d) transmittances of the samples for wavelengths 400 and 700 nm. (a) and (c) show transmittance of the flat samples, (b) and (d) show transmittances of the textured samples. (e) Transmittance of all the textured samples on day 50. (f) Transmittance for the sample 5 on different days.

Different test configurations of the replicas result in different behaviour. Samples where lacquer is on the bottom side (2 and 5) experience smaller change in transmission than samples with lacquer side up. Again, the sample that was on black surface fares worse, the peak in diffuse component of the texture sample drops by 20%. This is likely caused by yellowing effect and long exposure to heat. The samples should be thermally stable up to 200 °C but the long exposure to temperatures around 70 °C for over 8 hours a day might have the same effect as high temperatures around 200 °C, melting the lacquer and its texture, making it less rough. The reference replicas (3 and 6) remain the same except, interestingly, the diffuse component drops slightly for the textured replica after day 1.

2.7.1.2 Surface morphology measurements

AFM measurements were performed after 2 months to determine if any physical damage was done to the samples. The scans in Figure 2.12 reveal that the samples with lacquer on the top side have higher amount of defects. The defects are rather small and are on top of the surface, attached strongly enough to the surface that they were not removed by water rinsing. Either way, the dust particles are a reality for the outdoor applications and cannot be neglected or eliminated before the measurements with more thorough cleaning. For the samples with lacquer on the bottom side, the glass acts as a protecting layer. The amount of defects there is therefore much lower.

The roughness parameters σ_{RMS}, l_{c} and Θ_{avg} are presented in Table 2.6. The reference samples were taken as a benchmark since they are not expected to change in dry and dark environment. The results are in accordance with previous results and assumptions. The flat samples with lacquer facing up have higher amount of particles on the surface than the sample with lacquer facing down. This results in higher σ_{RMS} and Θ_{avg}. Some of the measurements had to even be excluded due to particles on surface being so large that they corrupted the measurement results (σ_{RMS} = 160 nm for a flat sample). For the textured replicas all the roughness parameters are lower when lacquer is facing up. The samples with lacquer facing down fare better. Due to the higher outdoor temperature and consequently the temperature of the sample, the values are lower than for the reference sample, however, still higher than for the samples with lacquer facing up. As discussed in previous section (2.7.1.1), this is most likely due to the samples with lacquer facing up heating up more than the samples with lacquer facing down (see Figure 2.10 (b)). It is also probable that glass facing up, protects the lacquer from other external effects, such as small particles hitting the surface and damaging the layer.

(a) Sample 1

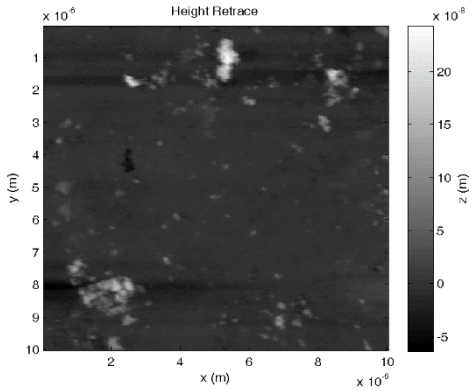

(b) Sample 4

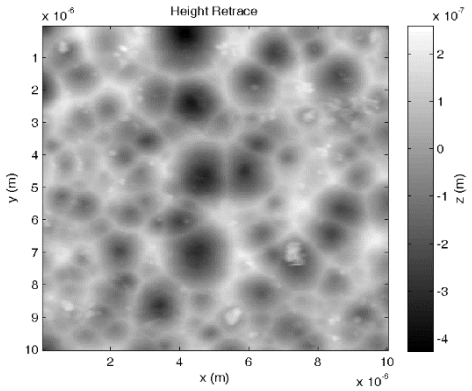

(c) Sample 1 d

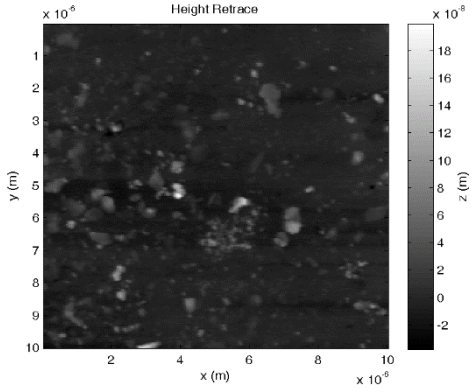

(d) Sample 4 d

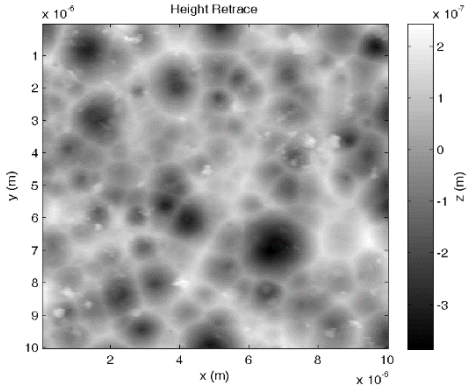

(e) Sample 2

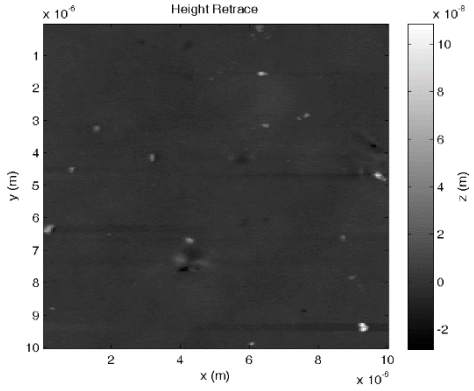

(f) Sample 5

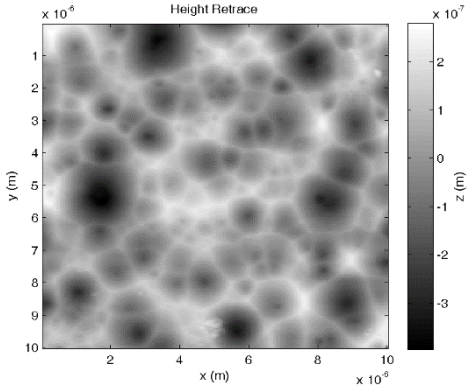

Figure 2.12: AFM scans of the samples outdoor after 2 months. (a), (c) and (e) are flat samples, while (b), (d) and (f) are textured samples. Name of the sample is stated above the AFM scan.

Table 2.6: Roughness parameters, extracted from AFM measurements, as measured after 2 months of the outdoor testing for all the samples.

Sample name	σ_{RMS} [nm]	l_c [nm]	Θ_{avg} [°]
1	23.1 ± 5.3	343.7 ± 57.1	6.4 ± 1.0
1 d	17.1 ± 4.8	226.0 ± 30.5	5.8 ± 1.1
2	3.7 ± 1.7	180.4 ± 62.0	1.3 ± 0.1
3	6.3 ± 2.5	330.3 ± 108.5	1.5 ± 0.2
4	101.5 ± 5.6	584.2 ± 34.3	19.7 ± 0.2
4 d	95.1 ± 6.0	548.2 ± 77.0	19.3 ± 0.9
5	106.2 ± 4.8	592.6 ± 38.1	19.8 ± 0.3
6	115.0 ± 7.2	611.0 ± 47.5	19.6 ± 0.4

2.7.2 Conclusion

Fabricated UV NIL replicas were placed outdoor to investigate how environmental conditions affect their characteristics. During the three-month test, the samples turned yellow. This yellowing effect was confirmed by transmittance measurements which revealed reduction in total transmittance below 500 nm. The diffuse transmittance worsened with time and in the whole wavelength range. This is most likely caused by drop in total transmittance and long exposure to high temperature that slowly melts the texture, reducing its roughness. This was confirmed by AFM measurements that showed lower values of roughness parameters for the samples exposed to higher temperature. For the use in practical applications, where the samples are exposed to sun, lacquers with more stable chemical composition without yellowing should be used. Nevertheless, the replicas survived the test without any substantial damage, did not peel off the glass substrate and preserved scattering properties, though not as great as the reference samples.

2.8 UV NIL replicas as substrates for TCO deposition

Light scattering phenomenon can also be caused by textured surfaces within the device structure. In thin-film solar cells, the scattering layer is usually TCO, however, its morphology is connected and limited by the deposition or post-deposition processes.

To replace the additional treatment of the TCO and exploit different morphologies, the created replicas can be used as a scattering layer within the device structure. As the lacquers are not conductive, they have to be coated with a conductive layer to form electrical contact - a TCO. Nowadays, a variety of different TCOs exist, containing different metal oxides with various metal ratios, e.g. SnO_2:F – FTO, SnO_2:In – ITO, ZnO:Al [44]–[48]. Depending on the material composition and doping, different thicknesses of TCO are needed to ensure good conductivity. For example, typical thicknesses for FTO, ITO and ZnO:Al are around 700, 150 and 500 nm, respectively. Since the conformal growth can turn into isotropic one for thicker layers, thin TCOs, such as ITO, are preferable for deposition on nanotextured substrates if we want to preserve the nanotexture [49], [50]. Nevertheless, some scattering remains even if the TCO deposition on the textured replica is so thick that the texture on the front surface the original replica texture is smoothened. In this case, the scattering occurs at the textured replica/TCO interface due to their different refractive indices: UV NIL lacquer has $n = 1.55$ and TCOs usually have $n = 2$.

Recently, a new material, ITO doped with Gallium (GITO - $Ga_{0.08}In_{1.28}Sn_{0.64}O_{3.32}$) drew attention due to its promising electrical and optical properties [51]–[54]. Good results have already been obtained with GITO sputtered on a glass substrate [55], [56], therefore we decided to deposit it also on our replicas.

2.8.1 Experimental

To test our UV NIL replicas as (textured) substrates for TCO deposition, replicas with two different texture types were created from two different masters: 4 samples were made with a flat surface obtained from glass (later referenced as texture A) and 4 samples with the surface as obtained from sputtered and then etched ZnO (later referenced as texture B). All the samples then underwent a GITO sputtering process, which is a standard deposition process for GITO.

A Sputron sputtering system (Oerlikon Balzers) with a low voltage thermionic arc as a source of ions for sputtering was used. Substrates (Corning Eagle glass, 1 mm thick) were mounted on a planetary drive system which permits a double rotation of substrates, therefore the deposition rate and thickness reproducibility were better than 2%. The target-substrate distance is about 225 mm, meaning that the substrates were out of plasma. The substrates can therefore be at a temperature below 100 °C or heated up

with a quartz lamp to a desired temperature. The sputtering lasted 48 min at the oxygen flow 0.583 cm^3 min^{-1} and RF power 750W. Two different temperatures of deposition were applied. First, 2 samples with texture A were coated with GITO under the temperature of 170 °C. Despite the used lacquers being thermally stable till 200 °C, the two samples looked slightly melted. Therefore, we decided to use the deposition temperature of 120 °C for all the other samples. More on the sputtering target preparation and sputtering itself can be found in [55], [56]. The expected thickness of GITO layer for the used parameters is around 120 - 150 nm. This was confirmed from the optical measurements when determining n and k spectra, the SEM cross-section measurements were not carried out though. For such thickness of the deposited TCO material, predominantly conformal growth is expected [49].

Since the sputtered GITO has less conductive amorphous structure some of the samples were annealed for GITO to crystallize and improve conductivity [51]. Higher the temperature, more crystalline the GITO is. The best conductivity results were achieved with GITO annealed for 30 min at 340 °C [55], [56]. However, due to thermal stability of the UV NIL lacquers, lower temperatures are advised. Still, 30 min annealing was carried out at 2 different temperatures. The annealing at 200 °C was conducted successfully, while the annealing at 300 °C resulted in lacquers cracking, as they are not thermally stable at that temperature. The history of the samples is shown in Table 2.7. The names of the samples are structured as: texture and the number of the sample/GITO deposition temperature/annealing temperature. – denotes that the process was not performed.

Table 2.7: Sample list and GITO preparation process. The names of the samples are structured as: texture and the number of the sample/GITO deposition temperature/annealing temperature. – denotes that the process was not performed.

Sample name	Texture	Deposition T (°C)	Annealing	
A1/170/200	A	170	200 °C	
A2/170/-	A	170	-	
A3/120/200	A	120	200 °C	
A4/120/300	A	120	300 °C	Lacquer cracked
B1/120/200	B	120	200 °C	
B2/120/300	B	120	300 °C	Lacquer cracked
B3/120/-	B	120	-	
B4/120/-	B	120	-	

2.8.2 Results and discussion

The samples were prepared successfully, the GITO adhered on the lacquers and did not peel off even after a longer time. The thickness of GITO layer was estimated to be 120 - 150 nm as it was measured for a sample where glass substrate was coated under the same conditions with GITO only (no UV NIL layer). It is harder to determine the thickness of the GITO layer deposited on more complex substrates, therefore we assumed that GITO with such thickness was also deposited on the textured substrates samples.

To fulfill their purpose, the (TCO) samples should not only be conductive electrically but also optically. As much photons as possible should be transmitted through the lacquer and GITO (to the active solar cell layers) without being absorbed or reflected. The initial texture should also be preserved after deposition to maintain its scattering abilities. 3 different types of measurements were used to establish the successfulness and suitability of the deposition process and the fidelity of the texture transfer:

- Sheet resistance measurements
- Optical measurements
- Surface morphology measurements – AFM

2.8.2.1 Sheet resistance measurements

Sheet resistance R_{sh} measurements were done using a RIG Mode C (A.&M. Fell) 4-probe head and a Keithley 2602 source meter. Non-uniformity was considered thus the measurements were done at 16 different spots on each sample. Average was then calculated together with standard deviation. The sheet resistance measurement results are presented in Table 2.8. As expected, if the deposition takes place under higher temperature the sheet resistance is lower. This can be observed for the first two samples which have a very low sheet resistance under 100 Ω sq^{-1}. The other samples have sheet resistivity around 400 Ω sq^{-1}. By annealing a decrease in resistance is achieved, for the samples with lower deposition temperature by a factor of almost 4. The standard deviation is low for all the samples, implying their uniformity.

Table 2.8: Sheet resistance measurements before and after the annealing: 16 different spots were measured per sample from which average value and standard deviation were calculated.

Sample name	R_{sh} [Ω sq^{-1}]	R_{sh} after annealing [Ω sq^{-1}]
A1/170/200	97,0 ± 6,7	70,0 ± 4,2
A2/170/-	92,2 ± 29,6	-
A3/120/200	373,3 ± 13,4	118,9 ± 9,3
A4/120/300	381,1 ± 14,8	Lacquer cracked
B1/120/200	457,8 ± 25,5	118,7 ± 23,8
B2/120/300	404,9 ± 33,1	Lacquer cracked
B3/120/-	403,9 ± 28,2	-
B4/120/-	427,6 ± 19,4	-

2.8.2.2 Optical measurements

The optical measurements were performed before and after GITO deposition and after annealing. Some of the most interesting results are presented in Figure 2.13. Figure 2.13 (a) shows transmittance of the samples with texture A. Typical GITO curve can be observed, however, its peak is defined with deposition temperature: around 500 nm for 170 °C and around 550 nm for 120 °C. Higher deposition temperature has a big effect on transmission, which increases for the wavelengths shorter than 500 nm and longer than 850 nm. In-between those wavelengths, the transmission drops. The samples with higher deposition temperature also have higher diffuse transmission. This is probably due to the higher deposition temperature which made the flat surface wavier. All the measurements show that the samples were relatively uniform as the measurements for all three spots on each sample returned similar results (not shown here). Figure 2.13 (b) shows the "evolution" of transmission for the samples with texture B. Diffuse and total transmittance are compared for bare replica without GITO, replica coated with GITO, and annealed replica coated with GITO. A drop in total transmission due to additional absorption in the GITO layer over all wavelengths can be observed while all the samples exhibit diffuse transmission typical for their texture. The diffuse transmission also drops for the wavelengths shorter than 450 nm. Similarly to the samples with texture A, the annealing slightly increases the transmission for the wavelengths shorter than 450 nm and longer than 700 nm. In-between, the transmission after annealing drops. As seen, different temperatures of both deposition and annealing change the transmission

significantly. Further testing with different deposition and annealing parameters is needed to obtain optimum optical and electrical properties.

(a) (b)

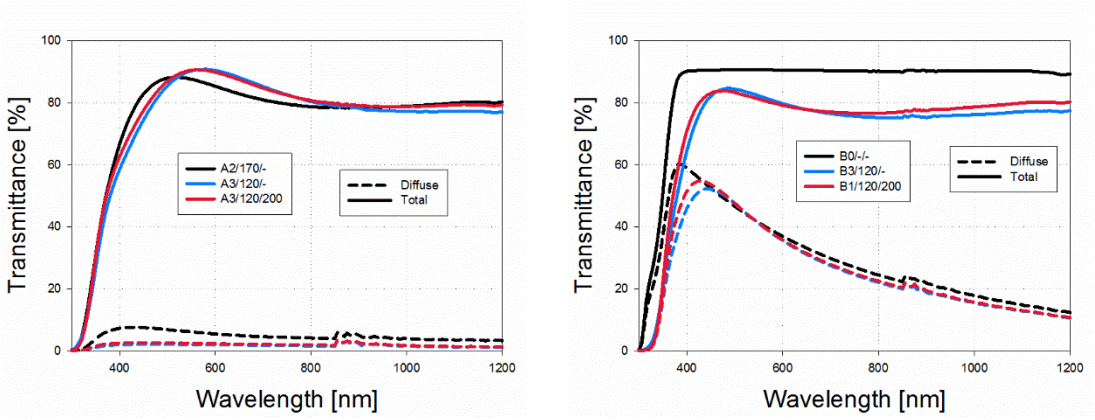

Figure 2.13: Transmittance of (a) samples with texture A and (b) "evolution" of transmittance for each step of the sample preparation for texture B.

2.8.2.3 Surface morphology measurements

The surface morphology measurements are presented in Figure 2.14, where selected AFM scans sized 10 x 10 μm^2 of replicas with texture A and B before and after GITO deposition and after annealing are shown. Visual comparison reveals good fidelity as the surfaces for both types of textures look very similar. Also, all the samples look defect free, except for a few small particles on the sample A0/-/- (Figure 2.14 (a)). Roughness parameters from multiple different areas on each of the samples were averaged and used to quantify the texture preservation after GITO deposition. The results are presented in Table 2.9.

Bare flat replica A0/-/- shows small values for all three parameters. The σ_{RMS} is higher for the samples A1/170/- and A2/170/- together with the average angle, most likely due to the higher deposition temperature. The sample A3/120/200 had a lower deposition temperature, which resulted in a lower σ_{RMS} even compared to the A0/-/-. If this is due to the annealing, it still has to be discovered by further testing. All the parameters for the texture B samples have similar values for each step of the preparation. Annealing does not change or diminish the surface roughness – the texture is preserved.

Comparing the results, it seems that higher temperatures during the deposition can melt the lacquer, resulting in less flat, wavy surface for replicas with texture A. However, once GITO is deposited, the temperature of annealing 200 °C does not harm the lacquer

even though this temperature is the border of the lacquers thermal stability. It is possible that GITO layer acts as some sort of a protection layer. Nevertheless, once the temperatures of annealing are too high, e.g. 300 °C, this protection is not sufficient and the samples (lacquers) crack.

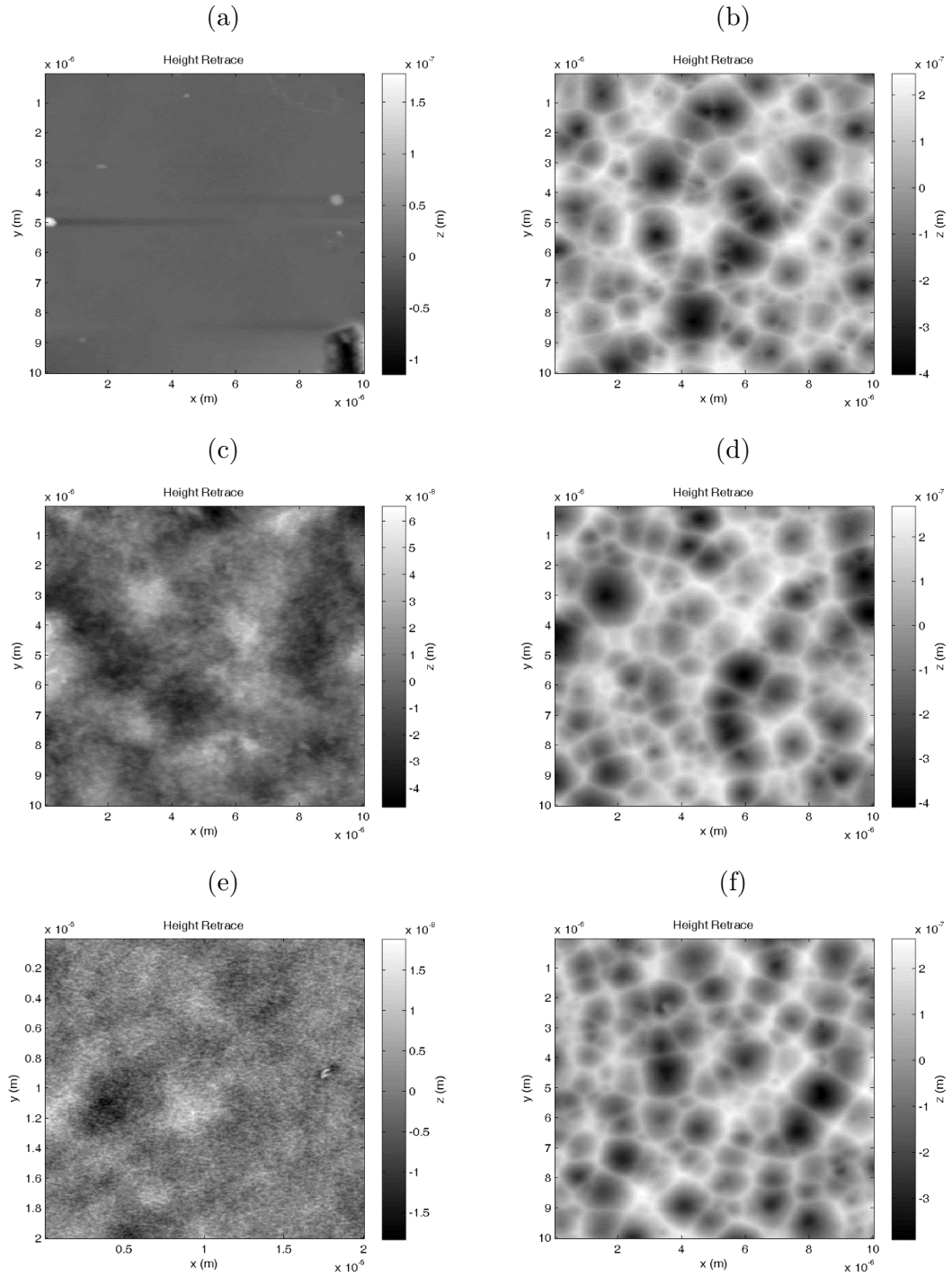

Figure 2.14: Selected AFM scans for: (a) A0/-/-, (b) B0/-/-, (c) A1/170/-, (d) B4/120/- (e) A3/120/200 and (f) B1/120/200. The annealing for sample A1/170/- was done after AFM measurements.

Table 2.9: Roughness parameters, extracted from AFM measurements, for GITO samples or replica substrate. The annealing for sample A1/170/- was done after AFM measurements.

Sample name	σ_{RMS} [nm]	l_c [nm]	Θ_{avg} [°]
A0/-/-	6.3 ± 2.5	330.3 ± 108.5	1.5 ± 0.2
A1/170/-	18.7 ± 3.7	931.2 ± 90.0	3.6 ± 0.0
A2/170/-	27.6 ± 3.3	815.6 ± 76.7	4.8 ± 0.2
A3/120/200	4.0 ± 0.4	795.9 ± 253.2	2.1 ± 0.1
A4/120/300	Lacquer cracked during annealing		
B0/-/-	111.3 ± 3.2	592.4 ± 18.1	20.6 ± 0.2
B1/120/200	117.1 ± 8.4	597.6 ± 52.7	21.5 ± 0.2
B2/120/300	Lacquer cracked during annealing		
B3/120/-	116.5 ± 6.0	590.2 ± 42.0	21.5 ± 0.5
B4/120/-	120.3 ± 2.4	603.3 ± 24.7	21.4 ± 0.5

2.8.3 Conclusion

Nanoimprinted textures, obtained with UV NIL process were used as a substrate for GITO deposition. The deposition was successful which was confirmed with extensive measurements. The best conductivity results were acquired for GITO deposited at 170 °C while for lower deposition temperatures we get higher sheet resistance. The resistance is effectively lowered by annealing. AFM measurements revealed that GITO deposition does not harm the texture. Both visual and surface roughness parameters comparison showed good matching between bare replicas, replicas coated with GITO and annealed replicas with GITO, also indicating conformal growth. The AFM results combined with transmittance measurements show that the samples were relatively uniform. Since the deposition was done and tested only for a small set of parameters, the conductivity and transmittance could still be improved.

2.9 Summary

In this chapter, we presented UV Nanoimprint Lithography. It is a replication process of a surface texture from a master via stamp to the final substrate. Quality of the created replicas was determined using transmittance and AFM measurements. The AFM measurements confirmed good transfer fidelity. Additionally, a software “AFM

analyzer", developed for an easier and fast analysis of the AFM measurements, was described.

The fabricated replicas were thoroughly characterized. Optical parameters, n and k spectra, needed for optical simulations were extracted. The repeatability of the replication process and thermal stability of the lacquers were investigated. The results showed that each stamp can be used at least 12 times with very little deterioration in performance. The lacquers also showed low outgassing and good thermal stability up to 200 °C for up to half an hour, afterwards the yellowing effect occurred. At temperatures above 200 °C the lacquer cracks. This makes replicas suitable for a broad spectrum of low temperature deposition processes.

The fabricated replicas can be used in photovoltaic or optoelectronic devices. Two different cases were investigated. First, if the replicas are used as a light management foil on top of the devices, they need to endure different environmental conditions. Therefore, a three-month outdoor testing was carried out. Transmittance and AFM measurements revealed some damage to the samples. Long exposure to sun caused the samples to turn yellow, reducing the transmission below 500 nm, while high temperatures slightly melted the lacquer, making it less rough and consequently less scattering. Second, the replicas can be used as a scattering layer inside the device structure. This requires an additional conductive layer, usually a TCO. In our case, a gallium doped ITO (GITO) was sputtered on top of the replica. The measurements revealed a moderate sheet resistance, good transmission and conformal growth, with no damage done to the texture due to the sputtering and annealing of GITO.

The results show that UV NIL is an effective tool for replicating textures from masters. However, in a real application, the replicas should withstand different environmental conditions. For this, lacquers with more stable chemical composition should be used since our lacquers showed yellowing effect which deteriorates the transmission of light through the lacquer and therefore the performance of the device.

3 Organic-inorganic perovskite solar cells

This chapter is devoted to organic-inorganic perovskite solar cells. Perovskite solar cells are a new class of solar cells that has drawn attention due to achieved high conversion efficiencies. Promising results have been shown for both single junction and tandem perovskite based solar cells. In order to improve the device performance, especially that of the tandem device, light management techniques have to be implemented as has been shown for conventional solar cells. Until now, not much research has been conducted on light management in perovskite solar cells, therefore we decided to use perovskite solar cells to test the light management foils created by UV Nanoimprint Lithography on a concrete case. For this, we fabricated perovskite solar cells with inverted structure and analyzed their performance without and with a light management foil. Experimental results are supported by optical simulations. The validated optical model is then used to predict improvements with light management foils in both single junction and tandem perovskite devices.

The contents of sections 3.2., 3.3 and 3.4 on experimental analysis and optical modelling of perovskite single junction solar cells with LM foil have been submitted under the title "Efficient Light Management by Textured Nanoimprinted Layers for Perovskite Solar Cells" to the journal *ACS Photonics* [57]. The contents of section 3.4.4 on optical modelling of tandem perovskite/silicon heterojunction solar cells were published in 2016 under the title "Back- and Front-side Texturing for Light-management in Perovskite / Silicon-heterojunction Tandem Solar Cells" in journal *Energy Procedia* [58].

3.1 Introduction

3.1.1 Perovskite

The name perovskite stands for a class of compounds with a crystal structure of ABX_3 (Figure 3.1 (a)). The first perovskite crystal, $CaTiO_3$, was discovered in 1839 and already attracted some research interest in the 20^{th} century [59]–[61]. In 1994 it was

reported that halide perovskites exhibit semiconductor properties [62]. However, first successful device followed only in 2009 after Miyasaka et al. used a $CH_3NH_3PbI_3$ as an inorganic sensitizer in dye-sensitized solar cells and showed a 3.8% efficiency [63]. A real boom in research started in 2012 when liquid electrolyte was replaced by a solid hole transport material which not only improved stability but also increased the efficiency to 9.7% [64] and 10.9% [65]. $CH_3NH_3PbI_3$, methylammonium lead iodide, is now a typical representative of the perovskite absorbers in perovskite solar cells.

To form a perovskite crystal structure (ABX_3), a geometric tolerance factor $t=(r_a+r_x)/(\sqrt{2}(r_b+r_x))$ has to satisfy a condition $0.813 < t < 1.107$ [66], where r_a, r_b and r_x are effective ionic radii for A, B and X ions. For organic-inorganic halide perovskites (referenced as perovskites throughout the dissertation), A is a large cation methylammonium ($CH_3NH_3^+$), ethylammonium ($CH_3CH_2NH_3^+$), formamidinium ($NH_2CHNH_2^+$) or even caesium (Cs^+). Cation B is most commonly lead (Pb^{2+}), however, tin (Sn^{2+}) can also be used. X is a halide ion, either iodide (I^-), bromine (Br^-) or chlorine (Cl^-) or their combinations (e.g. $I_{3-x}Br_x$). Different A, B and X combinations are possible, resulting in different optoelectronic properties [67].

Perovskites are excellent absorbers of the visible light. The direct bandgap of $CH_3NH_3PbI_3$ at 1.55 eV corresponds to a sharp absorption onset at around 800 nm [68] and can be tuned by incorporating bromide or chloride ions (e.g. $Ch_3NH_3PbI_{3-x}Br_x$) [69], [70], as shown in Figure 3.1 (b). The higher the bromide content, the higher is the bandgap. A high absorption coefficient also enables relatively thin layers, in the range around 300 nm, to absorb most incident photons with energies above the bandgap.

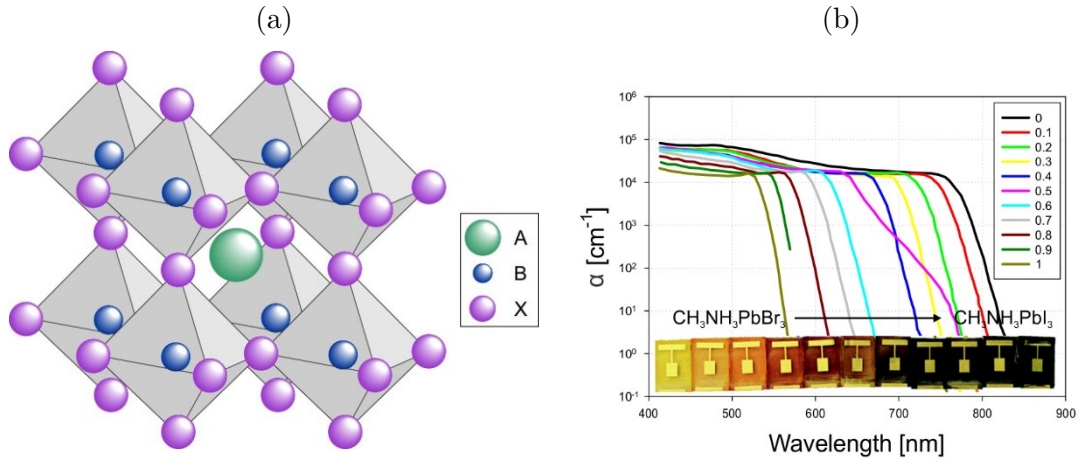

Figure 3.1: (a) Perovskite ABX_3 crystal structure and (b) absorption and bandgap tuning of $Ch_3NH_3Pb(I_{1-x}Br_x)_3$ by incorporation of the bromide ions, data taken from [69].

Besides having good optical properties, perovskite is also an excellent electrical conductor as it has a relatively high carrier mobility for both electrons and holes. Electron mobility was determined to be 7.5 $cm^2\ V^{-1}\ s^{-1}$ [71], while for the holes they range between 12.5 and 66 $cm^2\ V^{-1}\ s^{-1}$ [72]. Long recombination times in the range of hundreds of nanoseconds also result in long diffusion lengths in the range of 100 to above 1000 nm [73]–[75], allowing enough time to extract the photogenerated charges before they recombine.

Thanks to the excellent optical and electrical properties, and extensive knowledge of organic and dye-sensitized solar cells, the solar cells based on perovskite absorbers have attracted a lot of interest of the scientific community in recent years [76]–[78]. Extensive research resulted in a remarkable jump in conversion efficiency from 3.8% in 2009 [63] to 22.1% in 2016 [6], [79], which is the fastest increase in efficiency in the history of photovoltaics. Beside single-junction solar cells, bandgap tuning and processing steps at low temperatures (such as spin-coating) make perovskites an interesting partner also for tandem solar cells with either silicon [80]–[83], CIGS solar cells [84], or other low-bandgap solar cells, even perovskite [85], [86].

3.1.2 Single junction perovskite solar cells

First perovskite solar cells originated from dye-sensitized solar cells (DSSC) which needed a (TiO_2) scaffold to increase the interface area between the dye absorber and electron transport material (ETM) [87]. Compared to DSSC, the perovskite solar cells work even if perovskite fully infiltrates the scaffold and not only covers it as an overlayer [78]. Such a structure with a scaffold is called a mesoporous structure and is to this day still the most efficient perovskite structure. However, once high mobility and long diffusion length were discovered, planar devices (without a scaffold) have also become very popular [88]–[90]. Both structures are shown in Figure 3.2; the left side of each schematic shows a mesoporous structure, and the right side a planar structure.

Typically, perovskite solar cells are built on a glass substrate; however, flexible substrates are also possible [91], [92]. The front electrode is a TCO, most commonly ITO (SnO_2:In) or FTO (SnO_2:F). The back electrode is usually either gold (Au) or silver (Ag); however, aluminum and copper are also possible. In-between the electrodes, the perovskite absorber is sandwiched between the electron transport material (ETM) and the hole transport material (HTM); some of the most common ETMs and HTMs are

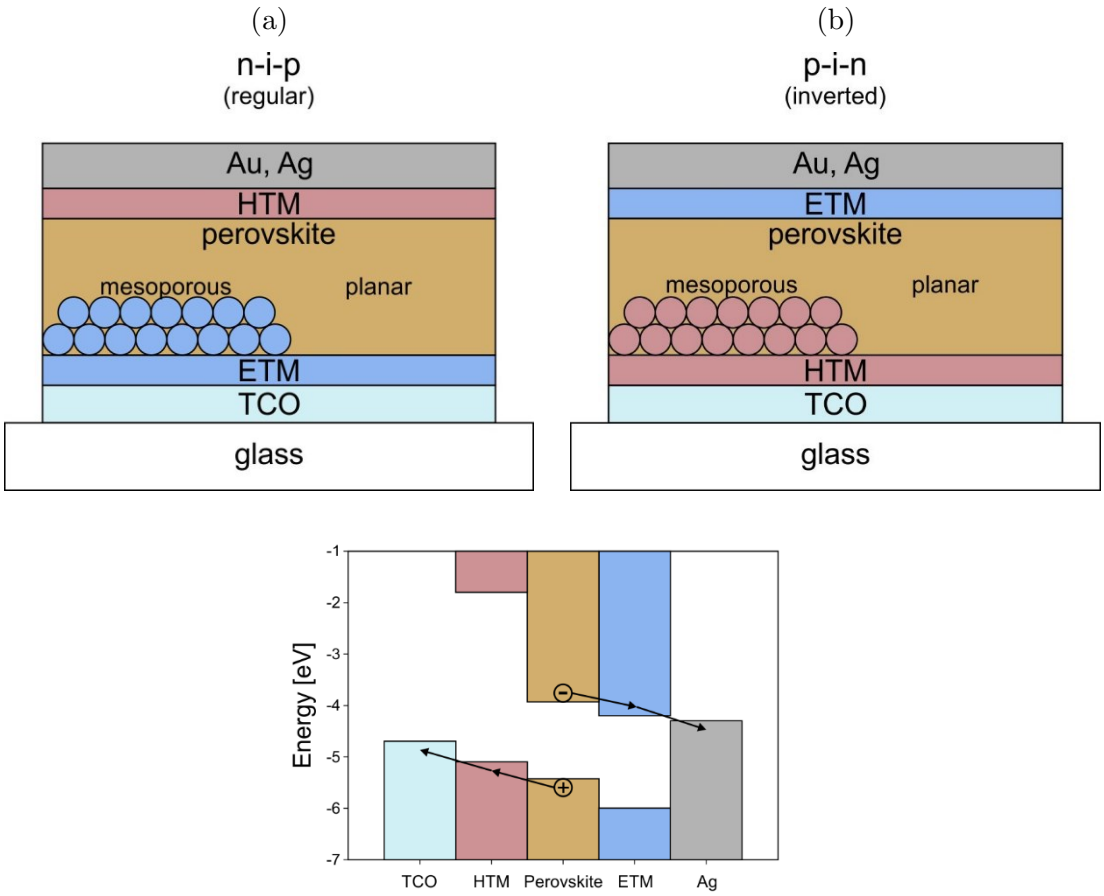

Figure 3.2: Schematics of (a) n-i-p and (b) p-i-n perovskite solar cell structures. The left side of each schematic shows a mesoporous structure, and the right side a planar structure. (c) Energy diagram for a p-i-n perovskite solar cell structure.

listed in Table 3.1. The function of the ETM is to let the electrons generated in the perovskite pass through towards the electrode while at the same time blocking the holes. The function of HTM is to let the holes from the perovskite absorber pass through towards the other electrode while at the same time blocking the electrons. The basic operation principle with charge separation and energy diagram is shown in Figure 3.2 (c). We distinguish between two configurations:

- n-i-p (regular) configuration:
  glass/TCO/ETM/perovskite/HTM/back contact (Figure 3.2 (a))
- p-i-n (inverted) configuration:
  glass/TCO/HTM/perovskite/ETM/back contact (Figure 3.2 (b))

Table 3.1: Some of the most popular ETMs [93] and HTMs [94], divided by their organic or inorganic origin and typical n-i-p or p-i-n configuration.

		n-i-p	p-i-n
ETM	Organic	PCBM, ICBA	C60, PCBM, BCP
	Inorganic	TiO_2, SnO_2, ZnO	
HTM	Organic	spiro-OMeTAD, poly-triarylamine.	PTAA, PEDOT:PSS, polyTPD, NPD
	Inorganic		NiO_x, CuI, CuSCN

Perovskite solar cell fabrication is presented on a concrete case in section 3.2.1 and schematically in Figure 3.3. Just briefly, the fabrication starts from a glass substrate, already pre-coated with a TCO. To deposit ETM and HTM, spin-coating is usually utilized; however, some of the materials can also be evaporated. When spin-coated, the compound is first dissolved in a solvent and then deposited by spin-coating and subsequent annealing to remove the solvent. The back electrode is usually evaporated. The fabrication and formation of the perovskite layer is slightly different. The perovskite is usually formed from two precursors, e.g. PbI_2 and CH_3NH_3I. Different deposition processes then exist, such as one step spin-coating [88], [95], two step spin-coating [96], sequential deposition process utilizing dip coating [89] and vapor deposition [90]. However, for the precursors to react and form perovskite crystals, annealing or high temperature (80–120 °C) are needed. Solvents, time and temperature of the annealing all influence the conversion of the perovskite.

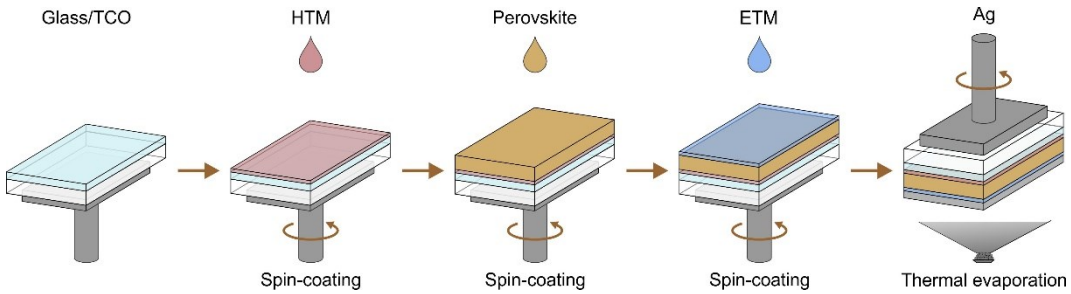

Figure 3.3: Solution-processed inverted perovskite solar cell fabrication. On top of a glass/TCO substrate, HTM, perovskite and ETM are sequentially spin-coated and annealed. In the last step, Ag is thermally evaporated.

Solution processing (spin-coating) is to date the most widespread and efficient technique of perovskite solar cell fabrication. This makes solar cell fabrication simple and fast (from personal experience, 8 substrates can be prepared in around 5 hours, see

section 2.2.1). Consequently, the fabrication of high efficiency perovskite solar cells should be cheap (complex and energy consuming deposition devices are not needed) and therefore interesting for photovoltaic applications. However, to reach commercial production of the perovskite solar cells, some questions have to be answered. The fabricated devices are very small (commonly in the range of 0.1 cm^2, with the largest devices reaching around 1 cm^2 [97]–[99]) while modules are only rarely researched [100]–[102]. Additionally, lead toxicity [103] and stability of the perovskite absorber [104] also present an obstacle in perovskite solar cell use. The main causes of degradation are ultraviolet exposure (mostly connected to the TiO_2 ETM in regular structure) and humidity [105]–[107]. Degradation can be seen visually as the perovskite color changes, e.g. it turns yellow due to decomposing into PbI_2 and CH_3NH_3I. This can happen within days or even minutes. However, due to recent developments, a stabile conversion efficiency of over 20% for over 500 hours was achieved [79], as well as 6-month stability [108] under appropriate polymer coating that down-converts the UV light into visible light. Additional hydrophobic layer on the back side of the device was also applied. This shows that perovskite solar cells are constantly improving and that there is potential for perovskite solar cells in the global market.

As seen earlier, there is a large variety of options for the fabrication of perovskite solar cells. Mesoporous and planar structures, p-i-n and n-i-p configurations and different deposition processes have all been extensively researched. Plenty attention has also been put on ETMs [93] and HTMs [94], and different A, B and X combinations that can form a perovskite crystal structure [70], [109]–[113]. Perovskite material properties, such as detrimental hysteresis [114], [115] and crystal formation, are significant for the device operation. Little hysteresis and pinhole-free (fully covering the surface) crystalline perovskite films with large grains in the order of micrometers and a reduced defect density are beneficial for the solar cell performance.

Creating an efficient perovskite absorber with large crystals from spin-coated solutions, however, does not only depend on the materials and the deposition process but also on kinetics and dynamics of the perovskite crystal formation (conversion) [116], [117]. Different additives or dopants have been tried in order to improve crystal growth, wetting properties and uniformity/homogeneity of the created layers. Amongst others, there are additives such as hypophosphorous acid (HPA, H_3PO_2) [118]–[120], doping has been shown via metal ions (Al^+) [121], and complexing agents such as DMSO or

thiourea [122] have been reported. One can also use a treatment with anti-solvents [95] to affect the dynamics of the conversion into the final perovskite film.

The first part of this chapter covers experimental work. We describe solar cell fabrication and characterization and show performance results of the fabricated devices. We start by analyzing the effect of the HPA additive on the perovskite morphology and electrical performance [120]. For the analysis, an inverted perovskite device design as shown in Figure 3.4 is utilized. We use the basic methylammonium lead iodide composition with organic charge selective layers formed by PTAA as HTM and PCBM as ETM. SEM measurements are used to determine the morphology of the devices, and current density-voltage (*J-V*) and external quantum efficiency (EQE) measurements are carried out to determine electrical characteristics and performance.

We analyze the effects of light management in two types of inverted (p-i-n) perovskite solar cells, one with PTAA and one with PEDOT:PSS as HTM. Utilizing light management (LM) foils is an effective way to reduce optical losses. Using replication techniques, such as UV NIL, an additional transparent layer with an arbitrary texture on top of the planar tandem cell can be created that enables light scattering and/or AR. Such textured LM foil, created by UV NIL, is studied as an addition to the front glass side of the devices to reduce the reflection losses and enhance light trapping and consequently increase the short-circuit current density. The short-circuit current density (J_{SC}) is used as a measure to determine the improvement of solar cell performance.

The second half of the chapter is dedicated to optical modelling. 3D optical simulations based on experimentally obtained parameters show good agreement between the experimental results and the simulations, which validates our optical model and explains experimental results of the fabricated devices. This opens possibilities for the use of optical simulations in the field of perovskite solar cells. Here, the optical simulations are used to determine losses, predict improvements for different textures and potential light management improvements for large area devices (solar modules) that can be realized with perovskite solar cells with the front surface LM foil.

A manuscript describing the experimental analysis and the optical modelling of perovskite single junction solar cells with LM foil was submitted to the journal *ACS Photonics*, under the title "Efficient Light Management by Textured Nanoimprinted Layers for Perovskite Solar Cells".

3.1.3 Perovskite/silicon-heterojunction tandem solar cells

The perovskite/silicon-heterojunction (SHJ) tandem solar cell is an interesting candidate to exceed the Shockley-Queisser limit [4], [123], [5] for single junction solar cells due to the high conversion efficiency of both solar cells [124], [125] and their complementary bandgaps. By tuning the bandgap of the perovskite [70] we can even reach the optimum ratio of 1.73 eV to 1.12 eV [126], [127]. The optical simulations have indeed shown the potential in both the monolithic 2-terminal and the 4-terminal configuration [126], [128] followed by the experimental attempts that also show promising results [80]–[83]. Compared to the 4-terminal devices which have two separate solar cells stacked one above the other, the monolithic 2-terminal devices have 2 subcells connected in series and processed sequentially. Series connection results in a higher voltage of the full device since the voltages of the two subcells are summed. However, to reach the optimum efficiency, the current of the subcells has to match.

Currently, most of the experimental monolithic tandem devices have a planar configuration and are therefore partially limited by photocurrent generation. Further gains in photocurrents can be achieved by introducing structures for light scattering and anti-reflection (AR) [81]. However, commonly used random pyramid texturization of silicon wafers is not yet suitable for the deposition of thin perovskite layers when implementing deposition techniques such as spin coating that gives the highest efficiency to date. An alternative way to reduce optical losses on planar wafers is again to utilize a light management (LM) foil on top of the planar tandem cell that enables light scattering and/or AR.

Since the fabrication of the tandem devices is complex and expensive, optical simulations are needed to predict and optimize the device performance before its fabrication. This is especially important for the monolithic tandem devices where the currents of the subcells have to match for optimum performance. Despite not taking into account electrical properties of the individual materials and their interfaces, optical simulations provide a good indication of the amount of current generated in each of the subcells and unavoidable optical losses.

This is why in the optical modelling part of the chapter we also focus on the optical optimization of the planar monolithic perovskite/SHJ tandem solar cell by means of optical simulations. We consider three different device designs to optimize light management: the planar device, and the devices with back-side and both-side textured

Si wafer. LM foils with different textures on top of the planar device are also considered. For the selected device architectures, we optimize the thickness of the perovskite layer to achieve matching currents in monolithic perovskite/SHJ tandem solar cell. This current is then used, together with experimentally achievable performance parameters, to estimate the efficiencies of the investigated device designs.

A paper describing optical modelling of tandem perovskite/silicon heterojunction solar cells was published in *Energy Procedia*, entitled "Back- and Front-side Texturing for Light-management in Perovskite / Silicon-heterojunction Tandem Solar Cells" [58].

3.2 Experimental

3.2.1 Sample fabrication

3.2.1.1 Perovskite solar cells with PTAA as a hole transport material

The fabricated single-junction perovskite solar cell devices have an inverted (p-i-n) planar structure and a layer configuration of glass/ITO/PTAA/$CH_3NH_3PbI_3$/PCBM/BCP/Ag (Figure 3.4). The PTAA is poly [bis (4-phenyl) (2,5,6-trimentlyphenyl) amine], PCBM is [6,6]-phenyl-C61-butyric acid methyl ester and BCP is bathocuproine. Patterned ITO coated glass (Lumtec, R = 15 Ω sq^{-1}) was used as a substrate. The substrate is 25 x 25 mm^2 big and has 6 ITO pads, with the size of the individual active area being 4 x 4 mm^2. First, the substrates were sequentially cleaned in ultrasonic baths using an acetone, washing solution (Mucasol, 2%), H_2O and isopropanol, and then subjected to a 20 min UV-ozone treatment. All the layer deposition steps were conducted in a nitrogen atmosphere. The hole transport material PTAA (EM Index, Mw = 17.5 g mol^{-1}) was deposited using spin-coating (4000 rpm for 30 s) and annealed for 10 min at 100 °C. The perovskite was spun using one step solution process and crystallized at 80 °C for 5 min. The precursor solution was created from $PbAc_2$ (99.9%, Sigma Aldrich) and CH_3NH_3I (Dyesol) in 3:1 ratio, dissolved in anhydrous *N*,*N*-dimethylformamide (DMF, Sigma Aldrich) with a final concentration of 46 wt%. An appropriate amount of HPA was added to produce a 0.2% concentrated perovskite solution. Before perovskite spin-coating a pure DMF spin-coating step was utilized to enable better wetting of the perovskite on the PTAA surface [82]. The PCBM (Solenne, purity = 99.5%) was dissolved in anhydrous chlorobenzene (Sigma Aldrich) at a concentration of 20 mg ml^{-1}, spun at 1500 rpm for 1 min and annealed at

100 °C for 10 min. The BCP (Sigma Aldrich, purity = 99.99%) was dissolved in anhydrous ethanol (Sigma Aldrich) at a concentration of 0.5 mg ml^{-1}, spun at 4000 rpm for 1 min and annealed at 70 °C for 15 min. Finally, 100 nm Ag was deposited by thermal evaporation (10^{-7} mbar base pressure, 1 Å s^{-1}) to form the back contact. A photography of the substrate with fabricated solar cells is shown in Figure 3.6 (a). Figure 3.6 (b) shows the sample schematic with positions of 6 solar cells per substrate and front (FC) and back (BC) contacts.

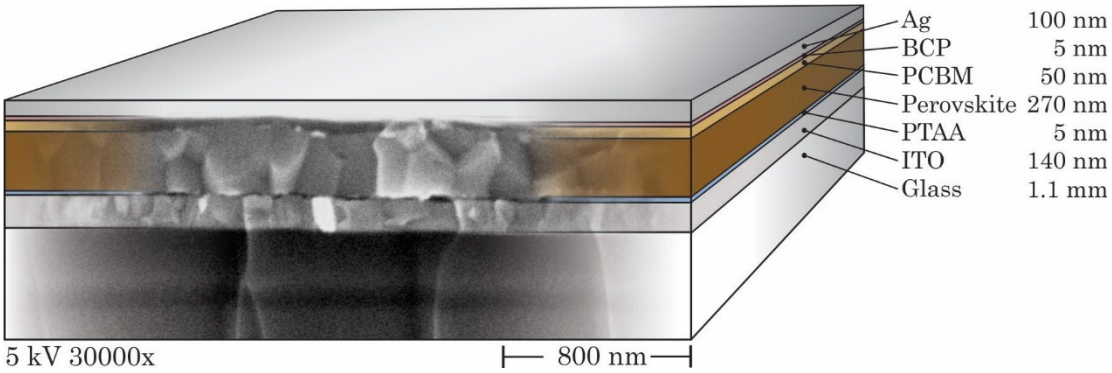

Figure 3.4: Schematic of the inverted planar perovskite solar cell structure with PTAA as HTM including the layer thicknesses, superimposed on a corresponding SEM cross-section image.

3.2.1.2 Perovskite solar cells with PEDOT:PSS as a hole transport material

The PEDOT:PSS based perovskite solar cells have an inverted planar structure and a layer configuration of glass/ITO/PEDOT:PSS/$CH_3NH_3PbI_3$/PCBM/BCP/Ag. The solar cell preparation is the same is for the solar cells with the PTAA as HTM described in previous section, except for the following parts. The hole transport material PEDOT:PSS (Heraeus, AI 4083) was deposited using spin-coating (3000 rpm for 30 s) and annealed for 20 min at 140 °C in air. All the next steps were conducted in nitrogen atmosphere. The perovskite was spun using one step solution process and crystallized at 100 °C for 10 min. The precursor solution was created from 0.8 M PbI2 (99.8%, Sigma Aldrich) and CH_3NH_3I (synthesized from HI and CH_3NH_2, Sigma Aldrich) dissolved in γ-butyrolactone (GBL) and dimethyl sulfoxide (DMSO) in a 70:30 ratio. The solar cell structure and the cross-section SEM are presented in Figure 3.5.

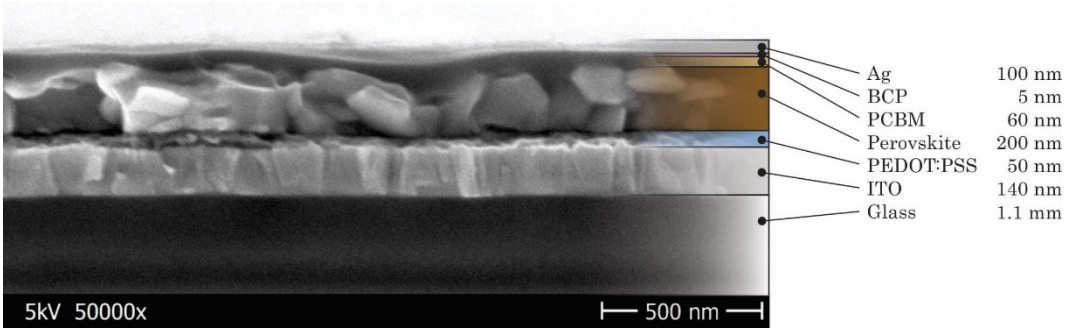

Figure 3.5: Schematic of the planar inverted perovskite solar cell structure with PEDOT:PSS as HTM including the layer thicknesses with corresponding SEM cross-section image.

3.2.1.3 UV Nanoimprint Lithography

The UV NIL process was carried out in air following the steps as schematically shown in Figure 2.1 and explained in Chapter 2. Just briefly, a textured sample (i) is used as a master for the replication. A stamp lacquer, deposited on a substrate (ii), is imprinted on the textured master. Viscous lacquer adjusts to the structure of the master and is cured under UV light (iii). After the separation of the stamp from the master, the stamp can be used as a (quasi)master and is imprinted in the lacquer 2 (iv) that is deposited on the substrate. UV illumination cures the second lacquer (v). Once separated from the stamp, the acquired replica (vi) is ready for use as a light management foil. Thin microscope glass slides were used as substrates for the replica, which was then fixed on the glass side of the devices using an index matching liquid (Norland Products Inc.). For the PEDOT:PSS based solar cells, the UV NIL replica deposition was done directly on the perovskite solar cell. No degradation was observed due to UV curing of the lacquer on the device performance. A silicon wafer with <100> orientation, etched in KOH with up to 8 μm resulting randomly distributed pyramids [30]–[32], typical for wafer based silicon solar cells [13], was used as a master. Figure 3.6 (c) shows an SEM image of the replica on a glass substrate. Randomly distributed pyramids with sharp peaks and edges as transferred from the master are clearly visible, confirming the success of the UV NIL replication process. Figure 3.6 (e) and (f) show reflectance and transmittance 3D ADF measurements of the etched Si replica on glass, respectively. Left side of both graphs is for light entering glass first and right side for light entering the textured lacquer first. A big difference can be observed. If laser light passes first through the textured lacquer, the transmittance is increased and reflection is reduced, which shows good anti-reflection properties. If laser light pass first through glass, excellent light trapping properties are observed since the transmission is reduced and reflection increased.

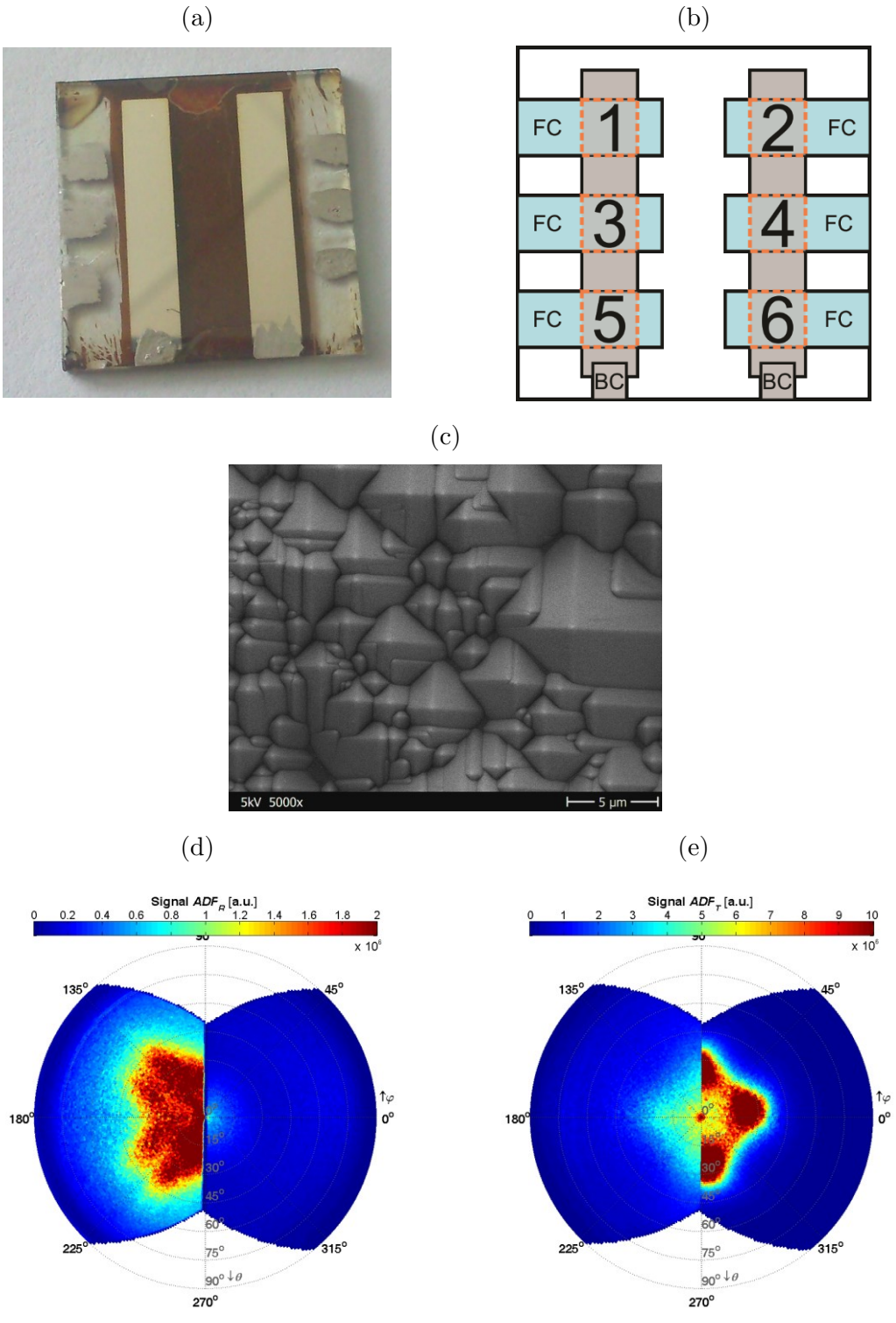

Figure 3.6: (a) A photograph of substrate with 6 fabricated perovskite solar cells and (b) schematic of the substrate with 6 solar cells and front (FC) and back (BC) contact positions. (c) SEM image of a replica on a glass substrate. Etched Si wafer was used as a master. (c) Reflectance and (d) transmittance 3D ADF measurements of the etched Si replica on glass. Left side of both graphs is for laser light ($\lambda = 633$ nm) entering glass first and right side for the laser light entering the textured lacquer first. Note that the scales are different due to different range 3D ADF values for reflectance and transmittance.

3.2.2 Sample characterization

The *J-V* curve was measured using a Keithley 2400 Source Meter Unit in inert atmosphere under the illumination of simulated AM 1.5G solar light from an Oriel solar simulator system (class ABB according to IEC 60904-9), adjusted with a calibrated silicon reference cell (Fraunhofer ISE). The scan rate was 0.25 V s^{-1} with a voltage step of 20 mV. The maximum power point tracking was controlled by in-house written LabView application. Note that the solar cells were measured without the use of an aperture mask to account for light scattered in and out of the active areas as denoted in the text. However, the good agreement between the integrated EQE spectra and the J_{SC} measured with unmasked devices ensures a good solar simulator and active area calibration and the absence of any edging effects. EQE was measured as a function of wavelength from 300 to 850 nm with a step of 10 nm using an Oriel Instrument's QEPVSI-b system with 300 W Xenon arc lamp, controlled by TracQ™-Basic software. The illumination beam size of the EQE setup is 2.5 x 2.5 mm^2. The external quantum efficiency was measured without background illumination or applied bias voltage in inert atmosphere. The integrated EQE was in good agreement with J_{SC} from *J-V*. Reflection was measured as a function of wavelength from 300 to 850 nm with a step of 5 nm using an integrating sphere with a Perkin Elmer Lambda – 1050 UV/VIS/NIR spectrophotometer, calibrated with a white Spectralon. The illumination beam size of this setup is 3.5 x 3.5 mm^2

3.3 Results and discussion

During my PhD education, a special attention was paid on planar inverted perovskite solar cells. A schematics of the fabricated devices superimposed on an SEM image is shown in Figure 3.4. Hypophosphorous acid (HPA) was tested as an additive to improve the film morphology. The HPA serves as a stabilizer in HI when that is used as a precursor for the synthesis of Ch_3NH_3I (MAI). Its role is to prevent the decomposition of the HI into H_2O and I_2. After synthetization process, MAI is purified and can then be used in perovskite preparation process. However, based on previous reports a small amount of HPA can be present in the purified precursor that can be beneficial for the device performance since by adding impurities the grain growth is slowed down, resulting in bigger grain sizes [120]. Results without and with HPA additive on PTAA as HTM

will be shown. Results of perovskite solar cells with PEDOT:PSS as HTM will also be presented.

3.3.1 *Hypophosphorous acid as an additive for inverted perovskite solar cells*

To establish the effect of the HPA on the device performance, we carried out SEM, *J-V* and EQE measurements of the devices with no HPA and with 0.2% HPA additive. The top view SEM images of perovskite without and with HPA on PTAA layer are presented in Figure 3.7 (a) and (b) for the selected device without and with HPA, respectively. The difference in morphology is clear. No HPA results in small flake-like structures, while adding even such a small amount of HPA as is 0.2% results in grains, with sizes up to a few 100 nm. This is in very good agreement with recent findings by Snaith et al. [118]. Both films exhibit good coverage and no pinholes.

Figure 3.7 (c) and (d) show *J-V* characteristics of the devices without and with HPA. Each substrate contains 6 devices and we show the results for all 6 devices in order to present the (in)homogeneity, each depicted with a different color. Solid lines stand for forward scanning direction (from negative to positive voltages) and dashed for reverse (from positive to negative voltage). Both types of the devices, without and with HPA, have good uniformity between different devices on the same substrate, with 5 out of 6 devices per substrate working very similarly and only one not working, caused by shunting. Interestingly, compared to the SEM measurements, the *J-V* characteristics show no such difference in electrical performance due to HPA additive. The devices without HPA have slightly more pronounced hysteresis and slightly higher spread of open circuit voltage (V_{OC}), however, the devices exhibit comparable short-circuit density J_{SC}, high V_{OC} and fill factor (FF) (see Table 3.2). The maximum power point (MPP) tracking over 60 seconds reveals a stabilized power conversion efficiency (PCE) of 15.8% for the sample without HPA and 16.1% for the sample with HPA (Figure 3.7 (e) and (f)). Both values experience a severe drop within first second and then relatively quickly stabilize at the end value.

Since the J_{SC} of the devices in the *J-V* measurements can easily be wrongly measured due to the solar spectrum and light source as well as device under test and reference cell spectral mismatch and difference in actual and defined active area, we measure the EQE spectra, that enables to determine the J_{SC} in addition to detect spectral

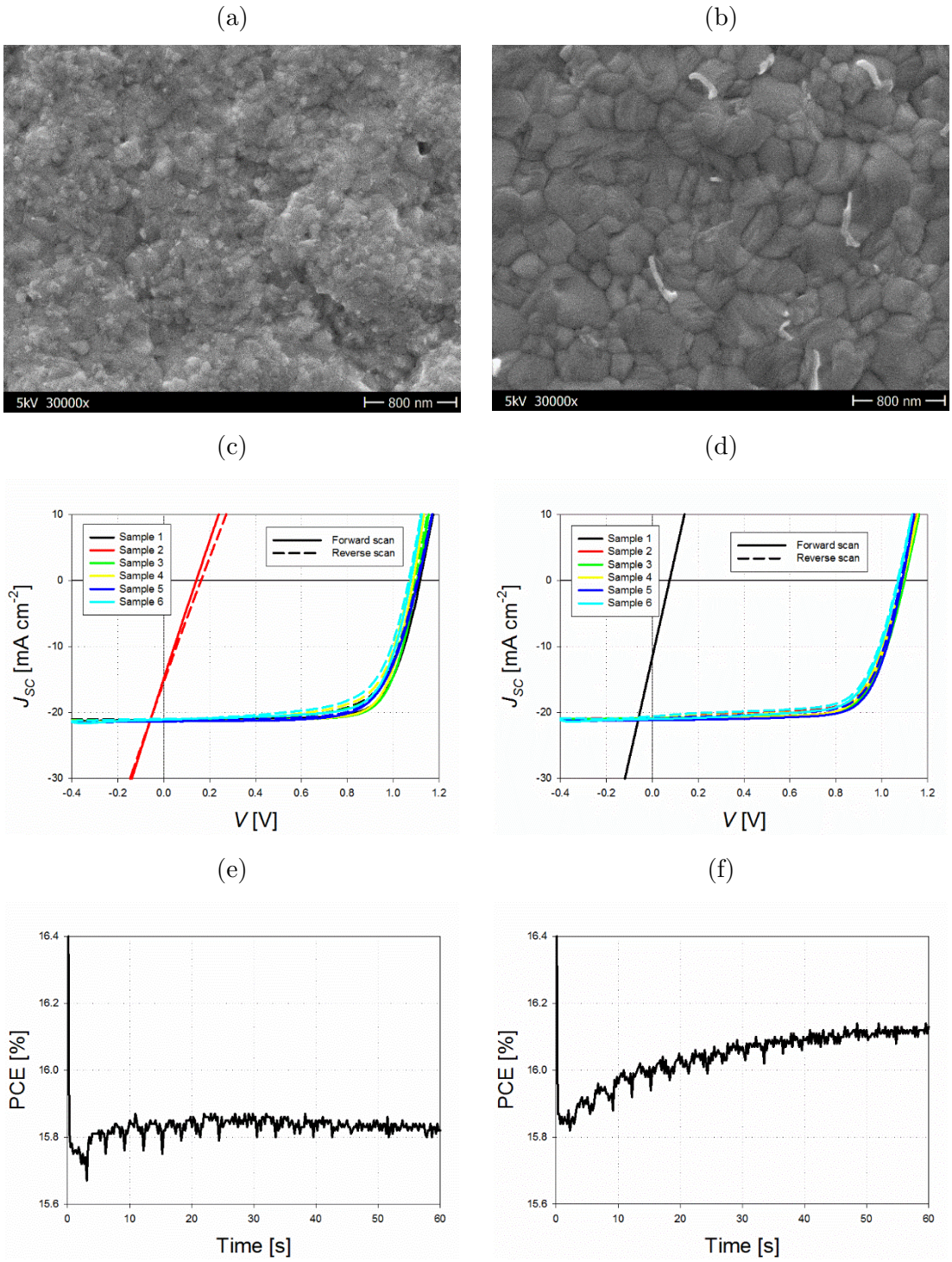

Figure 3.7: Top view SEM images of a perovskite on a PTAA layer, *J-V* measurement and MPP tracking of the devices a), c) and e) without and b), d) and f) with HPA.

changes induced by the HPA additive. The measurement results of the two best performing devices are presented in Figure 3.8.

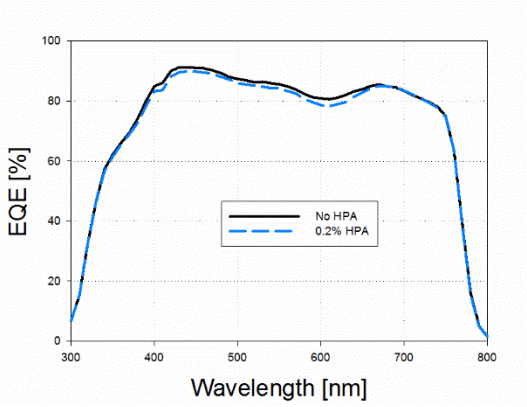

Figure 3.8: EQE spectra of the two best performing devices without (black solid line) and with HPA (blue dashed line).

Both EQE spectra exhibit similar shape, however, the sample without HPA reaches slightly higher absolute values which fits with the J_{SC} from *J-V* measurements. Finally, we calculate the conversion efficiency of the two best devices from both types, for forward and reverse scanning direction. We determine the short-circuit current density by solar-spectrum wavelength integration of the EQE spectra (J_{SC_EQE}) while V_{OC} and FF are obtained from *J-V* characteristics. The conversion efficiency is then calculated by the multiplication of the above mentioned parameters. All the performance parameters are shown in Table 3.2.

Table 3.2: Performance parameters of the best devices with PTAA as HTM under test – for the forward and reverse scanning direction. J_{SC_EQE} was obtained from the EQE measurement and V_{OC} and FF from the *J-V* measurement. PCE was than calculated from the obtained results. PCE from maximum power point track is also added.

	Scanning direction	J_{SC_JV} [mA cm^{-2}]	J_{SC_EQE} [mA cm^{-2}]	V_{OC} [V]	FF [%]	PCE_{JV} [%]	PCE_{MPP} [%]	PCE_{EQE} [%]
No HPA	Forward	21.2	20.9	1.10	74.6	17.5	15.8	17.2
	Reverse	21.1	20.9	1.09	69.5	16.1		15.8
0.2 % HPA	Forward	20.9	20.5	1.10	72.0	16.5	16.1	16.2
	Reverse	20.8	20.5	1.10	70.5	16.0		15.9

The J_{SC} from *J-V* measurements (J_{SC_JV}) to the J_{SC_EQE} deduced from the EQE is in the range of 2%, relatively which is in very good agreement. Similar is also the difference in J_{SC} between the devices without and with HPA additive. In our case, the HPA did not affect the V_{OC}, however, there is a difference in the FF. Due to the hysteresis

the difference between forward and reverse scanning direction is higher for the samples without HPA. The obtained PCEs of all the cases are above 15%, with the highest for forward scan for the sample without HPA (17.2%). As the grains are in general better for the device performance and stability, the addition of the HPA [88] should be beneficial. However, despite clear improvement in the perovskite film morphology, we find only minor differences in the electrical properties of our devices without and with HPA.

3.3.2 Results with the light management foil

To further improve the device performance, we apply an LM foil on top of the fabricated inverted perovskite solar cells with the HPA additive and PTAA as HTM. A similar analysis is also carried out for the perovskite solar cells with PEDOT:PSS as HTM. With the LM foil, the reflection should be reduced and more in-coupled light should result in increased absorption in the perovskite absorber. The LM foil was created by UV NIL process with randomly distributed pyramids, obtained from the silicon wafer, as a texture (see section 3.2.1.3).

3.3.2.1 Perovskite solar cells with PTAA as a hole transport material

The *J-V* measurements of the PTAA based fabricated devices are presented in Figure 3.9 (a). The black lines represent results of a device without the LM foil and the blue lines for a device with the LM foil. To highlight the absence of pronounced hysteresis in our inverted devices, which agrees well with other inverted device structures [131]–[133], we performed *J-V* measurements using different scan directions, i.e. from J_{SC} to V_{OC} (forward scan, full lines) and from V_{OC} to J_{SC} (reverse scan, dashed lines), both obtained at a scan rate of 0.25 V s^{-1}. The biggest change between the devices is in J_{SC}. The *J-V* measurements reveal an increase in J_{SC} from 20.7 mA cm^{-2} to 21.7 mA cm^{-2}, which is a 4.8% relative improvement for the device with the LM foil. The high open-circuit voltage (V_{OC}) remained the same (1.11 V), while change in FF is negligible (70.9% to 71.2%). Overall, the PCE increases from 16.3% to 17.1%, which is a 5% relative improvement for the LM foil device over the flat device. A stabilized PCE of 16.1% for the device without the LM foil was obtained using MPP tracking under operational conditions (Figure 3.7 (f)). This fits with the PCEs obtained in the reverse and forward scans. Table 3.3 lists the performance parameters of the device without and with the LM foil.

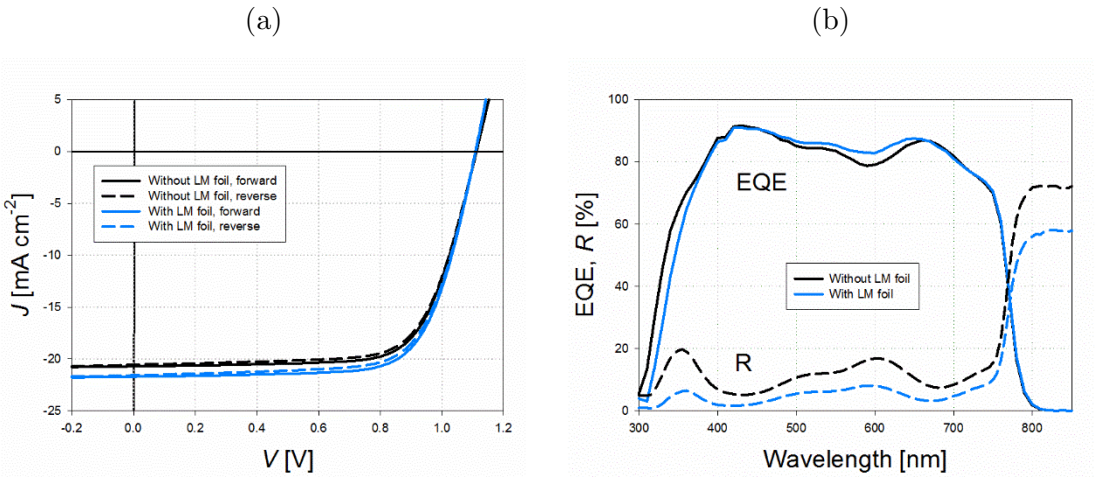

Figure 3.9*:* (a) *J-V* measurement for the solar cell with PTAA as HTM and HPA additive without (black lines) and with the LM foil (blue lines). The solid lines are forward scanning direction (J_{SC} to V_{OC}) and the dashed lines correspond to reverse scans (V_{OC} to J_{SC}). (b) EQE (solid lines) and *R* (dashed lines) spectra for a device without the LM foil (black) and with the LM foil (blue).

Figure 3.9 (b) shows the measured EQE (solid lines) and the total reflection spectra (dashed lines). The black lines represent the device without the LM foil and the blue lines with the LM foil. Two main regions of change can be identified in the spectra: The first region of differences is found in the wavelength range between 300 and 380 nm. Here, the EQE is lower when using the LM foil due to the absorption of UV light in the UV NIL layer. However, the relative share of the AM1.5G spectrum in this range is small and accounts for a current loss of only 0.08 mA cm^{-2}. The second region of differences is between 450 nm and 650 nm, in which the EQE increases (compare also Figure 3.15 (a)). This can be attributed to the reduced reflection of the incident light and improved light trapping as a consequence of the LM foil, as proven by reduction in total reflection in Figure 3.9 (b).

The LM foil reduces the total reflection (*R*) significantly across the whole wavelength range. *R* of the cell stack with the LM foil over the high EQE plateau between 400 and 700 nm is on average more than 50% lower. The positions of the peaks and valleys in the *R* and EQE spectra match well for both cases, without and with the LM foil. However, only at the wavelengths where the reduction in *R* is the highest are then translated to the EQE increase in Figure 3.9 (b). In the visible light range (400 – 700 nm), the EQE and *R* curves added together amount to more than 94%, indicating small optical parasitic losses in the hole and electron transporting materials and the contact layers, and good extraction of the charge carriers. The sum of the EQE

and R with the LM foil is slightly lower and we attribute this to refracted light escaping towards the sides of the device. The active area of the device (4 x 4 mm^2) is small compared to its thickness (including thick glass substrate – 1.1 mm) and also to the light spot of the EQE measurement setup (2.5 x 2.5 mm^2). Therefore, a significant portion of the incident light, when refracted into large angles, escapes from the device to substrate regions without electrodes. Photogenerated charges in these regions are not collected and consequently lost, resulting in the lower EQE values [134]. For example, the effectiveness at $\lambda = 600$ nm is 42% ($\Delta R_{600} = 8.84\%$, $\Delta A_{600} = 3.75\%$). This phenomenon is referred to as "escaped light" and is discussed in more detail in section 3.3.3.

Table 3.3: Performance parameters, integrated J_{SC_EQE} from the EQE and equivalent J_{SC} loss from the reflection measurements R_{eq} of the fabricated solar cells without and with the LM foil. Relative changes are also shown.

		J_{SC} [mA cm^{-2}]	J_{SC_EQE} [mA cm^{-2}]	R_{eq} [mA cm^{-2}]	V_{OC} [V]	FF [%]	PCE [%]
w/o LM foil	for	20.7	20.5	6.63	1.11	70.9	16.3
	rev	20.5			1.11	70.2	16.0
w/ LM foil	for	21.7	20.7	4.37	1.11	71.2	17.1
	rev	21.6			1.11	70.3	16.8
Rel. change		+4.8%	+1%	-34%	0%	0%	+5%

By integrating the weighted EQE spectra over the solar-spectrum, a relative increase in J_{SC_EQE} up to 1% is calculated (Table 3.3). The J_{SC_EQE} agrees well with the J_{SC_JV} from the J-V measurement for the device without the LM foil, proving the accuracy of the measurements (good solar simulator, active area calibration and the absence of any edging effects). The J_{SC_EQE} for the device with the LM foil is, however, lower compared to that obtained by the J-V measurement. As mentioned before, this is attributed to the small device area and different illumination areas in EQE and J-V measurements. Equivalent reflection current loss (R_{EQ}), obtained by integrating the reflectance spectrum over the solar-spectrum, reveals that with the LM foil 34% less current is lost due to reflection when using the LM foil. Ideally, for large area devices most of the 2.2 mA cm^{-2} gained by reducing reflection would be converted to useful current. The difference to the 0.2 mA cm^{-2} gained in the EQE measurement is attributed to the escaped light. However, the gain of 1 mA cm^{-2} in the case of illumination with an

area larger than the active solar cell area (*J-V* measurement) is more realistic to real module application due to the balance of light scattered into and outside the active area.

3.3.2.2 *Perovskite solar cells with PEDOT:PSS as a hole transport material*

The *J-V* and EQE measurements of the perovskite solar cells with PEDOT:PSS as HTM are shown in Figure 3.10 and are presented in the same way as in the previous section. Again, the biggest change between the cells without and with the LM foil is in J_{SC}, the *J-V* measurements reveal the increase in J_{SC} from 16.3 mA cm^{-2} to 17.7 mA cm^{-2} with the LM foil, which is an 8.6% relative improvement. The V_{OC} of our devices is limited due to the wetting properties and imperfect band alignment at the PEDOT:PSS/$CH_3NH_3PbI_3$ boundary [117], [133], [135]. Its value slightly increases from 0.72 to 0.74 V, while *FF* drops from 0.68 to 0.66. Combined all together, the efficiency increases from 8.0% to 8.6%, which is a 7.9% relative improvement with the LM foil over the flat device. The performance parameters of the devices without and with the LM foil are stated in Table 3.4.

(a) (b)

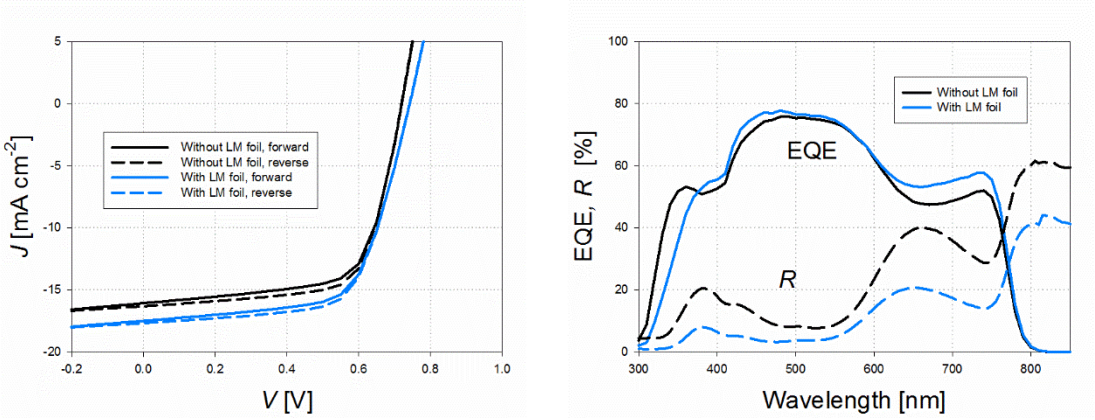

Figure 3.10: (a) *J-V* measurement of the solar cell without (black lines) and with the LM foil (blue lines). The solid lines are forward scanning direction and the dashed reverse. (b) EQE (solid lines) and *R* (dashed lines) spectra. The black lines stand for the solar cell without the LM foil (flat) and blue lines for the solar cell with the LM foil.

The introduction of the LM foil reduces the reflection significantly across in the whole wavelength range. The increase in the EQE is again lower than the reduction in the *R* due to the escaped light. However, compared to the PTAA device, the EQE increase is higher here. This is most likely due to a thinner perovskite absorber benefiting more from the LM foil (see Figure 3.17 for the thickness analysis of the PTAA devices).

By solar-spectrum weighted wavelength integration of the EQE results, increase in J_{SC_EQE} up to 4.6% is calculated (Table 3.4). The values are lower compared to those obtained by the *J-V* measurement. As mentioned before, this is attributed to the small device area and different illumination areas in EQE and *J-V* measurements. Equivalent reflection current loss (R_{EQ}), obtained by solar-spectrum weighted wavelength integration of the reflectance spectrum, shows that with the LM foil 43% less current is lost due to reflection.

Table 3.4: Performance parameters, integrated J_{SC_EQE} from the EQE and equivalent J_{SC} loss from the reflection measurements R_{eq} of the fabricated solar cells before and after UV NIL deposition. Relative change is also shown.

		J_{SC} [mA cm^{-2}]	J_{SC_EQE} [mA cm^{-2}]	R_{eq} [mA cm^{-2}]	V_{OC} [V]	FF [%]	PCE [%]
w/o LM foil	for	16.1	15.1	8.79	0.72	66.9	7.74
	rev	16.3			0.72	68.3	8.02
w/ LM foil	for	17.5	15.8	4.98	0.74	65.1	8.46
	rev	17.7			0.74	66.0	8.65
Rel. change		+8.6%	+4.6%	-43%	+2.8%	-2.9%	+7.9%

3.3.3 Conclusions

We analyzed the effect of the hypophosphorous acid (HPA) additive on the morphology and electrical performance of the perovskite solar cells following previous reports. We adopted a spin-coating process to fabricate devices with inverted device architecture. For improving the film crystallization, a 0.2% concentration of HPA was added to the perovskite solution before spin-coating. The fabricated solar cell exhibit high efficiencies above 15% for both cases, without and with HPA. Morphology measurements showed that adding HPA results in bigger grains in perovskite layer which is in agreement with the literature. However, the electrical performance was largely unaffected with lower hysteresis being the only observed improvement due to HPA.

We have also presented and analyzed a light management option for perovskite solar cells. A light management (LM) foil was fabricated by UV Nanoimprint Lithography process and attached on top of the device using index matching liquid. Inverted perovskite solar cells (p-i-n) with an efficiency of 16.3% and negligible hysteresis have been fabricated to test the effect of the LM foil. The measurements with the LM

foil reveal an increase in efficiency to 17.1%, which represents a 5% relative enhancement. The improvement in the performance can be contributed mainly to the increase in the short-circuit current density of 4.8%, as determined from *J-V* measurements. A similar analysis was done also for the perovskite solar cells with PEDOT:PSS as a hole transport material. Again, the measurements showed an improvement in performance, the 8.6% enhancement in short-circuit current density translated to a 7.9% enhancement in power conversion efficiency. This demonstrates the beneficial role of the LM foil on device performance.

3.4 Optical modelling

Optical modelling is a useful tool to investigate where the further improvements in the device performance (EQE and J_{SC}) lie and to provide an insight into changes in parasitical optical loss distribution. This way we can optimize device performance or establish where the limits are. Optical modelling is also a cost- and time-effective way of predicting and quantifying the potential improvements in the performance due to modifications in the device structure without spending money and time to fabricate the device.

To conduct optical simulations, 3D Optical simulator CROWM by Benjamin Lipovšek et al. [134], [136], [137] which is based on combined ray and wave optics model is used. It enables us to correctly simulate a stack of an arbitrary number of thin and thick layers, as is the case in our fabricated devices. We use optical simulations to reveal why the differences between the enhancement measured in EQE and J_{SC}, and to establish the potential benefits of the LM foil: what is the potential increase for the large-area device and if the LM foil is beneficial even for the highest performing devices. We also test different textures to determine which one performs best. Optical simulations are also used to investigate the potential of tandem perovskite/silicon-heterojunction solar cells.

3.4.1 Optical simulator CROWM

CROWM simulator is based on combined ray and wave optics models that enable simultaneous simulations of both segments of the device, textured thick LM foil (incoherent light propagation) and thin-film solar cell stack (coherent light propagation). Wave optics model, based on transfer matrix algorithm, is used to simulate thin layers

(coherent light propagation) in the solar cell stack, while non-coherent ray tracing approach is used for thick layers (> 1 μm) – glass substrate and LM foil (and c-Si wafer in tandem devices). The main outputs of the simulator are total reflectance, transmittance and absorptance in each layer. Their solar-spectrum weighted wavelength integration equals to the J_{SC} or equivalent current loss in the individual layer. The simulations were carried out in the wavelength range from 350 to 800 nm, which is a sufficient range for the single junction perovskite solar cells, and in the wavelength range from 350 to 1200 nm for the tandem devices.

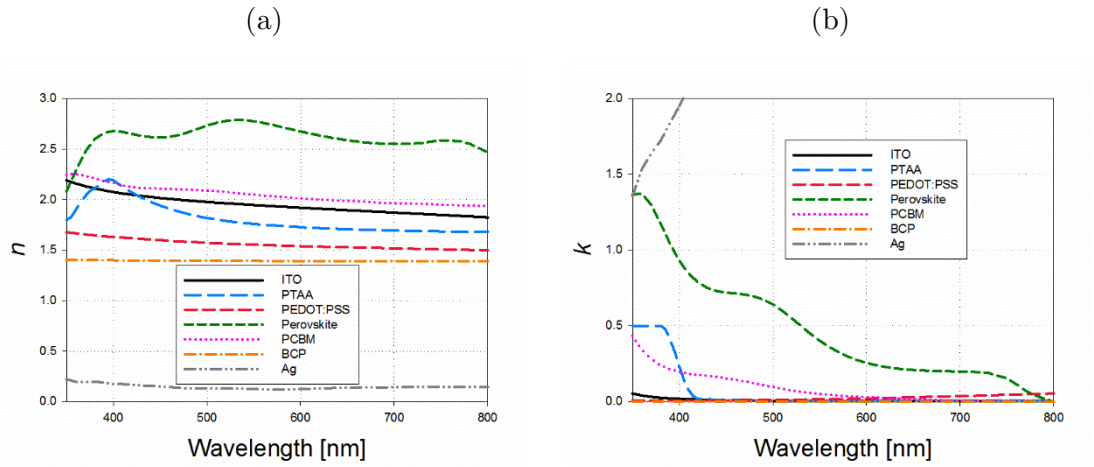

Figure 3.11: (a) *n* and (b) *k* spectra of the of the materials employed in the simulated solar cells.

3.4.2 Model validation

To make any relevant conclusions from the results of the optical simulations, we need to validate the optical model using realistic experimentally obtained parameters, such as thicknesses of the layers and their *n* and *k* spectra. The thicknesses of the individual layers are estimated from the cross-section SEM image and are 140 nm for ITO, 5 nm for PTAA, 270 nm for the perovskite absorber, 50 nm for PCBM, 5 nm for BCP and 100 nm for Ag as shown in Figure 3.4. The fabricated solar cells also exhibit low roughnesses which enable successful matching with our simulations that assume planar interfaces. When simulating devices with the LM foil, we set the thickness of the LM foil to 50 μm and apply texture profile on the front surface. To include a realistic texture in the simulator, the texture profile of the random pyramids was measured using AFM. The wavelength-dependent *n* and *k* spectra needed to conduct the simulations were obtained using reflectance/transmittance (RT) method [42] and from the literature for spiro-OMeTAD [128] and perovskite absorber [138]. *n* and *k* spectra of the materials

employed in the fabricated and simulated single junction devices are shown in Figure 3.11.

Additionally, both the device area and the illumination beam size were set to actual experimental values, which is necessary to get comparable results (and is as we will see the main reason for small increase in the EQE and J_{SC}). Such case, in which the realistic geometrical dimensions are taken into account, is referred to as a "confined" device. For our devices, the confinement (geometrical dimensions) was 4 x 4 mm^2 for the device area and 2.5 x 2.5 mm^2 and 3.5 x 3.5 mm^2 for the EQE and R illumination spots, respectively.

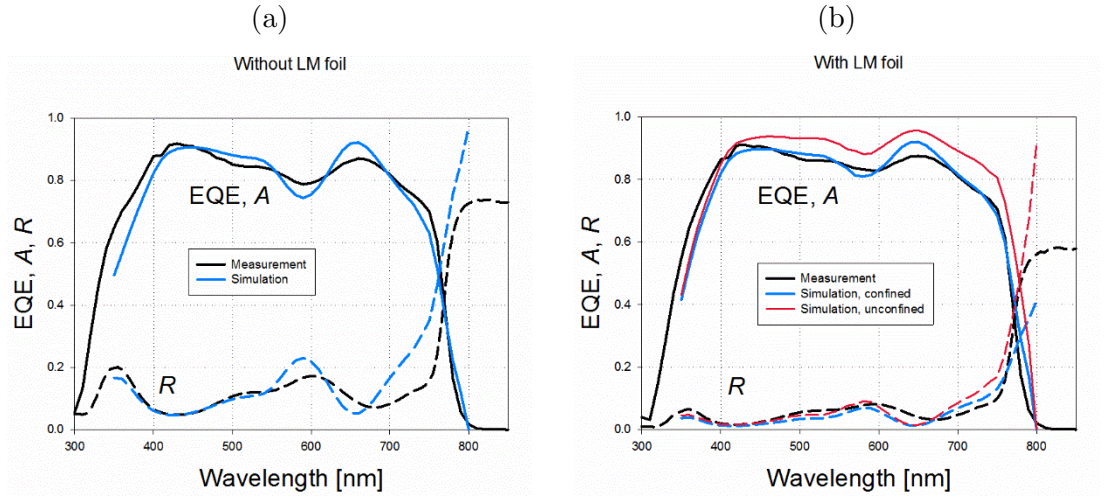

Figure 3.12: Comparison of the EQE (solid) and R (dashed) between experiment (black) and simulations (blue) for a PTAA based device (a) without and (b) with the LM foil. In the case with the LM foil, we distinguish in simulations between confined device (blue) and unconfined device (red).

The comparison between measured (black lines) and simulated (blue lines) EQE/absorptance (A) and R is presented in Figure 3.12 (a) and (b). It is assumed that all the absorbed photons result in charges that can be collected under short circuit conditions [139] and is proven by the good match between the measured EQE and A (solid lines). A good match is also obtained between the R curves (dashed lines) for both cases, without and with the LM foil. There are, however, slight discrepancies in terms of shape and values due to interferences (at 580 and 650 nm) from the thin layers, which are slightly less pronounced in the measurements. This is due to a slight roughness of the perovskite absorber that reduces interferences within the device while simulations assume planar interfaces. In the case with the LM foil, the textured front surface reduces interferences due to the refracted light beams now having different optical paths, thus also losing constant phase difference. Consequently, interference peaks are diminished

and the simulation compares better to the experiment. Comparing the simulated integrated absorption spectra J_{SC_SIM}, the increase is from 20.5 mA cm^{-2} for the flat device to 21.1 mA cm^{-2} for the confined device with the LM foil, which is similar to the measured values.

The comparison between experiment and simulation was also done for the analyzed solar cell devices with PEDOT:PSS as an HTM. The results are presented in Figure 3.13. The thicknesses for the model were extracted from the SEM cross-section image and are as following: 140 nm for ITO, 50 nm for PEDOT:PSS, 200 nm for perovskite absorber, 60 nm for PCBM, 5 nm for BCP and 100 nm for Ag. Again, there is a good match between experiments and simulations. The absolute values for the EQE and A spectra do not match as well as for the PTAA solar cells, which indicates worse photogenerated carrier extraction. However, both spectra have similar shapes, also the match between measured and simulated reflectance spectra is very good.

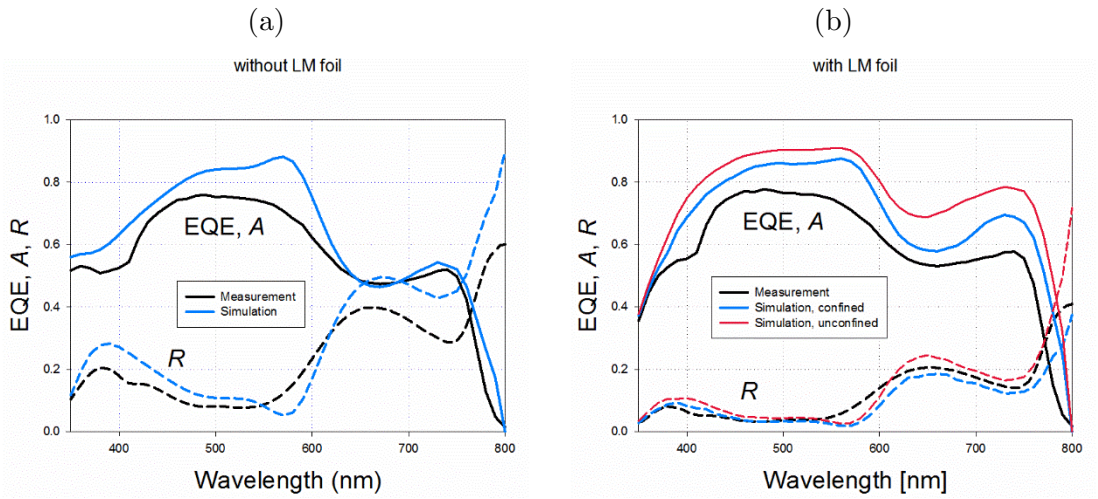

Figure 3.13: Comparison of the EQE (solid) and R (dashed) between experiment (black) and simulations (blue) for a PEDOT:PSS based device (a) without and (b) with the LM foil. In the case with the LM foil, we distinguish in simulations between confined device (blue) and unconfined device (red).

Finally, we apply our optical model also on a monolithic planar perovskite/SHJ tandem solar cell, presented by Albrecht et al. [129]. The perovskite solar cell, on top of a typical SHJ solar cell, has an inverted structure. MoO_3 was evaporated on top of the spiro-OMeTAD HTM to protect it from the ITO sputtering process. The device schematic is shown in Figure 3.20 (a), where also all the layer thicknesses are stated. The thicknesses of spiro-OMeTAD and perovskite layer, however, were extracted from the SEM image and are 300 and 500 nm, respectively. The comparison between the

experiment and simulation is shown in Figure 3.14. The match is again good, especially when considering that the tandem devices have more complex structure with more parameters and are therefore more prone to any deviations.

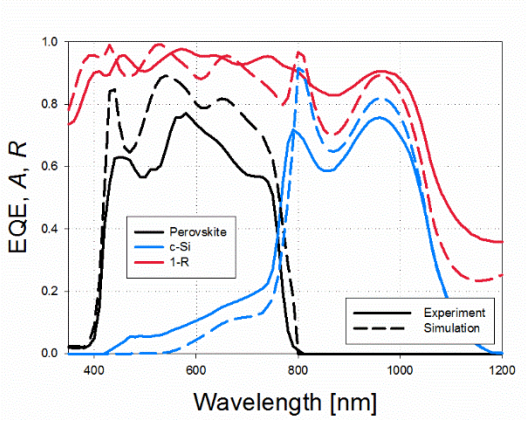

Figure 3.14: Comparison of the EQE, A and R between experiment (solid) and simulations (dashed) for a monolithic planar perovskite/SHJ tandem solar cell. Perovskite A is denoted with black, c-Si with blue and R with red color.

Following this results, we believe that our optical simulations describe our solar cell structure well, therefore validating the optical model and making it first successful perovskite experiment-versus-simulation study conducted. Since the results are based on experimentally obtained parameters, the optical model can be used for further analysis, as well as for other device structures (provided that n and k spectra are known), configurations and texture optimization.

3.4.3 Optical analysis of single junction perovskite solar cells

3.4.3.1 Large area device and loss analysis

First, we use the validated optical model to investigate the expected improvements for large devices, relevant for practical applications in solar modules. Since such devices are much larger than our test device, it is now assumed in the simulations that the active area has infinite lateral dimensions in both directions and we refer to this as an "unconfined" device. Keeping the same input parameters, the increase in simulated current J_{SC_SIM} due to the LM foil is 11.2% (2.3 mA cm^{-2}, see Table 3.5). This means that the large area devices would benefit more from the LM foil than the test device. The A and R curves are plotted in Figure 3.12 (b) with red lines. The simulations show the largest increase in the wavelength region around 580 nm. This is also where the

highest increase in the EQE was measured. Additionally, compared to the confined case, there is an increase in the absorption for the longer wavelengths that is typical for other solar cell types. In the unconfined case, the longer wavelengths have more passes through the active layer and are thus more likely to be absorbed while for the confined/experimental case a high amount of long wavelength light leaves the active area before being absorbed. The R spectra for the unconfined and confined case are very similar, the A is, however, lower for the confined device over the whole spectrum. This confirms our conclusion from the EQE study that in small devices a high amount of light escapes the device area due to the refractions in the LM foil.

(a) (b)

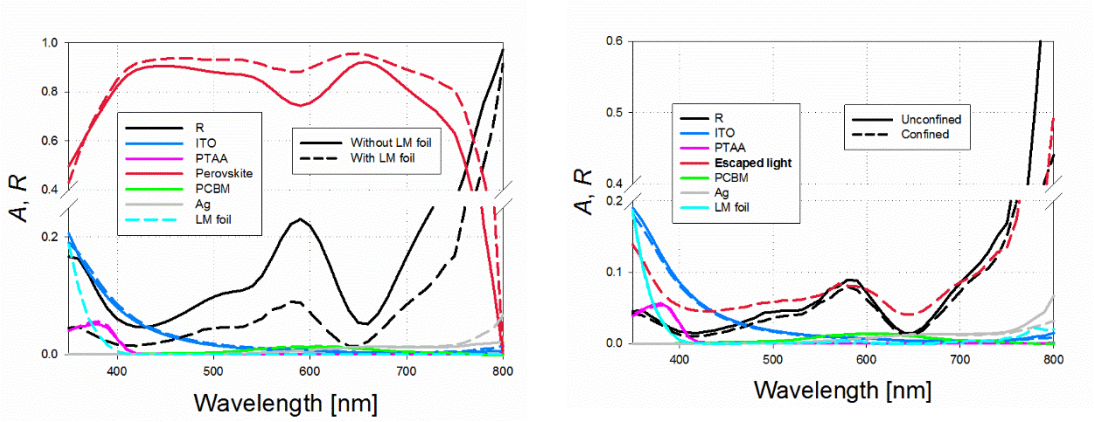

Figure 3.15: (a) Spectral loss analysis for the (unconfined) device without and with the LM foil and an absorber thickness of 270 nm. Integrated values are shown in Table 3.5. (b) Comparison of the optical losses for the confined and unconfined PTAA based device. The escaped light is almost the same to the difference between absorption in the perovskite for the confined and unconfined device.

Figure 3.15 (a) displays the absorption spectra of the individual layers for the (unconfined) device without and with the LM foil. Most of the incident light is absorbed in the perovskite absorber while the main parasitic loss can be attributed to the total reflection and absorption of the layers located above the perovskite in the UV and blue spectrum. The LM foil reduces the reflection over the whole analyzed spectrum. Similarly to the experimental results presented above, the simulated equivalent reflection current density loss R_{SIM} is reduced by almost 50%. Most of the gained in-coupled light contributes to the useful current density in the absorbing perovskite layer, with an increase in the simulated photocurrent density of 11.2%. The additional absorption due to the LM foil in the other layers is negligible. The solar-spectrum weighted wavelength integrated absorptances of all the layers are shown in Table 3.5. Figure 3.15 (b) compares

losses between confined and unconfined device. No pronounced difference other than the escaped light can be observed. The escaped light is almost the same to the difference between absorption in perovskite for the confined and unconfined device (a (very) small difference is a result of the absorption in the other layers). Most of this refracted light escapes the device area already in the glass substrate due to its relative large thickness (1.1 mm) compared to the device's active area (see Figure 3.15 (b)). This shows that when having small area devices, such as our fabricated ones, the glass should be as thin as possible.

Table 3.5: Simulated current J_{SC_SIM} [mA cm^{-2}] that is produced in the perovskite absorber layer, lost as parasitic absorption in the other layers, or lost via reflection under AM 1.5G illumination for an unconfined PTAA based device for the thicknesses as stated in Figure 3.4. The spectra for these two cases are presented in Figure 3.15 (a).

Texture	Reflection, R_{SIM}	ITO	PTAA	Perovskite, J_{SC_SIM}	PCBM	Ag
Flat	5.78	0.44	0.07	20.5	0.16	0.22
LM foil	3.24	0.50	0.08	22.8	0.16	0.30
Change	- 2.55	+ 0.06	+ 0.01	+2.3 (11%)	+ 0	+ 0.08

(a) (b)

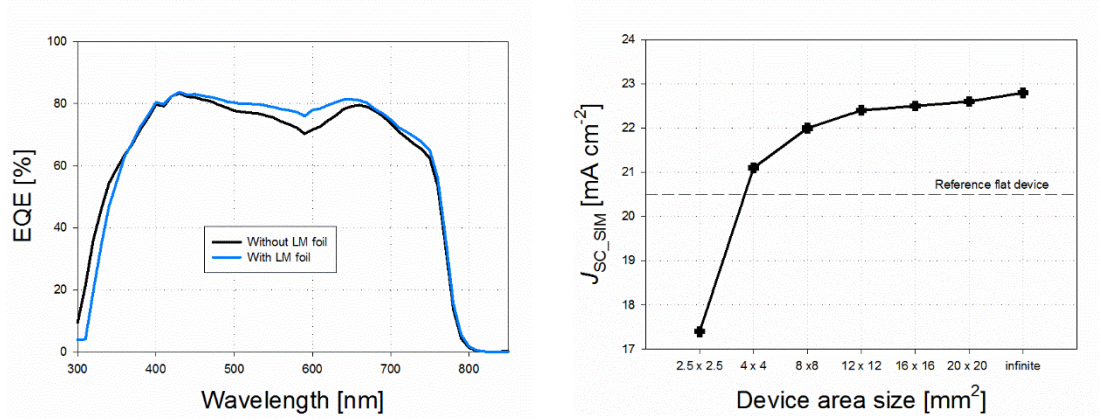

Figure 3.16: (a) EQE of the PTAA based device fabricated on a thinner substrate (700 μm). (b) J_{SC} for different active area sizes of the device. The dashed line represents reference (simulated) flat device. The beam spot size was 2.5 x 2.5 mm^2. The fabricated solar cell active area is 4 x 4 mm^2.

For comparison, Figure 3.16 (a) and Table 3.6 show results for a device fabricated on a thinner substrate (0.7 mm). Overall, this device performs slightly worse, however, the increase in the EQE is higher due to the increased amount of light reaching the

perovskite absorber and not exiting the cell (in the glass substrate). This is also confirmed by optical simulations, which also reveal that for the unconfined device the performance is the same as for the device with a thicker glass substrate. To fully harvest the improvements of the LM foil, a device with around 10 times bigger area is needed for the same beam spot (Figure 3.16 (b)).

Table 3.6: Experimental and simulated J_{SC} values for the PTAA based device with a thinner glass substrate (0.7 mm), without and with the LM foil.

	Experiment: J_{SC_EQE} [mA cm^{-2}]	Simulation, confined: J_{SC_SIM} [mA cm^{-2}]	Simulation, unconfined: J_{SC_SIM} [mA cm^{-2}],
w/o LMF	18.6	20.5	20.5
w/ LMF	19.2	21.5	22.8
Change	+3.2%	+4.9%	+11.2%

3.4.3.2 Devices with different thicknesses of perovskite absorber

Second, the J_{SC_SIM} enhancement due to the LM foil was also determined for devices with different perovskite absorber thicknesses. These devices might benefit less or not at all since the effect of the prolonged optical path of the oblique light beams after refraction at the front surface might be negligible due to the thicker absorber. Figure 3.17 shows J_{SC_SIM} (solid lines) and R_{SIM} (dashed lines) for perovskite layer thicknesses between 50 nm and 1000 nm without (black) and with the LM foil (blue). The red line shows the relative enhancement and the vertical dashed line the case for the perovskite absorber thickness of 270 nm investigated above. The J_{SC_SIM} increases only slowly for perovskite thicknesses above 700 nm in both cases, without and with the LM foil. A small interference effect is observable, which diminishes with increasing thickness of the perovskite absorber. The J_{SC_SIM} increases with the LM foil for all thicknesses of the absorbing layer. Thus, even devices that have a very thick perovskite absorber layers generating a very high photocurrent density should benefit using the LM foil. For example, a device with a 1 µm thick perovskite absorber still shows a 1.7 mA cm^{-2} (7.8% relative) increase with the LM foil. This is the case because the reduction in reflection and light trapping in the layers above the perovskite absorber remain regardless of the absorber thickness. The usage of the LM foil is therefore also beneficial for thicker devices.

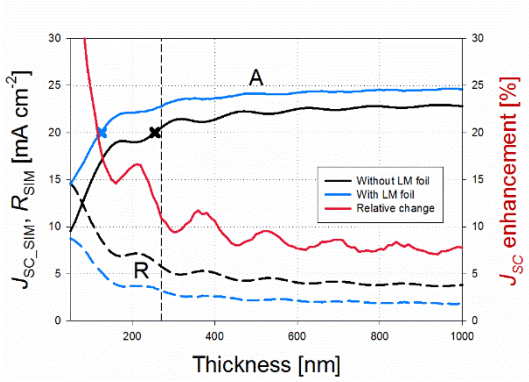

Figure 3.17: Left axis: J_{SC_SIM} (solid) and R_{SIM} (dashed) for perovskite absorber thicknesses from 50 nm to 1000 nm for a PTAA based device. The 270 nm thick perovskite absorber case is marked with a dashed line. The points were the flat and the textured device reach 20 mA cm^{-2} are denoted with crosses. Right axis: the dark red line represents the relative J_{SC_SIM} enhancement.

3.4.3.3 V_{OC} enhancement

Third, we calculate the potential theoretical increase in V_{OC} due to the higher carrier density. This can be achieved when using the LM foil to create the same amount of photocurrent density at significantly reduced active layer thickness, thereby enhancing the generated carrier density [140]. Since V_{OC} is affected by generation and recombination, an enhanced generation rate (the same number of charges per smaller volume) has the potential to enhance the V_{OC}. Using the equations (equations 3 and 5 in the paper) and parameters presented by Leijtens et al. [140], where they show how the recombination dynamics of perovskite solar cells is dominated by long lived holes and trapped electrons with strongly reduced trap mediated recombination (electron lifetime: $\tau_n = 100$ ns, long lived hole lifetime: $\tau_p = 10$ µs), we calculate a potential V_{OC} increase of 36 mV (Equation (3.2)).

First, from the recombination rate equation (Equation (3.1)), the different charge carrier lifetime gives us the charge carrier density ratio:

$$R = \frac{n}{\tau_n} = \frac{p}{\tau_p} \rightarrow p = \frac{\tau_p}{\tau_n} n = 100n \tag{3.1}$$

Second, the current density is kept constant (20 mA cm^{-2}) but the thickness is changed to achieve such current – 130 nm in the case with the LM foil and 260 nm (d_2=2d_1) in the case without the LM foil (denoted with the crosses in Figure 3.17) giving us the concentration ratio between the two cases $n_1 = 2n_2$ (in the calculations, index 1

stands for the case with the LM foil while index 2 for the case without). For the V_{OC} enhancement we then get:

$$\begin{aligned}\Delta V_{OC} &= V_{OC1} - V_{OC2} \\ &= E_{g1} + kT\ln\frac{n_1}{N_c} + kT\ln\frac{p_1}{N_v} \\ &\quad - \left(E_{g1} + kT\ln\frac{n_2}{N_c} + kT\ln\frac{p_2}{N_v}\right) = \\ &= kT\ln\frac{n_1 p_1}{n_2 p_2} = kT\ln\frac{2n_2 * 2 * 100n_2}{n_2 * 100n_2} = kT\ln 4 = 36\,mV\end{aligned} \tag{3.2}$$

This indicates another benefit of the LM foil – besides increasing the J_{SC}, the V_{OC} can also be enhanced by using thinner active layers to enhance the charge carrier density.

3.4.3.4 Different textures of the light management foil

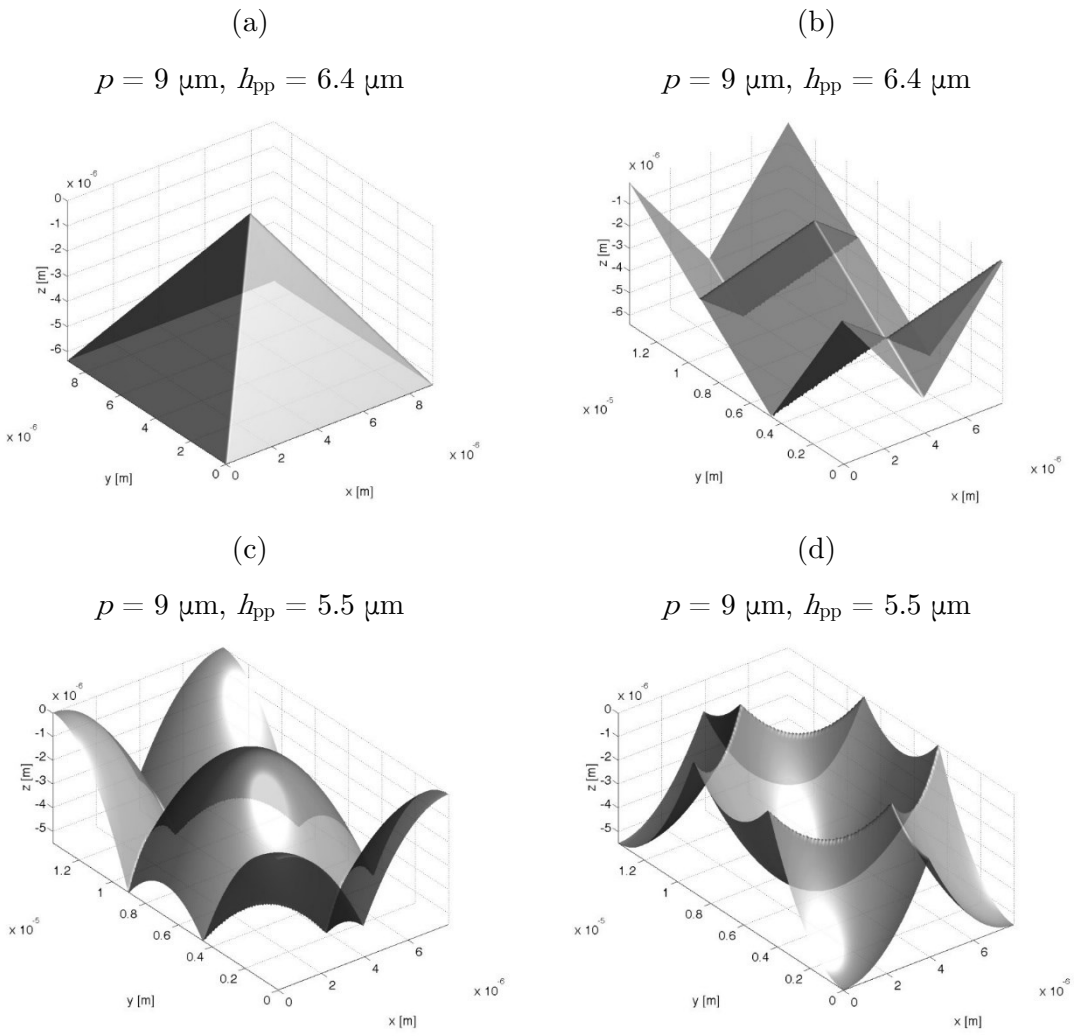

Figure 3.18: Considered 4 different textures of the LM foil: (a) regular pyramid, (b) cornercube, (c) convex parabolic O texture and (d) concave parabolic U texture. Period p and height h_{pp} of the textures are also stated.

Finally, we simulate the expected improvements for various possible textures of the LM foil for the perpendicular incidence of light. Besides randomly distributed pyramids, periodically distributed regular pyramids, cornercubes and parabolic micro-lens textures were investigated. Such textures can be fabricated experimentally and have also been investigated using optical simulations [137], [141], [142]. Textures for our simulations were created artificially, their images as exported from CROWM are shown in Figure 3.18. To ensure relevant comparison, the textures were scaled to the same period of 9 μm. Three different thicknesses of the perovskite absorber were considered: 200, 270 and 600 nm. The thicknesses of the other layers were as stated earlier.

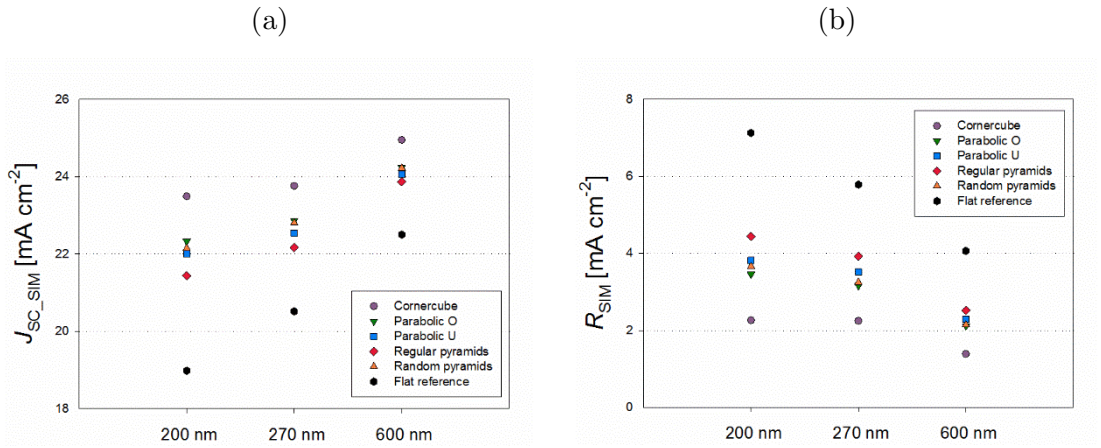

Figure 3.19: (a) J_{SC_SIM} and (b) R_{SIM} for the PTAA perovskite solar cells for different textures and different perovskite absorber thicknesses.

The simulation results of the J_{SC_SIM} and R_{SIM} are presented in Figure 3.19. As expected, all the textures proved to be beneficial for the device performance compared to the flat reference without an LM foil. It is also noticeable that the increase in J_{SC_SIM} is smaller for thicker absorbers. The best performing texture for perpendicular incident of light by far is cornercube, while the worst are regular pyramids. There is not much difference between parabolic textures and random pyramids. Here, it is also clearly seen that the reduction in R is directly transferred to the increase in J_{SC}.

3.4.4 Optical analysis of tandem perovskite/silicon-heterojunction solar cells

After analyzing the perovskite single-junction devices, we turn our attention to tandem devices that can theoretically overcome the efficiencies of the single junction solar cells. For the purpose of this study, we base our optical simulations on the

monolithic planar perovskite/silicon-heterojunction (SHJ) tandem solar cell shown in Figure 3.20 (a) and presented and fabricated by Albrecht et al. [129]. In the proposed configuration, the top cell is a perovskite solar cell with the bandgap of 1.54 eV as found in the literature [138] and in agreement with the quantum efficiency measurement. Despite being 0.19 eV away from the optimum bandgap [126], this should still result in high efficiencies and the effect of different textures can be translated to the case with a slightly higher perovskite bandgap. Since the SHJ solar cell is already well optimized, we keep its structure as a constant and only focus on the perovskite absorbing layer to achieve the highest possible current matching point. Again, CROWM was used to conduct optical simulations.

We consider three main cases in our simulations as shown in Figure 3.20. Figure 3.20 (a) shows the planar device [129]. Derived from this structure, there are three main possibilities of implementing textured surfaces to cause light scattering. Option 1 is to start with a one-side textured silicon wafer and deposit the layers on the textured surface towards the bottom conformally, while depositing the layers to the top as in the planar device (Figure 3.20 (b)). Option 2 is to start from the both-side textured silicon wafer and deposit the rest of the layers conformally on both sides of the wafer (Figure 3.20 (c)). This way the original texture from the Si wafer is preserved to the top (under condition that non-conformal growth is not taking place [49]). This is believed to be the route to the most efficient tandem devices. However, such devices are currently not feasible, since spin-coating as the most common and efficient deposition technique of the perovskite layers to date is not suitable for the high roughness of the randomly distributed pyramids of the textured Si wafer. Nevertheless, in the simulations we assume the texture of the Si wafer to be randomly distributed pyramids with up to 8 μm in size (same texture on both sides when simulating the both-side textured device) as shown in Figure 3.6 (b). Additionally, we also consider an attractive option of putting an LM foil on top of a planar device as shown in Figure 3.21. For our analysis of the LM foil, we simulated random pyramids and 4 other textures since UV NIL process allows us to use a texture of our choice (as long as a master with the same texture can be provided). In this case, LM foil ($n = 1.55$) replaced the LiF ($n = 1.39$) AR coating used in the other cases. As the analysis of the devices with the textured surfaces requires much computational time, we decided to keep the thicknesses as shown in Figure 3.20 (a) and only alter the perovskite absorber thickness in order to reach the current matching point. Compared to the report by Filipič et al. [128] we performed the simulations for the back-side texture

and different textured LM foils, and compared to Albrecht et al. [126] we considered textured interfaces in our structure, albeit not for the optimum perovskite bandgap.

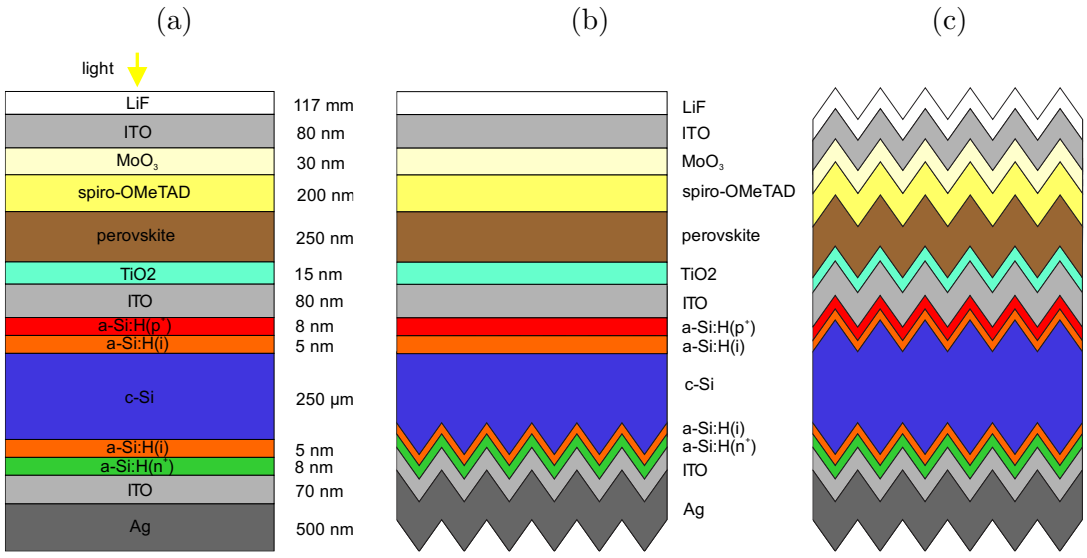

Figure 3.20: Schematic illustration of the investigated tandem perovskite/SHJ devices, built on (a) planar, (b) back-sided and (c) both-sided textured Si wafer.

3.4.4.1 Results and discussion

The results of the optical simulations for the three cases depicted in Figure 3.20 are presented in Table 3.7. The textured devices indeed have reduced reflection, namely for 2.5 mA cm^{-2} and almost 6.8 mA cm^{-2} with the back-side and both-side textured Si wafer, respectively. The so-gained light is then absorbed in the absorbing layers with the extracted J_{SC_SIM} increased from 16.2 mA cm^{-2} for the planar device to 16.9 mA cm^{-2} and 18.7 mA cm^{-2} for the back-side and both-side textured Si wafer, respectively. Note that the current gained due to reduced reflection is then equally spread between both subcells. Since the SHJ bottom cell is kept as a constant and the amount of light absorbed within is increased, the perovskite absorber must be thicker to absorb more light for the current matching point to be reached (see Table 3.7). We can also estimate the efficiency we could reach by assuming the experimentally achievable parameters [129] open-circuit voltage (V_{OC}) to be 1.80 V (1.10 V for perovskite and 0.70 V for SHJ solar cell) and a fill factor (FF) of 0.80. For the cases presented here, the highest efficiency would be 26.9%. This means a 15.2% relative increase over the planar device performance. Further improvements can be obtained by optimizing thicknesses of all the layers (not only perovskite absorber) and by tuning perovskite bandgap.

Table 3.7: J_{SC_SIM} and R_{SIM} in a current matching point for the three device designs from Figure 3.20 and estimated efficiency based on experimentally achievable parameters of the V_{OC} and FF. Perovskite layer thickness in the current matching point is also stated.

	PK thickness	R_{SIM} (mA cm^{-2})	J_{SC_SIM} (mA cm^{-2})	V_{OC} (V)	FF	PCE (%)	Change
Planar	250 nm	9.53	16.2			23.4	0
Back-textured	280 nm	7.00	16.9	1.80	0.80	24.4	4.3%
Double textured	320 nm	2.77	18.7			26.9	15.2%

Figure 3.21 (b) shows the reflection (1-R) and the absorption for the three studied cases. Compared to the planar device, for the back-side texture the reflection is mostly reduced in the long-wavelength region, where we also get the highest increase in the current in the c-Si due to light trapping. However, it has little effect on the device performance in the visible light region as only wavelengths above 1000 nm can reach the back side of the device. Therefore, one would expect that for the wavelengths below 1000 nm the absorption/reflection spectra would be the same for the back-side textured Si wafer and the planar device. However, to reach the current matching point, we had to increase the thickness of the perovskite absorber layer for the back-side texture, which resulted in different interferences and therefore different absorption spectra. The best performing device out of the three is the both-side textured wafer. The additional texture on the front side is very effective at anti-reflection. The reflection is decreased in the whole wavelength range, especially for the wavelengths below 900 nm where there is almost no reflection at all. Consequently, the absorption is also increased for all wavelengths. In the range between 600 and 800 nm, the increased absorption in perovskite means less absorption in c-Si. However, there is a significant reduction of the reflection and increase in absorption in c-Si due to light trapping for the longer wavelengths where we make up for that loss. Even more, the gain is such that we again have to compensate for it with almost 30% thicker perovskite layer compared to the planar device.

Figure 3.21 (b) presents the absorption spectra of the individual layers for the textured Si wafer while Figure 3.21 (c) the losses in the form of the equivalent short-circuit current density. The main loss, besides reflection, presents the HTM spiro-OMeTAD with considerable absorption in the whole wavelength range and strong absorption peaks at 380, 480 nm and in the long-wavelength range. To gain better

efficiency one has to replace spiro-OMeTAD with a less absorbing (and also cheaper) HTM or change the device design to regular structure. Minor losses are also in the front ITO, MoO_3 protection layer (for ITO deposition) and in the back contact if we used textured surfaces. This happens due to increased transmission of the longer wavelengths through the stack to the back contact and weak absorption of c-Si in the long wavelength range.

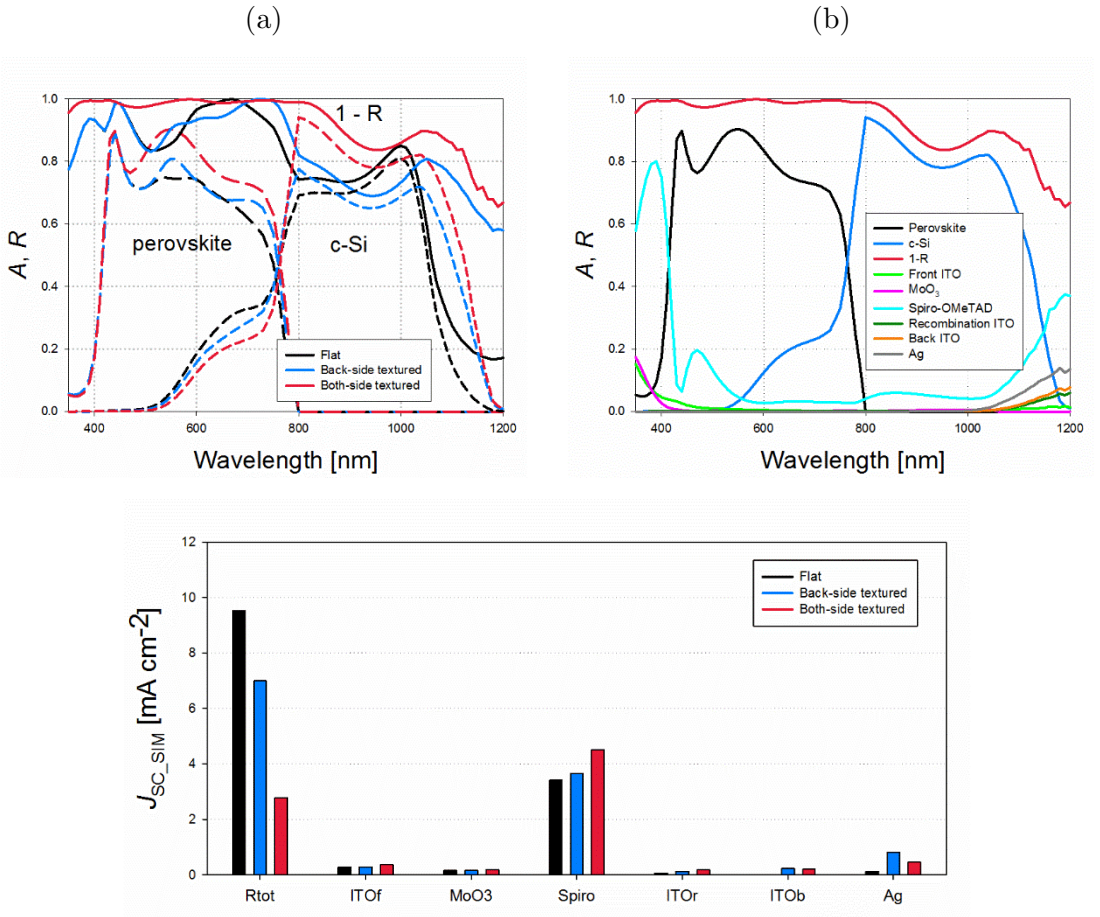

Figure 3.21: (a) Reflection and perovskite and c-Si absorption spectra for all three device designs (flat device, back-side and both-side textured Si wafer). (b) Absorption of the individual layers for the textured Si wafer device. (c) Loss comparison between the three device designs.

3.4.4.2 Different textures of the light management foil

Similarly to the single-junction analysis, we also consider the LM foil for the planar tandem device. We simulate the expected improvements for the textures shown in Figure 3.6 (b) and Figure 3.18 and described in 3.4.3.4. For the purpose of this simulations, we keep the planar device structure and add the LM foil with different textures instead of the LiF AR coating as shown in Figure 3.22. The results in a current matching point are

shown in Figure 3.22 (b) and are very similar to the single-junction analysis. The cornercube textured again proved to be the most successful at reducing reflection and increasing the performance. It is only 0.4 mA cm^{-2} below the device with the textured Si wafer. The random pyramids from Si wafer and hexagonally arranged convex parabolic textures have very similar performances with around 0.8 mA cm^{-2} less harvested current density. The concave parabolic texture is next while the regular pyramids are again the worst. Nevertheless, the current density with regular pyramids is still improved by 1.1 mA cm^{-2}.

(a)

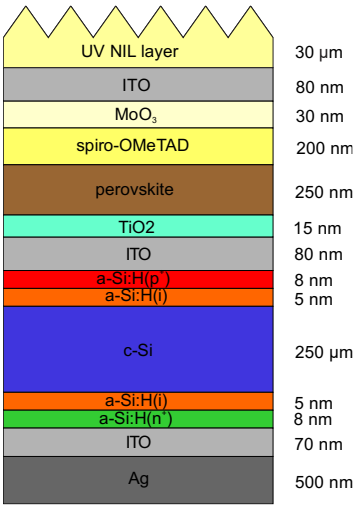

(b)

	PK thickness	R_{SIM} (mA cm^{-2})	J_{SC_SIM} (mA cm^{-2})
Cornercube	300 nm	4.02	18.3
Random pyramids	280 nm	5.67	17.5
Regular pyramids	270 nm	6.88	17.0
Parabolic O	280 nm	5.31	17.6
Parabolic U	270 nm	6.16	17.3

Figure 3.22: Schematic illustration of the investigated perovskite/SHJ tandem device with a planar design and textured UV NIL layer. (b) J_{SC} and R_{SIM} in a current matching point for the different textures. Perovskite layer thickness in the current matching point is also stated.

3.4.5 Conclusion

Optical 3D simulations based on experimentally obtained parameters (layer thicknesses, n, k) were used to support the experimental findings of the single-junction perovskite solar cells. A good match between the simulated and experimental data, without and with the LM foil, was obtained, validating the model. Optical simulations reveal that the main improvement in device performance is due to a reduction in total reflection and therefore increased absorption. We find that smaller area devices suffer from light escaping the active area, therefore a high amount of the refracted light not reaching the absorber. This confirmed the difference in EQE between simulation and experiment for devices with the LM foil. In general, a relative boost in photocurrent of ca. 8% is feasible for large area devices, even for active layers thicker than 1 µm.

Additionally, simulations revealed that optimized light management can be used to reduce the thickness of the active layer to reduce the amount of absorber material and enhance the photogenerated density, resulting in an expected 36 mV enhancement of the V_{OC} at an identical photocurrent. This study demonstrates the beneficial role of the LM foil in reducing reflection and increasing absorption in perovskite absorber, making the LM foil a promising solution for improving the performance of perovskite based solar cell.

We also performed optical simulations of the perovskite/silicon-heterojunction tandem solar cells. Three different device designs were tested: planar device and devices with back-side and both-side textured Si wafer, to optimize light management. LM foils with different textures on top of the planar device were also considered. All the designs improve the performance compared to the planar device structure. The best performing is a design with both-side textured Si wafer which increases the short-circuit current density by 2.5 mA cm^{-2}. Such increase is caused by reduced reflection in the whole wavelength range and prolonged optical path in the near infrared (NIR) region. Assuming V_{OC} =1.80 V and FF = 0.80 a 26.9% efficiency can be obtained. Further improvements can be achieved by using perovskite with the optimal bandgap and optimizing the thicknesses of all layers. This way, we anticipate the conversion efficiency to exceed 30%.

3.5 Summary

In this chapter, perovskite solar cells were presented. In the first part, we introduced perovskite material properties, single junction and tandem solar cells. In the second part, the fabrication and the characterization of the perovskite single junction devices were presented. The effect of the HPA additive in the perovskite solution was investigated. The addition of the HPA improved the surface morphology of the perovskite, however, only a small effect on the device performance was observed, mostly in FF. Both devices, without and with the HPA, reached efficiencies above 15%. The performance of the devices was then further improved by applying the light management foil, which reduced the reflection and consequently increased the absorption. Similar promising results were obtained for two device designs, one with PTAA and one with PEDOT:PSS as a hole transport material.

In the third part, optical simulations were used to confirm experimental findings. The optical model was first validated by a good match between simulations and

experiments, and then applied on single junction and tandem devices. Optical losses were investigated and different textures of the LM foil were considered. The results confirmed that by using textures, the planar devices are drastically improved. The single junction device with the LM foil can have up to 10% relative higher performance while the tandem device built on both-side textured Si wafer can reach 15% relative higher efficiency.

4 Camera-based light scattering measurement systems

This chapter is devoted to measurements of angular distribution of scattering light at textured surfaces. Angular distribution function is one of the most common parameters when discussing scattered light and characterizing textured surfaces. It is usually measured using goniometric systems; however, the measurements are time consuming and the systems measure angular distribution of scattered light in only one plane. To speed up the measurements and obtain light scattering in 3D space, camera-based systems can be used. Therefore, we developed two camera-based light scattering measurement systems, one with a reflective and one with a transmissive screen. Both systems enable fast, accurate and spatial measurements of scattered light. The system with the transmissive screen is used when characterizing light scattering of the UV NIL replicas.

The contents of section 4.2 on camera-based light scattering measurement system with reflective screen were published in 2014 under the title "Camera-based angular resolved spectroscopy system for spatial measurements of scattered light" in the journal *Applied Optics* [143]. The contents of section 4.3 on camera-based light scattering measurement system with transmissive screen were published under the title "Camera-based ARS system for complete light scattering determination/characterization" in the journal *Measurement Science and Technology* [144].

4.1 Introduction

Light scattering is an important phenomenon with a broad range of applications, in particular for efficient in-coupling of light in photovoltaic devices and/or out-coupling optoelectronic devices [22]. The scattering of light usually happens at (nano)textured surfaces in the device. In solar cells, scattered light rays have prolonged optical paths, ultimately resulting in a higher conversion efficiency [12]. In light sources, scattering at

nanorough surfaces is used to broaden the angular distribution of emitted light [145]. As different (nano)structures scatter light differently, it is of great importance to know and quantify the process of light scattering. The basic concepts of light scattering measurements are therefore standardized and described in ASTM [146], [147] and ISO [148] standards.

In the field of (thin-film) photovoltaics, two main techniques are used to characterize light scattering properties of rough surfaces: Total Integrating Scattering (TIS) and Angular Resolved Scattering (ARS). TIS measures the entire scattered light and does not include the directional (angular) information on scattered light [12]. Using a monochromator and an integrating sphere with openings, TIS measurements are performed in a broad wavelength range for both reflected and transmitted light.

ARS on the other hand provides information about angular distribution of scattered or emitted light of optoelectronic devices [12], [22]. Even measured in the surrounding air, it already gives an important indication about preferred textures for enhanced absorption in the structure [12], [149]. ARS systems are usually goniometric and measure angular distribution function (ADF) in one plane only (1D ADF). Different goniometric ARS systems have been developed, such as ones by Rifkin et al. [150], Krč et al. [151], Schröder et al. [152], Amra et al. [153] and Jäger et al. [154], where the last two can measure ADF in broader wavelength range. Usually using goniometric scanning method, ARS systems are quite time-consuming even if measuring in one plane only. In case of random textured surfaces, assuming rotational symmetry, one plane provides enough information to predict the intensity distribution in 3D space. However, goniometric scanning is not time-effective and sometimes not sufficient to accurately determine light scattering in 3D space. In order to acquire more complete information about 3D ADF in a short time, camera-based ARS systems are used. Some of them are commercial products [155], [156], with hemispherical reflective screens that are already fully compliant with standards typically used for light sources. Scattered light can be projected also on flat screens that are either reflective or transmissive.

A few camera-based systems on a lab scale were already reported. Berner et al. [157] introduced a system with a lens and transmissive screen for measurements of transmitted scattered light. A similar approach (but without a lens) was used for the characterization of optical films for 3D displays [158]. Foldyna et al. [159] reported on a system for spatial measurements of the reflected light in a broad range with a very complex conoscopy configuration. Some other publications on the measurements of the

reflected light were also reported [160], [161]. They, however, have been developed for the applications (road surface reflectivity and modelling for computer graphics, respectively), and samples that are very different to the application and samples discussed here. Additionally, light scattering systems were also built to analyze reflection under illumination with a linear light source [162] and to inspect surface roughness or defects [163]–[165].

The camera-based ARS systems are compact, inexpensive and enable quantification of light scattering over a broad angular range at one camera shot per wavelength. This makes them a powerful tool for the characterization of a versatile set of different samples or as an inspection tool in the high throughput industrial production. Randomly, periodically and quasi-periodically textured transparent samples or light sources, such as LEDs, can be characterized accurately and in a very short time (seconds).

In this chapter, we focus on the development and the application of ARS systems based on a digital CCD camera to determine 3D ADF of transmitted and reflected light. Two different systems are presented. The first one includes a lens to broaden the polar angle range and a reflective screen in order to gain in the signal. The second one is built with a transmissive screen and can be used to measure transmitted or reflected light but only in a part of a hemisphere. The mathematics behind both systems are presented. Projection screens are characterized. The systems are validated with diffraction gratings and randomly textured TCO samples.

4.2 Reflective screen

Camera-based ARS systems capture the scattered light, projected on the screen. Most of the studies used transmissive screen where scattered light that is transmitted through the screen is captured. We, however, introduce a new solution of the 3D measuring system for the measurements of scattered light based on highly reflective screen. Capturing the light reflected from the screen, results in lower screen losses due to no absorption in the screen and no refraction or scattering inside the screen. Thus, we can avoid optical losses in the diffusive transmission screens by employing inexpensive highly reflective and highly diffusive reflection screens, e.g. white paper. Moreover, in this approach it is also easier to avoid the direct specular beam entering the camera and saturating the central pixels of acquired image. The developed system is also applicable

for characterization of optical sources such as LEDs when determining their luminous intensity distribution of emitted light.

In the next subsections, the developed camera-based system, including all required computational transformations from raw image to 3D ADF representation and the analysis of related effects, is described. Sensitivity and resolution matters are discussed. The system is validated on a series of results of 3D ADF measurement on selected nanotextured superstrates used in thin-film silicon solar cells and on a selected light source. Qualitative and quantitative comparison between camera-based results and results obtained with the conventional goniometric ARS setup are given. A detailed analysis of possible measurement errors is also carried out.

A paper describing this system was published in the journal *Applied Optics*, entitled "Camera-based angular resolved spectroscopy system for spatial measurements of scattered light" [143]. The main scientific contributions were introduction of the reflective screen and the lens and detailed analysis of the possible lens errors.

4.2.1 Experimental

4.2.1.1 System setup

The scheme of the developed camera-based setup for the case of determination of 3D ADF of scattered transmitted light at a textured transparent sample is shown in Figure 4.1. Collimated laser light is used for illumination of a sample. In the case of determination of 3D ADF of a light source, the device is placed on the position of the sample and laser illumination is not used. Just behind the sample (or light source under test) a hemispherical lens is used to narrow the angular distribution of the light so that smaller screens can be used, resulting in a compact system. Light is then projected on a tilted (screen angle α) highly-reflective and diffusive flat screen, where the image is captured by a camera. Here, a commonly used white paper (100 µm) was employed as a screen. To eliminate the effect of the specular beam (which often presents a strong component on the image despite scattering at the sample and at the diffusive screen) a hole was made in the screen, enabling the beam to be transmitted (solid red line in Figure 4.1). For a tilted screen, an elliptic shape of the hole was used. Effects of saturation and pixel cross-talk in the camera can thus be avoided. As a result, only non-specular light is captured by the camera, which presents the required information to determine the ADF of scattered light (specular component excluded). In case of samples/light sources

where specular component is not pronounced, the hole is covered by the screen material. To capture the image a 1.4-megapixel CCD camera with 16-bit resolution was utilized in our system, positioned perpendicularly to the tilted reflective screen along the z' axis as shown in Figure 4.1. This way we avoid additional transformations due to camera asymmetry/rectilinear effect and only apply screen angle transformation. If the center of the specular beam is considered as a center of the signal ADF, we get the widest range of the signal ADF. If using a lens with high distortion, distortion or aberration correction also has to be considered and applied.

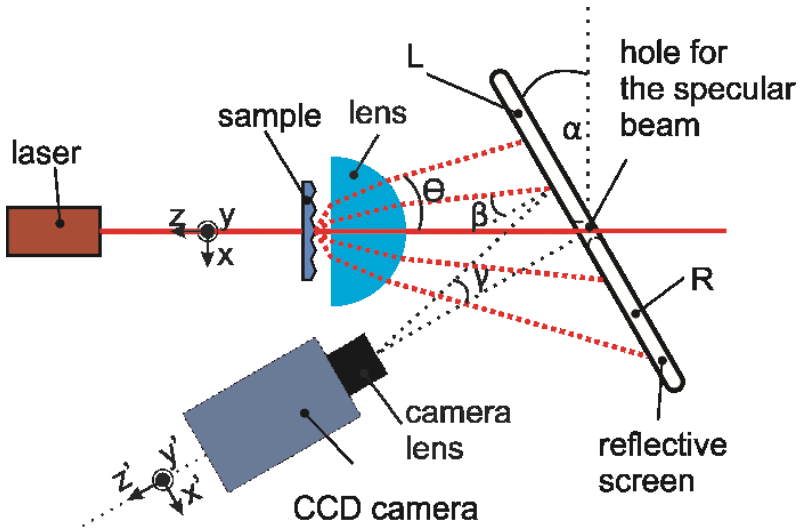

Figure 4.1: Camera-based system scheme for the case of detection of transmitted scattered light of a textured transparent sample: laser illuminates the sample and the scattered transmitted light is projected on the screen. The camera captures images of the 3D ADF from the screen.

The time of the measurement with a camera-based system is determined by the integration time of the CCD camera, which is limited by the intensity of the laser beam (or light source under test). We want to get as much signal as possible without saturating the camera. In our case, where a 10 mW He-Ne laser was used, the time of the measurement (integration time of the camera) can be set to a few seconds. Using conventional goniometric ARS with a rotating arm [12], scanning the intensities in a single measuring plane, the measurement usually takes more than 10 seconds per angular step, thus measurement in the comparable range (still in one plane only) of 80° with a step of 0.5° can last more than 30 minutes.

4.2.1.2 Range and resolution of the measurement

Range of the proposed system depends on many variables, such as distances between different components, lens focal length, screen size and camera lens viewing

angle. In the setup, a small screen in size of A4 paper format was used to make the system compact. Hemispherical lens made of glass with refractive index $n = 1.515$ and radius 5 cm was used, enabling to widen the range of spatial angle of light to be projected on such relatively small screen. With the lens, the angular range of acquired 3D ADF is almost doubled, in particular case it ranges from -38° to 30° in horizontal and from -48° to 48° in vertical direction of the screen. The asymmetry in the horizontal axis is a result of the tilt of the screen. Screen angle and camera distance should be set so that the camera does not block the signal and we get maximum ADF range while still avoiding specular reflection from the screen. Screen angle $\alpha = 20°$ was chosen for our setup. Improving the range of the system can be done by altering e.g. camera lens viewing angle, using larger screen and/or altering lens distance which will be briefly discussed in the results section, though, attention should be paid on the effects mentioned in the next section.

Contrary to the conventional goniometric ARS system where the angular resolution can be set constant along the scanning plane, here it varies due to tilted flat screen. Tilted flat screen demands a solid angle transformation (see section 4.2.2), causing that a discrete solid angle corresponds to different number of camera pixels, depending on the position on the screen. For this setup, a discrete solid angle of $\Omega = 0.000079$ srad is used in calculations, following the $\Omega = 2\pi(1 - \cos\delta)$ equation, where $\delta = 0.005$ rad, and the number of pixels, covering the area defined by the angle, varies from 36 to 99 depending on the position on the screen. Alternatively, one pixel represents solid angles from $\Omega = 8.1*10^{-7}$ srad to $\Omega = 2.2*10^{-6}$ srad. The angular resolution of the system, determined by the pixel resolution of the camera and its distance from the screen, could be improved by using a CCD camera with higher resolution.

4.2.2 Image processing and transformations

The captured image of the illuminated screen needs further processing in order to extract the 3D ADF of the sample. Following transformations and effects need to be included: (i) lens transformation, (ii) screen angle and solid angle transformation and (iii) ADF of the screen. In addition to mentioned transformations, a raw image as captured with CCD camera needs camera offset subtraction and outliers removal first. This is done in accordance with Bokalič et al. [166], [167]. In the following subsections we present the transformations and some of the related optical effects in more details.

4.2.2.1 *Lens transformation*

The Snell's law defines the refractions of the beams at the entrance and at the exit of the lens. Optical transformation of the lens was studied with optical simulator CROWM [134], [136], [137]. Refraction angles as calculated internally in our procedure were in perfect agreement with the angles simulated by CROWM.

With CROWM other effects related to the lens were studied, such as non-zero reflection at the surfaces of the lens and crossing of the refracted beams. Multiple refractions and reflections might occur in the lens if imperfect anti-reflecting coatings are used. There is a possibility that secondary refracted beams with non-negligible strength exit the lens and hit the screen and therefore influence the measurement. In our system a lens with no anti-reflecting coating was used, which was considered in simulations.

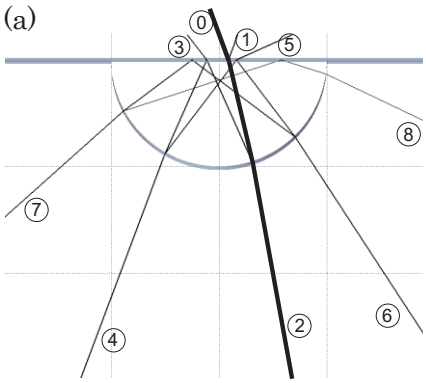

Beam	Relative intensity
⓪	100%
①	4.30 %
②	91.39 %
③	3.83 %
④	0.18 %
⑤	0.06 %
⑥	~0 %
⑦	~0 %
⑧	~0 %

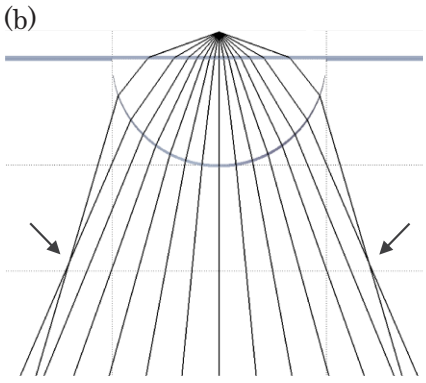

Figure 4.2: (a) Some of refracted and reflected beams corresponding to a single incident beam applied under 20° incident angle to the lens front surface. Relative intensities of the beams are given in the table. (b) Refraction of incident beams (no reflected beams considered in this case) applied under different incident angles. Note that the crossing of the refracted beams can occur (denoted with arrows), limiting the highest value of allowed incident angle.

Results of a simulation for a two-dimensional problem (not 3D) where the beam is applied under 20° incident angle is shown in Figure 4.2 (a) for the purpose of easier representation. Relative intensities of the series of reflected/refracted beams are listed in the table aside the figure. The results of the complete analysis where the beams were applied under various incident angles are summarized in Table 4.1.

Intensities of the direct beam and all transmitted beams were obtained from simulations. At the incident angle 40°, total reflection occurs in the selected lens (from beam ③ to ④). This results in total transmission being considerably higher than the direct beam transmission. However, in our system the total reflected beams corresponding to these incident angles already miss the screen and do not influence the measurement.

Table 4.1 was used as a basis for calibration of the system (direct beam intensity) with respect to non-zero reflection at the lens surfaces.

Table 4.1: Lens transmission considering different refracted beams.

Incidence Angle (°)	Transmission (direct beam ② only)	Total transmission (beams ②+④+⑥+⑦+⑧)	Difference [%]
0	0.9142	0.9159	0.19
10	0.9141	0.9159	0.20
20	0.9139	0.9157	0.20
30	0.9127	0.9155	0.31
40	0.9085	0.9501	4.58
50	0.8970	0.9362	4.37
60	0.8666	0.9040	4.32
70	0.7878	0.7898	0.25

Another effect that was studied by simulation is an overlapping of the refracted beams at high angles (Figure 4.2 (b)). A border angle at which this effect happens is 62° for our case where the distance between the sample and the lens d was set to 9 mm. The dependence of the border angle on d is shown in Table 4.2. Lens shape and size are also very important. With appropriate plano-convex lens we can almost completely eliminate the overlapping effect – extending the angles of ADF measurement above $> 80°$ (with our lens up to 79° at $d = 1$ mm would be possible). However, in this case also a large screen and camera lens with a wide angle of view have to be used. Thus, the angular limitations specified for the presenting system are not linked to the concept but to the specific equipment used in the setup. This effect was in our setup eliminated by sticking a black ring on the lens that blocked all incident beams with angle greater than 60° for $d = 9$ mm (not depicted in Figure 4.1).

Table 4.2: Border angle for different distances between the lens and the sample for a hemispherical lens.

Distance d	9 mm	7 mm	8 mm	10 mm	11 mm
Border angle	62°	65°	64°	61°	60°

4.2.2.1.1 Sample-to-lens distance sensitivity

Illuminated sample is considered as a point source of the scattered light as the laser beam is collimated. Distance between the sample and the lens appears to be an important parameter, not only in determination of the border angle described above. Since the d is usually relatively small, its measuring error can result in ADF angular inaccuracy. We checked the errors in scattering (radiation) angle determination related to $\Delta d = +/-1$ mm adjustment tolerance applied to $d = 9$ mm. The results are presented in Table 4.3.

Table 4.3: The effect of inaccurate determination of the distance between sample and the lens on angular error in ADF as a function of scattering angle.

Scattering angle at $d = 9$ mm, θ (°)	$\Delta\Theta$ (°) error if $\Delta d = -1$ mm ($d = 8$ mm)	$\Delta\Theta$ (°) error if $\Delta d = +1$ mm ($d = 10$ mm)
0	0	0
10	0.18	-0.2
20	0.38	-0.41
30	0.64	-0.68
40	1.00	-1.17

Angular error as a consequence of inaccurate adjustment of d increases with the scattering angle. Positive difference means that the determined ADF is broadened, whereas negative difference means narrowed ADF. The distance between sample and lens has to be chosen correctly and measured precisely in order to avoid these errors.

4.2.2.1.2 Sensitivity on lens tilt from x-y plane

Ideally the lens axis is perpendicular to the x-y plane of our system (see Figure 4.1). Effect of lens tilt deviation was studied next. In the tests the angular tolerance of +/-1° lens deviation from the perpendicular position was assumed. Related errors in determination of scattering angles of ADF are presented in Table 4.4. The scattering angles error for tilted lens reaches up to $|\Delta\theta| = 3°$ for selected parameters of our system. Such an error is not insignificant, however, an extreme case was studied here. In application a deviation of lens rotation less than 0.5° can easily be achieved and the corresponding error minimized to $|\Delta\theta| < 1.5°$ at scattering angle 40°.

Table 4.4: The effect of inaccurate angular alignment of the lens on the angular error in ADF as a function of scattering angle.

Scattering angle (°)	−40	−30	−20	−10	0	10	20	30	40
Δθ(°)	-1.05	-0.05	0.1	0.4	1.0	1.65	2.05	2.2	3.0

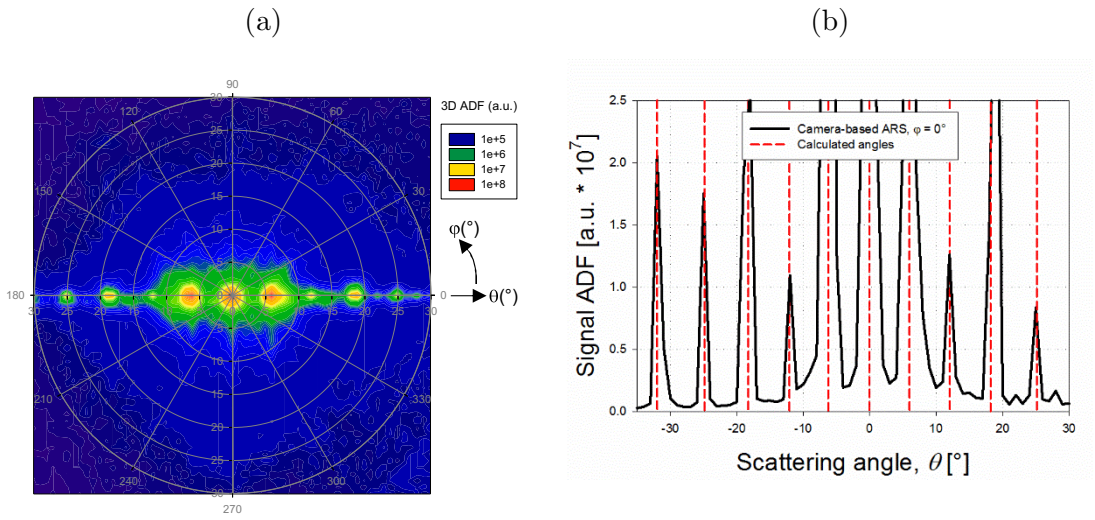

Figure 4.3: (a) 3D ADF of a linear (1D) diffraction grating and (b) line scan from 3D ADF (solid black line) compared with calculated angles (dashed red line), screen angle $\alpha = 20°$.

4.2.2.2 Screen angle and solid angle transformation

Screen angle and solid angle transformations are needed as the screen is flat (not hemispherical) and tilted for the screen angle α (non-perpendicular to the laser beam), respectively. Light is discretized into equal differential solid angles ($\Omega = 0.000079$ srad), defined by differential azimuth and polar angle - referred to as discrete light beams in further. The beams are projected into differential spot areas on the screen, depending on the screen angle and the scattering/emission angle of the beam. Geometrical rules are followed to transform spot areas at certain positions of the screen to the angles and intensities of the ADF. To test the transformation we measured the 3D ADF of a linear periodic grating where the angles of the discrete scattered beams (modes) can be calculated based on diffraction theory [168]. Results of the measurements are shown in Figure 4.3 (a) - 3D ADF presented in a polar plot and Figure 4.3 (b) - ADF in a selected plane where the beams are present (central horizontal line from Figure 4.3 (a)). Since the grating was linear (lines), scattered beams appear only in one (in this case horizontal) plane. Similar tests were also done for 90° rotated grating where the vertical plane was

tested (not shown here). Good agreement was acquired between both measurements and calculated angles, validating all the described angular transformations (the amplitude asymmetry, most notably seen at angles +/-25°, is a result of camera saturation).

4.2.2.3 Screen characteristics

It is a key requirement of the reflective screen to be highly diffusive. It is also convenient to have a uniform ADF of scattered light at the screen. In case of a specular screen (mirror), most of the light projected on the mirror would be specularly reflected, thus outside the acquisition (view) angle of the camera. Diffusive nature enables that each of the illuminated point of the screen, directs a proportion of light towards the camera. Therefore, to correctly calculate the 3D ADF of the sample, the ADF of the screen has to be known.

For the characterization of screen's ADF in reflection, we used the conventional goniometric based ARS setup [169]. ADF of the used white paper screen was measured at different incident angles. Selected results are presented in Figure 4.4. As the measurements showed isotropic behaviour of 3D scattering we present here the results of the ADF measurements in one plane only. All ADF curves corresponding to different incident angles of the illumination can be approximated with a cosine function, which is typical for Lambertian diffusors, except at the angle of specular reflection where ADF signals are increased. The angular adjustment of the screen ($\alpha = 20°$) and the camera was selected in the way that the specular part of the ADF of the screen is not in the range of camera acquisition, thus approximation with cosine function is justified. Furthermore, linear dependence between amplitude of the cosine approximation and the incident angles was detected (the effect is relatively small and thus not visible in Figure 4.4). Equation (4.1 was used to describe this effect in $ADF_{Rscreen}$ determination.

$$ADF_{Rscreen} = (a * \beta + b) * \cos(\gamma) \tag{4.1}$$

The β is the incident angle of the approaching beam to the screen and γ is the angle between the camera and the scattered beam position on the screen (see Figure 4.1). Each discrete light beam has different β and γ, therefore ADF of the screen is calculated for each discrete light beam separately. Coefficients a and b represent the linear dependence of the amplitude, their values were a =-0.000133 and $b = 0.042$ for our system.

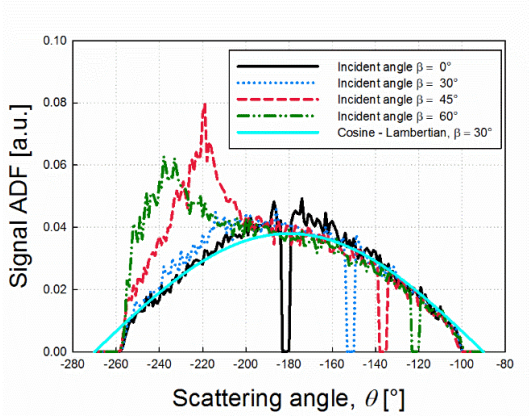

Figure 4.4: ADF line scan of the white paper screen at 4 incident angles β and cosine approximation for $\beta = 30°$.

4.2.3 *Results and discussion*

We have validated the developed system with two types of samples: (i) transparent surface-textured samples and (ii) a reference light source. Measurements were compared with the existing goniometric ARS system [169]. First, surface textured ZnO:Al transparent conductive oxide (TCO) films sputtered on glass and etched in diluted HCl [170] were characterized. These TCO samples are commonly used as a superstrate in thin-film silicon solar cells, introducing textured interfaces in the cell. Here, bare glass/TCO samples with nanotextured surface of TCO facing the lens were characterized with respect of light scattering in air. Although this situation may not directly refer to the scattering inside the solar cell, we still get valuable information on scattering characteristics from the measurement.

(a) (b)

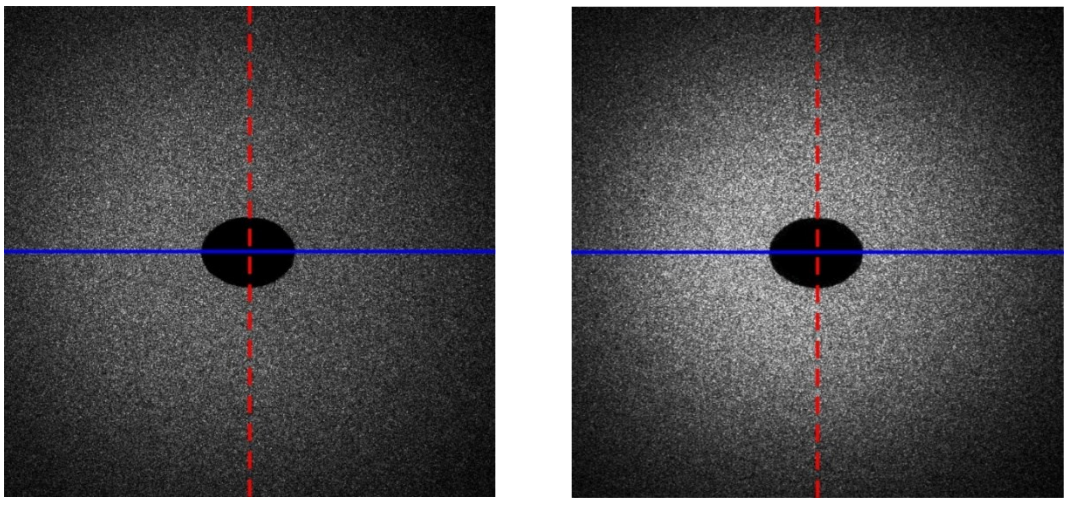

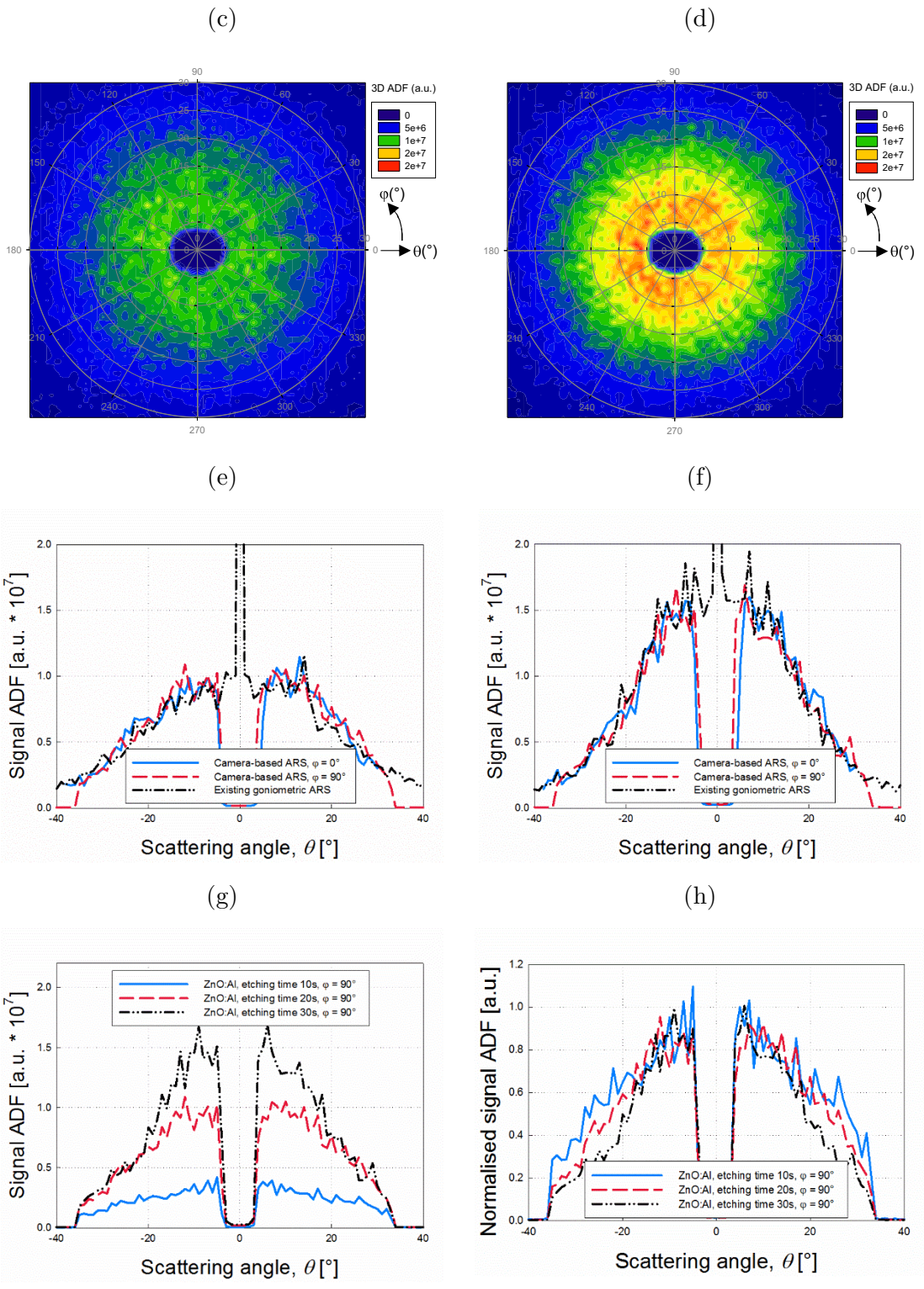

Figure 4.5: (a,b) CCD images, (c,d) 3D ADF and (e,f) ADF line scans for etched ZnO:Al – etching time 20 s (left side) and 30 s (right side) and (g,h) comparison of ADF line scans for three samples (10, 20 and 30 s etching times). Screen angle $\alpha = 20°$.

In the case of the TCO sample measurement, the screen's hole was left open due to relatively high intensity of the transmitted specular beam. For experiments different

lasers were used, here we present the results obtained with the He-Ne red ($\lambda = 633$ nm, $P = 10$ mW) laser.

Results for three samples of sputtered and etched ZnO:Al (corresponding to etching time 10 s, 20 s and 30 s) [171] are shown in Figure 4.5. Figure 4.5 (a) and (b) show unprocessed raw image as captured by the CCD camera for the 20 s and 30 s etched samples. The hole of elliptic shape in the screen can be observed. Blue and red dashed lines represent the direction of the horizontal and vertical ADF line scan respectively, corresponding to the results presented in Figure 4.5 (e) and (f). Figure 4.5 (c) and (d) show the 3D ADF after all required transformations (see Section 4.2.2) are applied. For clear representation of 3D ADF polar plots were chosen. Directions of spherical coordinates (the azimuthal angle, φ, and the polar angle, θ) are denoted with arrows. The polar angle is assigned to scattering angle when showing horizontal or vertical line scan (constant φ). For the polar angle θ a range of +/- 30° was chosen, as for positive polar angles this was the limitation for acquiring the ADF with the given screen size and camera used. Capturing the signal up to the border angle would be possible with a camera lens with a wider angle of view. Signal ADF values are in arbitrary units and depend on camera's integration time, which was set to $t = 250$ ms for all three samples. As the samples are randomly textured they scatter light isotropically with respect to azimuthal angle. Symmetry of the ADFs around the specular direction can be seen also in our measurements which implies that transformations for a tilted flat screen were applied adequately. Good agreement can be observed from Figure 4.5 (e) and (f), where comparison between ADF in selected plane (polar angle θ at azimuth angle $\varphi = 0°$ for blue line and $\varphi = 90°$ for red line) obtained with the developed camera-based system and the reference goniometric ARS system. The ADF values obtained from the reference goniometric ARS system were scaled to the ones acquired with the developed ARS system to enable comparison. A low ADF signal around the specular beam ($|\theta| < 5°$) is a result of the hole in the screen, whereas existing goniometric ARS system has high values due to the specular beam.

For all the measurements we have minimized the errors described in section 4.2.2.1 as much as possible by calibrating the system as well as by careful alignment of the components and distances between. However, to demonstrate the effect of distance between the lens and the sample and lens tilt error we show in Figure 4.6 the error zone corresponding to the errors Δd = -1 mm with lens tilt 1° and $\Delta d = +1$ mm. for the ZnO:Al sample (etching time 30 s, $\varphi = 90°$). The error zone is colored grey and the error

values were chosen to match those from error analysis in section 4.2.2.1. As already mentioned, the errors considered here are rather extreme cases. By careful adjustment of the system components much smaller errors are expected in our measurements.

Figure 4.5 (g) shows absolute comparison between the ADF measurements of ZnO:Al samples as obtained with the camera-based system whereas in Figure 4.5 (h) normalized comparison is shown. Measurements show that the sample with longest etching time (30 s) scatters higher amount of light while the sample with shorter etching time (10 s) scatters less light as it is less rough. However, normalized signal ADF shows that samples with shorter etching time scatter light better at larger angles (far away from specular direction), relatively.

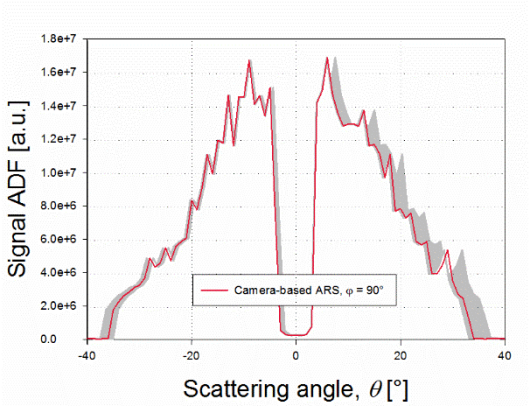

Figure 4.6: Error analysis for ZnO:Al etching time 30 s, $\varphi = 90°$. Error zone corresponds to the extreme cases presented in section 4.2.2.1 – Δd = - 1 mm with lens tilt 1° and Δd = +1 mm.

In addition to characterization of light scattering properties of the TCO superstrates used in thin-film solar cell technology our system is also applicable to characterize the luminous intensity distribution of light sources as well. For demonstration purpose, we present here the application of the system for characterization of the calibration light LS1 for spectrophotometers from Ocean optics [172]. Whenever characterizing samples or sources where specular beam does not cause camera saturation a screen without a hole for the specular beam can be used. Figure 4.7 (a) shows 3D ADF (proportional to 3D luminous intensity distribution) and Figure 4.7 (b) shows selected line scans and comparison with reference goniometric ARS system. Good matching between the camera-based and reference goniometric system was again acquired, as seen in Figure 4.7 (b).

(a) (b)

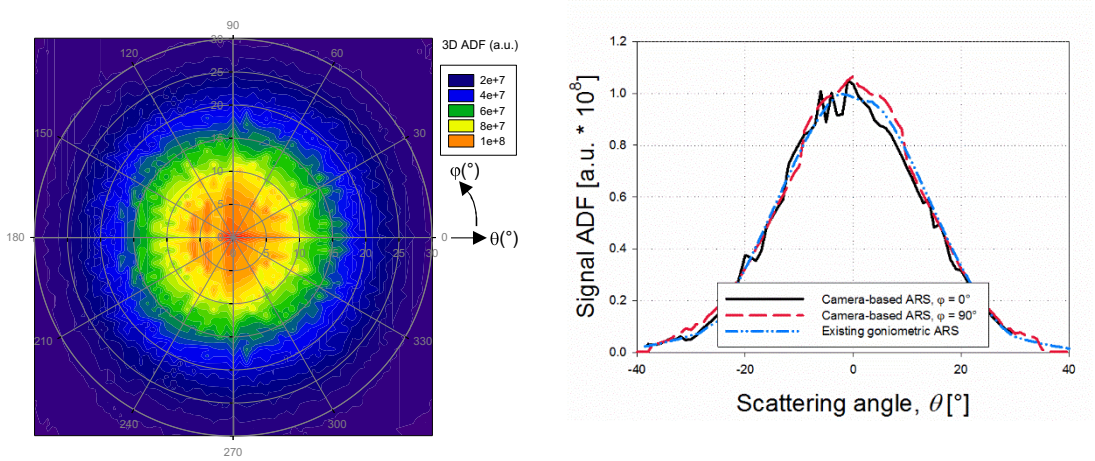

Figure 4.7: (a) 3D ADF and (b) line scans for light source LS1 ($t = 5$ s), screen angle $\alpha = 20°$.

4.2.4 *Conclusion*

Camera-based ARS system using a reflective screen for the characterization of scattered or emitted light along with all the transformations needed to extract the 3D ADF was presented. The system is based on a reflective screen and a hemispherical lens that is used to broaden the range of the system. The system was tested with three TCO samples and a reference light source while sensitivity analysis was also carried out. Results show good matching with the results obtained with the conventional ARS system. Using a hemispherical glass lens with radius $r = 5$ cm the angular range was almost doubled to $\pm$ 48°. The angular range of the presented system can be further extended by using a camera lens with wider angle of view. The resolution of the system can also be simply improved by using a CCD camera with higher resolution.

4.3 *Transmissive screen*

Transmissive screens have one big advantage over reflective screens – it is easier to achieve greater angular range of measurements since the position of the elements have less influence on the camera angle view (the sample might block the camera view). Here presented upgrade of the proof-of-the camera-based system from a reflective screen to the transmissive screen enables measurements of reflected and transmitted scattered

light, the aimed range after additional transformations being a full sphere. The hole to let the laser/specular beam through is kept, but the lens is omitted.

In this setup we use a transmissive screen, positioned non-perpendicularly at the specular beam to cover large scattering angles. Compared to the other reported setups, mentioned in the introduction 4.1, such configuration enables measurements of all the polar angles θ, from 0° to 90°. To broaden the range for azimuthal angles φ, we apply a few step rotation of the sample or/and the screen with the camera. This camera-based system is useful for both scattering samples and light emitting samples (LED and OLED). Besides transmitted, the new setup enables also measurements of reflected light which has not been reported yet. In addition to the fast and accurate determination of the (full) 3D ADF, we show how to obtain the haze parameter (ratio between integrated diffused over total light) with the new setup. We also carried out basic repeatability and uncertainty analysis.

In the first part, we present the configuration of the system and image processing procedure to acquire light scattering parameters of the sample from raw image. In the results section we present the results of measurements of the two selected samples: nanotextured transparent conductive oxide on a glass substrate and periodically textured silicon sample. The results of the haze determination are also shown.

A paper describing this system was published in the journal *Measurements Science and Technology*, entitled "Camera-based ARS system for complete light scattering determination/characterization" [144]. The main scientific contributions were the ability to measure both reflectance and transmittance and in the full (hemi)sphere range.

4.3.1 Experimental

4.3.1.1 System setup

The setup of the novel camera-based system is illustrated in Figure 4.8 (a). A collimated laser source with $\lambda = 633$ nm is used to illuminate the sample. A collimated light from a monocromator can be used if a scan over wavelength range is needed. The scattered or emitted light from the sample is projected on the transmissive screen and captured by the camera. The screen, positioned at $\alpha = 45°$ to the sample plane, is used for either reflectance or transmittance measurement, denoted with position R and position T in Figure 4.8 (a). When measuring the reflected light, the laser beam is first let through the hole in the screen R so that it can reach the sample. When measuring

the transmitted light, the specular beam needs to be blocked with a pin on the screen T if it causes camera saturation and/or blooming effect. A hole could also be used instead of the pin. However, when measuring specular beam, the hole would have to be filled with the screen material. To capture the image from a screen, a 1.4-Mpixel CCD camera with 16-bit resolution was utilized in our system, positioned perpendicularly to the screen(s). This way we avoid additional asymmetry transformations.

(a)

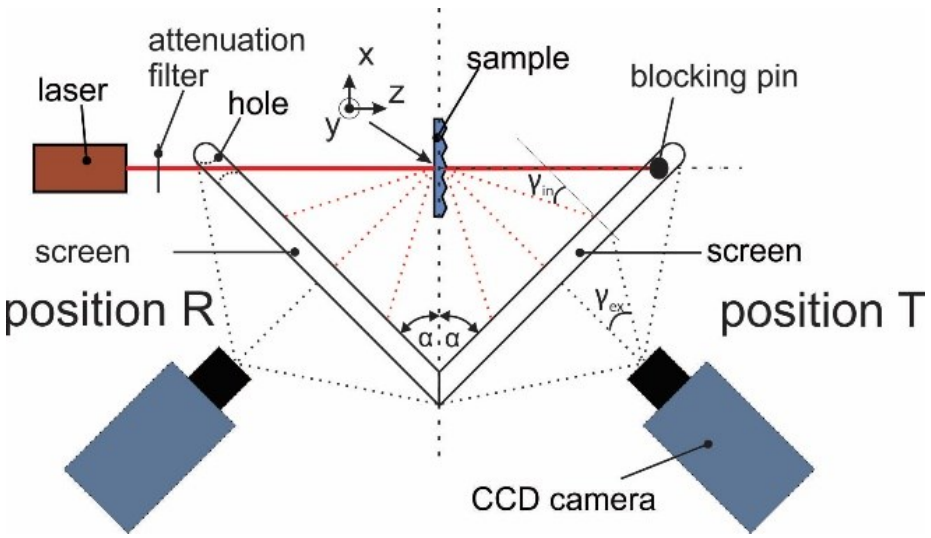

(b)

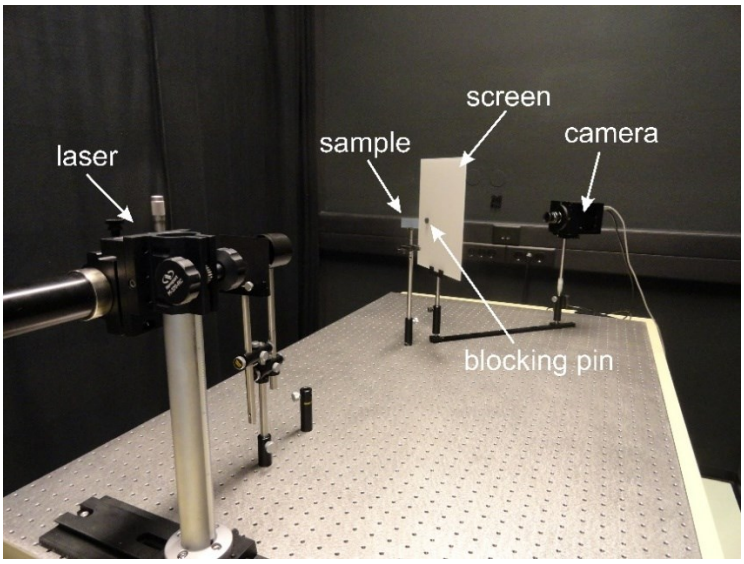

Figure 4.8: (a) Schematics of the camera-based system for measurements of reflected and transmitted light. The screen angle $\alpha = 45°$. In case of measurement of reflected light the laser beam is let through the screen via a hole in the screen. In case of a measurement of the transmitted light the specular beam is blocked to prevent camera saturation. The camera captures the light that is projected on the screen. Attenuation filter position is also depicted, as it will be later referenced in haze results section. (b) Photograph of the camera-based system for the measurement of transmitted light (screen in position T).

In Figure 4.8 two configurations are presented, one for reflectance (position R) and one for transmittance (position T). It requires two cameras and two screens to measure scattered light in R and T simultaneously. In case of a single camera, an automatic (or manual) rotation of 90° is needed to change the camera from one position to the other, allowing us to sequentially measure both R and T. Due to possible reflections from one screen onto another, additional care is advised.

With the placement of the screen as shown in Figure 4.8, we do not cover the entire hemisphere of reflected or transmitted light, but only a part of it. This way, however, we get full polar range θ, from 0° to 90°, at a cost of a smaller azimuth range. Range can be extended to almost full sphere (in R or T) by, e.g. rotating the camera (and screen) around the sample for 90°, 180° and 270° or, as will be proposed here, by rotating the sample. Nonetheless, if samples scatter light isotropically, one measurement is sufficient and can be extended to other azimuthal angles considering rotational symmetry.

4.3.2 Image processing and transformations

Once an image is captured with the camera, further processing and transformations are needed to acquire the correct 3D ADF from its pixel values. Camera effects, such as noise offset and outliers, have to be removed first. Furthermore, to gain comparable results from different measurements, the intensities of the pixels in the images are normalized with their integration time as the used camera has linear time dependency. Here we follow standard procedure, as described in [167]. In case that the light source intensity changes, the pixel intensities need to be normalized once more.

4.3.2.1 Coordinate system

In our transformations and 3D ADF presentations we will refer to the spherical coordinate system as presented in Figure 4.9. Symbol θ denotes the polar angle and φ the azimuth angle. The origin of the spherical coordinate system is set at the illumination point of the laser beam on the sample.

Despite the angular distribution of scattered light being a continuous function in general, a discrete representation of the ADF at the specific angles is widely accepted and applied also in our case. The 3D ADF is here defined as a light intensity in a discrete solid angle $\Delta\Omega = \sin\theta\,\Delta\theta\Delta\varphi$. We measure it at a certain distance from the sample (in the far field region). A solid angle $\Delta\Omega$ at the specific coordinates θ and φ, is also depicted in Figure 4.9. Figure 4.9 (b) presents a hemisphere where lines with constant $\Delta\theta = \Delta\varphi =$

15° are shown. It is noticeable that over the sphere the areas with constant $\Delta\varphi$ and $\Delta\theta$ are different, therefore they have different $\Delta\Omega$. For a valid presentation of the 3D ADF, the $\Delta\Omega$ should remain constant over the sphere. To ensure the same $\Delta\Omega$ at each coordinate, the $\Delta\theta$ should stay the same, but $\Delta\varphi$ has to be weighted with $\sin\theta$ following the solid angle formula.

When presenting the 3D ADF, our discrete spherical coordinate system is defined with the angular step of 1°: θ_i = 0°, 1°, 2°...90° and φ_i = 0°, 1°, 2°...360° to cover the whole (hemi)sphere, while the same $\Delta\Omega_i$ was set with $\Delta\theta = \Delta\varphi =$ 0.5° and appropriate $\sin\theta_i$.

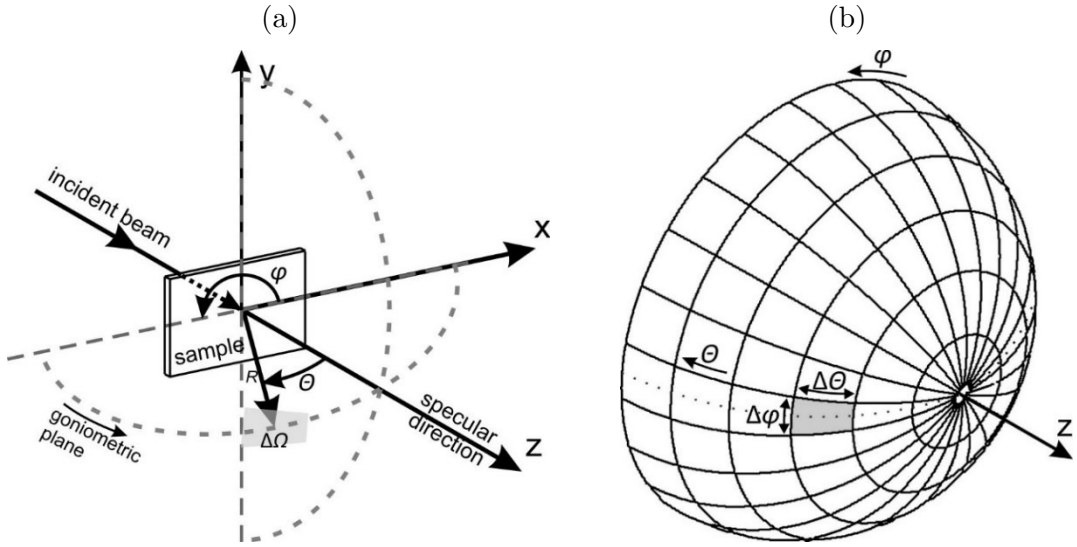

Figure 4.9. (a) Coordinate system for the camera-based system. Spherical and Cartesian coordinates are denoted together with specular direction. A selected solid angle area $\Delta\Omega$ for 3D ADF in transmission is presented. A goniometric plane is drawn for further reference. (b) A hemisphere with lines with constant $\Delta\theta$ and $\Delta\varphi$. Spherical coordinates θ and φ are shown together with z as specular direction. The goniometric plane is presented with a dotted line.

Below we show the image transformation procedure for the transmission case (position T in Figure 4.8). The procedure for reflection, however, is the same, just for the other hemisphere.

4.3.2.2 Angle transformation/determination

The scattered light is projected on the screen that is flat and not hemispherical, therefore same $\Delta\Omega$ cover different areas on the screen for different θ_i and φ_i. The following procedures have to be carried out to ensure that the scattered light intensity at a chosen spherical coordinate corresponds to the same solid angle $\Delta\Omega$ and its projection on the

screen. First, central points of each pixel from the image are positioned in a spherical coordinate system:

$$pixel(m,n) \rightarrow pixel(\theta,\varphi) \tag{4.2}$$

Indices m and n determine lateral and vertical positions in a pixel matrix (m = 1...1040, n = 1...1392, 1.4-Mpixel camera). Second, pixels with central point coordinates within certain $\Delta\Omega$ region are summed. The scattered light intensity in a certain $\Delta\Omega_i$ at a chosen spherical coordinate (θ_i, φ_i) is therefore proportional to the sum of pixel intensities I_{pixel} within the $\Delta\Omega_i$:

$$I'(\theta_i,\varphi_i) = \sum_{\Delta\Omega_i} I_{pixel} = \sum_{\theta_i=\theta_i-\Delta\theta}^{\theta_i+\Delta\theta} \sum_{\varphi_i=\varphi_i-\frac{\Delta\varphi}{\sin\theta_i}}^{\varphi_i+\frac{\Delta\varphi}{\sin\theta_i}} I_{pixel(\theta,\varphi)} \tag{4.3}$$

4.3.2.3 Screen characteristics

It is of a key importance to use highly transmissive and diffusive screens in order to assure sufficiently large signal in the case of the samples with low scattering level. Diffusive nature of the screen enables that each of the illuminated points on the screen directs a portion of light towards the camera. From the transformation point of view, the ideal light scattering distribution of the screen - the ADF of the screen, ADF_{screen} – would be uniform, i.e. equal intensity in all scattering angles and independent on the incident angle of the illumination ray. As this is not the case, the ADF_{screen} has to be known or determined in advance.

Two isotropic diffusive screens were used: a) Opal Diffusing Glass (25x30 cm^2) [173] and b) PLEXIGLAS® (21x30 cm^2) [174]. RTA measurements in a broad wavelength range were conducted for both screens, the results are presented in Figure 4.10 (a) and (b). Both screens have around 30% transmission at λ = 633 nm (later used in measurements), such transmission is sufficient for camera-based measurements. At longer wavelengths, the PLEXIGLAS® has higher transmission, making it more suitable for NIR measurements. Optical losses of transmissive screens are presented by reflected light and internal absorption losses in Figure 4.10 (a) and (b). Low reflection is desired as the reflected light can reach the sample and distort the measurements. This, and the size of the screen, has to be considered when choosing the distance between the sample and the screen.

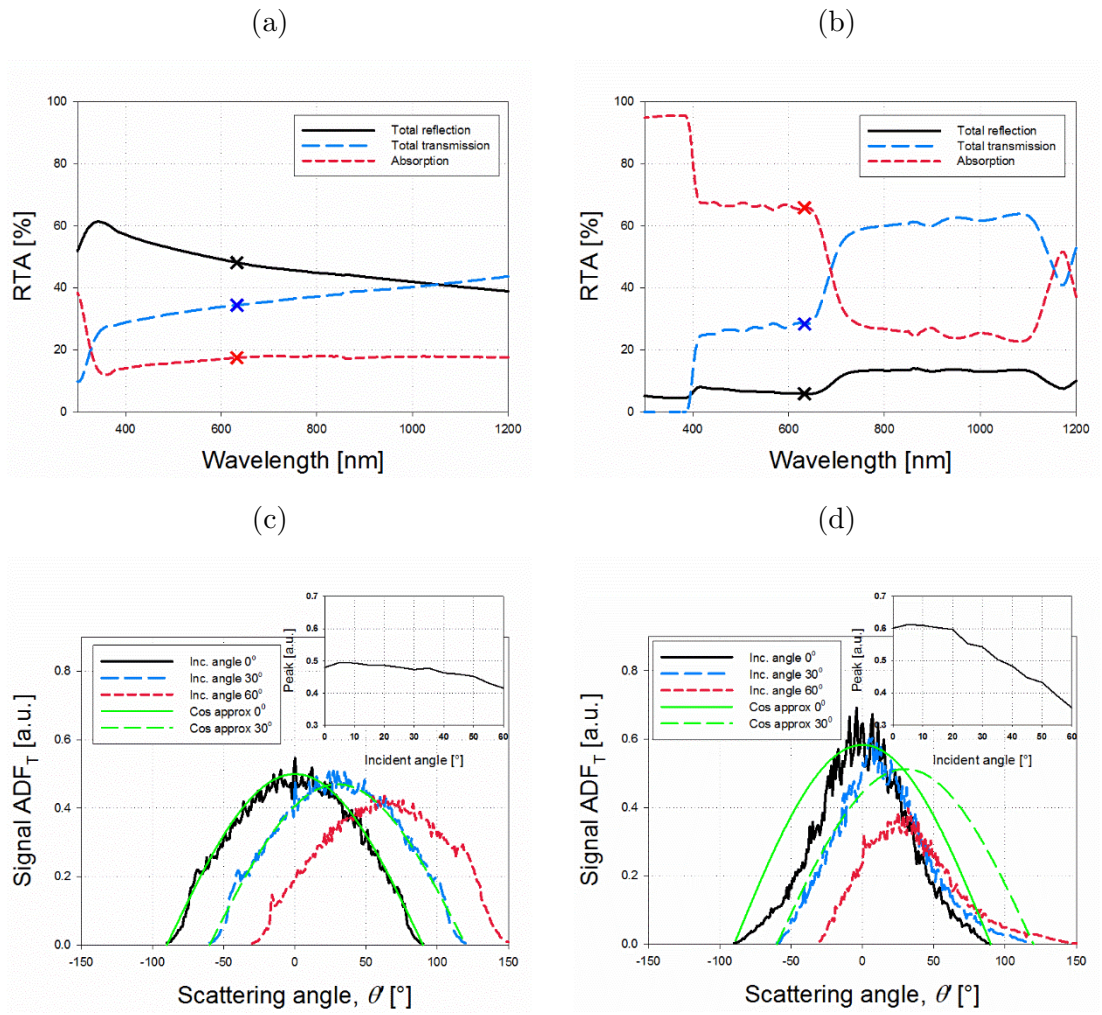

Figure 4.10. RTA measurements of (a) Opal Diffusing Glass and (b) PLEXIGLAS®. Goniometric ARS measurements of ADF_T in a plane at $\lambda = 633$ nm for (c) Opal Diffusing Glass and (d) PLEXIGLAS® at selected incident angles. Cosine approximations for angles 0° and 30° were added. Amplitude peaks (after interpolation) dependent on incident angle for Opal Diffusing Glass and PLEXIGLAS® are also shown as inserts in top right corner in (c) and (d), respectively.

For both screens ADF in transmission $ADF_{Tscreen}$ in a horizontal plane $-90° < \theta' < 90°$ was measured with the goniometric ARS system, isotropy of the screens was assumed. Incident angle of the 633 nm laser beam towards the screen was altered between 0° and 60° with a step of 5° to acquire all the needed data, the results for selected incident angles are presented in Figure 4.10 (c) and (d). Compared to the PLEXIGLAS®, the Opal Diffusing Glass exhibits almost perfect cosine (Lambertian) distribution (the cosine approximation is also plotted as a reference). With increasing incident angle a peak amplitude drops (see inserts top right corner in Figure 4.10 (c) and (d)) and angle shift can be observed.

As shown, different screens have different ADFs, so $ADF_{Tscreen}$ needs to be included in the image processing procedure. First, for each $\Delta\Omega_i$ (summation area) the resulting average incident angle γ_{in} of the scattered rays from the sample to the screen is calculated based on the system configuration. Second, for the same $\Delta\Omega_i$ exiting angle γ_{ex} from the screen towards the camera is also calculated. Both angles are denoted in Figure 4.8. The γ_{in} is used to select the appropriate $ADF_{Tscreen}$ curve while γ_{ex} defines the scattering angle of the screen. The intensity $I'(\theta_i, \varphi_i)$ of each $\Delta\Omega_i$ is then weighted with the obtained value. Finally, the correct scattered light intensity, equal to ADF, is therefore:

$$I(\theta_i, \varphi_i) = ADF(\theta_i, \varphi_i) = I'(\theta_i, \varphi_i)/ADF_{Tscreen}(\gamma_{in_i}(\theta_i, \varphi_i), \gamma_{ex_i}(\theta_i, \varphi_i))$$

The screen thicknesses for Opal diffusing glass and PLEXIGLAS® are 3 and 5 mm, respectively, the refractions inside the screen may exist but are neglected in the calculations. As both screens are commercially available and intended for the general purpose usage, such as rear projection, no polarization effects due to the screens were expected or observed in our system. By putting a polarization filter after the light source or the sample, one is also able to measure the scattered polarized light with the camera-based system [158].

4.3.2.4 Image processing in graphics

As a conclusion to the image processing section, the discussed transformations parameters are graphically shown for system configuration described in the section 4.3.3. Figure 4.11 (a) shows the number of pixels summed per summation area, determined by $\Delta\theta = 0.5°$ and $\Delta\varphi = 0.5°$. The amount increases as we move outwards of the perpendicular direction to the screen, $(\theta, \varphi) = (45°, 180°)$ where the projection of the solid angle area on a (flat) screen surface is the smallest. Just around the origin of the coordinate system, the amount of summed pixels is the highest due to the azimuth angles being so congested (see Figure 4.9 (b) around specular beam). Figure 4.11 (b) shows PLEXIGLAS® screen weight function that can be composed from the $ADF_{Tscreen}$ values. The peak is again at perpendicular incident angle on the screen, $(\theta, \varphi) = (45°, 180°)$, outwards of this peak the value decreases, resulting in a higher value of the ADF after weighting. Both figures show vertical symmetry ($\varphi = 0°, 180°$). The edges of the graphs (colored, signal area) are determined by the camera angle of view (shape of the sensor), defining the range of the single measurement. These matrices are dependent on the system configuration (distances between the elements), camera resolution and screen, not on the sample, and can therefore be considered as a constant for the individual system setup configuration.

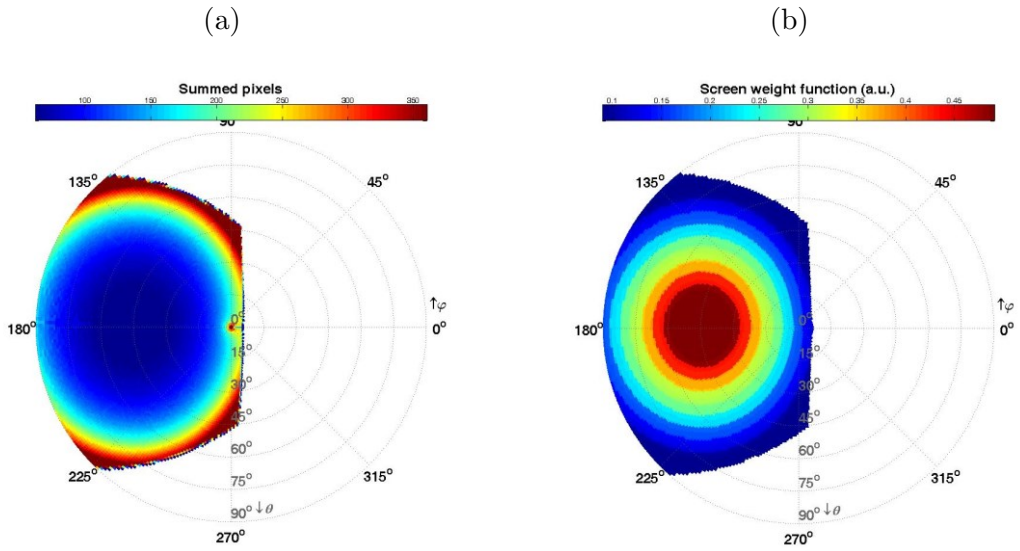

Figure 4.11. (a) Number of summed pixels per summation area (θ_i, φ_i) and (b) screen weight function (θ_i, φ_i) for PLEXIGLAS®.

4.3.2.5 Haze determination

Moreover, besides the determination of the ADF we also tested whether our system can be applied to determine the haze parameter based on the ADF measurements. This requires the measurement of the specular component of the light which presents a challenge and also affects the accuracy of the haze determination procedure [154]. In this section we will show how to calculate it for the case of transmitted light, the same procedure can be followed for the reflected light (substitution T with R, slight sample rotation is needed so that the specular beam can be caught on the screen instead of passing back through the hole). Our approach to the measurements of the specular component will be described in the results section. Haze in transmission is defined as [12]:

$$H_T = \frac{I_{Tdif}}{I_{Ttot}} = \frac{T_{dif}}{T_{tot}} = \frac{T_{dif}}{T_{spec} + T_{dif}} \tag{4.4}$$

where I_{Tdif} and I_{Ttot} are diffuse and total light scattering intensities. When used in a ratio we can describe haze with diffuse and total (T_{dif} and T_{tot}) transmittance, where T_{tot} consists of diffuse and specular (T_{spec}) part. This means measurements with the camera must be in our system performed without a blocking pin on screen to capture the specular part. However, camera saturation must be avoided (see section 4.3.3.2). The values for T_{dif} and T_{tot} are in general obtained by integrating the diffuse and specular light over the hemisphere [154]:

$$T_{dif} = \int_{\theta_i+1}^{90°} \int_{0}^{360°} ADF(\theta,\varphi) \sin\theta \, d\theta d\varphi \tag{4.5}$$

$$T_{tot} = \int_{0}^{\theta_i} \int_{0}^{360°} ADF(\theta,\varphi) \sin\theta \, d\theta d\varphi \tag{4.6}$$

The symbol θ_i denotes the boundary angle between the specular and diffuse part. In case of light scattering by isotropic sample, the azimuth component can be neglected and the integrals can be simplified into following auxiliary equations:

$$ADF_{3D}(\theta) = 2\pi * ADF_{1D}(\theta) * (\cos(\theta - \Delta\theta) - \cos(\theta + \Delta\theta)) \tag{4.7}$$

$$SBV = \pi\Delta\theta^2 * \sum_{0}^{360°} ADF(0,\varphi) \tag{4.8}$$

ADF_{1D} is the average line and is extracted by averaging the 3D ADF for each θ through all φ that we measured with the system. ADF_{1D} is then transformed to ADF_{3D} where we expand the line over the whole hemisphere [12]. $\Delta\theta$ was set at 0.5°. Specular beam value (SBV, $\theta = 0°$) in ADF_{3D} is 0 because of the cosine part, therefore we calculate SBV by summing all the azimuth values for polar angle $\theta = 0°$ and weighting it with the solid angle a beam with $2^* \Delta\theta = 1°$ would cover. The specular and diffuse component are then calculated as following:

$$T_{dif} = \sum_{\theta=\theta_{i+1}}^{90°} ADF_{3D}(\theta) \tag{4.9}$$

$$T_{spec} = SBV + \sum_{\theta=1}^{\theta_i} ADF_{3D}(\theta) \tag{4.10}$$

4.3.3 *Results and discussion*

The applicability of the presented system is demonstrated on two different light scattering samples: for transmittance measurements we selected a textured transparent conductive oxide (TCO), used as a substrate in thin-film solar cells, and for reflectance a periodically textured silicon sample. The SEM images of the tested samples are shown in Figure 4.12.

(a) (b)

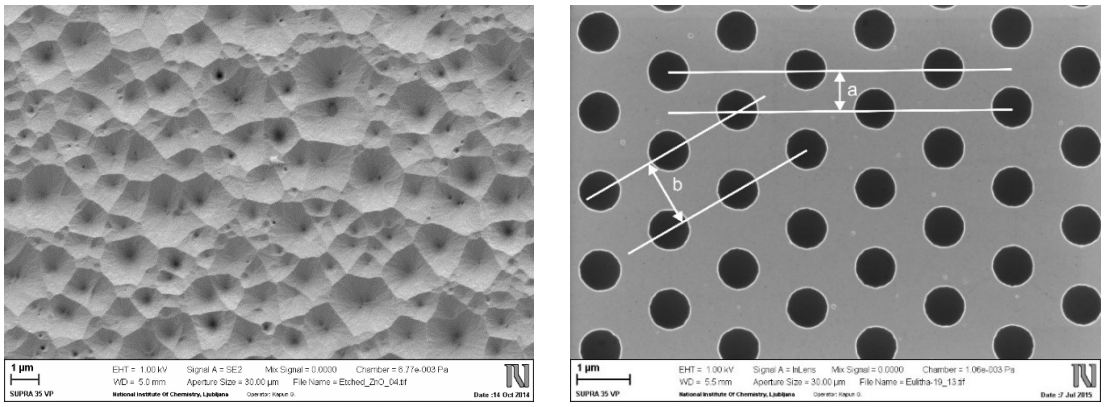

Figure 4.12. SEM/AFM images of (a) textured TCO - magnetron sputtered ZnO:Al, etched in HCl for 30 seconds and (b) for periodic hexagonal hole array with a period of 1500 nm and depth of 550 nm on silicon substrate. Main planes of the sample are drawn for further reference (a = 750 nm and b = 1299 nm).

4.3.3.1 3D angular distribution function

For the measurements presented below, the distance between the sample and the screen was set to 11.4 cm in specular direction (direction of the laser beam) to avoid strong reflection relation between the screen and the sample. The distance between the screen and the camera was 35.7 cm so that all polar angles could be captured with our camera. HeNe gas laser with a $\lambda =$ 633 nm and P = 10 mW was used in the measurements. Other lasers/wavelengths can also be used, with screen characteristics

(a) (b)

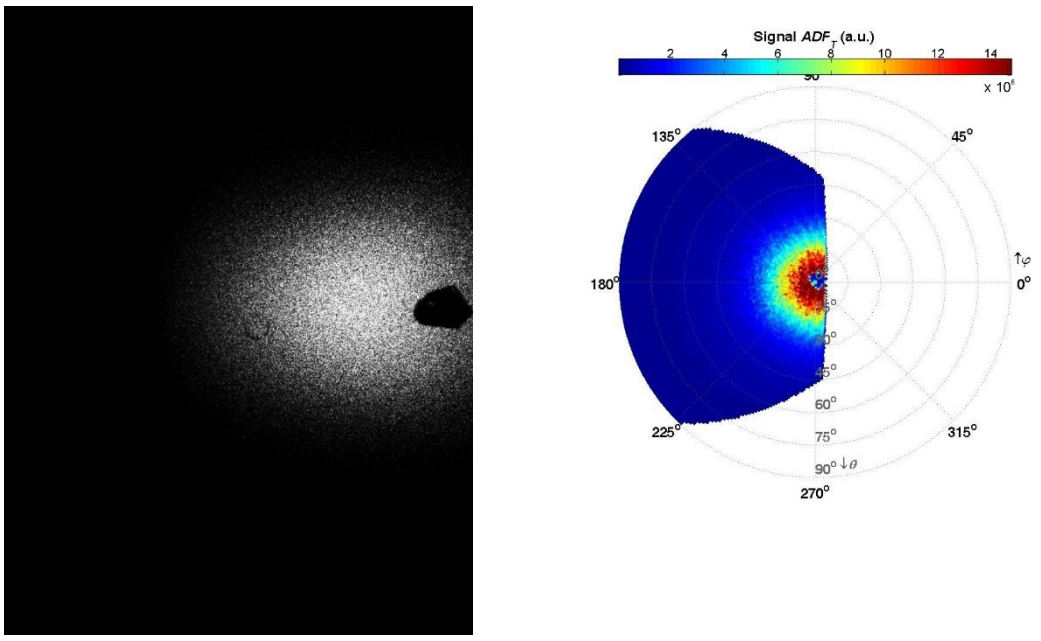

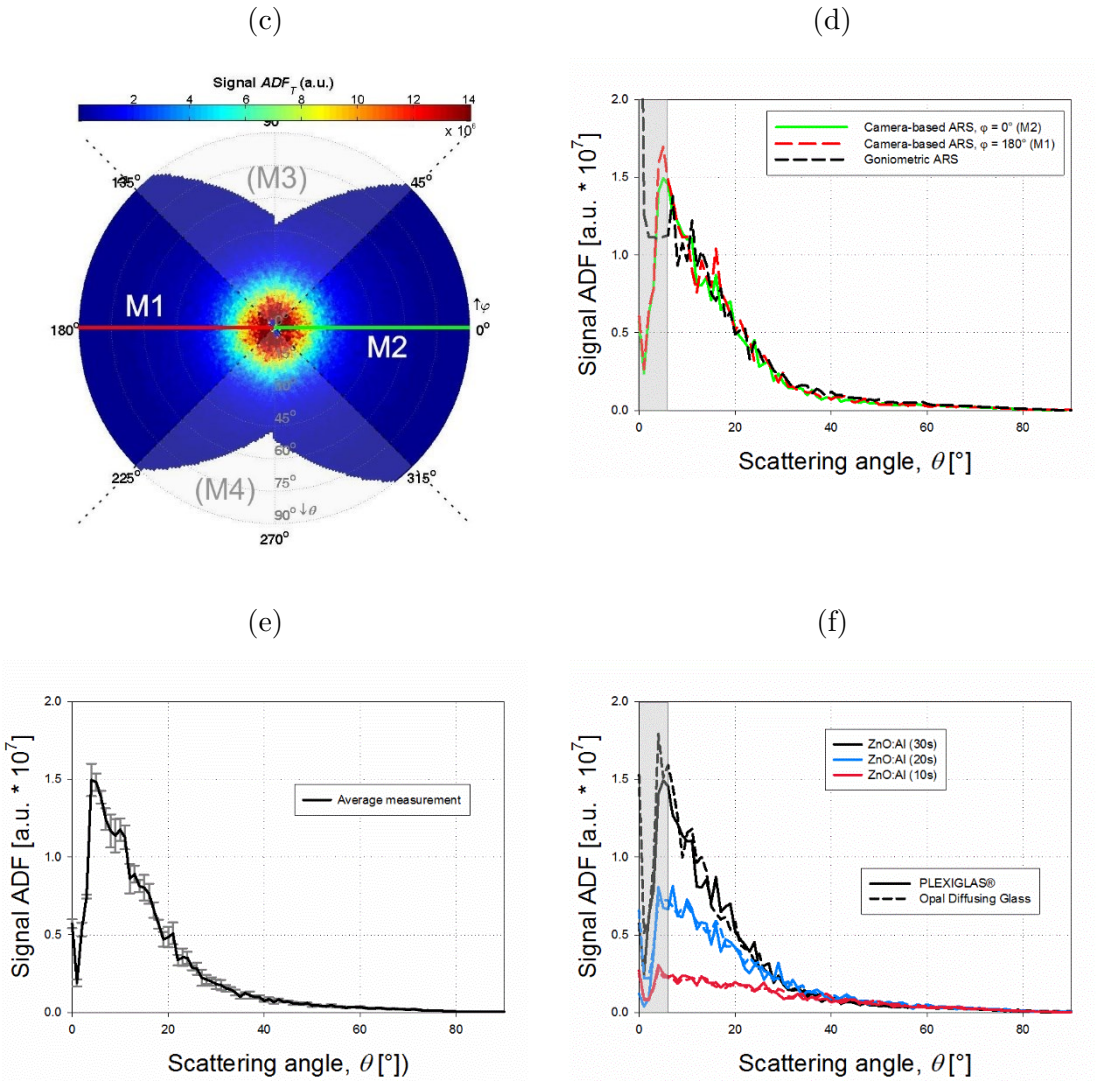

Figure 4.13. Transmittance measurement results for ZnO:Al, etched in HCl for 30 seconds, for λ = 633 nm with PLEXIGLAS® as a screen: (a) image from the camera, (b) measured 3D ADF_T, single measurement M1 (c) 2 measurements M1+M2 combined where the sample was rotated for 180°. (d) Comparison between camera-based ARS and goniometric ARS. Red and green solid lines from (c) match those in (d). (e) Average line scan and standard uncertainty at each polar angle for the selected sample obtained from 12 measurements with PLEXIGLAS® as a screen. Comparison between the measurement results with both screens for three different TCO samples. The grey areas in (d), (e) and (f) show where the error due to the blocking pin and spike just after it is.

($ADF_{Tscreen}$) accordingly applied. The samples were perpendicularly illuminated. Normally, camera integration time varies between 0.5 and 2 seconds, depending on scattering abilities of the sample, the power of the laser and the screen used. All the images are therefore time normalized to gain comparative results.

First, we show the result of 3D ADF_T for magnetron sputtered ZnO:Al, etched in HCl for 30 seconds, exhibiting crater like random texturization with vertical root-mean-

square roughness of around 110 nm [14]. PLEXIGLAS® was used as a screen here. Figure 4.13 (a) shows raw image as captured with the camera before any processing, camera integration time was $t = 0.25$ s. Quasi-elliptic bright area and dark black spot, where the pin blocks the specular beam, can be observed. After applying the transformations described in section 4.3.2 an expected circular pattern (rotationally symmetric isotropic scattering) is acquired (Figure 4.13 (b)). A much lower signal at the position of the specular beam (0, 0) is a result of a pin blocking the specular beam. This figure also shows the available range of the single measurement (M1) of the setup for the selected distances between the elements, which is $0° < \theta < 90°$ and approximately $130° < \varphi < 230°$. Confined by the rectangular shape of the camera sensor (before the image processing), the polar angles increase from 45° at $\varphi = 90°$ (270°) to 90° at $\varphi = 130°$ (230°).

Greater angular range can be obtained by e.g. one additional measurement by rotating the sample for 180° (M2) and recapturing the screen image with the camera; this is presented in Figure 4.13 (c). This way with our setup only a minor part of the hemisphere was not measured (white/light grey area in Figure 4.13 (c)), but could be fully measured by additional rotation of the sample by 90° (M3) and 270° (M4). The lines denote the range of the individual measurement (M1, M2, M3 and M4) if all four measurements would have been performed. Nevertheless, rotational symmetry in the 3D ADF of the sample can clearly be observed with two and even one measurement. To validate the system, conventional goniometric ARS system was used as a reference, where the scattering in a selected plane (denoted in Figure 4.9) perpendicular to the sample is measured. A scan from such measurement was compared with line scans at $\varphi = 180°$ (M1) and $\varphi = 0°$ (M2) from 3D ADF_T and shown in Figure 4.13 (d). Besides the differences around angle 0° due to the blocking pin and the spike just after (the area where greater error appears was marked grey in Figure 4.13 (d), (e) and (f)), good matching between both measurements is obtained. While the matching is not 100%, it is more than sufficient for the inspection systems in photovoltaics where fast throughput often prevails over accuracy.

For the selected sample and PLEXIGLAS® as a screen, we also investigated the uncertainty of the measurements. 12 measurements were carried out under the same conditions, from which the average value and standard deviation at each scattering angle were calculated. The standard deviation was then used as a standard uncertainty. The results are shown in Figure 4.13 (e). The average values are presented as an ADF curve and the standard uncertainty with error bars. We can conclude good repeatability and

low standard uncertainty of the measurement system, which combined with the obtained good matching validates the system.

To compare the performance of the two analyzed screens, the light scattering from three ZnO:Al samples with different etching times (30 s, 20 s and 10 s, σ_{RMS} values 110 nm, 90 nm and 50 nm, respectively) was measured using both screens. The line scans from the obtained 3D ADF_T are compared in Figure 4.13 (f). Measurements with both screens result in very similar ADFs, making them both suitable for the ADF measurements if their characteristics are accordingly applied.

Second, reflection measurements will be presented on a case of a periodic hexagonal hole array on silicon substrate with a period of 1500 nm and depth of 550 nm (commercially available sample [175]). The system was also successfully calibrated by linear 1D gratings. However, compared to periodic 1D gratings, periodic samples with 2D hexagonal grating scatter light not only in one plane but in space. This makes them perfect candidates to show the advantage of the camera-based 3D measurement system which enables us detecting multiple spatially distributed modes with a single measurement. Following the diffraction grating equation, different modes at different polar angles can be calculated for the selected sample (Table 4.5).

Table 4.5. Calculated modes for hexagonal hole array with a period of 1500 nm for $\lambda = 633$ nm.

Mode order	Effective period, d (nm)	Notation on Figure 4.12 (b)	Mode angle, θ (°)
1	1500/2=750	a	57.57
1	1500*$\sqrt{3}$/2 =1299	b	29.16
2	1500*$\sqrt{3}$/2=1299	b	77.05

The mode angles for the inspected sample were calculated using the diffraction grating equation [176]:

$$\theta = \arcsin\frac{m\lambda}{d} \tag{4.11}$$

Symbol θ denotes the scattering mode angle, m is the mode order, d is the period or as is the case with 2D gratings, the effective period as the distance between the planes rather than the period has to be considered. Two main effective periods, a and b shown

schematically on SEM image in Figure 4.12 (b) with corresponding planes, were used in calculations. Incident wavelength $\lambda = 633$ nm in air was assumed.

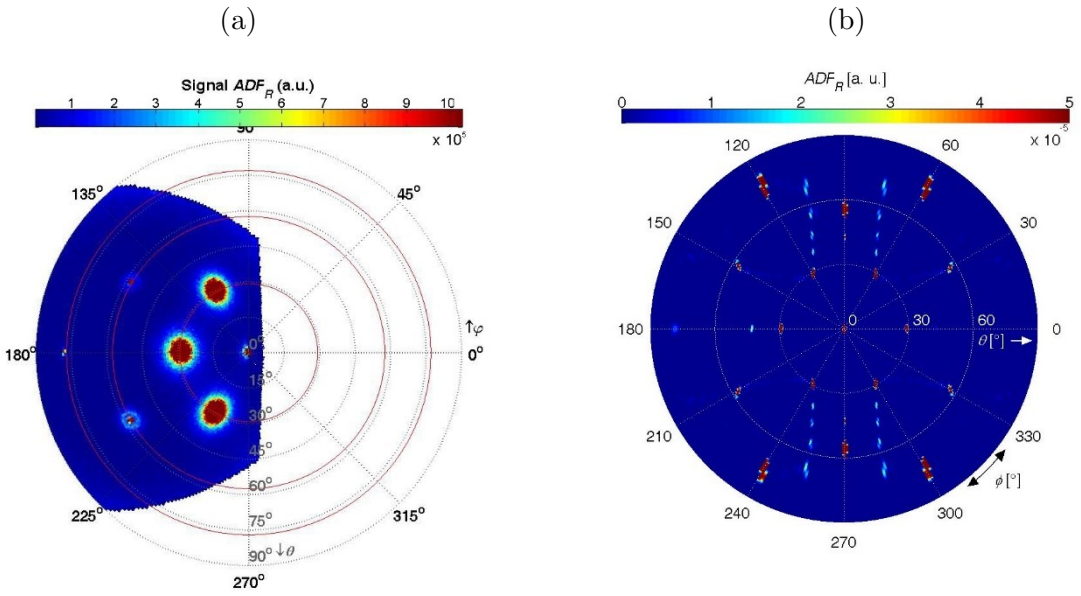

Figure 4.14. Reflectance of hexagonal hole array (period 1500 nm) for $\lambda = 633$ nm: (a) measured 3D ADF_R and (b) simulated 3D ADF_R. Opal Diffusing Glass was used as a screen, $t = 0.1$ s. In figure (a) red lines with θ as calculated in Table 4.5 were added to the plot for validation.

Figure 4.14 (a) shows the measured 3D ADF_R of the periodic sample. Opal Diffusing Glass was used as a screen, camera integration time was $t = 0.1$ s. The measured modes are in good agreement with the calculated modes – the red lines with θ as calculated in Table 4.5 were added to the plot. In addition, for this sample we simulated the 3D ADF_R using combined FEM (finite element method) and Huygens expansion approach [177], providing the additional validation of the system (Figure 4.14 (b)).

As previously mentioned, all the measurements were carried out under perpendicular illumination. With presented camera-based system, light scattering at different non-perpendicular illumination angles can also be measured. Since the non-perpendicular illumination will most likely cause asymmetrical ADF pattern, both sides have to be measured rather than rotating the sample. Therefore, the screen and/or camera have to be placed on the other side (rotated for 90° - manually or by rotating arm), with the camera looking perpendicularly at the screen and the screen angle being 45° at the sample at any illumination angle.

4.3.3.2 ***Haze***

As a proof of concept, we present the haze obtained with our system for the three above mentioned ZnO:Al samples with different etching times (30 s, 20 s and 10 s), resulting in different hazes. PLEXIGLAS® was used as a screen for all the haze measurements. The diffuse part was measured exactly as described above in section 4.3.2 (normal, single measurement, t = 250 ms). Specular part, however, required additional measurements due to strong specular component. The specular beam can exceed the scattered light intensity by a few decades depending on the scattering abilities of the sample and would in normal (ADF) measurement cause saturation of the camera. Therefore, multiple images are needed to gradually measure the specular beam - the peak itself and the small area just around the peak. This way we get the signal to fill the black spot caused by the pin (see Figure 4.13 (a)) and obtain the correct value of the specular beam. If the used camera has higher resolution as ours (16-bit), single measurement may be sufficient.

The additional measurements of the specular part were performed without the blocking pin, but with an attenuation filter with 9.12% transmission at 633 nm and decreasing integration times of the camera (250 ms, 50 ms, 1 ms and 0.5 ms) to prevent camera saturation. All images were normalized with camera integration time and composed together. After the new full image was acquired, the haze was determined as explained in section 4.3.2.5. Following the results shown in Figure 4.13, rotational symmetry was assumed for all three samples. Simplified equations for average line scan were correspondingly applied. The boundary angle θ_i was set to 4°, corresponding to the opening size in the integrating sphere.

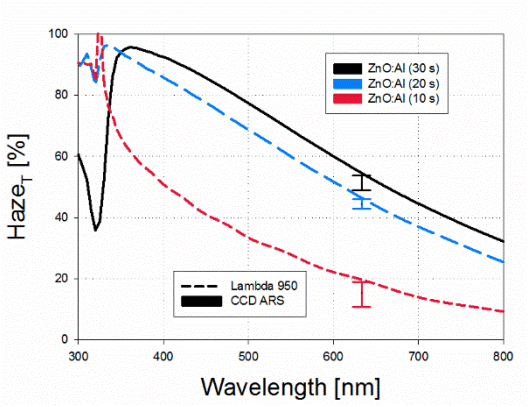

Figure 4.15. Haze curve obtained with Lambda 950. Measerument results obtained with camera-based system are added at λ = 633 nm.

The haze results obtained from camera-based measurements were compared with measurements done with spectrophotometer Lambda 950 and are shown in Figure 4.15. The haze scans with Lambda 950 were done in a broad wavelength range, while the camera-based haze determination was carried out at the selected wavelength $\lambda = 633$ nm. 3 camera-based haze measurements were done for each sample, allowing us to also plot the error bar. The comparison shows moderate matching, with the highest discrepancies for the third sample (red color). The system is primarily built for the determination of light scattering – diffuse part, ADF – for which it shows good accuracy. The main error in haze determination, however, is caused by the specular part. This could be due to the laser instability combined with extremely short camera integration times (0.5 – 1 ms). Even small errors can escalate when they are normalized by a couple of decades different factors. Still, the results are good enough for the haze estimation. As mentioned above, they could be improved by using a camera with higher resolution.

4.3.4 Conclusion

The described camera-based ARS system using a transmittive screen enables fast and accurate measurements of light scattering properties of textured surfaces and light emitting devices with a single shot in a 3D space in broad angular range in a few seconds. We presented the solution which can be used for measurements of reflected or transmitted scattered or emitted light. The tilted screen position allows us to measure full polar range at the cost of the limited azimuthal range. However, with appropriate (automatic) rotation of the sample scattered light in full sphere can be obtained. Additionally, the system was also applied to the determination of haze parameter at the wavelength of the laser light.

Measurements of two types of scattering samples were presented. Randomly textured ZnO:Al was used to show, how to acquire full sphere 3D *ADF* by rotating the sample. Characterization of periodically textured silicon substrate was used to demonstrate the advantage of using spatial (camera-based) systems instead of conventional goniometric systems. With one measurement we were able to detect all the modes of the periodic sample in the angular range of the measurement. Goniometric system, together with simulations, was used for validation of the newly developed system. Comparison with other methods showed good matching.

4.4 Summary

In this chapter, we presented 2 camera-based light scattering measurement systems. Compared to the conventional goniometric systems, the described camera-based ARS systems enable fast and sufficiently accurate measurements of light scattering properties of textured surfaces and light emitting devices with a single shot in a 3D space in broad angular range within a few seconds. Both systems were described along with all the transformations needed to extract the 3D ADF.

The first system is based on a reflective screen and uses a lens to broaden the range of the measurement. The system was tested on three TCO samples and a reference light source. All the necessary transformations were explained and sensitivity analysis was also carried out. The results show good matching with the results obtained with the conventional ARS system. The range of the presented system can be extended by using a camera lens with a wider angle of view. The resolution of the system can also be simply improved by using a CCD camera with a higher resolution.

The second system is based on a transmissive screen and can be used for measurements of reflected or transmitted scattered or emitted light. The tilted screen position allows us to measure the full polar range at the cost of the limited azimuthal range. However, with the appropriate (automatic) rotation of the sample, scattered light in a full sphere can be obtained. Additionally, the system was also applied to the determination of the haze parameter at the wavelength of the laser light. Measurements of two types of scattering samples were presented. Randomly textured ZnO:Al was used to show how to acquire a full sphere 3D ADF by rotating the sample. The characterization of a periodically textured silicon substrate was used to demonstrate the advantage of using spatial (camera-based) systems instead of conventional goniometric systems. With one measurement we were able to detect all the modes of the periodic sample in the angular range of the measurement. The goniometric system, together with simulations, was used for validating the newly developed system. The comparison with other methods showed good matching.

The developed camera-based ARS systems are powerful tools for the characterization of a versatile set of different samples or illuminating devices, or as inspection tools inthe high throughput industrial production. Randomly, periodically and quasi-periodically textured samples or light sources, such as LEDs, can be characterized accurately and in a very short time (seconds). The 3D ADF of the scattered light or the

luminous intensity distribution of light sources can be easily determined with only one measurement, whereas with a conventional line-scan ARS system several time-consuming measurements are required.

5 Conclusions and outlook

5.1 General conclusion

Light management is an effective way of improving the photovoltaic device performance, either through reduced reflection (anti-reflection effect) or light scattering. The anti-reflection increases the light in-coupling, while scattered light has a longer optical path in the active layer; consequently, a higher amount of photons is absorbed. Commonly, light management is induced by (nano-, micro-) textured surfaces which cause both anti-reflection and light scattering. In the dissertation, we focused on the fabrication and the characterization of the textures for light management in photovoltaic devices. The content of the dissertation was divided into three main chapters that cover three topics – UV Nanoimprint Lithography (UV NIL) as a tool for creation of (replicated) textures, perovskite solar cells as photovoltaic devices, to which light management foil has been applied, and camera-based systems for light scattering measurement as a characterization technique.

In the second chapter, we presented how to create textures that can be integrated into a device structure. For that, we utilized UV NIL which is a replication process of a surface texture from a master via stamp to the final substrate (replica). This way it is possible to simplify the introduction of textured surfaces into a device structure. The texture is created from a transparent polymer lacquer which enables us to implement textures that can otherwise only be made on non-transparent substrates. However, the UV NIL process is applicable only up to 200 °C. The replication process is simple and fast which significantly shortens the time and costs of texture creation, since from one expensive master lots of cheap and high-fidelity replicas can be created.

The transmittance and the AFM measurements were used to analyze the created replicas. To speed up the analysis of the AFM measurements, a software "AFM analyzer" was developed and its functionalities were described. Measurements confirmed a good

transfer fidelity, even after multiple use of a stamp, and a thermal stability up to 200 °C. However, longer exposure to 200 °C already causes yellowing effect. Both options, the replica inside and outside the device in superstrate configuration, were looked into. Outdoor testing revealed moderate durability of the lacquers used. The texture roughness was in general preserved, however, a lot of particles stuck firmly on the surface and the heat slightly melted the texture. This resulted in a lower diffuse transmittance. Another downside was the yellowing effect that reduced the transmittance and scattering in the UV-blue wavelength range. However, the electrical measurements of the perovskite solar cells using a textured UV NIL layer as a light management (LM) foil showed an improvement in short-circuit current density. As the replicas can also be used as a scattering layer inside the device, we deposited a transparent conductive oxide GITO on top of the replica. Measurements showed a moderate sheet resistance, good transmission and conformal growth, with no damage done to the texture or its smoothening due to the sputtering and annealing of GITO. The results demonstrate the suitability of the replicas for further use in photovoltaic devices. However, to exploit the LM foil benefits for a longer time, lacquers with a more stable chemical composition that do not yellow are needed.

In the third chapter, a new class of photovoltaic devices was presented, namely the perovskite solar cells. The perovskites, as an absorber material, gained popularity due to their excellent optical and electrical properties that resulted in an unprecedented rise in efficiency, reaching 22.1% in 2016. Since the light management in the perovskite solar cells has not been extensively researched yet, we chose them as the photovoltaic devices in our research.

We started by describing the perovskite crystal material characteristics and the optical and electrical properties. We introduced perovskite single junction and tandem devices. Special focus was put on single junction devices based on PTAA as a hole transport material (HTM). The experimental fabrication was presented in detail. The hypophosphorous acid (HPA) was studied as an additive to perovskite for a better film formation. The morphology was improved; however, the electrical performance stayed largely the same, regardless of HPA. Both devices, without and with HPA, performed well and reached high conversion efficiencies under STC above 15%.

Using UV NIL, an LM foil with a random pyramid texture was created in attempt to further improve device performance and also test the suitability of UV NIL replicas as LM foils on top of the front glass side. Promising results were obtained for two planar device designs, one with PTAA and one with PEDOT:PSS as HTM. In both cases the reflection was drastically reduced. However, the absorption increase in the active layer was lower than expected. This was attributed to refracted light escaping the device before reaching the active layer.

To confirm the light escaping assumption, in the third part of the chapter we studied fabricated devices using optical simulations. The optical model and the input parameters were first validated by a good match between the simulations and the experiments. The results indeed confirmed that small area devices, like our fabricated ones, suffer from light escaping when the LM foil is applied. Detailed simulations revealed that a relative boost in photocurrent of ca. 10% relative is feasible for large area devices. The results confirmed that by using textures, the planar devices can be drastically improved. Optical simulations were also used to study perovskite/silicon-heterojunction tandem devices. Different configurations were tested. Derived from the planar device, devices built on a back-side and both-side textured Si wafer were analyzed. The latter can achieve a 15% relative higher efficiency. Applied on the planar device, the LM foil with different textures was also simulated, showing positive results. Both the experiments and the simulations showed an improved device performance when using a LM foil with any texture. Therefore, we recommend using textured LM foils in perovskite solar cell devices.

Textured surfaces can be characterized by different characterization techniques. Since the main role of the texture is to reduce the reflection and prolong the optical path in the active layer, light scattering and its angular distribution are some of the most important and telling properties of the texture. The conventional way of determining the angular distribution function (ADF) of the scattered light is the goniometric measurement which is very time-consuming and measures the ADF in one plane only. To counter these two problems, we focused on the development of a camera-based system. In the camera-based system, the scattered light is projected on the screen and then captured with a digital camera. In the fourth chapter, we present two solutions, one based on a reflective screen and one on a transmissive. The system with a reflective screen uses a lens to widen the angular range of the measurement. In the system with a

transmissive screen, the wide angular range was reached by positioning the screen at 45°. The tilted screen position allows us to measure the full polar range at the cost of the limited azimuthal range, which is solved by taking multiple images. Both described camera-based ARS systems enable fast and accurate measurements of light scattering properties of textured surfaces and light emitting devices with a single shot in a 3D space in a broad angular range in a few seconds, providing a clear advantage over the goniometric systems.

The two camera-based systems were validated using the goniometric system. A good match between all the systems was obtained when analyzing textured TCOs and silicon substrates. The developed system, based on a transmissive screen, was then used to characterize the UV NIL replicas but can also be used for the characterization of light sources. Since the camera-based systems are fast and sufficiently accurate, they are suitable for industrial inspection.

5.2 Outlook for future research

Throughout the dissertation the focus was on textured surfaces for light management in photovoltaic devices. Experimentally, only the random crater-like texture from etched ZnO:Al and the randomly distributed pyramids from etched silicon wafer were analyzed. This leaves us with lots of other textures, both random and periodic, that can be tested in practical applications. Some of them have already been analyzed using optical simulations and showed better performance than randomly distributed pyramids from silicon wafer. We have also shown that the UV Nanoimprint Lithography is a compatible and suitable process of implementing the texture into the device structure as an LM foil, either as a top anti-reflection foil or inside as a scattering layer. Providing there is a master, any texture can be replicated and simulations can be used as a predictive tool. If integrated in a device, simulated results can be experimentally confirmed.

The field of perovskite solar cells also offers plenty of possibilities. The device fabrication can be improved by trying different hole and electron transport materials and by optimizing perovskite conversion. New materials and techniques could lead not only to higher conversion efficiencies but also to an improved stability and repeatability of the fabrication process. The optical simulations can serve as a tool to find the best performing texture. The validated optical model can be used to optimize the single

junction and tandem devices, with and without textures. Especially for the tandem devices there is still a lot of optimization to be done and optical simulations can be an indispensable tool when designing a device structure or analyzing its performance.

5.3 List of publications

5.3.1 Journal publications

Results obtained during my Ph.D. training are presented in two original scientific papers published in international journals with impact factor:

- JOŠT, Marko, KRČ, Janez, TOPIČ, Marko. "Camera-based angular resolved spectroscopy system for spatial measurements of scattered light," *Applied Optics*, vol. 53, no. 21, p. 4795, Jul. 2014 [143]
- JOŠT, Marko, KRČ, Janez, TOPIČ, Marko. "Camera-based ARS system for complete light scattering determination/characterization," *Measurement Science and Technology*, vol. 27, no. 3, p. 035202, Mar. 2016 [144]
- JOŠT, Marko, ALBRECHT, Steve, KEGELMANN, Lukas, WOLFF, Christian M., LANG, Felix, LIPOVŠEK, Benjamin, KRČ, Janez, KORTE, Lars, NEHER, Dieter, RECH, Bernd, TOPIČ, Marko "Efficient Light Management by Textured Nanoimprinted Layers for Perovskite Solar Cells", submitted to ACS Photonics [57]

Additionally, some of the contributions were published in peer-reviewed journals without impact factor or in conference proceedings:

- TOPIČ, Marko, JOŠT, Marko, SEVER, Martin, FILIPIČ, Miha, LOKAR, Žiga, LIPOVŠEK, Benjamin, ČAMPA, Andrej, KRČ, Janez. "Design challenges for light harvesting in photovoltaic devices," in *Proc. SPIE*, 2016, vol. 9898, p. 98980D–98980D–7 [178]
- JOŠT, Marko, TOPIČ, Marko. "Efficiency limits in photovoltaics: Case of single junction solar cells," *Facta universitatis - series: Electronics and Energetics*, vol. 27, no. 4, pp. 631–638, 2014 [5]
- JOŠT, Marko, ALBRECHT, Steve, LIPOVŠEK, Benjamin, KRČ, Janez, KORTE, Lars, RECH, Bernd, TOPIČ, Marko "Back- and Front-side Texturing for Light-management in Perovskite / Silicon-heterojunction Tandem Solar Cells," Energy Procedia, vol. 102, pp. 43–48, Dec. 2016 [58]

5.3.2 Conference proceedings

Results of the dissertation were presented at international conferences:

- European Photovoltaic Solar Energy Conference
    - 2015: 3D camera-based system for measurements of scattered or emitted light [179]
- European Materials Research Society Meeting
    - 2016: Back- and front-side texturing for light-management in perovskite / silicon-heterojunction tandem solar cells [58]
- International Conference on Microelectronics, Devices and Materials
    - 2013: Camera-based measurement of light scattering intensity distribution [180]
    - 2014: UV nanoimprint lithography for replication of textured surfaces in thin-film photovoltaics [181]
    - 2015: Nanoimprinted textures on glass as a substrate for GITO deposition [182]
    - 2016: Hypophosphorous acid as an additive for inverted perovskite solar cells [183]

5.4 Original scientific contributions

The summarized original scientific contributions of the dissertation are:

- AFM analyzer with key roughness parameters of micro- and nanotextures,
- Improved light management in perovskite solar cells using light management foil based on validated optical models and simulations,
- Camera-based system for measurements of light-scattering in transmission using lens and reflective screen including transformation model with calibration procedure for wide angles ,
- Camera-based system for combined measurements of light scattering in transmission and reflection using transmissive screen including transformation formalism and calibration procedure for full sphere scattering characterization.

References

[1] "Solargis :: iMaps." [Online]. Available: https://solargis.info/imaps/#. [Accessed: 22-Feb-2017].

[2] "IPCC - SRREN." [Online]. Available: http://www.ipcc.ch/report/srren/. [Accessed: 22-Feb-2017].

[3] "Renewable Energy Data - Fraunhofer ISE," *Fraunhofer Institute for Solar Energy Systems ISE*. [Online]. Available: http://www.ise.fraunhofer.de/en/renewable-energy-data.html. [Accessed: 22-Feb-2017].

[4] W. Shockley and H. J. Queisser, "Detailed Balance Limit of Efficiency of p-n Junction Solar Cells," *Journal of Applied Physics*, vol. 32, no. 3, pp. 510–519, Mar. 1961.

[5] M. Jošt and M. Topič, "Efficiency limits in photovoltaics: Case of single junction solar cells," *Facta universitatis - series: Electronics and Energetics*, vol. 27, no. 4, pp. 631–638, 2014.

[6] "efficiency_chart.jpg (4349×2456)." [Online]. Available: http://www.nrel.gov/ncpv/images/efficiency_chart.jpg. [Accessed: 16-Jun-2016].

[7] "Tesla Solar." [Online]. Available: https://www.tesla.com/solar. [Accessed: 15-Nov-2016].

[8] A. Shah, *Thin-Film Silicon Solar Cells*. EPFL Press, 2010.

[9] J. Springer, B. Rech, W. Reetz, J. Müller, and M. Vanecek, "Light trapping and optical losses in microcrystalline silicon pin solar cells deposited on surface-textured glass/ZnO substrates," *Solar Energy Materials and Solar Cells*, vol. 85, no. 1, pp. 1–11, Jan. 2005.

[10] J. Müller, B. Rech, J. Springer, and M. Vanecek, "TCO and light trapping in silicon thin film solar cells," *Solar Energy*, vol. 77, no. 6, pp. 917–930, Dec. 2004.

[11] P. Beckmann and A. Spizzichino, "The scattering of electromagnetic waves from rough surfaces," *Norwood, MA, Artech House, Inc., 1987, 511 p.*, vol. 1, 1987.

[12] J. Krč and M. Topič, *Optical Modeling and Simulation of Thin-Film Photovoltaic Devices*. CRC Press, 2013.

[13] C. Battaglia, A. Cuevas, and S. D. Wolf, "High-efficiency crystalline silicon solar cells: status and perspectives," *Energy Environ. Sci.*, vol. 9, no. 5, pp. 1552–1576, May 2016.

[14] O. Kluth *et al.*, "Texture etched ZnO:Al coated glass substrates for silicon based thin film solar cells," *Thin Solid Films*, vol. 351, no. 1–2, pp. 247–253, Aug. 1999.

[15] S. Y. Chou, P. R. Krauss, and P. J. Renstrom, "Nanoimprint lithography," *Journal of Vacuum Science & Technology B*, vol. 14, no. 6, pp. 4129–4133, Nov. 1996.

[16] C. Battaglia *et al.*, "Efficient light management scheme for thin film silicon solar cells via transparent random nanostructures fabricated by nanoimprinting," *Applied Physics Letters*, vol. 96, no. 21, p. 213504, May 2010.

[17] J. Escarré, K. Söderström, C. Battaglia, F.-J. Haug, and C. Ballif, "High fidelity transfer of nanometric random textures by UV embossing for thin film solar cells applications," *Solar Energy Materials and Solar Cells*, vol. 95, no. 3, pp. 881–886, Mar. 2011.

[18] M. Meier, U. W. Paetzold, M. Prömpers, T. Merdzhanova, R. Carius, and A. Gordijn, "UV nanoimprint for the replication of etched ZnO:Al textures applied in thin-film silicon solar cells," *Prog. Photovolt: Res. Appl.*, vol. 22, no. 12, pp. 1226–1236, Dec. 2014.

[19] C. Battaglia *et al.*, "Nanoimprint Lithography for High-Efficiency Thin-Film Silicon Solar Cells," *Nano Lett.*, vol. 11, no. 2, pp. 661–665, Feb. 2011.

[20] H. K. Raut *et al.*, "Multiscale Ommatidial Arrays with Broadband and Omnidirectional Antireflection and Antifogging Properties by Sacrificial Layer Mediated Nanoimprinting," *ACS Nano*, vol. 9, no. 2, pp. 1305–1314, Feb. 2015.

[21] N. B. Abu Talip[a]Yusof and J. Taniguchi, "Fabrication of self-supporting antireflection-structured film by UV–NIL," *Microelectronic Engineering*, vol. 110, pp. 163–166, Oct. 2013.

[22] D. Abou-Ras, *Advanced characterization techniques for thin film solar cells*. Weinheim: Wiley-VCH-Verl., 2011.

[23] U. W. Paetzold, W. Qiu, F. Finger, J. Poortmans, and D. Cheyns, "Development of perovskite solar cells with nanophotonic front electrodes for improved light incoupling," in *Photovoltaic Specialist Conference (PVSC), 2015 IEEE 42nd*, 2015, pp. 1–3.

[24] S. M. Kang *et al.*, "Moth-Eye TiO2 Layer for Improving Light Harvesting Efficiency in Perovskite Solar Cells," *Small*, vol. 12, no. 18, pp. 2443–2449, May 2016.

[25] M. M. Tavakoli *et al.*, "Highly Efficient Flexible Perovskite Solar Cells with Antireflection and Self-Cleaning Nanostructures," *ACS Nano*, vol. 9, no. 10, pp. 10287–10295, Oct. 2015.

[26] B. Dudem, J. H. Heo, J. W. Leem, J. S. Yu, and S. H. Im, "CH3NH3PbI3 planar perovskite solar cells with antireflection and self-cleaning function layers," *J. Mater. Chem. A*, vol. 4, no. 20, pp. 7573–7579, May 2016.

[27] P. Campbell and M. A. Green, "Light trapping properties of pyramidally textured surfaces," *Journal of Applied Physics*, vol. 62, no. 1, pp. 243–249, Jul. 1987.

[28] S. Faÿ, J. Steinhauser, S. Nicolay, and C. Ballif, "Polycrystalline ZnO: B grown by LPCVD as TCO for thin film silicon solar cells," *Thin Solid Films*, vol. 518, no. 11, pp. 2961–2966, Mar. 2010.

[29] M. Berginski, J. Hüpkes, W. Reetz, B. Rech, and M. Wuttig, "Recent development on surface-textured ZnO:Al films prepared by sputtering for thin-film solar cell application," *Thin Solid Films*, vol. 516, no. 17, pp. 5836–5841, Jul. 2008.

[30] K. E. Bean, "Anisotropic etching of silicon," *IEEE Transactions on Electron Devices*, vol. 25, no. 10, pp. 1185–1193, Oct. 1978.

[31] J. D. Hylton, R. Kinderman, A. R. Burgers, W. C. Sinke, and P. M. M. C. Bressers, "Uniform pyramid formation on alkaline-etched polished monocrystalline (100) silicon wafers," *Prog. Photovolt: Res. Appl.*, vol. 4, no. 6, pp. 435–438, Nov. 1996.

[32] I. Zubel and I. Barycka, "Silicon anisotropic etching in alkaline solutions I. The geometric description of figures developed under etching Si(100) in various solutions," *Sensors and Actuators A: Physical*, vol. 70, no. 3, pp. 250–259, Oct. 1998.

[33] C. Battaglia *et al.*, "Light Trapping in Solar Cells: Can Periodic Beat Random?," *ACS Nano*, vol. 6, no. 3, pp. 2790–2797, Mar. 2012.

[34] W. Cai and V. Shalaev, *Optical Metamaterials*. New York, NY: Springer New York, 2010.

[35] J. Escarré *et al.*, "UV imprinting for thin film solar cell application," *J. Opt.*, vol. 14, no. 2, p. 024009, Feb. 2012.

[36] J. C. Lötters, W. Olthuis, P. H. Veltink, and P. Bergveld, "The mechanical properties of the rubber elastic polymer polydimethylsiloxane for sensor applications," *J. Micromech. Microeng.*, vol. 7, no. 3, p. 145, Sep. 1997.

[37] K. Söderström, J. Escarré, O. Cubero, F.-J. Haug, S. Perregaux, and C. Ballif, "UV-nano-imprint lithography technique for the replication of back reflectors for n-i-p thin film silicon solar cells," *Prog. Photovolt: Res. Appl.*, vol. 19, no. 2, pp. 202–210, Mar. 2011.

[38] M. Steltenpool *et al.*, "Nano-Imprint Technology Combined with Rough TCO Morphology as Double Textured Light-Trapping Superstrate for Thin Film Solar Cells," presented at the 28th European Photovoltaic Solar Energy Conference and Exhibition (EU PVSEC 2013), 2013.

[39] J.-Y. Cho, G. Kim, S. Kim, and H. Lee, "Replication of surface nano-structure of the wing of dragonfly (Pantala Flavescens) using nano-molding and UV nanoimprint lithography," *Electron. Mater. Lett.*, vol. 9, no. 4, pp. 523–526, Jul. 2013.

[40] S. Choo, H.-J. Choi, and H. Lee, "Replication of rose-petal surface structure using UV-nanoimprint lithography," *Materials Letters*, vol. 121, pp. 170–173, Apr. 2014.

[41] R. Hünig *et al.*, "Flower Power: Exploiting Plants' Epidermal Structures for Enhanced Light Harvesting in Thin-Film Solar Cells," *Advanced Optical Materials*, vol. 4, no. 10, pp. 1487–1493, Oct. 2016.

[42] A. Čampa, "NIKA - model for extracting refractive indices," in *Proceedings of the 48th International Conference on Microelectronics, Devices and Materials & the Workshop on Ceramic Microsystems*, Otočec, Slovenija, 2012.

[43] "Refractive index of Al:ZnO (Aluminium-doped zinc oxide, AZO) - Treharne." [Online]. Available: http://refractiveindex.info/?shelf=other&book=Al:ZnO&page=Treharne. [Accessed: 27-Jan-2017].

[44] D. S. Ginley, Ed., *Handbook of Transparent Conductors*. Boston, MA: Springer US, 2011.

[45] E. Fortunato, P. Barquinha, and R. Martins, "Oxide Semiconductor Thin-Film Transistors: A Review of Recent Advances," *Adv. Mater.*, vol. 24, no. 22, pp. 2945–2986, Jun. 2012.

[46] C. G. Granqvist and A. Hultåker, "Transparent and conducting ITO films: new developments and applications," *Thin Solid Films*, vol. 411, no. 1, pp. 1–5, May 2002.

[47] W. Beyer, J. Hüpkes, and H. Stiebig, "Transparent conducting oxide films for thin film silicon photovoltaics," *Thin Solid Films*, vol. 516, no. 2–4, pp. 147–154, Dec. 2007.

[48] H. Liu, V. Avrutin, N. Izyumskaya, Ü. Özgür, and H. Morkoç, "Transparent conducting oxides for electrode applications in light emitting and absorbing devices," *Superlattices and Microstructures*, vol. 48, no. 5, pp. 458–484, Nov. 2010.

[49] M. Sever *et al.*, "Combined model of non-conformal layer growth for accurate optical simulation of thin-film silicon solar cells," *Solar Energy Materials and Solar Cells*, vol. 119, pp. 59–66, Dec. 2013.

[50] J. Krc *et al.*, "Design of periodic nano- and macro-scale textures for high-performance thin-film multi-junction solar cells," *J. Opt.*, vol. 18, no. 6, p. 064005, 2016.

[51] H.-J. Lee and P.-K. Song, "Crystallinity, etchability, electrical and mechanical properties of Ga doped amorphous indium tin oxide thin films deposited by direct current magnetron sputtering," *Thin Solid Films*, vol. 559, pp. 53–57, May 2014.

[52] J. H. Choi, S. H. Kang, H. S. Oh, T. H. Yu, and I. S. Sohn, "Design and characterization of Ga-doped indium tin oxide films for pixel electrode in liquid crystal display," *Thin Solid Films*, vol. 527, pp. 141–146, Jan. 2013.

[53] A. Dolgonos, S. A. Wells, K. R. Poeppelmeier, and T. O. Mason, "Phase Stability and Optoelectronic Properties of the Bixbyite Phase in the Gallium–Indium–Tin–Oxide System," *J. Am. Ceram. Soc.*, vol. 98, no. 2, pp. 669–674, Feb. 2015.

[54] J.-H. Hwang, D. D. Edwards, D. R. Kammler, and T. O. Mason, "Point defects and electrical properties of Sn-doped In-based transparent conducting oxides," *Solid State Ionics*, vol. 129, no. 1–4, pp. 135–144, Apr. 2000.

[55] M. Berginc, A. Čampa, K. Vojisavljević, B. Malič, P. Panjan, and M. Topič, "Relation Between Sputtering Parameters and Optical and Electrical Properties of Ga Doped ITO Transparent Conductive Oxide," *Energy Procedia*, vol. 84, pp. 183–189, Dec. 2015.

[56] A. Čampa, M. Berginc, K. Vojisavljević, B. Malič, P. Panjan, and M. Topič, "Optical and electrical properties of gallium doped indium tin oxide optimized for low deposition temperature applications," *Thin Solid Films*, vol. 621, pp. 52–57, Jan. 2017.

[57] M. Jošt *et al.*, "Efficient Light Management by Textured Nanoimprinted Layers for Perovskite Solar Cells," *submitted to ACS Photonics*, 2017.

[58] M. Jošt *et al.*, "Back- and Front-side Texturing for Light-management in Perovskite / Silicon-heterojunction Tandem Solar Cells," *Energy Procedia*, vol. 102, pp. 43–48, Dec. 2016.

[59] H. L. Wells, "On the caesium- and the potassium-lead halides," *Am J Sci*, vol. Series 3 Vol. 45, no. 266, pp. 121–134, Feb. 1893.

[60] C. K. Møller, "Crystal Structure and Photoconductivity of Cæsium Plumbohalides," *Nature*, vol. 182, no. 4647, pp. 1436–1436, Nov. 1958.

[61] D. Weber, "CH3NH3PbX3, ein Pb(II)-System mit kubischer Perowskitstruktur / CH3NH3PbX3, a Pb(II)-System with Cubic Perovskite Structure," *Zeitschrift für Naturforschung B*, vol. 33, no. 12, pp. 1443–1445, received 1978 2014.

[62] D. B. Mitzi, C. A. Feild, W. T. A. Harrison, and A. M. Guloy, "Conducting tin halides with a layered organic-based perovskite structure," *Nature*, vol. 369, no. 6480, pp. 467–469, Jun. 1994.

[63] A. Kojima, K. Teshima, Y. Shirai, and T. Miyasaka, "Organometal Halide Perovskites as Visible-Light Sensitizers for Photovoltaic Cells," *J. Am. Chem. Soc.*, vol. 131, no. 17, pp. 6050–6051, May 2009.

[64] H.-S. Kim *et al.*, "Lead Iodide Perovskite Sensitized All-Solid-State Submicron Thin Film Mesoscopic Solar Cell with Efficiency Exceeding 9%," *Scientific Reports*, vol. 2, p. 591, Aug. 2012.

[65] M. M. Lee, J. Teuscher, T. Miyasaka, T. N. Murakami, and H. J. Snaith, "Efficient Hybrid Solar Cells Based on Meso-Superstructured Organometal Halide Perovskites," *Science*, vol. 338, no. 6107, pp. 643–647, Nov. 2012.

[66] C. Li, X. Lu, W. Ding, L. Feng, Y. Gao, and Z. Guo, "Formability of ABX3 (X = F, Cl, Br, I) halide perovskites," *Acta Cryst B, Acta Cryst Sect B, Acta Crystallogr B, Acta Crystallogr Sect B, Acta Crystallogr Struct Sci, Acta Crystallogr Sect B Struct Sci, Acta Crystallogr B Struct Sci Cryst Eng Mater*, vol. 64, no. 6, pp. 702–707, Dec. 2008.

[67] J. S. Manser, J. A. Christians, and P. V. Kamat, "Intriguing Optoelectronic Properties of Metal Halide Perovskites," *Chem. Rev.*, vol. 116, no. 21, pp. 12956–13008, Nov. 2016.

[68] S. De Wolf *et al.*, "Organometallic Halide Perovskites: Sharp Optical Absorption Edge and Its Relation to Photovoltaic Performance," *J. Phys. Chem. Lett.*, vol. 5, no. 6, pp. 1035–1039, Mar. 2014.

[69] E. T. Hoke, D. J. Slotcavage, E. R. Dohner, A. R. Bowring, H. I. Karunadasa, and M. D. McGehee, "Reversible photo-induced trap formation in mixed-halide hybrid perovskites for photovoltaics," *Chem. Sci.*, vol. 6, no. 1, pp. 613–617, Dec. 2014.

[70] S. A. Kulkarni, T. Baikie, P. P. Boix, N. Yantara, N. Mathews, and S. Mhaisalkar, "Band-gap tuning of lead halide perovskites using a sequential deposition process," *J. Mater. Chem. A*, vol. 2, no. 24, pp. 9221–9225, May 2014.

[71] D. B. Mitzi, "Templating and structural engineering in organic–inorganic perovskites," *J. Chem. Soc., Dalton Trans.*, no. 1, pp. 1–12, Jan. 2001.

[72] C. C. Stoumpos, C. D. Malliakas, and M. G. Kanatzidis, "Semiconducting Tin and Lead Iodide Perovskites with Organic Cations: Phase Transitions, High Mobilities, and Near-Infrared Photoluminescent Properties," *Inorg. Chem.*, vol. 52, no. 15, pp. 9019–9038, Aug. 2013.

[73] G. Xing *et al.*, "Long-Range Balanced Electron- and Hole-Transport Lengths in Organic-Inorganic CH3NH3PbI3," *Science*, vol. 342, no. 6156, pp. 344–347, Oct. 2013.

[74] S. D. Stranks *et al.*, "Electron-Hole Diffusion Lengths Exceeding 1 Micrometer in an Organometal Trihalide Perovskite Absorber," *Science*, vol. 342, no. 6156, pp. 341–344, Oct. 2013.

[75] Y. Li *et al.*, "Direct Observation of Long Electron-Hole Diffusion Distance in CH3NH3PbI3 Perovskite Thin Film," *Scientific Reports*, vol. 5, p. 14485, Sep. 2015.

[76] M. A. Green, A. Ho-Baillie, and H. J. Snaith, "The emergence of perovskite solar cells," *Nat Photon*, vol. 8, no. 7, pp. 506–514, Jul. 2014.

[77] H. J. Snaith, "Perovskites: The Emergence of a New Era for Low-Cost, High-Efficiency Solar Cells," *J. Phys. Chem. Lett.*, vol. 4, no. 21, pp. 3623–3630, Nov. 2013.

[78] M. Grätzel, "The light and shade of perovskite solar cells," *Nature materials*, vol. 13, no. 9, pp. 838–842, 2014.

[79] M. Saliba *et al.*, "Incorporation of rubidium cations into perovskite solar cells improves photovoltaic performance," *Science*, p. aah5557, Sep. 2016.

[80] S. Albrecht *et al.*, "Monolithic perovskite/silicon-heterojunction tandem solar cells processed at low temperature," *Energy Environ. Sci.*, vol. 9, no. 1, pp. 81–88, 2016.

[81] J. Werner *et al.*, "Efficient Monolithic Perovskite/Silicon Tandem Solar Cell with Cell Area >1 cm2," *J. Phys. Chem. Lett.*, pp. 161–166, Dec. 2015.

[82] B. Chen *et al.*, "Efficient Semitransparent Perovskite Solar Cells for 23.0%-Efficiency Perovskite/Silicon Four-Terminal Tandem Cells," *Adv. Energy Mater.*, vol. 6, no. 19, Oct. 2016.

[83] P. Löper *et al.*, "Organic–inorganic halide perovskite/crystalline silicon four-terminal tandem solar cells," *Phys. Chem. Chem. Phys.*, vol. 17, no. 3, pp. 1619–1629, Dec. 2014.

[84] T. Todorov *et al.*, "Monolithic Perovskite-CIGS Tandem Solar Cells via In Situ Band Gap Engineering," *Adv. Energy Mater.*, vol. 5, no. 23, p. n/a-n/a, Dec. 2015.

[85] G. E. Eperon *et al.*, "Perovskite-perovskite tandem photovoltaics with optimized bandgaps," *Science*, p. aaf9717, Oct. 2016.

[86] F. Jiang *et al.*, "A two-terminal perovskite/perovskite tandem solar cell," *J. Mater. Chem. A*, vol. 4, no. 4, pp. 1208–1213, Jan. 2016.

[87] M. Grätzel, "Dye-sensitized solar cells," *Journal of Photochemistry and Photobiology C: Photochemistry Reviews*, vol. 4, no. 2, pp. 145–153, Oct. 2003.

[88] G. E. Eperon, V. M. Burlakov, P. Docampo, A. Goriely, and H. J. Snaith, "Morphological Control for High Performance, Solution-Processed Planar Heterojunction Perovskite Solar Cells," *Adv. Funct. Mater.*, vol. 24, no. 1, pp. 151–157, Jan. 2014.

[89] D. Liu and T. L. Kelly, "Perovskite solar cells with a planar heterojunction structure prepared using room-temperature solution processing techniques," *Nat Photon*, vol. 8, no. 2, pp. 133–138, Feb. 2014.

[90] M. Liu, M. B. Johnston, and H. J. Snaith, "Efficient planar heterojunction perovskite solar cells by vapour deposition," *Nature*, vol. 501, no. 7467, pp. 395–398, Sep. 2013.

[91] Y. Li *et al.*, "High-efficiency robust perovskite solar cells on ultrathin flexible substrates," *Nature Communications*, vol. 7, p. 10214, Jan. 2016.

[92] F. D. Giacomo, A. Fakharuddin, R. Jose, and T. M. Brown, "Progress, challenges and perspectives in flexible perovskite solar cells," *Energy Environ. Sci.*, vol. 9, no. 10, pp. 3007–3035, Oct. 2016.

[93] G. Yang, H. Tao, P. Qin, W. Ke, and G. Fang, "Recent progress in electron transport layers for efficient perovskite solar cells," *J. Mater. Chem. A*, vol. 4, no. 11, pp. 3970–3990, Mar. 2016.

[94] L. Calió, S. Kazim, M. Grätzel, and S. Ahmad, "Hole-Transport Materials for Perovskite Solar Cells," *Angew. Chem. Int. Ed.*, vol. 55, no. 47, pp. 14522–14545, Nov. 2016.

[95] N. J. Jeon, J. H. Noh, Y. C. Kim, W. S. Yang, S. Ryu, and S. I. Seok, "Solvent engineering for high-performance inorganic–organic hybrid perovskite solar cells," *Nature Materials*, vol. 13, no. 9, pp. 897–903, Jul. 2014.

[96] J.-H. Im, I.-H. Jang, N. Pellet, M. Grätzel, and N.-G. Park, "Growth of CH3NH3PbI3 cuboids with controlled size for high-efficiency perovskite solar cells," *Nat Nano*, vol. 9, no. 11, pp. 927–932, Nov. 2014.

[97] W. Chen *et al.*, "Efficient and stable large-area perovskite solar cells with inorganic charge extraction layers," *Science*, vol. 350, no. 6263, pp. 944–948, Nov. 2015.

[98] C.-Y. Chang, W.-K. Huang, Y.-C. Chang, K.-T. Lee, and C.-T. Chen, "A solution-processed n-doped fullerene cathode interfacial layer for efficient and stable large-area perovskite solar cells," *J. Mater. Chem. A*, vol. 4, no. 2, pp. 640–648, Dec. 2015.

[99] X. Li *et al.*, "A vacuum flash–assisted solution process for high-efficiency large-area perovskite solar cells," *Science*, p. aaf8060, Jun. 2016.

[100] S. Razza *et al.*, "Perovskite solar cells and large area modules (100 cm2) based on an air flow-assisted PbI2 blade coating deposition process," *Journal of Power Sources*, vol. 277, pp. 286–291, Mar. 2015.

[101] "Imec news-imec." [Online]. Available: http://www2.imec.be/be_en/press/imec-news/perovskite-eng.html. [Accessed: 16-Feb-2017].

[102] "Imec news-imec." [Online]. Available: http://www2.imec.be/be_en/press/imec-news/semitransparent-perovskite-pv-module.html. [Accessed: 16-Feb-2017].

[103] "WHO | Lead poisoning and health," *WHO*. [Online]. Available: http://www.who.int/mediacentre/factsheets/fs379/en/. [Accessed: 15-Feb-2017].

[104] T. A. Berhe *et al.*, "Organometal halide perovskite solar cells: degradation and stability," *Energy Environ. Sci.*, vol. 9, no. 2, pp. 323–356, Feb. 2016.

[105] G. Niu, X. Guo, and L. Wang, "Review of recent progress in chemical stability of perovskite solar cells," *J. Mater. Chem. A*, vol. 3, no. 17, pp. 8970–8980, Apr. 2015.

[106] D. Wang, M. Wright, N. K. Elumalai, and A. Uddin, "Stability of perovskite solar cells," *Solar Energy Materials and Solar Cells*, vol. 147, pp. 255–275, Apr. 2016.

[107] Y. Bai *et al.*, "Enhancing stability and efficiency of perovskite solar cells with crosslinkable silane-functionalized and doped fullerene," *Nature Communications*, vol. 7, p. 12806, Oct. 2016.

[108] F. Bella *et al.*, "Improving efficiency and stability of perovskite solar cells with photocurable fluoropolymers," *Science*, vol. 354, no. 6309, pp. 203–206, Oct. 2016.

[109] G. E. Eperon, S. D. Stranks, C. Menelaou, M. B. Johnston, L. M. Herz, and H. J. Snaith, "Formamidinium lead trihalide: a broadly tunable perovskite for efficient planar heterojunction solar cells," *Energy Environ. Sci.*, vol. 7, no. 3, pp. 982–988, Feb. 2014.

[110] N. K. Noel *et al.*, "Lead-free organic–inorganic tin halide perovskites for photovoltaic applications," *Energy Environ. Sci.*, vol. 7, no. 9, pp. 3061–3068, Aug. 2014.

[111] G. E. Eperon *et al.*, "Inorganic caesium lead iodide perovskite solar cells," *J. Mater. Chem. A*, vol. 3, no. 39, pp. 19688–19695, Sep. 2015.

[112] R. J. Sutton *et al.*, "Bandgap-Tunable Cesium Lead Halide Perovskites with High Thermal Stability for Efficient Solar Cells," *Adv. Energy Mater.*, vol. 6, no. 8, p. n/a-n/a, Apr. 2016.

[113] S. J. Lee *et al.*, "Fabrication of Efficient Formamidinium Tin Iodide Perovskite Solar Cells through SnF2–Pyrazine Complex," *J. Am. Chem. Soc.*, vol. 138, no. 12, pp. 3974–3977, Mar. 2016.

[114] H. J. Snaith *et al.*, "Anomalous Hysteresis in Perovskite Solar Cells," *J. Phys. Chem. Lett.*, vol. 5, no. 9, pp. 1511–1515, May 2014.

[115] B. Chen, M. Yang, S. Priya, and K. Zhu, "Origin of J–V Hysteresis in Perovskite Solar Cells," *J. Phys. Chem. Lett.*, vol. 7, no. 5, pp. 905–917, Mar. 2016.

[116] D. T. Moore *et al.*, "Crystallization Kinetics of Organic–Inorganic Trihalide Perovskites and the Role of the Lead Anion in Crystal Growth," *J. Am. Chem. Soc.*, vol. 137, no. 6, pp. 2350–2358, Feb. 2015.

[117] C. Bi, Q. Wang, Y. Shao, Y. Yuan, Z. Xiao, and J. Huang, "Non-wetting surface-driven high-aspect-ratio crystalline grain growth for efficient hybrid perovskite solar cells," *Nature Communications*, vol. 6, p. 7747, Jul. 2015.

[118] W. Zhang *et al.*, "Enhanced optoelectronic quality of perovskite thin films with hypophosphorous acid for planar heterojunction solar cells," *Nature Communications*, vol. 6, p. 10030, Nov. 2015.

[119] D. W. deQuilettes *et al.*, "Photo-induced halide redistribution in organic–inorganic perovskite films," *Nature Communications*, vol. 7, p. 11683, May 2016.

[120] Z. Xiao *et al.*, "Unraveling the hidden function of a stabilizer in a precursor in improving hybrid perovskite film morphology for high efficiency solar cells," *Energy Environ. Sci.*, vol. 9, no. 3, pp. 867–872, Mar. 2016.

[121] J. T.-W. Wang *et al.*, "Efficient perovskite solar cells by metal ion doping," *Energy Environ. Sci.*, vol. 9, no. 9, pp. 2892–2901, Aug. 2016.

[122] J.-W. Lee, H.-S. Kim, and N.-G. Park, "Lewis Acid–Base Adduct Approach for High Efficiency Perovskite Solar Cells," *Acc. Chem. Res.*, vol. 49, no. 2, pp. 311–319, Feb. 2016.

[123] A. D. Vos, "Detailed balance limit of the efficiency of tandem solar cells," *J. Phys. D: Appl. Phys.*, vol. 13, no. 5, p. 839, 1980.

[124] M. Saliba *et al.*, "Cesium-containing triple cation perovskite solar cells: improved stability, reproducibility and high efficiency," *Energy Environ. Sci.*, Mar. 2016.

[125] K. Masuko *et al.*, "Achievement of More Than 25 #x0025; Conversion Efficiency With Crystalline Silicon Heterojunction Solar Cell," *IEEE Journal of Photovoltaics*, vol. 4, no. 6, pp. 1433–1435, Nov. 2014.

[126] S. Albrecht *et al.*, "Towards optical optimization of planar monolithic perovskite/silicon-heterojunction tandem solar cells," *J. Opt.*, vol. 18, no. 6, p. 064012, 2016.

[127] D. P. McMeekin *et al.*, "A mixed-cation lead mixed-halide perovskite absorber for tandem solar cells," *Science*, vol. 351, no. 6269, pp. 151–155, Jan. 2016.

[128] M. Filipič *et al.*, "CH_3NH_3PbI_3 perovskite / silicon tandem solar cells: characterization based optical simulations," *Optics Express*, vol. 23, no. 7, p. A263, Apr. 2015.

[129] S. Albrecht *et al.*, "Monolithic perovskite/silicon-heterojunction tandem solar cells processed at low temperature," *Energy Environ. Sci.*, vol. 9, no. 1, pp. 81–88, Jan. 2016.

[130] N. J. Jeon, J. H. Noh, Y. C. Kim, W. S. Yang, S. Ryu, and S. I. Seok, "Solvent engineering for high-performance inorganic–organic hybrid perovskite solar cells," *Nat Mater*, vol. 13, no. 9, pp. 897–903, Sep. 2014.

[131] J. H. Heo, H. J. Han, D. Kim, T. K. Ahn, and S. H. Im, "Hysteresis-less inverted CH3NH3PbI3 planar perovskite hybrid solar cells with 18.1% power conversion efficiency," *Energy Environ. Sci.*, vol. 8, no. 5, pp. 1602–1608, May 2015.

[132] C.-G. Wu, C.-H. Chiang, Z.-L. Tseng, M. K. Nazeeruddin, A. Hagfeldt, and M. Grätzel, "High efficiency stable inverted perovskite solar cells without current hysteresis," *Energy Environ. Sci.*, vol. 8, no. 9, pp. 2725–2733, Aug. 2015.

[133] L. Meng, J. You, T.-F. Guo, and Y. Yang, "Recent Advances in the Inverted Planar Structure of Perovskite Solar Cells," *Acc. Chem. Res.*, vol. 49, no. 1, pp. 155–165, Jan. 2016.

[134] B. Lipovšek, F. Guo, C. J. Brabec, K. Forberich, J. Krč, and M. Topič, "Detailed multi-dimensional optical modeling of thin-film organic solar cells including light-management structure," *submitted to Optics Express*, 2016.

[135] J.-Y. Jeng *et al.*, "CH3NH3PbI3 Perovskite/Fullerene Planar-Heterojunction Hybrid Solar Cells," *Adv. Mater.*, vol. 25, no. 27, pp. 3727–3732, Jul. 2013.

[136] B. Lipovšek, J. Krč, and M. Topič, "Optical model for thin-film photovoltaic devices with large surface textures at the front side," *Informacije Midem*, vol. 41, no. 4, pp. 264–271, 2011.

[137] B. Lipovšek, J. Krč, and M. Topič, "Optimization of Microtextured Light-Management Films for Enhanced Light Trapping in Organic Solar Cells Under Perpendicular and Oblique Illumination Conditions," *IEEE Journal of Photovoltaics*, vol. 4, no. 2, pp. 639–646, Mar. 2014.

[138] P. Löper *et al.*, "Complex Refractive Index Spectra of CH3NH3PbI3 Perovskite Thin Films Determined by Spectroscopic Ellipsometry and Spectrophotometry," *J. Phys. Chem. Lett.*, vol. 6, no. 1, pp. 66–71, Jan. 2015.

[139] B. Yang *et al.*, "Perovskite Solar Cells with Near 100% Internal Quantum Efficiency Based on Large Single Crystalline Grains and Vertical Bulk Heterojunctions," *J. Am. Chem. Soc.*, vol. 137, no. 29, pp. 9210–9213, Jul. 2015.

[140] T. Leijtens *et al.*, "Carrier trapping and recombination: the role of defect physics in enhancing the open circuit voltage of metal halide perovskite solar cells," *Energy Environ. Sci.*, Sep. 2016.

[141] C. Ulbrich, A. Gerber, K. Hermans, A. Lambertz, and U. Rau, "Analysis of short circuit current gains by an anti-reflective textured cover on silicon thin film solar cells," *Prog. Photovolt: Res. Appl.*, vol. 21, no. 8, pp. 1672–1681, Dec. 2013.

[142] J. Muller, A. Herman, A. Mayer, and O. Deparis, "A fair comparison between ultrathin crystalline-silicon solar cells with either periodic or correlated disorder inverted pyramid textures," *Opt Express*, vol. 23, no. 11, pp. A657-670, Jun. 2015.

[143] M. Jošt, J. Krč, and M. Topič, "Camera-based angular resolved spectroscopy system for spatial measurements of scattered light," *Applied Optics*, vol. 53, no. 21, p. 4795, Jul. 2014.

[144] M. Jošt, J. Krč, and M. Topič, "Camera-based ARS system for complete light scattering determination/characterization," *Measurement Science and Technology*, vol. 27, no. 3, p. 035202, Mar. 2016.

[145] M. C. Gather and S. Reineke, "Recent advances in light outcoupling from white organic light-emitting diodes," *J. Photon. Energy*, vol. 5, no. 1, pp. 057607–057607, 2015.

[146] *ASTM E2387-05(2011), Standard Practice for Goniometric Optical Scatter Measurements, ASTM International, West Conshohocken, PA*. 2011.

[147] *ASTM E1392-96(2002), Standard Practice for Angle Resolved Optical Scatter Measurements on Specular or Diffuse Surfaces (Withdrawn 2003), ASTM International, West Conshohocken, PA*. 1996.

[148] *ISO 13696:2002 - Optics and optical instruments -- Test methods for radiation scattered by optical components, International Organization for Standardization, Geneva, Switzerland*. 2002.

[149] G. Jost, T. Merdzhanova, T. Zimmermann, and J. Hüpkes, "Process monitoring of texture-etched high-rate ZnO:Al front contacts for silicon thin-film solar cells," *Thin Solid Films*, vol. 532, pp. 66–72, Apr. 2013.

[150] J. Rifkin *et al.*, "Design Review Of A Complete Angle Scatter Instrument," 1989, vol. 1036, pp. 116–124.

[151] J. Krč, M. Zeman, O. Kluth, F. Smole, and M. Topič, "Effect of surface roughness of ZnO:Al films on light scattering in hydrogenated amorphous silicon solar cells," *Thin Solid Films*, vol. 426, no. 1–2, pp. 296–304, Feb. 2003.

[152] S. Schröder, T. Herffurth, H. Blaschke, and A. Duparré, "Angle-resolved scattering: an effective method for characterizing thin-film coatings," *Appl. Opt.*, vol. 50, no. 9, pp. C164–C171, Mar. 2011.

[153] C. Amra, D. Torricini, and P. Roche, "Multiwavelength (0.45-10.6 μm) angle-resolved scatterometer or how to extend the optical window," *Appl. Opt.*, vol. 32, no. 28, pp. 5462–5474, Oct. 1993.

[154] K. Jäger, O. Isabella, R. A. C. M. M. van Swaaij, and M. Zeman, "Angular resolved scattering measurements of nano-textured substrates in a broad wavelength range," *Meas. Sci. Technol.*, vol. 22, no. 10, p. 105601, Oct. 2011.

[155] "Table-top system for light scatter measurement »Albatross-TT« - Fraunhofer IOF," *Fraunhofer Institute for Applied Optics and Precision Engineering IOF*. [Online]. Available: http://www.iof.fraunhofer.de/en/competences/measurement-methods-and-characterization/surface-and-thin-film-characterization/scattered-light-measurement-analysis/table-top-system-albatross-tt.html. [Accessed: 30-Oct-2015].

[156] "Imaging Spheres | Radiant Vision Systems." [Online]. Available: http://www.radiantvisionsystems.com/products/imaging-spheres. [Accessed: 30-Oct-2015].

[157] M. Berner, M. Sämann, A. Garamoun, and M. B. Schubert, "Quantification of Optical Deflection by Laser-structured ZnO:Al," *IEEE Journal of Photovoltaics*, vol. 3, no. 1, pp. 590–592, 2013.

[158] D.-Y. Kim and J.-W. Seo, "A diffuser-based three-dimensional measurement of polarization-dependent scattering characteristics of optical films for 3D-display applications," *Opt. Express*, vol. 23, no. 2, pp. 1063–1072, Jan. 2015.

[159] M. Foldyna, M. Moreno, P. R. i Cabarrocas, and A. De Martino, "Scattered light measurements on textured crystalline silicon substrates using an angle-resolved Mueller matrix polarimeter," *Appl. Opt.*, vol. 49, no. 3, pp. 505–512, Jan. 2010.

[160] M. Roser and P. Lenz, "Camera-based bidirectional reflectance measurement for road surface reflectivity classification," in *2010 IEEE Intelligent Vehicles Symposium (IV)*, 2010, pp. 340–347.

[161] S. R. Marschner, S. H. Westin, E. P. F. Lafortune, and K. E. Torrance, "Image-Based Bidirectional Reflectance Distribution Function Measurement," *Applied Optics*, vol. 39, no. 16, p. 2592, Jun. 2000.

[162] K. Takase, N. Tsumura, T. Nakaguchi, and Y. Miyake, "Measurement of bidirectional reflectance distribution function with a linear light source," *OPT REV*, vol. 15, no. 4, pp. 187–195, Aug. 2008.

[163] R. Brodmann, O. Gerstorfer, and G. Thurn, "Optical Roughness Measuring Instrument For Fine-Machined Surfaces," *Opt. Eng*, vol. 24, no. 3, p. 243408-243408-, 1985.

[164] R.-S. Lu and G. Y. Tian, "On-line measurement of surface roughness by laser light scattering," *Meas. Sci. Technol.*, vol. 17, no. 6, p. 1496, 2006.

[165] N. A. Feidenhans'l *et al.*, "Comparison of optical methods for surface roughness characterization," *Meas. Sci. Technol.*, vol. 26, no. 8, p. 085208, 2015.

[166] M. Bokalič, J. Raguse, J. R. Sites, and M. Topič, "Analysis of electroluminescence images in small-area circular CdTe solar cells," *Journal of Applied Physics*, vol. 114, no. 12, p. 123102, 2013.

[167] M. Bokalič and M. Topič, *Spatially Resolved Characterization in Thin-Film Photovoltaics*. Cham: Springer International Publishing, 2015.

[168] J. Peatross and M. Ware, "Physics of Light and Optics: A Free Online Textbook," in *Frontiers in Optics 2010/Laser Science XXVI*, 2010, p. JWA64.

[169] J. Krč and M. Topič, *Optical Modeling and Simulation of Thin-Film Photovoltaic Devices*. CRC Press, 2013.

[170] O. Kluth *et al.*, "Texture etched ZnO:Al coated glass substrates for silicon based thin film solar cells," *Thin Solid Films*, vol. 351, no. 1–2, pp. 247–253, Aug. 1999.

[171] J. A. Sap, O. Isabella, K. Jäger, and M. Zeman, "Extraction of optical properties of flat and surface-textured transparent conductive oxide films in a broad wavelength range," *Thin Solid Films*, vol. 520, no. 3, pp. 1096–1101, Nov. 2011.

[172] "LS-1 Tungsten Halogen Light Source." [Online]. Available: http://www.oceanoptics.com/products/ls1.asp. [Accessed: 25-Feb-2014].

[173] "250 x 300mm Opal Diffusing Glass | Edmund Optics." [Online]. Available: http://www.edmundoptics.com/optics/windows-diffusers/optical-diffusers/opal-diffusing-glass/43042/. [Accessed: 17-Jun-2015].

[174] "PLEXIGLAS® - Shop - PLEXIGLAS® Optical (RP) 7D007 RP - film cut-to-size." [Online]. Available: http://www.plexiglas-shop.com/GB/en/film-cut-to-size-7amim86q5ps/plexiglas-optical-rp-7d007-rp-5elj8eam8sn~p.html. [Accessed: 17-Jun-2015].

[175] "PHABLE^{TM} Made Nanostructures - EULITHA." [Online]. Available: http://www.eulitha.com/products/standard-patterns/phable-made/. [Accessed: 17-Jul-2015].

[176] N. W. Aschroft and N. D. Mermin, *Solid State Physics*, 1 edition. New York: Brooks Cole, 1976.

[177] M. Sever, J. Krč, A. Čampa, and M. Topič, "Rigorous modelling of light scattering in solar cells based on finite element method and Huygens' expansion," *Optics Express*, vol. 23, no. 24, p. A1549, Nov. 2015.

[178] M. Topic *et al.*, "Design challenges for light harvesting in photovoltaic devices," in *Proc. SPIE*, 2016, vol. 9898, p. 98980D–98980D–7.

[179] M. Jošt, J. Krč, and M. Topič, "3D Camera-Based System for Measurements of Scattered or Emitted Light," *31st European Photovoltaic Solar Energy Conference and Exhibition*, pp. 1293–1296, Nov. 2015.

[180] M. Jošt, J. Krč, and M. Topič, "Camera-based measurement of light scattering intensity distribution," in *49th International Conference on Microelectronics,*

Devices and Materials & theWorkshop on Digital Electronic Systems, Kranjska Gora, Slovenia, 2013.

[181] M. Jošt, J. Krč, and M. Topič, "UV nanoimprint lithography for replication of textured surfaces in thin-film photovoltaics," in *50th International Conference on Microelectronics, Devices and Materials*, Ljubljana, Slovenia, 2014.

[182] M. Jošt *et al.*, "Nanoimprinted textures on glass as a substrate for GITO deposition," in *51th International Conference on Microelectronics, Devices and Materials and the Workshop on Terahertz and Microwave Systems*, Bled, Slovenia, 2015.

[183] M. Jošt, S. Albrecht, J. Krč, B. Rech, and M. Topič, "Hypophosphorous acid as an additive for inverted perovskite solar cells," in *52nd International Conference on Microelectronics, Devices and Materials and the Workshop on Biosensors and Microfluidics*, Ankaran, Slovenia, 2016.

Appendix A

Total and diffuse transmittance graphs from outdoor testing

Figure A 1 shows total and diffuse transmittance spectra of all the samples that underwent the outdoor testing and were presented in section 2.7 on outdoor testing. Comparison between different samples measured on days 0, 1, 19, 50 and 91, is shown. Left column shows results of the flat samples and right one is for the textured samples. The summary of the results, extracted points for the wavelengths of 400 and 700 nm, is already shown in Figure 2.11, together with the discussion.

a)

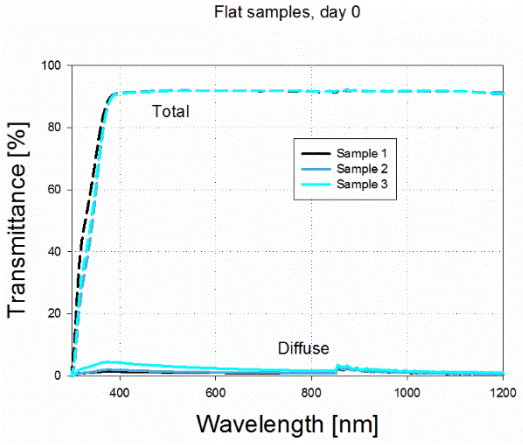

b)

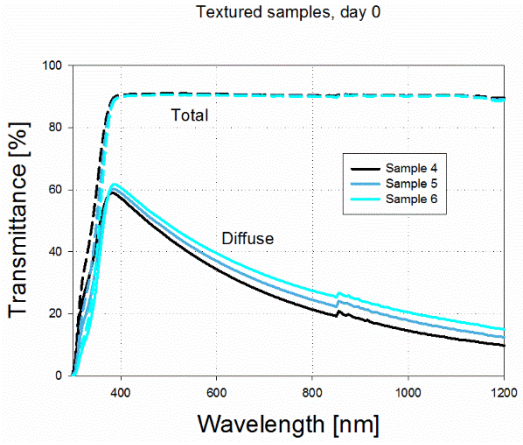

c)

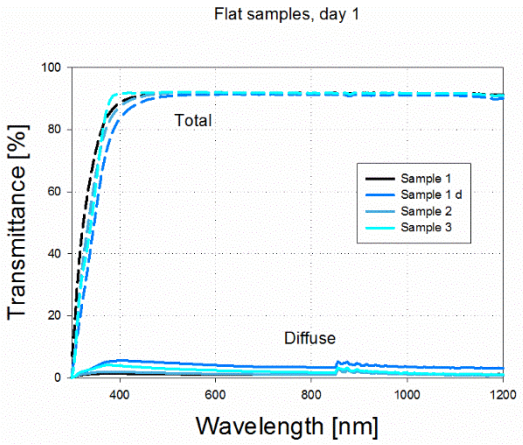

d)

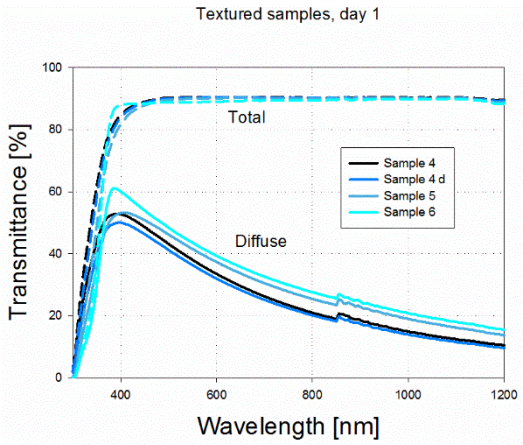

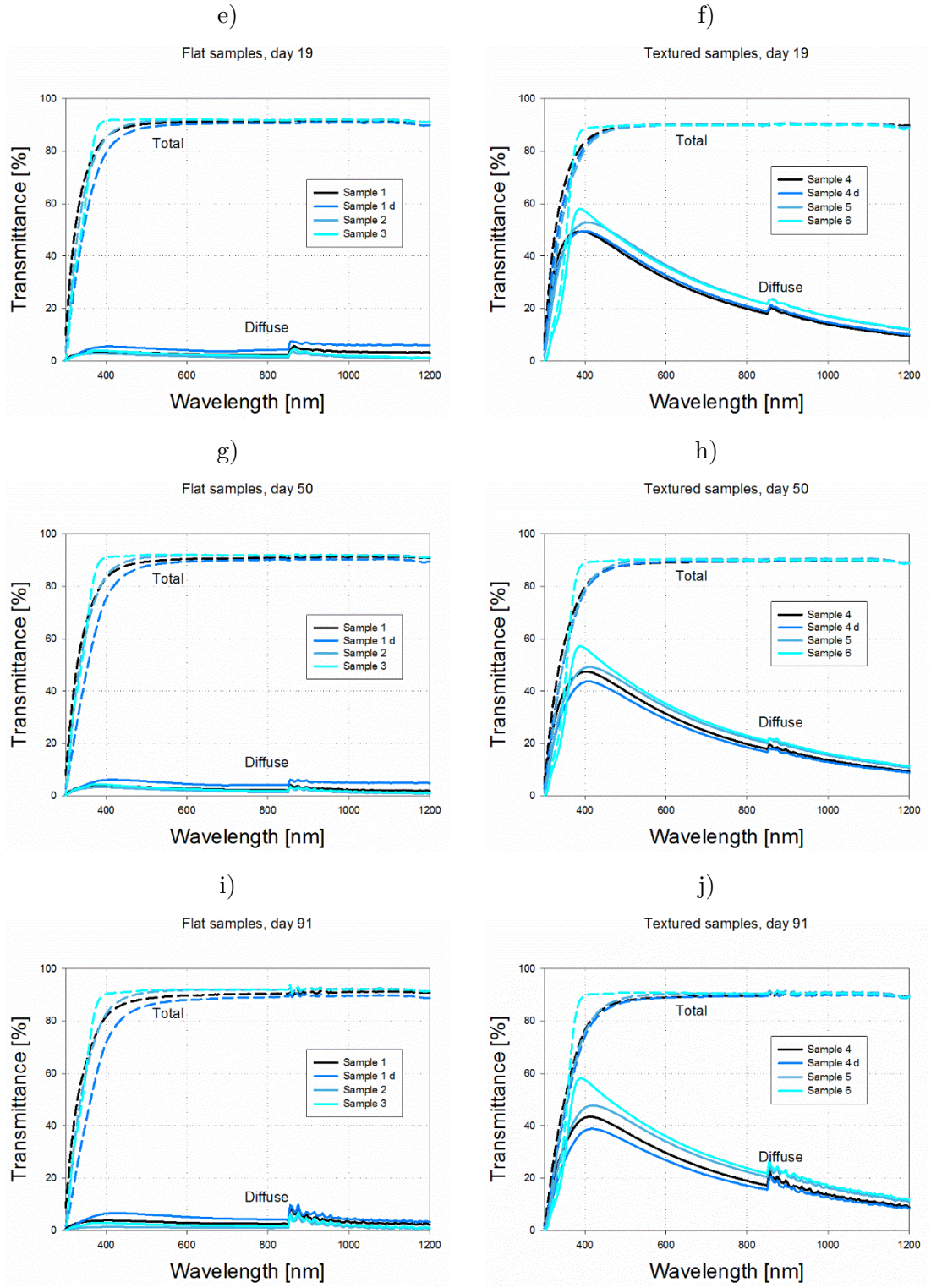

Figure A 1: Total and diffuse transmittance spectra for all the samples that underwent the outdoor testing. Left column shows flat and right column textured samples. Spectra measured on days 0, 1, 19, 50 and 91 is shown.

Figure A 2 shows total and diffuse transmittance spectra of all the samples, measured on different days. Comparison between measurements on days 0, 1, 19, 50 and 91 for each of the samples is shown. Left column shows results of the flat samples and right one is for the textured samples. The results have already been discussed in section 2.7.1.1.

a)

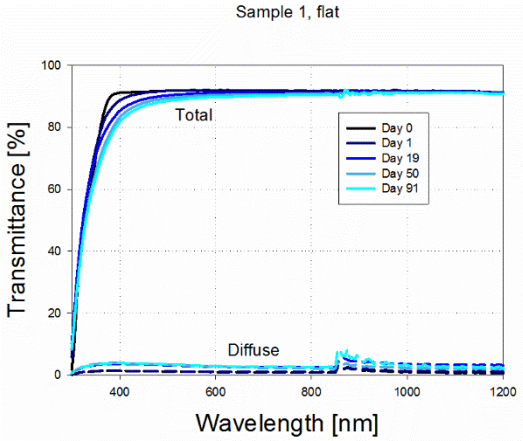

b)

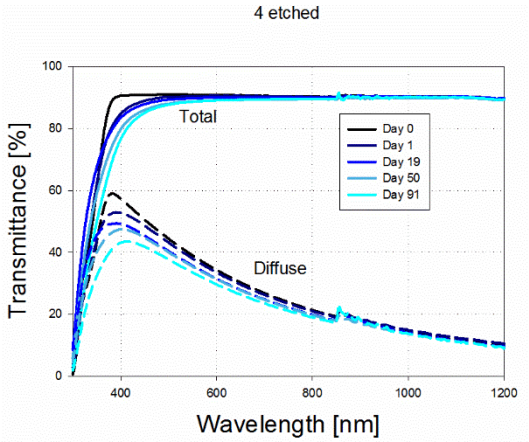

c)

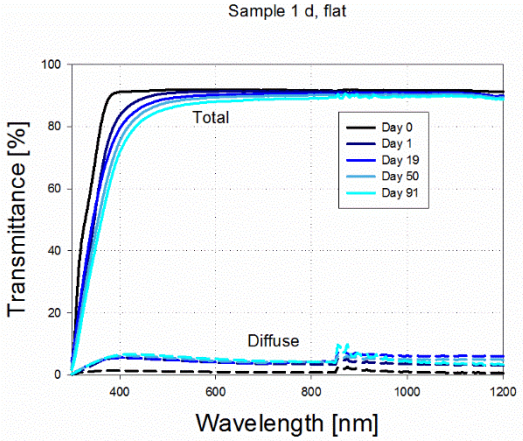

d)

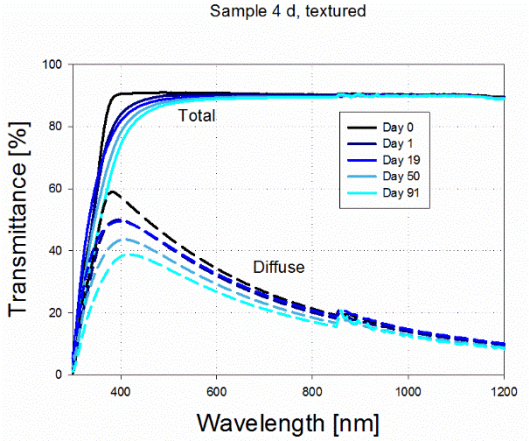

e)

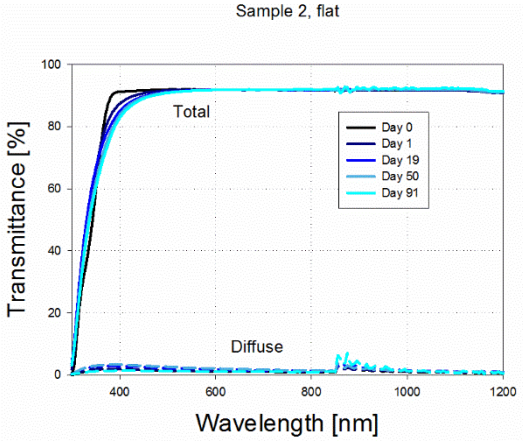

f)

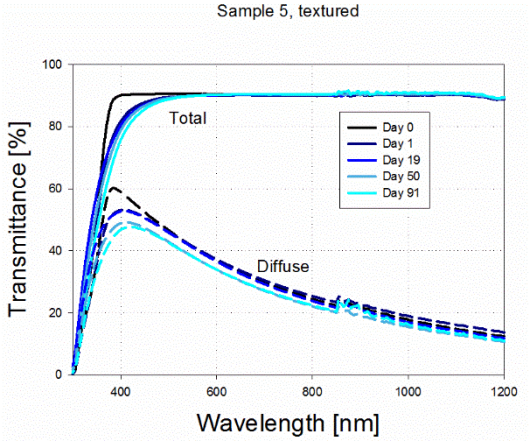

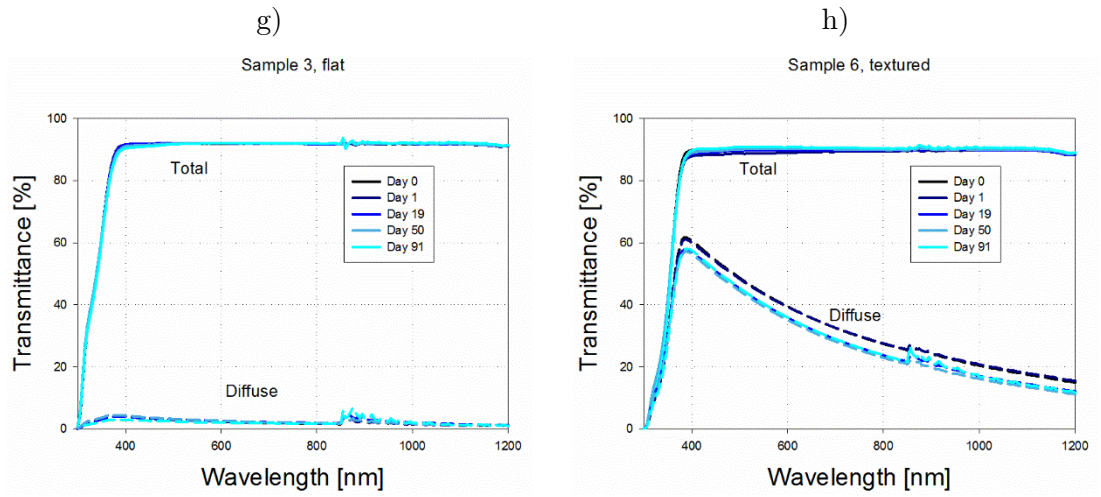

Figure A 2: Diffuse and total transmittance spectra for each replica. Comparison between days 0, 1, 19, 50 and 91 is shown.

Appendix B

PTAA based perovskite solar cells

Here we show performance parameters of additional PTAA based solar cells without and with LM foil. All the results show very similar trend as the selected device presented in section 3.3.2.1.

Table B 1: Performance parameters, integrated J_{SC_EQE} from the EQE and equivalent J_{SC} loss from the reflection measurements R_{eq} of the fabricated solar cells without and with the LM foil. Relative changes are also shown.

			J_{SC} [mA cm^{-2}]	J_{SC_EQE} [mA cm^{-2}]	R_{eq} [mA cm^{-2}]	V_{OC} [V]	FF [%]	PCE [%]
1	w/o LM foil	for	20.9	20.6	6.70	1.11	70.2	16.2
		rev	20.7			1.10	69.1	15.8
2	w/ LM foil	for	21.8	20.7	4.45	1.10	70.5	17.0
		rev	21.7			1.10	68.8	16.4
3	w/o LM foil	for	20.7	20.5	6.63	1.11	70.9	16.3
		rev	20.5			1.11	70.2	16.0
4	w/ LM foil	for	21.7	20.7	4.37	1.11	71.2	17.1
		rev	21.6			1.11	70.3	16.8
5	w/o LM foil	for	20.7	20.5	6.81	1.10	69.9	16.0
		rev	20.6			1.10	69.2	15.7
6	w/ LM foil	for	21.7	20.5	4.25	1.10	70.4	16.8
		rev	21.6			1.10	69.4	16.4

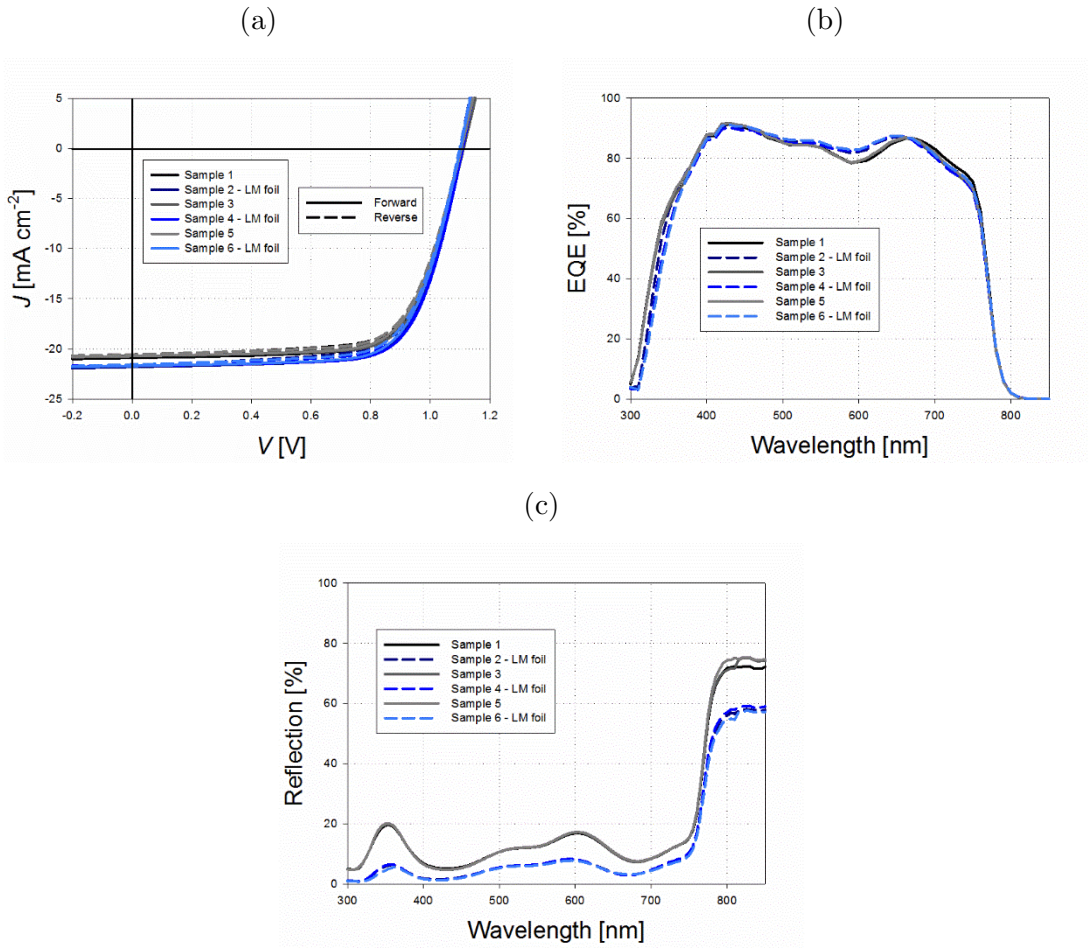

Figure B 1: (a) *J*-*V*, (b) EQE and (c) *R* measurements of the additional PTAA based perovskite solar cells without (black-ish lines) and with LM foil (blue-ish lines).

PEDOT:PSS based perovsite solar cells

Here we show performance parameters of additional PEDOT:PSS based solar cells with LM foil. All the results show very similar trend as the selected device presented in section 3.3.2.2.

Table B 2: Performance parameters, integrated J_{SC_EQE} from the EQE and equivalent J_{SC} loss from the reflection measurements R_{eq} of the fabricated solar cells before and after UV NIL deposition. Relative change is also shown.

			J_{SC} [mA cm^{-2}]	J_{SC_EQE} [mA cm^{-2}]	R_{eq} [mA cm^{-2}]	V_{OC} [V]	FF [%]	PCE [%]
1	w/o LM foil	for	16.1	15.1	8.79	0.72	66.9	7.74
		rev	16.3			0.72	68.3	8.02
2	w/ LM foil	for	17.5	15.8	4.98	0.74	65.2	8.46
		rev	17.7			0.74	66.0	8.65
3	w/o LM foil	for	15.7	15.0	8.63	0.73	68.4	7.78
		rev	15.9			0.72	69.2	7.98
4	w/ LM foil	for	17.1	15.2	5.69	0.75	64.8	8.55
		rev	17.9			0.75	65.5	8.72
5	w/o LM foil	for	15.9	15.0	9.25	0.71	69.4	7.79
		rev	16.1			0.70	70.2	7.97
6	w/ LM foil	for	17.3	15.3	5.99	0.71	60.5	7.47
		rev	17.4			0.71	61.2	7.61

(a) (b)

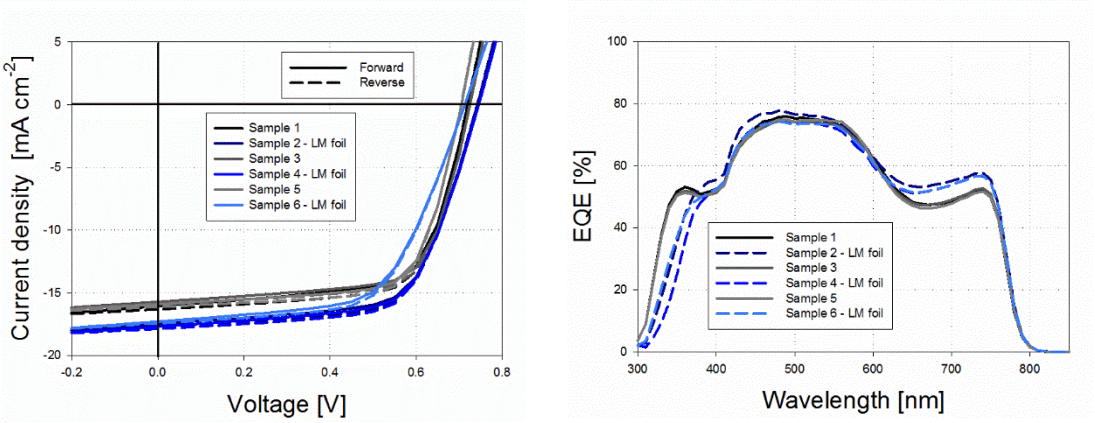

(c)

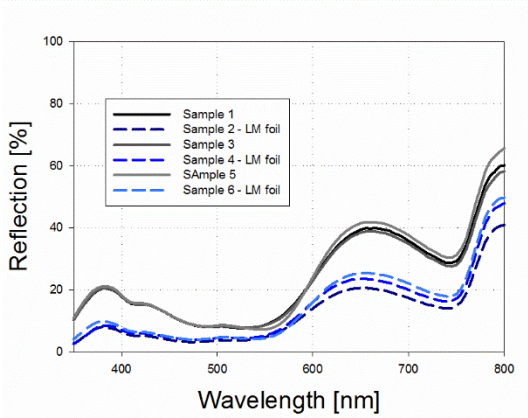

Figure B 2: (a) *J*-*V*, (b) EQE and (c) *R* measurements of the additional PEDOT:PSS based perovskite solar cells without (black-ish lines) and with LM foil (blue-ish lines).